Dealloying of Al-based alloys and their mechanisms

A thesis submitted in fulfilment of the requirements for the degree of Doctor of Philosophy

Tingting Song

M.E.

School of Aerospace Mechanical and Manufacturing Engineering

College of Science Engineering and Health

RMIT University

October 2015

Declaration

I certify that except where due acknowledgement has been made, the work is that of the author alone; the work has not been submitted previously, in whole or in part, to qualify for any other academic award; the content of the thesis is the result of work which has been carried out since the official commencement date of the approved research program; any editorial work, paid or unpaid, carried out by a third party is acknowledged; and, ethics procedures and guidelines have been followed.

Tingting Song

29 January 2016

Abstract

Metal based anodes, like tin (Sn), are promising candidate anodes for lithium ion batteries (LIBs) due to their higher specific capacities than traditional graphite electrodes. However, their dramatic volume expansion during lithiation and delithiation could lead to pulverization of the material as well as inadequate cycle life. Materials with nano/microporosity hold promise to accommodate the volume change. This thesis focuses on preparing porous metallic materials for batteries through a dealloying approach. Dealloying is a selective dissolution process, during which one or more active components dissolve from a binary or multicomponent alloy, leaving behind a (nano)porous-structured material enriched in the nobler or less active alloy component(s). In this thesis, porous Sn and nanoporous Cu-Sn composites, which can be used as anodes, and bimodal porous Cu, which can be used as current collector, have been fabricated by dealloying immiscible Al-Sn alloys, ternary Al-Cu-Sn alloy and two-phase Al-Cu alloy, respectively. The dealloying mechanisms of these precursor alloys have been systematically investigated by a variety of means including both ex-situ and in-situ synchrotron X-ray diffraction (XRD). The following findings are most notable.

- **Micro-sized porous Sn (anode material) dealloyed from immiscible Al-Sn alloys**

Dealloying has been extensively employed to synthesize porous noble metals such as Au, Ag and Pt from various forms of precursor materials (e.g. amorphous, solid solution, or intermetallic compound). This study shows that micro-sized porous non-noble Sn metal can be produced by dealloying immiscible Al-Sn alloys in hydrochloric acid (HCl) solutions. The resulting morphology and size of the pores are dependent on the morphology and size of the primary α-Al phase in respective precursor Al-Sn alloys. As a result, the produced porous Sn structures can be manipulated through control of the composition and microstructure of the precursor alloy. The as-dealloyed porous Sn anode showed an outstanding initial charging-discharging capacity and a high coulombic efficiency in preliminary LIB performance tests.

- **Nanoporous Cu-Sn composite structures (anode material) fabricated by concurrent dealloying and realloying of a ternary Al-Cu-Sn alloy**

The concurrence of dealloying and realloying was identified in a ternary $Al_{67}Cu_{18}Sn_{15}$ alloy (at.%) dealloyed in a 5 wt% HCl solution at 70 ± 2 °C compared to dealloying alone in binary Al-Cu alloys. The process led to the fabrication of three-dimensional (3D) nanoporous

Cu_3Sn-Cu-Cu_6Sn_5 composites in the form of self-supporting foils. Both Cu_3Sn and Cu_6Sn_5 phases formed through an accompanied realloying process. The temperature sensitivity of phase formation in the Cu-Sn system was discussed in relation to the literature results obtained from Cu-Sn diffusion couple studies. This study demonstrates the capability of designing and creating nanoporous composite materials *via* dealloying a multicomponent alloy.

- **Bimodal porous Cu materials (current collector) fabricated from annealing-electrochemical dealloying of Al-Cu alloys**

Hierarchical (bimodal) porous Cu materials with micro- and nano-sized pores are desired for a variety of applications (e.g. current collectors in LIBs). An annealing-electrochemical dealloying approach has been developed for the creation of bulk bimodal porous Cu materials from an as-cast hypereutectic $Al_{75}Cu_{25}$ (at.%) precursor alloy, which consists of pre-eutectic Al_2Cu and lamellar eutectic α-Al(Cu)-Al_2Cu. Annealing of the precursor alloy played a critical role in forming the desired microstructure for subsequent electrochemical dealloying for the creation of bimodal porous Cu. Annealing decouples the lamellar eutectic structure and substantially increases the size of the α-Al(Cu) phase which determines the size of the subsequently produced micropores. In addition, annealing at a low temperature ensures low solubility of Cu in α-Al(Cu), which noticeably decreases the critical potential of the $Al_{75}Cu_{25}$ alloy thereby enabling more flexible electrochemical dealloying. A variety of bimodal porous Cu structures were produced using this approach. The most homogeneous bimodal porous Cu structure showed an average ligament width of 52 nm. It was produced by electrochemical dealloying of the annealed $Al_{75}Cu_{25}$ alloy at -0.5 V, which is above the critical potential of the α-Al (Cu) but below that of the Al_2Cu phase.

- **Quantitative assessment *via* synchrotron radiation to understand the dealloying of a two-phase Al-Cu alloy**

Dealloying of Al-Cu alloys in acid solution is a simple method to fabricate nanoporous Cu required as current collectors in LIBs. However, this basic dealloying process has remained unclear due to overlapped diffraction peaks from the Al-Cu phases involved and the inadequate resolution of lab XRD. In this research the dealloying behaviour of a dual intermetallic phase $Al_{65}Cu_{35}$ alloy, which consists of only Al_2Cu and AlCu, has been investigated in a 10 vol.% HCl solution using Synchrotron XRD. The dealloying of Al_2Cu (first dealloyed) and AlCu occurred in sequence and resulted in a hierarchical nanoporous

structure. A hypothesis has been proposed to understand the different dealloying responses from Al_2Cu and AlCu, which are expected to show similar dealloying responses due to their very similar corrosion potentials in HCl solutions. In addition, an α-Cu(Al) solid solution phase was detected as an intermediate phase during the dealloying process Al-Cu alloy which is a new observation. A complete description of the dealloying process of Al-Cu alloys is now possible, thanks to synchrotron studies.

- **Synchrotron-based understanding of the dealloying of Al-Cu alloys with a variety of phase constitutions**

Synchrotron radiation experiments were performed to understand the dealloying process of Al-Cu alloys from the perspective of crystal structure evolution. The crystal structure evolution may alter the expected sequential dealloying behaviours of different intermetallic compounds. For instance, Al_2Cu and AlCu were expected to be dealloyed simultaneously due to their very similar corrosion potentials. However, they were dealloyed in clear sequence (Al_2Cu was dealloyed first). The reason can be attributed to different crystal structure evolution processes. In addition, the crystal structure evolution may have played a significant role in dictating which phase is dealloyable.

- **Synchrotron-based understanding of the dealloying-realloying of $Al_{67}Cu_{18}Sn_{15}$ alloy at different temperatures**

The temperature sensitivity of intermetallic formation in the Cu-Sn system was confirmed by synchrotron studies of the $Al_{67}Cu_{18}Sn_{15}$ alloy subjected to dealloying at different temperatures (55 °C, 70 °C and 90 °C). The lowest temperature at which Cu_3Sn forms in the Cu-Sn system is now lowered to 55 °C. In addition, it has been confirmed that Cu_3Sn forms by the consumption of Cu_6Sn_5 and Cu.

Publications during candidature

Peer-reviewed journal papers

[1] **T. Song**, M. Yan, M. Qian, A dealloying approach to synthesizing micro-sized porous tin (Sn) from immiscible alloy systems for potential lithium-ion battery anode applications, **Journal of Porous Materials**, (2015) 1-7.

[2] **T. Song**, M. Yan, Y. Gao, A. Atrens, M. Qian, Concurrence of de-alloying and re-alloying in a ternary $Al_{67}Cu_{18}Sn_{15}$ alloy and the fabrication of 3D nanoporous Cu-Sn composite structures, **RSC Advances**, 5 (2015) 9574-9580.

[3] **T. Song**, M. Yan, Z. Shi, A. Atrens, M. Qian, Electrochemical dealloying of a ternary $Al_{67}Cu_{18}Sn_{15}$ alloy compared with that of a binary $Al_{75}Cu_{25}$ alloy, **ECS Transactions**, 66 (2015) 23-30.

[4] **T. Song**, M. Yan, Z. Shi, A. Atrens, M. Qian, Creation of bimodal porous copper materials by an annealing-electrochemical dealloying approach, **Electrochimica Acta**, 164 (2015) 288-296.

[5] **T. Song**, M. Yan, N.A.S. Webster, M.J. Styles, J.A. Kimpton, M. Qian, Towards a complete understanding of dealloying of Al-Cu by in-situ and ex-situ synchrotron X-ray diffraction, (ready for submission).

[6] S. Jia, **T. Song**, B. Zhao, Q. Zhai, Y. Gao, Dealloyed Fe_3O_4 octahedra as anode material for lithium-ion batteries with stable and high electrochemical performance, **Journal of Alloys and Compounds**, 617 (2014) 787-791.

[7] S. Jia, **T. Song**, B. Zhao, Q. Zhai, Y. Gao, Regular Fe_3O_4 octahedrons with excellent soft magnetic properties prepared by dealloying technique, **Journal of Alloys and Compounds**, 585 (2014) 580-586.

[8] M. Yan, M. Qian, **T. Song**, M.S. Dargusch, X.S. Wei, Significant α-phase growth confinement in Grade 4 titanium and substantial β-phase refinement in Grade 7 titanium, **MRS Communications**, FirstView (2014) 1-6.

Conference presentations

[1] **T. Song**, M. Yan, Z. Shi, A. Atrens, and M. Qian. Electrochemical dealloying of a ternary $Al_{67}Cu_{18}Sn_{15}$ alloy compared with that of a binary $Al_{75}Cu_{25}$ alloy. Abstract of **227th ECS Meeting**, 24th-28th May 2015, Chicago, USA.

[2] T. Song, M. Yan, N.A.S. Webster, M.J. Styles, J.A. Kimpton, and M. Qian. Time-resolved phase evolution during creation of nanoporous Cu current collectors by a dealloying approach. Abstract of **AOFSRR 2015 in conjunction with User Meeting 2015**, 25th -27th Nov. 2015, Melbourne, Australia.

[3] **T. Song**, M. Yan, N.A.S. Webster, J.A. Kimpton, and M. Qian. Time-resolved phase evolution during creation of nanoporous Cu current collectors by a dealloying approach. Abstract of **Australian Synchrotron User Meeting 2014**, 20th -21st Nov. 2014, Melbourne, Australia.

[4] **T. Song**, M. Yan, D. Wang, M. Qian. A dealloying route to synthesizing microporous tin (Sn) for potential battery anode application. **International Conference on Nano Science & Technology**, 5th -7th Sep. 2013, Beijing, China.

Publications included in this thesis

Chapter 3

1. **T. Song**, M. Yan, M. Qian, A dealloying approach to synthesizing micro-sized porous tin (Sn) from immiscible alloy systems for potential lithium-ion battery anode applications, **Journal of Porous Materials**, (2015) 1-7.

Contributor	Statement of contribution
Author Tingting Song (Candidate)	Designed experiments (70%) Wrote the paper (50%)
Author Ming Yan	Designed experiments (20%) Wrote and edited paper (15%)
Author Ma Qian	Designed experiments (10%) Wrote and edited paper (35%)

Chapter 4

2. **T. Song**, M. Yan, Y. Gao, A. Atrens, M. Qian, Concurrence of de-alloying and re-alloying in a ternary $Al_{67}Cu_{18}Sn_{15}$ alloy and the fabrication of 3D nanoporous Cu-Sn composite structures, **RSC Advances**, 5 (2015) 9574-9580.

Contributor	Statement of contribution
Author Tingting Song (Candidate)	Designed experiments (80%) Wrote the paper (50%)
Author Ming Yan	Designed experiments (10%) Wrote and edited paper (15%)
Author Yulai Gao	Assisted with alloy sample preparation
Author Andrej Atrens	Wrote and edited paper (5%)
Author Ma Qian	Designed experiments (10%) Wrote and edited paper (30%)

3. **T. Song**, M. Yan, Z. Shi, A. Atrens, M. Qian, Electrochemical dealloying of a ternary $Al_{67}Cu_{18}Sn_{15}$ alloy compared with that of a binary $Al_{75}Cu_{25}$ alloy, **ECS Transactions**, 66 (2015) 23-30.

Contributor	Statement of contribution
Author Tingting Song (Candidate)	Designed experiments (80%) Wrote the paper (50%)
Author Ming Yan	Designed experiments (15%) Wrote and edited paper (15%)
Author Zhiming Shi	Assisted with electrochemical dealloying experiment Wrote and edited paper (5%)
Author Andrej Atrens	Wrote and edited paper (5%)
Author Ma Qian	Designed experiments (5%) Wrote and edited paper (25%)

Chapter 5

4. **T. Song**, M. Yan, Z. Shi, A. Atrens, M. Qian, Creation of bimodal porous copper materials by an annealing-electrochemical dealloying approach, **Electrochimica Acta**, 164 (2015) 288-296.

Contributor	Statement of contribution
Author Tingting Song (Candidate)	Designed experiments (80%) Wrote the paper (50%)
Author Ming Yan	Designed experiments (10%) Wrote and edited paper (15%)
Author Zhiming Shi	Assisted with electrochemical dealloying experiment Wrote and edited paper (5%)
Author Andrej Atrens	Wrote and edited paper (5%)
Author Ma Qian	Designed experiments (10%) Wrote and edited paper (25%)

Chapter 6, 6.1

5. **T. Song**, M. Yan, N.A.S. Webster, M.J. Styles, J.A. Kimpton, M. Qian, Towards a complete understanding of dealloying of Al-Cu by in-situ and ex-situ synchrotron X-ray diffraction, (ready for submission).

Contributor	Statement of contribution
Author Tingting Song (Candidate)	Designed experiments (50%) Wrote the paper (50%)
Author Ming Yan	Designed experiments (25%) Wrote and edited paper (15%)
Author Nathan A.S. Webster	Designed experiments (10%) Assisted with synchrotron powder diffraction experiment and refinement analysis
Author Mark J. Styles	Assisted with synchrotron powder diffraction experiment and refinement analysis
Author Justin A. Kimpton	Designed experiments (5%) Assisted with synchrotron powder diffraction experiment
Author Ma Qian	Wrote and edited paper (35%)

Contributions by others to the thesis

No contributions by others.

Statement of parts of the thesis submitted to qualify for the award of another degree

None.

List of Figures

Fig. 2.10 (a) Schematic of sacrificial template assisted technique. (b) SEM image of nickel inverse opal structure forming a film. (c-f) SEM image of nickel inverse opal structures exemplifying the possibility to trigger the window size (and cell wall resp. strut thicknesses) by adjusting the corresponding etching time.

Fig. 2.11 Metallic aerogel and ‘‘aerogel-like’’ structures. (a and b) SEM and (c and d) TEM micrographs of platinum aerogels. (e and f) SEM and TEM micrographs of gold–platinum bimetallic porous structures.

Fig. 2.12 (a) Schematic illustration for the synthesis of nanoporous Cu by a hydrothermal method; (b) proposed formation process of nanoporous Cu during the hydrothermal method; (c) a cross-sectional SEM image with high magnification of the nanoporous Cu film and (d) digital image of the synthesized nanoporous Cu films rinsed in ethanol.

Fig. 2.13 (a) Anthropomorphic figure from Panama, a typical dilute gold alloy artefact and (b) SEM image of the surface of the artefact showing the porous structure of the unburnished depletion gilded surface (The scale bar at the bottom left reads 1µm).

Fig. 2.14 TEM images showing the nanoporous structure of nanoporous Pd from the dealloying of $Al_{80}Pd_{20}$ ribbon samples in 20 wt.% NaOH (a) and 5 wt.% HCl (b) solutions.

Fig. 2.15 SEM micrographs of dealloyed $Ag_{75}Au_{25}$ foam by (a) chemical dealloying and (b) electrochemical dealloying.

Fig. 2.16 Ag-Au phase diagram.

Fig. 2.17 Plan-view SEM images of nanoporous Au samples showing significant structure coarsening upon continued immersion in acid for an extended time (a-d: 5 min - 1 day) after the alloy is completely dealloyed (dealloying was completed after 5 min).

Fig. 2.18 SEM images showing the microstructure of nanoporous Au obtained through the electrochemical dealloying of a single Al_2Au phase (a) and a single AlAu phase (b) in the 10 wt.% NaCl solution at the potential of 1.5 V.

Fig. 2.19 Cross-sectional SEM images showing the microstructures of as-dealloyed $Al_{40}Ag_{60}$ (consisting of single Ag_2Al phase) ribbon sample (a, b) and $Al_{50}Ag_{50}$ (consisting of Ag_2Al and α-Al(Ag) phases) ribbon sample (c, d).

Fig. 2.20 Schematic illustrations showing the microstructure of (a) the starting $Al_{60}Au_{40}$ alloy and (b) nanoporous Au by chemical dealloying of $Al_{60}Au_{40}$. The starting $Al_{60}Au_{40}$ alloy is composed of Al_2Au and AlAu, and the primary Al_2Au is surrounded by AlAu. The resulting nanoporous structure comprises two kinds of microstructures: nanoporous Au1 (NPG 1) and nanoporous Au2 (NPG 2) with different length scales of ligaments/channels. The dealloying of Al_2Au and AlAu results in the formation of NPG 1 and NPG 2, respectively.

Fig. 2.21 SEM images of nanoporous samples dealloyed from (a) $Au_{25}Ag_{75}$ and (b) $(Pt_{0.05}Au_{0.95})_{25}Ag_{75}$ respectively. Both samples were dealloyed in 1 M $HClO_4$ aqueous solution at 1.03 V.

Fig. 2.22 (a) Schematic illustration shows the current/potential behavior of a single phase alloy undergoing selective dissolution. The critical potential (E_{crit}) corresponds to that associated with the knee in the curve and is not sharply defined. The shape of the knee is affected by sweep rate, alloy, and electrolyte composition. The dashed vertical lines indicate typical ambiguity in defining E_{crit}. (b) Tafel polarization curves of single phase alpha-Mg solid solution and Mg_2Cu intermetallics in the HCl solution.

Fig. 2.23 SEM images showing the microstructure of nanoporous Au by electrochemical dealloying the Al_2Au alloy in the 1 M NaCl solution at the temperature of 273 K at the potential of -0.15 V (a) and 0.05 V (b).

Fig. 2.24 Micrographs of $Au_{37.5}Ag_{62.5}$ films after annealing treatment and dealloying treatment showing that the annealing treatment of precursor alloy mitigates the formation of microscale voids during dealloying.

Fig. 2.25 Ligament size modulation by different annealing treatments: (a) as-dealloyed (15 nm), (b) after annealing at 300 °C for 2 min (50 nm), (c) after annealing at 300 °C for 30 min (150 nm) and (d) Vickers microhardness, H_v of nanoporous Au versus the ligament size, L.

Fig. 2.26 Binary Al-Sn and Al-Cu phase diagram and the selection of compositions.

Fig. 2.27 Simulated evolution of an artificial pit in Au10%Ag90% (at.%), f = 1.8 eV. Cross-sections along the $(11\bar{1})$ plane defined by the yellow line in (a) are shown below each plan view. (a) The initial condition is a surface fully passivated with gold except within a circular region (the artificial pit). (b) After 1 s, the pit has penetrated a few monolayers into the bulk. We note how there are fewer gold clusters near the side wall than at the center of the pit. (c)

Fig. 4.1.3 (a) SEM image showing preferential de-alloying of α-Al(Cu) (circled); (b) remnants of Sn (arrowed) and nanoporous Cu_3Sn and Cu on Al_2Cu substrate; (c) and (d) surface nanoporous structures after 120 min and 180 min de-alloying.

Fig. 4.1.4 (a) and (b) surface nanoporous structures of Cu_3Sn-Cu-Cu_6Sn_5; (c) inhomogeneous microstructure on the cross section; (d) TEM SAED results of Cu_3Sn and Cu_6Sn_5 after 240 min de-alloying; and (e) and (f) inhomogeneous microstructure after 300 min of de-alloying.

Fig. 4.1.5 Nanoporous structures of Cu_3Sn-Cu-Cu_6Sn_5 produced after 480 min de-alloying: (a) and (b) surface; (c) and (d) cross section; (e) bright field (BF) TEM image confirming the nanoporous structure; and (f) HRTEM image and TEM SAED results of Cu_3Sn and Cu_6Sn_5 phases. The nanoporous Cu_3Sn-Cu-Cu_6Sn_5 composite is produced in the form of self-supporting foils (0.6 mm thick and 8 mm in diameter).

Fig. 4.2.1 (a) XRD pattern and (b) SEM BSE microstructure of the $Al_{67}Cu_{18}Sn_{15}$ precursor consisting of α-Al, Al_2Cu and Sn; (c) and (d) EDX spectra of the Al_2Cu (I) and the mixture of three phases (II) marked in (b), respectively.

Fig. 4.2.2 (a) Polarization curves that define the E_{crit} values for the $Al_{67}Cu_{18}Sn_{15}$ precursor (-0.82 V), pure Al (-0.66 V), pure Sn (-0.55 V) and as-cast Al_2Cu (-0.41 V). (b) The E_{crit} values for each material and the two applied potentials selected for electrochemical dealloying.

Fig. 4.2.3 (a) Phase distribution of the $Al_{67}Cu_{18}Sn_{15}$ sample electrochemically dealloyed at -0.5 V with EDX information for resultant I and II phases (see Fig. 4.2.1(b)); (b) high-magnified SEM image of (a) showing preferential dealloying of α-Al.

Fig. 4.2.4 (a) SEM BSE image of the sample electrochemically dealloyed at -0.2 V showing two types of morphologies; (b) EDX results showing similar composition for the two types of structure in (a); (c) nanoporous Cu with an average width of 29 ± 7 nm and scallop-type Cu_6Sn_5 phase on the substrate of nanoporous Cu in I; (d) inhomogeneous and coarsened porous structure in II.

Fig. 4.2.5 (a) Current responses of the $Al_{67}Cu_{18}Sn_{15}$ alloy and the $Al_{75}Cu_{25}$ alloy during electrochemical dealloying; (b) charge density values when the current density decreased to 2.7 mA cm^{-2} at each applied potential. The data related to $Al_{75}Cu_{25}$ alloy is from Ref (7).

Fig. 5.1 (a) Al-Cu phase diagram showing the phase constitution information of $Al_{75}Cu_{25}$ and $Al_{67}Cu_{33}$ alloys and the solubility of Cu in α-Al at both the eutectic temperature and 490 °C.

(b) XRD pattern of the as-cast $Al_{67}Cu_{33}$ alloy confirming that the alloy is composed of essentially the $CuAl_2$ phase. (c) Back scattered electron (BSE) image showing the microstructure of the as-cast $Al_{75}Cu_{25}$ consisting of pre-eutectic $CuAl_2$ and eutectic α-Al(Cu)-$CuAl_2$. (d) The lamellar eutectic α-Al(Cu)-$CuAl_2$.

Fig. 5.2 (a) Microstructure of the annealed $Al_{75}Cu_{25}$ alloy consisting of the α-Al(Cu) and $CuAl_2$ phases. The lamellar eutectic α-Al(Cu)-$CuAl_2$ structure disappeared after annealing. (b) and (c) are EDX spectra of the α-Al(Cu) and $CuAl_2$ phases circled in (a), respectively.

Fig. 5.3 (a) Tafel curves that define the E_{crit} values for as-cast $Al_{75}Cu_{25}$ (-0.61 V), as-annealed $Al_{75}Cu_{25}$ (-0.77 V), pure Al (-0.66 V), pure Cu (-0.20 V) and as-cast $CuAl_2$ (-0.41 V) (see Fig. 5.1(a)). (b) Distribution of the E_{crit} values for each material and the three applied potentials selected for electrochemical dealloying.

Fig. 5.4 Bimodal porous structures of Cu electrochemically dealloyed at -0.1 V (a, b) with an EDX spectrum inset in (b) and -0.2 V (c, d). All the images are from second electron (SE) imaging mode.

Fig. 5.5 Bimodal nanoporous structure resulted from dealloying at -0.5 V: (a, b) SEM images; (c, e) Bright field (BF) TEM images confirming the nanoporous structure (an EDX spectrum inset is shown in (c)); (d) TEM SAED results confirming the final crystal structure of Cu (the remaining phase after complete dealloying); and (f) HRTEM image from (e) showing twins in Cu ligaments.

Fig. 5.6 (a) Cyclic Voltammetry (CV) curves for pure Al, as-annealed $Al_{75}Cu_{25}$ and $CuAl_2$. (b) and (c) show the evolution of the CV curves for as-annealed $Al_{75}Cu_{25}$ subjected to 600 cycles of CV measurements.

Fig. 5.7 (a) Current responses of as-annealed $Al_{75}Cu_{25}$ alloy during electrochemical dealloying; (b) charge density *vs.* time curves derived from (a); and (c) charge density values when the current density decreased to 2.7 mA cm^{-2} at each applied potential.

Fig. 6.1.1 Creation of hierarchical nanoporous Cu from dealloying of two-phase Al65Cu35. (a) Laboratory XRD patterns of the Al65Cu35 alloy before and after 120 min dealloying in a 10 vol.% HCl solution. The tick marks indicate the position and intensity of Bragg peaks of Al_2Cu (PDF#65-2695), AlCu (PDF#65-1228) and Cu (PDF#04-0836) phases. (b) Backscattered electron (BSE) image of the microstructure of the as-cast Al65Cu35

precursor alloy consisting of primary AlCu and Al_2Cu matrix. (c) Hierarchical nanoporous structures of Cu from dealloying of AlCu (surrounded by dash lines) and Al_2Cu phases in Al65Cu35 alloy respectively. (d) High magnification SEM image of the nanoporous structure from the dealloying of Al_2Cu phase.

Fig. 6.1.2 Figure 2 Experimental set-up for synchrotron in-situ dealloying and time-resolved sequential evolution of Al_2Cu and AlCu in Al65Cu35. (a) The synchrotron data is collected continuously while the heated electrolyte solution is re-circulated through the mounted alloy sample in the cell. (b) In-situ phase evolution for the dealloying of the Al65Cu35 alloy, which consists of Al_2Cu and AlCu, in a 5 wt.% HCl solution at 70 °C (X-ray wavelength = 0.7745 Å) (the fluctuations in intensity of, for example, the Al_2Cu peak at ~10°2θ, is caused by rocking of the sample stage ± 2° about its axis for improvement of data quality).

Fig. 6.1.3 Quantified sequential evolution of Al_2Cu and AlCu in Al65Cu35. (a) Ex-situ SXRD patterns of Al65Cu35 alloy powders after dealloying in a 10 vol.% HCl solution from 10 min to 40 min (X-ray wavelength = 0.6891 Å). (b) Rietveld refinement output of the Al65Cu35 precursor powder sample data using the TOPAS-Academic software. The black, red and grey solid lines indicate the observed and calculated patterns and their difference, respectively. The tick marks indicate the position of the Bragg reflection markers for Al_2Cu (upper) and AlCu (lower). (c) An expanded region of the fit in (b) between $19.1° \leq 2\theta \leq 19.9°$ showing the unidentified phase in the sample which can affect the fitting. (d) evolution of the Cu content, as a proportion of the total Cu available, in each of the Al_2Cu, AlCu and Cu phases from refinement analysis of each pattern in (a). (e) The microstructure of the as-dealloyed Al65Cu35-40 min sample consisting of the nanoporous structure from the dealloying of Al_2Cu and the un-dealloyed AlCu with just a rough surface. (f) and (g) EDX spectra of the as-dealloyed AlCu and Al_2Cu phases in (e), respectively.

Fig. 6.1.4 Sequential evolution of Al_2Cu and AlCu in Al55Cu45. (a) In-situ phase evolution for the dealloying of the Al55Cu45 alloy, which consists of Al_2Cu and AlCu, in a 5 wt.% HCl solution at 70 °C (X-ray wavelength = 0.7745 Å). (b) Ex-situ SXRD patterns of Al55Cu45 alloy powders after dealloying in a 10 vol.% HCl solution from 10 min to 60 min (X-ray wavelength = 0.6891 Å); (c) Evolution of the Cu content, as a proportion of the total Cu available, in each of the Al_2Cu, AlCu and Cu phases from refinement analysis of each pattern in (b).

Fig. 6.1.5 Schematic maps showing the unit cell evolution. The smaller red ball represents the Cu atom and the larger grey ball represents the Al atom. During dealloying of body-centered tetragonal Al_2Cu and base-centered monoclinic AlCu, once all Al atoms are removed, the residual Cu atoms may temporarily assume a precursor crystal structure and then evolve into a face-centered cubic crystal structure.

Fig. 6.1.6 Formation kinetics of Cu phase. (a) The development of the peak area of the Cu (111) diffraction peak as a function of dealloying time from the in-situ dealloying of Al65Cu35 in Figure 2(b). (b) The plot of Avrami-Erofe'ev equation to determine the value of the *n* parameter for the formation of Cu from dealloying of Al65Cu35. (c) The development of the peak area of the Cu (111) diffraction peak as a function of dealloying time from the in-situ dealloying of Al55Cu45 in Figure 4(a). (d) The plot of Avrami-Erofe'ev equation to determine the value of the *n* parameter for the formation of Cu from dealloying of Al55Cu45. The time of 840 s and 960 s for the observation of first Cu (111) peak in Figure 2(b) and Figure 4(a) is considered as the induction time t_0 for the formation of Cu. The area of Cu (111) diffraction peak was normalized considering the area in the final pattern of the in-situ dataset as one. The Cu (111) peak area fluctuations in both cases (Figure 6(a,c)) are due to the rocking the sample stage ± 2° about its axis during the in-situ experiments. The two *n* values for both cases (Figure 6(b,d)) indicates two kinetics during the formation of Cu from dealloying approach. A full discussion of the data is presented in the text.

Fig. 6.1.7 Consequences of diffusion of Cu. (a) Bright field (BF) TEM image of Al65Cu35-40 min sample with twins in the ligaments. (b) Corresponding HRTEM image showing twins in Cu ligaments. (c) Rietveld refinement output of Al65Cu35-40 min sample considering the isotropic broadening of Cu peaks and (d) anisotropic broadening of Cu (002) peak. The better fitting of (d) clarifies the anisotropic broadening in Cu diffraction peaks as a result of the presence of twins in the as-dealloyed samples.

Fig. 6.1.S1 (a) Rietveld plot of the Al65Cu35-10 min sample and (b) the peak broadening of Al_2Cu phase due to the uneven particle sizes.

Fig. 6.1.S2 (a) Rietveld plot of the Al65Cu35-20 min sample and (b) evidence of anisotropic broadening of (002) diffraction peak.

Fig. 6.1.S3 Rietveld plot of the Al65Cu35-40 min sample.

Fig. 6.1.S4 (a) Rietveld plot of the Al55Cu45-0 min sample and (b) expanded regions showing unidentified phases.

Fig. 6.1.S5 (a) Rietveld plot of the Al55Cu45-10 min sample and (b) expanded regions showing unidentified phases.

Fig. 6.1.S6 (a) Rietveld plot of the Al55Cu45-20 min sample, (b) expanded regions showing unidentified phases and (c) evidence of anisotropic broadening of (002) diffraction peak.

Fig. 6.1.S7 (a) Rietveld plot of the Al55Cu45-30 min sample, (b) expanded regions showing unidentified phases and (c) evidence of anisotropic broadening of (002) diffraction peak.

Fig. 6.1.S8 (a) Rietveld plot of the Al55Cu45-60 min sample, (b) expanded regions showing unidentified phases and (c) evidence of anisotropic broadening of (002) diffraction peak.

Fig. 6.2.1 In-situ phase evolution during the dealloying of the $Al_{75}Cu_{25}$ alloy, which consists of α-Al(Cu) and Al_2Cu, in a 5 wt.% HCl solution at 70 °C (the unlabelled peaks all correspond to the Al_2Cu phase).

Fig. 6.2.2 In-situ phase evolution for the dealloying of the $Al_{45}Cu_{55}$ alloy, which consists of AlCu and Al_4Cu_9, in a 5 wt.% HCl solution at 70 °C.

Fig. 6.2.3 In-situ phase evolution during dealloying of the $Al_{67}Cu_{18}Sn_{15}$ alloy in a 5 wt.% HCl solution at 55 °C (♦: a mixture of Cu_6Sn_5 and Cu_3Sn).

Fig. 6.2.4 In-situ phase evolution during the dealloying of the $Al_{67}Cu_{18}Sn_{15}$ alloy in a 5 wt.% HCl solution at 70 °C (∗: a mixture of Cu_6Sn_5, Cu_3Sn and Cu).

Fig. 6.2.5 Ex-situ phase evolution during the dealloying-realloying of the $Al_{67}Cu_{18}Sn_{15}$ alloy in a 10 vol.% HCl at 90 °C.

Fig. 6.2.6 (a-c) Examples of refinement analysis of synchrotron spectra with phase compositions, and (d) the evolution of phase compositions with increasing dealloying time.

List of Tables

Keywords

dealloying, immiscible alloys, Al–Sn alloys, porous tin, anode, annealing-electrochemical, bimodal, realloying, Cu-Sn composites, synchrotron radiation, intermetallic, phase transformation, crystal structure evolution

Australian and New Zealand Standard Research Classifications (ANZSRC)

ANZSRC code: 091207, Metals and Alloy Materials, 100%

Fields of Research (FoR) Classification

FoR code: 0912, Materials Engineering, 100%

Table of Contents

Chapter 1 Introduction

1.1 Background

Porous metals have found significant applications in various industrial sectors. Owing to the decisive roles of the high specific surface area in the applications, nanoporous metals with higher specific surface areas have attracted considerable attention over the last two decades. Currently nanoporous metallic materials are manufactured mainly by electrodeposition, nanoporous template scarification or the hydrothermal approach [1]. They are confined to the fabrication of nanoporous thin films (thinner than 500 nm in most cases) while being time-consuming and costly [1]. Dealloying (the selective dissolution approach) [2] is free of this restriction and it offers three other important advantages compared to these approaches: (i) easier and more practical to manufacture wide ranges of porous metallic structures (from nanoscale to micrometerscale) [3]; (ii) easier to adapt to new designs in terms of pore structures by changing either the precursor alloy composition or the electrolyte concentration or dealloying temperature [4]; and (iii) more flexible to produce either monolith nanoporous samples or nanoporous surfaces for different applications [5]. As a result, dealloying has been widely accepted as the most promising and practical approach to the manufacture of nano/microporous metallic materials.

Metal based anodes, like tin (Sn), are considered as promising candidate anode materials for lithium ion batteries (LIBs) due to their much higher specific capacities (i.e. 994 $mA{\cdot}h\ g^{-1}$ of Sn) than commercialized graphite electrodes (372 $mA{\cdot}h\ g^{-1}$) [6]. The main challenge for the implementation of metallic anodes is their dramatic volume expansion during lithiation and delithiation, which may lead to pulverization of the anode materials and, in turn, inadequate cycle life. Materials (e.g. Sn-based anodes, Cu-based current collectors) with nano/microporosity hold promise to accommodate such volume change [7-9]. In this regard, dealloying offers a unique approach to the fabrication of such porous metals for applications as current collectors and anodes in LIBs.

The new porous metallic materials to be created in this thesis project are aimed for such applications. However, it should be emphasized that the new knowledge and innovative methods to be developed are expected to significantly advance the knowledge base of the dealloying field.

1.2 Aims and objectives

Research on dealloying over the last decade has been largely focused on dealloying of the Ag-Au solid solution alloys [2, 10-14] to produce nanoporous structures of essentially pure Au, and understand the dealloying process. Dealloying of other precursor alloy systems has the potential to produce functional nanoporous metals and/or composites for various applications. In addition, the dissolution and diffusion behaviours during dealloying of these alloys are expected to differ from those established for dealloying of Ag-Au solid solution alloys. Understanding their dealloying characteristics is essential for the fabrication of advanced nanoporous metallic materials as well as enhancing the knowledge base of dealloying. In terms of methodology, conventional characterization methods like lab X-ray diffraction (XRD) are insufficient to reveal the detailed phase transformation and/or evolution processes due to the involvement of multiple crystalline phases and the complexity caused. Analytical means with a much higher resolution, such as synchrotron radiation, are required for such purposes.

The main objectives of this thesis include:

- to investigate the dealloying process of immiscible Al-Sn system and create porous Sn structures as potential anode materials in LIBs;
- to investigate the dealloying process of a ternary Al-Cu-Sn alloy and prepare nanoporous-structured Cu-Sn composites to buffer the volume expansion of Sn during the performance of LIBs;
- to understand the dealloying process of a two-phase Al-Cu system (one solid solution + one intermetallic, or two intermetallics) and prepare nanoporous Cu which can be used as current collectors in LIBs to accommodate the volume change of anode attached on the surface of them;
- to better understand the dealloying mechanism *via* in-situ/ex-situ synchrotron radiation and other means. This is critical for the precursor alloy design and the fabrication of advanced functional nanoporous metallic materials.

1.3 Thesis outline

This thesis is composed of seven chapters. Chapter 1 briefly introduces the background and objectives of this thesis. Chapter 2 provides a literature review of the requirements for porous metallic materials to be used in LIBs, current approaches to fabricating porous metallic

materials, dealloying methods and the current understanding of the dealloying mechanisms. Chapters 3, 4 and 5 investigate the dealloying of immiscible Al-Sn, ternary Al-Cu-Sn and two-phase Al-Cu alloys, respectively, based on the requirements for Sn-based and Cu-based porous metallic materials for LIBs applications. Chapter 6 focuses on the mechanism study of dealloying of the Al-Cu alloys with a variety of phase constitutions and of the Al-Cu-Sn alloys at different temperatures *via* in-situ and ex-situ synchrotron experiments. It provides new experimental findings related to phase transformation and/or crystal structure evolution during dealloying. Finally, Chapter 7 summarises the findings of this thesis and proposes future studies.

References

[1] C. Zhu, D. Du, A. Eychmüller, Y. Lin, Engineering ordered and nonordered porous noble metal nanostructures: Synthesis, assembly, and their applications in electrochemistry, Chem. Rev., 115 (2015) 8896-8943.

[2] H.W. Pickering, C. Wagner, Electrolytic dissolution of binary alloys containing a noble metal, J. Electrochem. Soc., 114 (1967) 698-706.

[3] Z. Qi, C. Zhao, X. Wang, J. Lin, W. Shao, Z. Zhang, X. Bian, Formation and characterization of monolithic nanoporous copper by chemical dealloying of Al-Cu alloys, J. Phys. Chem. C, 113 (2009) 6694-6698.

[4] T. Song, Y. Gao, Z. Zhang, Q. Zhai, Dealloying behavior of rapidly solidified Al-Ag alloys to prepare nanoporous Ag in inorganic and organic acidic media, CrystEngComm, 13 (2011) 7058-7067.

[5] J. Spradlin, W.K. Lye, M. Reed, M. Hudson, Nanoporous layers using thermal dealloying, US Patent 20060193889 A1(Priority date: November 13, 2002) 2006.

[6] W.J. Zhang, A review of the electrochemical performance of alloy anodes for lithium-ion batteries, J. Power Sources, 196 (2011) 13-24.

[7] S. Zhang, Y. Xing, T. Jiang, Z. Du, F. Li, L. He, W. Liu, A three-dimensional tin-coated nanoporous copper for lithium-ion battery anodes, J. Power Sources, 196 (2011) 6915-6919.

[8] H.C. Shin, M. Liu, Three-dimensional porous copper-tin alloy electrodes for rechargeable lithium batteries, Adv. Funct. Mater., 15 (2005) 582-586.

[9] L.J. Gibson, M.F. Ashby, Energy absorption in cellular materials, in *Cellular Solids: Structure and Properties*, Cambridge university press. (2001) pp. 309-343.

[10] H.W. Pickering, P.J. Byrne, On preferential anodic dissolution of alloys in the low-current region and the nature of the critical potential, J. Electrochem. Soc., 118 (1971) 209-215.
[11] J. Erlebacher, M.J. Aziz, A. Karma, N. Dimitrov, K. Sieradzki, Evolution of nanoporosity in dealloying, Nature, 410 (2001) 450-453.
[12] S. Parida, D. Kramer, C.A. Volkert, H. Rösner, J. Erlebacher, J. Weissmüller, Volume change during the formation of nanoporous gold by dealloying, Phys. Rev. Lett., 97 (2006) 035504.
[13] E. Detsi, S. Punzhin, J. Rao, P.R. Onck, J.T.M. De Hosson, Enhanced strain in functional nanoporous gold with a dual microscopic length scale structure, ACS Nano, 6 (2012) 3734-3744.
[14] Z. Qi, U. Vainio, A. Kornowski, M. Ritter, H. Weller, H. Jin, J. Weissmüller, Porous gold with a nested-network architecture and ultrafine structure, Adv. Funct. Mater., 25 (2015) 2530-2536.

Chapter 2 Literature review

A wide variety of porous materials exists in nature such as woods, human and animal bones, plant leaves, and stalks [1]. The porous structures in these materials with the pore size varying from nanoscale to microscale carry out various unique functions. For example, they serve as channels of supply of nutrition, offer lightweight but strong structures, and provide the required permeability to air and water. Fig. 2.1 shows the porous structures in the eggshells of hoopoes [2] and the leaves of walnut trees [3]. Materials researchers and designers have been turning to nature for inspiration to design and develop advanced materials for many decades. As a result, a big family of biomimetic materials including porous metals have been developed for various applications.

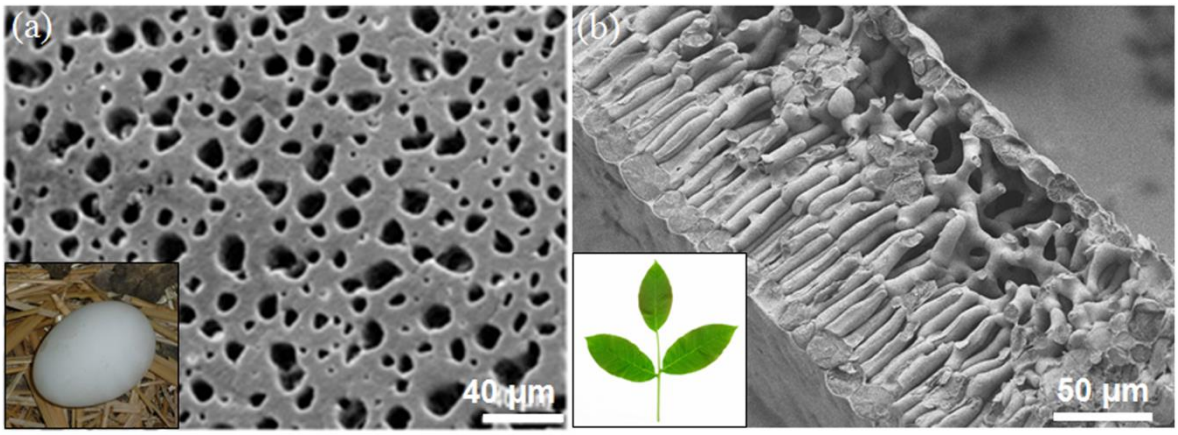

Fig. 2.1 (a) Porous structures on the surface of eggshells of hoopoes which provide flexibility, mechanical performance and matter exchange avenues with the outside [2]; (b) A cross-sectional view of the porous structures of the walnut tree leaf which offer frost resistance, thermal isolation and moisture transport [3].

Porous Copper (Cu) structures or Cu foams with micrometre- to millimetre-sized pores significantly outperform dense Cu materials in a number of applications because of their higher surface area per unit volume which favours efficient heat conduction, mass transformation and accommodation for volumetric expansion [4, 5]. For example, heat sinks utilizing lotus-type porous Cu with pore diameters of several tens of micrometres exhibit outstanding cooling performance (6.5 times better than conventional dense Cu) [6]. The Cu foam (with pore diameters of ten micrometres) current collector in lithium ion batteries (LIBs) showed better cyclic performance and higher charge capacity than did a planar Cu foil current collector [4]. Owing to the decisive role of surface area in many critical applications,

nanoporous metallic material, which offers a much higher specific surface area, has attracted extensive interests.

This chapter reviews the requirements for the applications of porous metallic materials in LIBs, the approaches to the fabrication of these porous metallic materials, especially the various dealloying approaches used for the creation of nanoporous structures and the mechanisms behind each these dealloying process.

2.1 The requirements for the applications of porous metallic materials in lithium ion batteries

2.1.1 Introduction to lithium ion batteries

Lithium ion batteries (LIBs) are the primary energy storage devices in the communications, transportation and renewable-energy sectors [7]. The basic working principles of commercialized LIBs are illustrated in Fig. 2.2 [8]. A lithium ion battery can work as an energy storage device by converting electric energy into electrochemical energy. There are three key components in an LIB system: cathode, anode and electrolyte. All Li^+ ions are initially on the cathode side and the battery system is assembled in a "discharged status". While charging, Li^+ ions are extracted from the cathode host; they solvate into and move through the Li^+ conducting electrolyte, and intercalate into the anode host. Meanwhile, electrons also move from the cathode to the anode through the current collector, and an electric circuit is therefore formed. The current collectors play a significant role in generating and transporting current. Copper (Cu) and aluminium (Al) foils are generally used as current collectors designated as anode and cathode, respectively, as shown in Fig. 2.2. The chemical potential of Li is much higher in the anode than in the cathode, thus the electric energy is stored in the form of (electro)chemical energy. Such a process is reversed when the battery is discharging where the electrochemical energy is released in the form of electric energy.

2.1.2 Metallic anode materials in lithium ion batteries

The current choice of anode materials for LIBs is graphite due to its long cycle life, abundant material supply and low cost. However, the graphite anode has the disadvantages of low energy density (375 $mA \cdot h\ g^{-1}$) and safety issues related to lithium deposition [9, 10]. Hence, there has been a growing interest in developing alternative anode materials with low cost, enhanced safety, high-energy density and long cycle life [11].

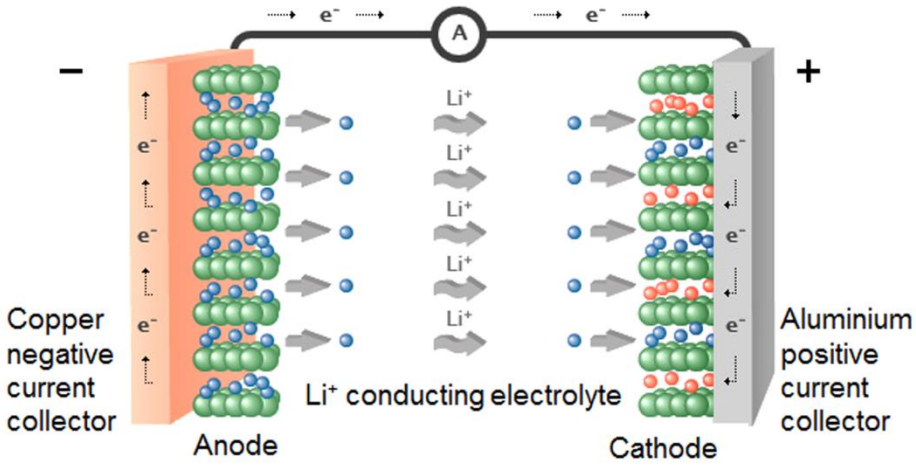

Fig. 2.2 Schematic illustration of the working principle of LIBs (discharging) [8].

Alloy anodes are known for their high specific capacity and safety characteristics [12]. Table 2.1 compares the electrochemical properties of alloy anodes, lithium metal, commercialized graphite and a new anode material, $Li_4Ti_5O_{12}$ (LTO). The theoretical specific capacities of alloy anodes are 2-10 times higher than that of the commercialized graphite, and 4-20 times higher than that of the LTO. The second merit of alloy anodes is their moderate operation potential versus lithium. For example, both Sn and Al anodes have an onset voltage potential of 0.3-0.6 V above Li/Li^+. This moderate potential reduces the safety concern with lithium deposition as with graphite anodes (~ 0.05 V vs. Li) while avoiding the energy penalty of battery cells assembled with the LTO anodes (1.5 V vs. Li).

Table 2.1 Comparison of the theoretical specific capacity, charge density, volume change and onset potential of various anode materials.

Materials	Li	C	$Li_4Ti_5O_{12}$	Si	Sn	Sb	Al	Mg	Bi
Density (g cm^{-3})	0.53	2.25	3.5	2.33	7.29	6.7	2.7	1.3	9.78
Lithiated phase	Li	LiC_6	$Li_7Ti_5O_{12}$	$Li_{4.4}Si$	$Li_{4.4}Sn$	Li_3Sb	LiAl	Li_3Mg	Li_3Bi
Theoretical specific capacity (mA·h g^{-1})	3862	372	175	4200	994	660	993	3350	385
Theoretical charge density (mA·h cm^{-3})	2047	837	613	9786	7246	4422	2681	4355	3765
Volume change (%)	100	12	1	320	260	200	96	100	215
Potential *vs.* Li (~V)	0	0.05	1.6	0.4	0.6	0.9	0.3	0.1	0.8

The main challenge to the implementation of metallic anodes in LIBs is their large volume change during lithium insertion and extraction (see Table 2.1), which often leads to pulverization of the active metallic materials, high initial irreversible capacities (the difference between charge and discharge capacity) and poor cycle stability [12]. Fig. 2.3(a) shows an example of the charge-discharge curves of Si anodes (Si anodes have similar issues as metallic anodes) [13]. The delithiation capacity (charge) is much lower than the lithiation (discharge) capacity at the first cycle. The first-cycle irreversible capacity loss is high (2650 mA·h g^{-1}) and the coulombic efficiency, measured as the ratio of discharge capacity to charge capacity, is only 25%. Furthermore, the capacity decreased quickly during the subsequent cycles. After five cycles, the reversible capacity dropped by 70%, showing poor cycle stability. Similar observations occurred to other alloy systems. Fig. 2.3(b) shows typical cracks (white network-like channels) in a Si anode resulted from the large volume change during lithium insertion and extraction, similar to a dried lake bed shown in Fig. 2.3(c) [14].

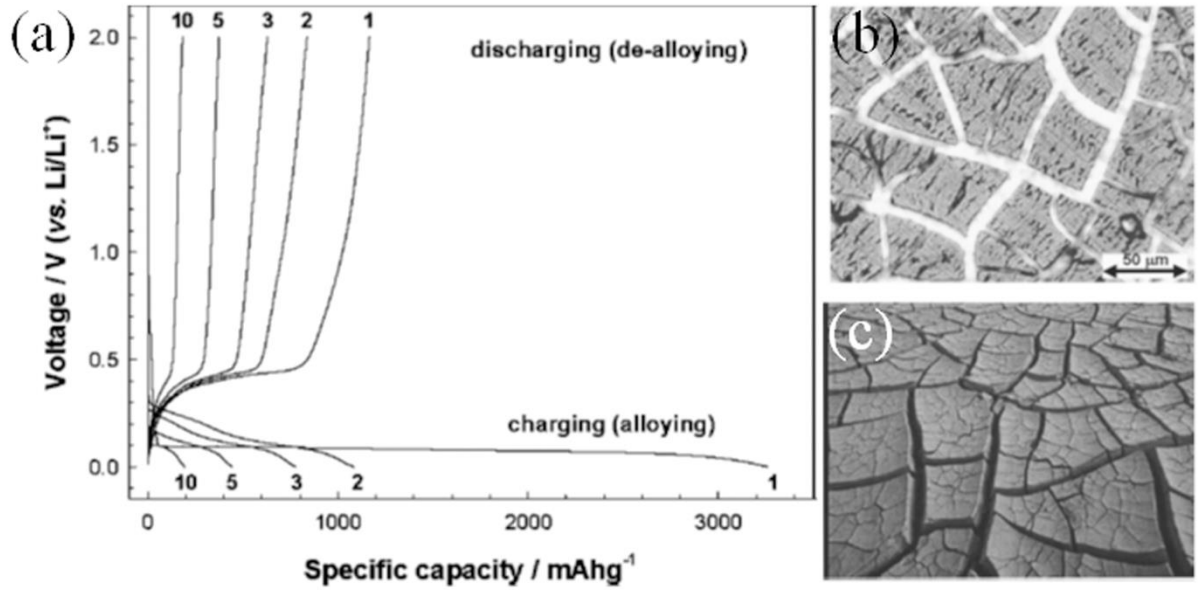

Fig. 2.3 (a) Charge/discharge voltage profiles obtained from Si powder anode; (b) An optical micrograph showing the resemblance between a Li-alloy film after expansion and contraction; (c) A cracked dry lake bed [14].

Electrode pulverization as reported in Refs. [12-14] is not unexpected when one considers the atom uptake of each anode material atom during the lithiation process. In contrast to a generic insertion process of Li^+ in an open oxide framework (MO_2 + Li = $LiMO_2$) which comes with a 33% rise in the number of atoms, a metallic atom (such as Sn) has to accommodate 4.4 Li atoms (e.g. 4.4Li + Sn = $Li_{4.4}Sn$: 440% rise in the number of atoms). In addition, the atomic

radius of Li (2.05 Å) is much greater than that of each commonly studied host atom (Sn: 1.72 Å, Si: 1.46 Å, Pb: 1.81 Å, Sb: 1.53 Å and Al: 1.82 Å). A lithiated particle thus has a much larger radius than the original unlithiated one. Both of the large atomic uptakes and large differences in atomic radius contribute to high volume changes [11]. These considerations suggest that the increase in the specific volume of electrode particles during an alloying reaction is intrinsic to the process itself.

Without a doubt, the high theoretical capacities expected from the formation of binary Li-richest Li_xM compounds are appealing for high-energy storage applications. In order to capitalize on this process (i.e. the formation of the Li-richest Li_xM binary compounds), it is essential to address the large volume change issue discussed above.

2.1.3 Porous metallic materials in lithium ion batteries

As pointed out earlier, to take advantage of the high specific capacities of alloy anodes, the dramatic volume expansion during lithiation must be mitigated. As shown in Fig. 2.4 [15], the porous structure (shown as FOAM in Fig. 2.4) is able to absorb and release the kinetic energy through progressive plastic yielding, as opposed to the rupture of a fully dense elastic solid. Porous materials thus hold promise for helping to address the large volume change issue. This may be realized by (1) application of 3D porous (from micrometre to millimetre) current collector or anode structures, (2) application of nanoporous metal current collector or anode structures, and (3) application of nanoporous composite anode materials.

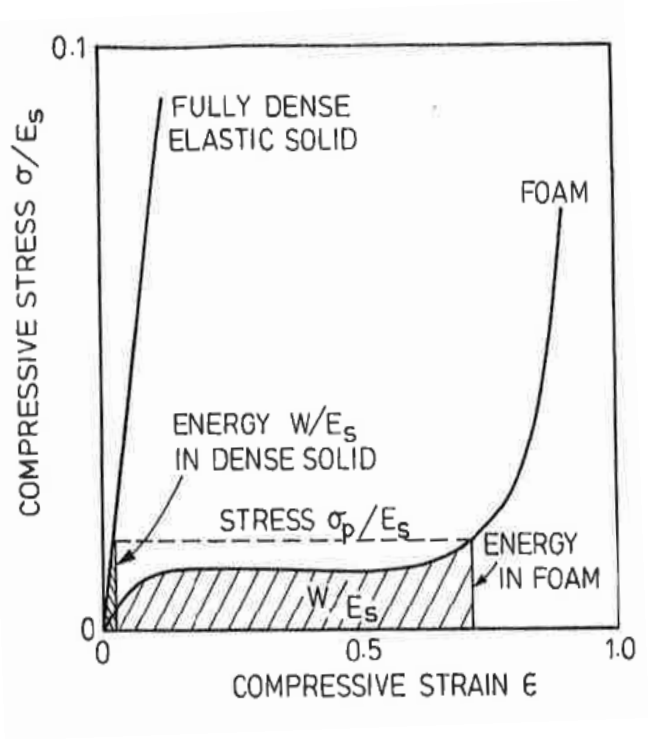

Fig. 2.4 Compressive stress-strain curves for fully dense elastic solid and foam material [15].

2.1.3.1 Current application of 3D porous (from micrometre to millimetre) current collector or anode structures

One way to overcome the problem of large volume expansion is to design 3D porous structures with sufficient porosity to accommodate the volume expansion/contraction. In some studies, Sn-based [16, 17] or Si-based [18-20] anode materials were fabricated into porous structures to improve their electrochemical stability performance. Various porous current collectors [21, 22] have been employed as well. The cycle performance of anodes using a porous substrate was significantly improved compared to those deposited on a planar collector [21, 22]. For example, silicon particles (~4 μm) electroless deposited and then sealed (by pressing) on an Cu foam current collector showed a stable cycle life of over 200 cycles at a reversible capacity of ~ 2500 mA·h g^{-1} while that on a Cu foil current collector only lasted for less than 20 cycles (see cycling test in Fig. 2.5(a)) [21]. Its working principle is illustrated in Fig. 2.5(b). However, the current size of porous structure or template is normally greater than 100 μm and the presence of a large volume of pores in the porous structure decreases the total volumetric energy density of the cell. Therefore, the challenge for porous structure electrodes and current collectors is to increase the active material loading to a practically acceptable level [23]. In addition, it should be noted that the electrodeposition

process of active materials is complex, and many chemicals that are involved in the process procedure may not be viable for the commercialization of LIBs.

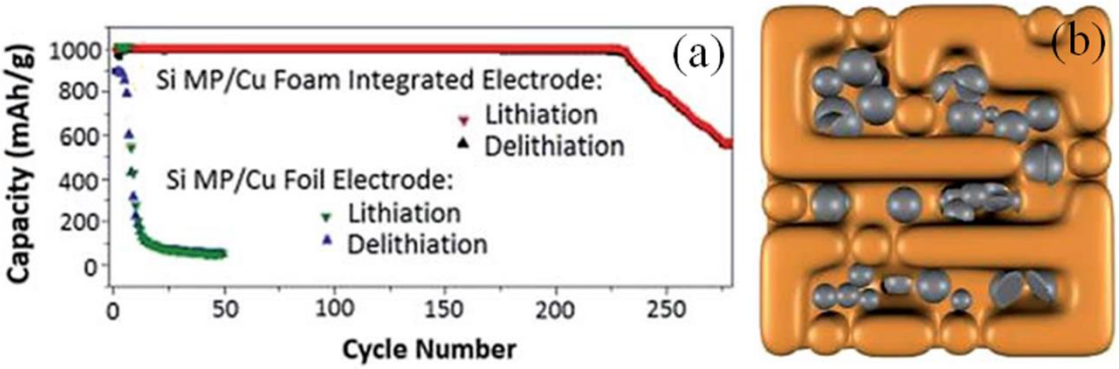

Fig. 2.5 (a) Constant lithiation and delithiation performance of Si anode using 3D porous Cu current collector and traditional one and (b) a schematic showing the design of Si particles sealed in porous Cu current collector [21].

2.1.3.2 Nanoporous metal current collector or anode structures

Nanostructured materials have unique advantages in mass transport including easier diffusion of electrons and lithium ions, higher electrode/electrolyte interfacial contact area and better accommodation of structural strain during lithiation/delithiation reactions [18, 24, 25]. It has been confirmed by many studies that reducing the active particle size to nanoscale can significantly improve the cycle performance of anodes, especially when an agglomeration of the particles is inhibited by a composite matrix [26, 27]. An early study by Yang et al. [28] found that when the particle size of Sn powders was decreased from 3 μm to 300 nm, the number of stable cycles increased from 3 to 70 (see Fig. 2.6).

The improved cycle stability is attributed primarily to the ability of nanosized particles to accommodate large stress and strain without cracking [29, 30]. As the grain size is decreased to the nanoscale, the yield and fracture strengths of metals and alloys may increase dramatically because the motion and pile-ups of dislocations are constrained or eliminated in nanosized grains or particles [31]. This implies that nanocomposite anodes have the potential to sustain much higher stress before pulverization. In fact, cracking has rarely been observed in nanosized alloy anodes. In addition, a smaller particle size reduces the electronic and ionic transport distance and reduces the stress or strain induced by inhomogeneous diffusion of Li ions [32, 33]. The high density of grain boundaries in nanocomposites also provide fast

diffusion paths for Li^+ ions and they can act as additional Li-storage sites as well [34]. Lithium insertion at grain boundaries may also reduce the total volume expansion of anodes because the packing density at nanocrystalline boundaries is somewhat lower than that of a perfect crystal by 10-30% [35, 36].

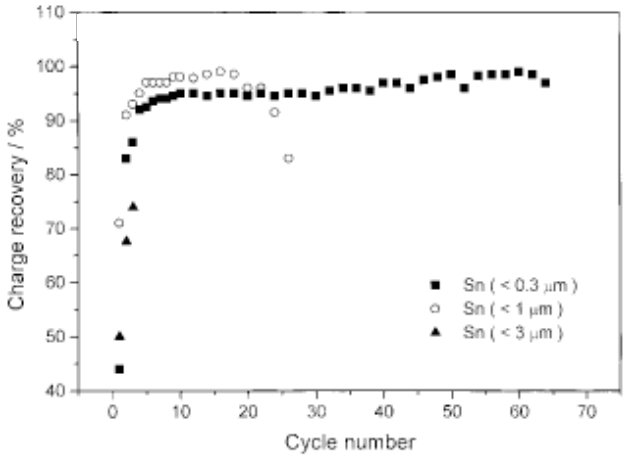

Fig. 2.6 Cycle behavior of Sn powders of various particle sizes [28].

However, it is worth noting that nanosized particles have disadvantages as well, such as the high manufacturing cost and safety issues in handling. Simpler methods to make nanoscale anodes, such as metal foils with nanoscale microstructures throughout the whole sample body, are more desirable in this sense.

2.1.3.3 Nanoporous composite anode materials

Apart from pure metal anodes (A type), the use of a hybrid multi-element or an alloy anode (AB type) is another strategy to reduce the volume change in order to improve the battery performance. The main difference between the AB mode and the A mode lies in the way how the volume expansion develops in the two modes. When Li reacts with element A, only Li_xA intermetallics will form. In contrast, when Li reacts with an appropriate AB material, the uptake of Li can be compensated by the squeezing of B concomitant to the formation of Li_xA binaries. This squeezing can take different forms (amorphous, crystallized, dendrites) but it is generally an efficient way to accommodate the excess volume occupied by Li atoms [37-39]. The mass or volume carried by element B is rightly acting as a buffer.

Fig. 2.7 shows the cyclic performance and charge-discharge behaviour of the Sn-Co alloy electrode deposited on the Cu foam and the pure Sn electrode deposited on the smooth Cu

sheet [40]. Compared to the Sn electrode, the Sn-Co alloy electrode exhibits an outstanding cyclic performance: a charge capacity of 444.7 mA·h g^{-1} is achieved after 50 cycles which corresponds to 91.8% of its initial charge capacity. Moreover, the Sn-Co alloy electrode retains high coulombic efficiency, for example, higher than 95% during the 50 cycles, with the exception of the initial cycle. These results demonstrate that the Sn-Co alloy reversibly reacts with Li in a highly stable way, and the capacity fading caused by volumetric changes of Sn is effectively inhibited. On the other hand, the abrupt degradation of capacity is a typical behaviour for the pure Sn electrode (Fig. 2.7(a)), due to the electrical isolation of Sn from the current collector caused by the pulverization associated with the significant volume changes in Sn during lithiation/delithiation.

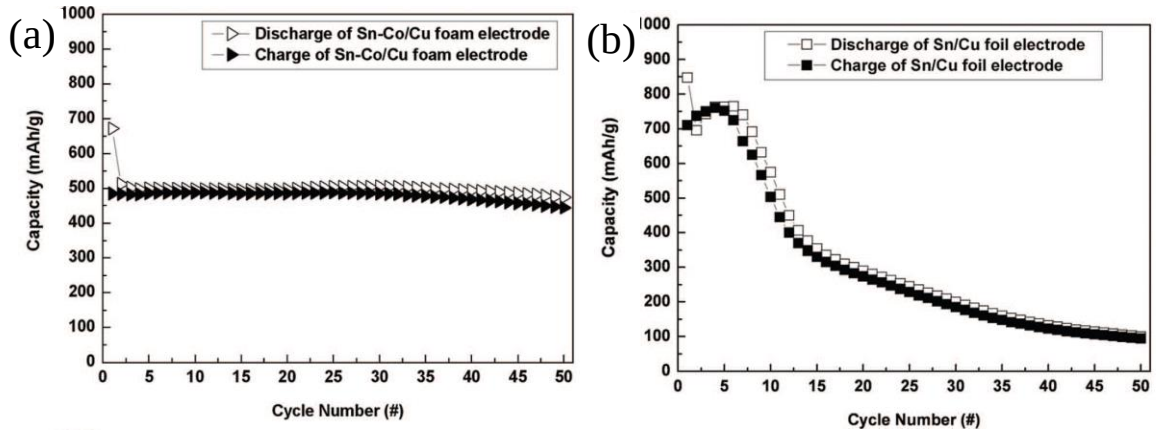

Fig. 2.7 Cyclic performance of (a) a Sn-Co alloy electrode deposited on a Cu foam and (b) a Sn electrode deposited on a smooth Cu sheet [40].

The drawback of this approach is the addition of another non-active element which may decrease the specific capacities [41]. Besides, the normally used electrodeposition technique to prepare the AB material is technically stringent and time and/or economic consuming [40].

2.1.4 Summary

The huge theoretical capacities linked to the formation of the Li-richest Li_xM binary compounds (e.g. $Li_{4.4}Sn$) are very appealing for high-energy storage applications. The associated large energy densities fit the present quest for good cycling behaviour. This goal could be achieved by ways of mitigating the large volume change. This thesis would take Sn anode material as an example and adopt the three solutions in Section 2.1.3 to offer a variety of porous-structured Sn-based anode materials or Cu current collectors for LIBs.

(i) to create porous Sn structures as potential anode materials in LIBs (Section **2.1.3.2 Nanoporous metal current collector or anode structures**)
(ii) to prepare nanoporous-structures Cu-Sn composites to buffer the volume expansion of Sn during the performance of LIBs (Section **2.1.3.3 Nanoporous composite anode materials**)
(iii) to prepare nanoporous Cu current collectors to accommodate the volume change of anode attached on the surface of them (Section **2.1.3.2 Nanoporous metal current collector or anode structures**)

2.2 Porous metallic materials

Selection of a material structure is generally based on requirements of the end-application. Depending upon the targeted applications, there are two types of basic pore-structures of choice: closed-pore structure for structural applications and open-pore structure for functional applications. Closed-pore structure metallic materials provide good mechanical properties but do not allow access to their internal surface. Therefore, they are mostly used in structural, load-bearing applications. Open-pore structure is generally required for functions associated with the interior of the material. Accordingly, open-pore structured materials are mostly used in functional applications where load-bearing capability is not the primary goal. This thesis aims to take advantage of porous metallic materials with open porosity for the reasons of: (i) better accommodation of the volume change during lithium insertion-extraction, with improved cycle life; (ii) higher electrode-electrolyte contact area leading to higher charge-discharge rates; and (iii) shorter path lengths for electronic or Li^+ to transport, which involves the access to the internal surface of pores and the open-pore structure. In general, open-pore structured metallic materials can be classified into metal sponges (micro-millimeter porous metals) and nanoporous metals according to the difference in their pore sizes. The following sections will discuss the major approaches developed so far for the fabrication of open-pore structured metallic materials.

2.2.1 Metal sponges

Most techniques applied nowadays to fabricate metal sponges are based on using a template structure. Polymeric sponges (typically prepared from polymeric foams by removal of the cell faces) are often applied as templates, either for the preparation of a castable mould (replication e.g., by investment casting) or for the direct deposition of the metal on the polymeric sponge, followed by its removal [42-44]. During the investment casting process,

the interconnected open pore space of a polyurethane foam is filled with a ceramic investment compound (Fig. 2.8a). After burning or melting out the polymer, the ceramic structure serves as the mould and is subsequently infiltrated by the metal melt. After solidification, the ceramic mould is removed and the metal foam replicates the structure of the polymer foam. In a similar approach, the surface of a polyurethane foam is coated with a thin metal layer (Fig. 2.8b). either by physical vapour deposition (PVD) to make it electrically conductive for the subsequent electroplating of a thick metal layer or by chemical vapour deposition (CVD) [44]. After removal of the polymer by heat treatment, the polymer's structure is reproduced but the struts are hollow.

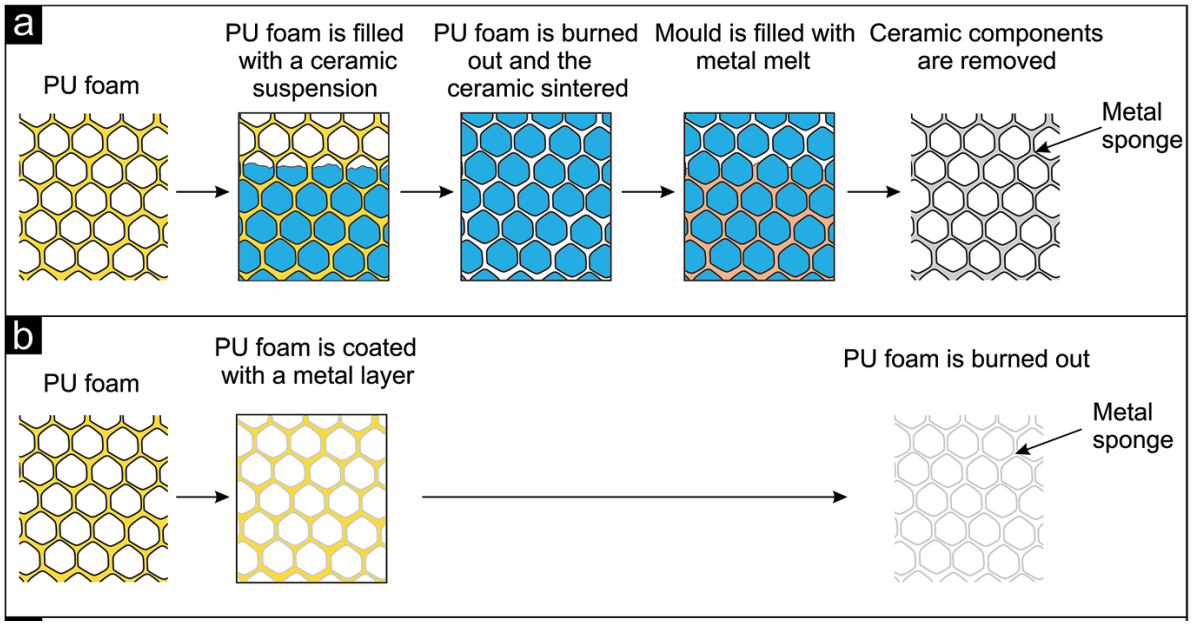

Fig. 2.8 Schematic representation of processes leading to metal sponges (after Refs. [42, 45]). (a) Investment casting process, (b) coating of a polyurethane sponge with a thin metal layer and subsequent removal of the polymer.

Fig. 2.9a shows a commercially available product Duocels® prepared by investment casting by ERG Materials and Aerospace Corp. [46]. The Duocels® product consists of porous Cu and Al panels. Fig. 2.9b displays a porous nickel structure (known as INCOFOAMs) fabricated by depositing Ni onto a polyurethane sponge. After removal of the template, an open-cell porous Ni structure forms, exhibiting a pore space inside the struts, which is revealed in the inset of Fig. 2.9b [47]. When the template material is used in the form of individual particles, they are called space holder particles. A variety of space holders has been employed for the production of porous metals. Sodium chloride (NaCl), sugar, carbonates, sand or even metals are prominent examples [42]. A schematic illustration of the

process using NaCl is given in Fig. 2.9c while Fig. 2.9d shows a porous titanium product produced this way [48].

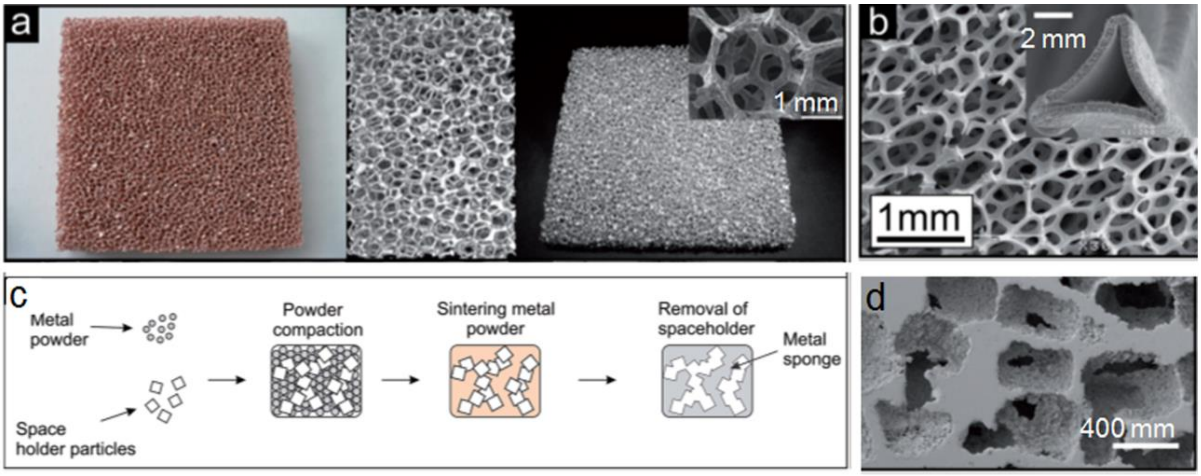

Fig. 2.9 Representative examples of metal sponge prepared by different routes. (a) Open porous metal sheets (Duocels® Cu and Al, ERG Materials and Aerospace Corp.) prepared by the investment casting technique [46]. Inset: structural connectivity [49]. (b) Open porous metal structure prepared by the deposition of nickel onto a polyurethane foam followed by the removal of the polymer template structure (INCOFOAM®). Inset: pore space inside the struts, which is created after removal of the polymer template [47]. (c) Using sodium chloride (NaCl) as space holder particles, compaction with metal powder, sintering and dissolution [45] and (d) open porous titanium prepared by the space holder approach with NaCl as space holder particles [48].

Irrespective of its composition, the space holder material must provide a percolating network throughout the body in order to be efficiently removed, thus creating the pores. The space holder technique enables the fabrication of macroscopic bodies with homogenous open-cell porosity and with a controllable average cell size. Another frequently adopted approach is solid-state sintering of preformed metallic macro-particles like spheres, hollow spheres, fibres or flakes into a macroscopic piece of spongy metal [42, 49-52]. The connectivity between individual particles is achieved through the formation of sintering necks. Advances in the preparation of metallic building blocks allow the fabrication of a wide variety of different metal sponges by this method.

2.2.2 Nanoporous metals

2.2.2.1 By the templating method

The principle is the same as that used in the space holder approach but the templates are of a much smaller size, and, in addition, their shape and arrangement can be controlled to some extent. Ideally, the hard or soft templates are defined by the size, shape, morphology and connectivity of the pores in the metal network after removal of the template. Advances in the synthesis of colloidal silica or polystyrene made it possible to use them as template materials [53, 54]. They are mono-disperse and their surface chemistry can easily be tuned so that they can be arranged into highly regular opal structures. In a subsequent step, the voids within the template particles are infiltrated either by metal precursors or by metal nanoparticles. In the case of precursors, they will be reduced to form the solid metal. In the last step, the template is removed in order to create the open-pore structure. An overview of the fabrication strategies and applications of nanoporous metals has been given by Zhang et al [54]. Various metals like Au, Pt, Ni, Cu, Ag and Co have been made into nanoporous configurations by templating opal structures as described above [55, 56]. These inverse opals are featured by a high structural order with periodically repeating unit cells over long ranges in two dimensions. The struts are sharply defined and reproduce the geometry of the corresponding pores in the colloidal template (see scanning electron microscopy (SEM) images in Fig. 2.10).

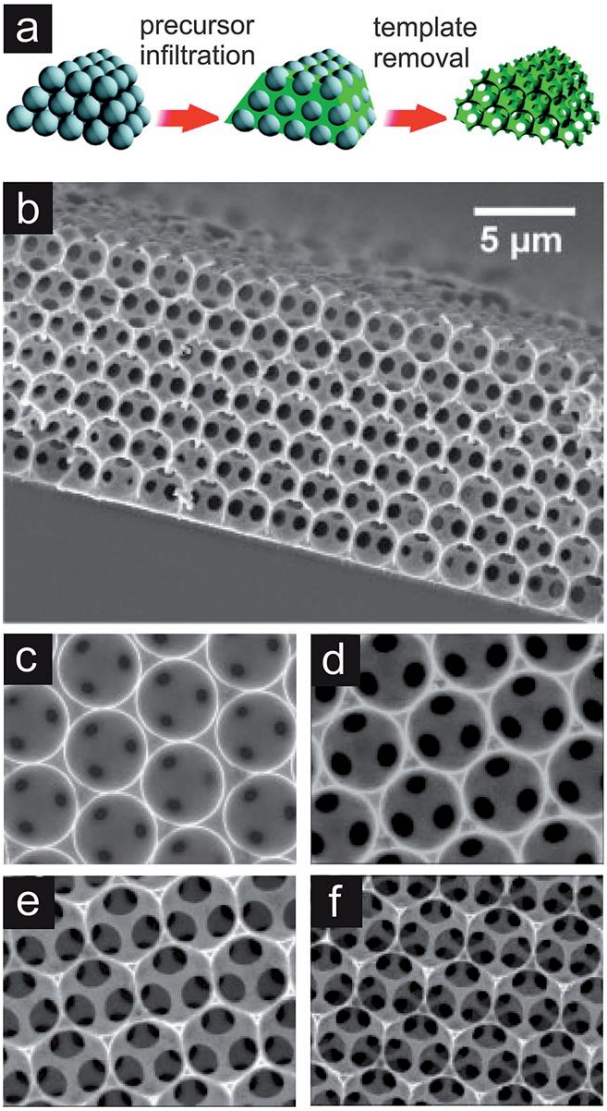

Fig. 2.10 (a) Schematic of sacrificial template assisted technique [53]. (b) SEM image of nickel inverse opal structure forming a film. (c-f) SEM image of nickel inverse opal structures exemplifying the possibility to trigger the window size (and cell wall resp. strut thicknesses) by adjusting the corresponding etching time [57].

2.2.2.2 By the aerogel method

Inspired by colloid chemistry, the idea of using metal nanoparticles as building blocks, followed by their assembly into three-dimensionally interconnected networks, has emerged since last decade. In the first step, a gel is prepared where the metallic building blocks fill a volume space by connecting each other into a percolating network structure, whose pores are filled by a solvent. In the second step, this gel is subjected to supercritical or freeze drying to replace the liquid in the pores with air in the absence of disruptive capillary forces. The as-produced aerogel structures consist of struts/ligaments made up of the connected building

blocks in a necklace-like appearance with pores of tens of nanometer size and highly irregular geometry (Fig. 2.11a-d). Recent work by Liu et al. [58] presents an interesting approach for the production of homogeneous bi-metallic nanoporous metals, without supercritical drying, in order to reproduce such "aerogel-like" architectures (Fig. 2.11e and f). These structures show great promise for the preparation of nanoporous metals with high specific surface areas.

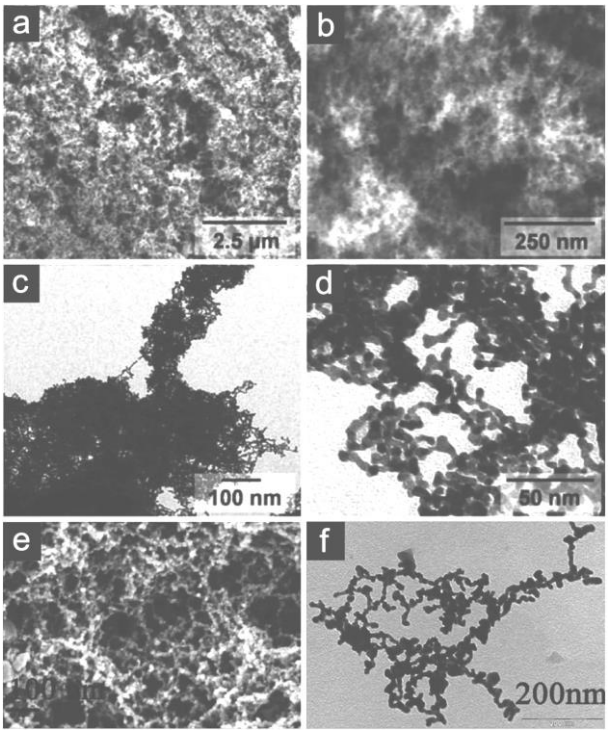

Fig. 2.11 Metallic aerogel and ''aerogel-like'' structures. (a and b) SEM and (c and d) transmission electron microscopy (TEM) micrographs of platinum aerogels [59]. (e and f) SEM and TEM micrographs of gold-platinum bimetallic porous structures [58].

2.2.2.3 By the hydrothermal method

The hydrothermal method is a one-step fabrication method for preparing nanoporous metals (see Fig. 2.12(c,d) [60]). It deals with the use of special chemicals and/or solutions, special autoclaves, high temperature and long duration (see Fig. 2.12(a,b)). The final nanoporous structure is chemical and device dependent. This process is neither suitable for scale-up nor for the fabrication of large scale nanoporous metals.

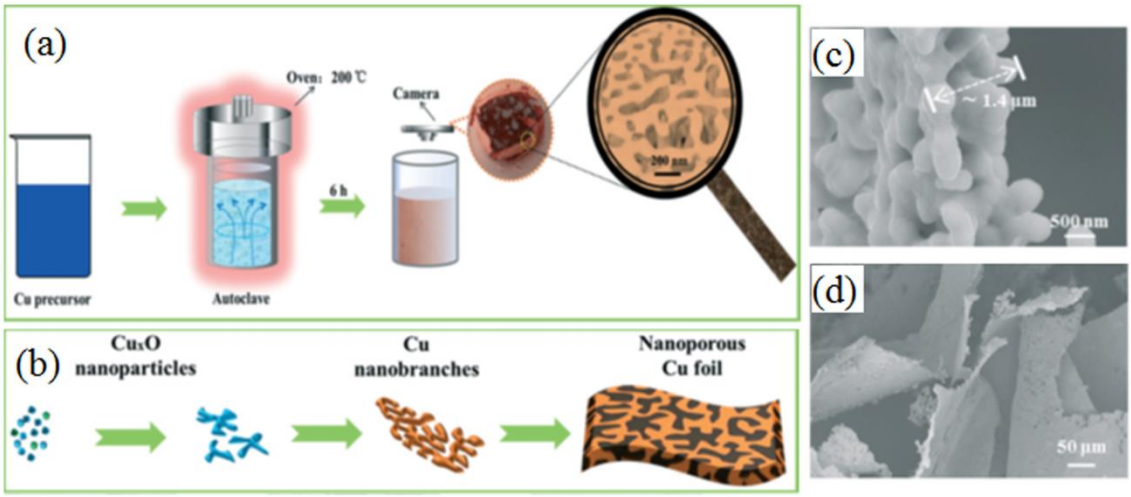

Fig. 2.12 (a) Schematic illustration for the synthesis of nanoporous Cu by a hydrothermal method; (b) proposed formation process of nanoporous Cu during the hydrothermal method; (c) a cross-sectional SEM image with high magnification of the nanoporous Cu film and (d) digital image of the synthesized nanoporous Cu films rinsed in ethanol [60].

The approaches discussed above are mostly performed on a lab-scale and they are mostly limited to producing thin films or powders with little control of the porous structure over length scales. To produce (nano)porous Sn-based and Cu-based materials for applications in LIBs, this research will focus on the dealloying approach to be introduced below in Sections 2.3 and 2.4. Dealloying can be regarded as the most prominent approach to realizing direct control over the pore size, the selection of materials and the type of samples with a (nano)porous structure.

2.3 The dealloying approach and nanoporous metallic materials

2.3.1 Introduction to dealloying

Dealloying is the selective (chemical or electrochemical) dissolution of one or more components from an alloy, leaving behind a material enriched in the nobler or less active alloy component. The remained component experiences a self-assembly process through diffusion, resulting in the formation of a solid-void bicontinuous structure with a random 3D distribution [61]. This approach was used as early as during the Incan civilization to dissolve the more active element Cu from dilute Au-Cu alloys to create the illusion of a pure gold artefact [62]. Fig. 2.13 shows a typical artefact made by this method and the corresponding SEM image taken afterwards in 1970 [63]. In addition, dealloying is related to the context of corrosion historically. As corrosion devours almost 3% of world's GDP per year [64, 65],

dealloying has been intensively investigated in the context of corrosion protection for more than a century. The last decade has seen a renewed interest in this approach due to its capability of producing nanoporous structures, which hold promise for applications as sensors and catalysts due to their high specific surface areas [66-69].

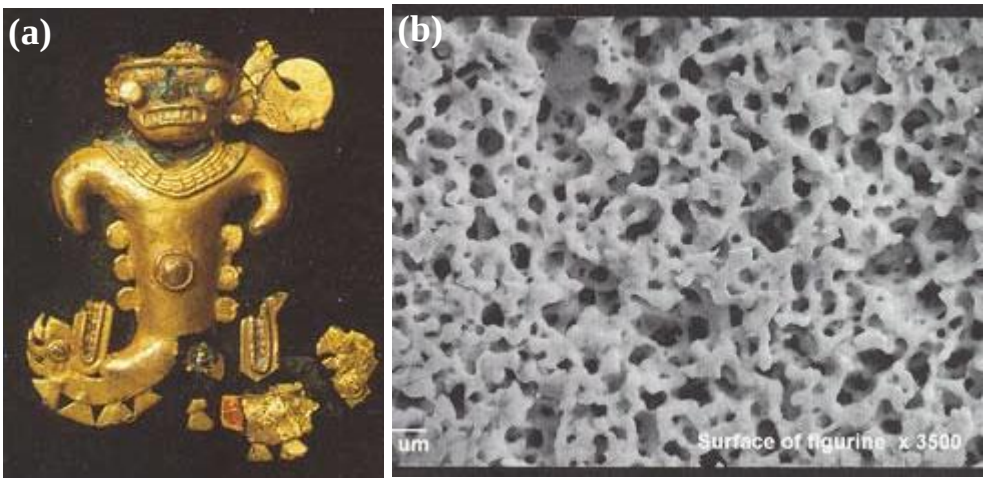

Fig. 2.13 (a) Anthropomorphic figure from Panama, a typical dilute gold alloy artefact and (b) SEM image of the surface of the artefact showing the porous structure of the unburnished depletion gilded surface (The scale bar at the bottom left reads 1µm) [63].

There are two prerequisites for an alloy to undergo dealloying [70-72]: (i) the constituting elements in the alloy should have well-differentiated equilibrium potentials (e.g. A is less noble whilst B is nobler in a binary AB alloy), allowing A to dissolve away while B remains intact [70]; and (ii) the concentration of the nobler element B is below a critical composition, referred to as *parting limit*, beyond which dealloying does not take place due to surface passivation by the nobler element B [71, 72]. Many binary alloys meet these two requirements, including single solid solution alloys of Ag-Au [73-75], Pt-Co [76], and Au-Cu [64, 77], and two-phase alloys of Al-Cu [78-80], Al-Ag [81, 82], Zn-Cu [83, 84] and Mg-Cu [85, 86]. They have been dealloyed to produce nanoporous pure metals of Au [64, 73, 74, 77], Pt [76], Ag [81, 82], Cu [78-80, 83, 84, 86]. The mechanisms that control the nanoporosity formation have been discussed as well [64, 74, 77, 82, 86, 87]. In addition, some studies have dealt with dealloying of alloys containing a third element such as $Mg_{90-x}Cu_xY_{10}$ [88], $Mg_{77}Ag_{18.4}Pd_{4.6}$ [89], $Ag_{64}Au_{30}Pt_6$ [90], $Al_{75}Pt_{15}Au_{10}$ [91], $Al_{66}Au_{27.2}X_{6.8}$ (X = Pt, Pd, PtPd, Ni, Co and NiCo) [92] and $Ag_{80}Au_{19}Pt_1$ [93]. All the compositions quoted in this thesis are in at.% unless otherwise stated.

Traditionally, dealloying can be classified into two categories, namely, chemical dealloying and electrochemical dealloying. Chemical dealloying can be also referred to as a free corrosion process. An alloy is immersed into a corrosion solution, normally acid or oxidative solutions which can dissolve the less noble component. Factors, i.e. the ions in the solution, the concentration and the temperature of the solution employed, can all affect the diffusivity of nobler elements and in turn, can be used to modify the resulting nanoporous microstructure. The transmission electron microscopy (TEM) images in Fig. 2.14 shows the microstructure of nanoporous Pd produced from the dealloying of $Al_{80}Pd_{20}$ in 20 wt.% NaOH (a) and 5 wt.% HCl (b) solutions [94]. The Cl^- in the HCl solution is able to accelerate the diffusion of noble atoms (Pd) [95]. As a result, the nanoporous structure from the dealloying in a 5 wt.% HCl solution (average ligaments width: 15-20 nm) is much coarser than that from the dealloying in a 20 wt.% NaOH (average ligaments width: 3-6 nm). The drawback of the chemical dealloying is that it is always performed in aggressive solutions, e.g. HNO_3 [75], HCl [96], NaOH [80] etc.

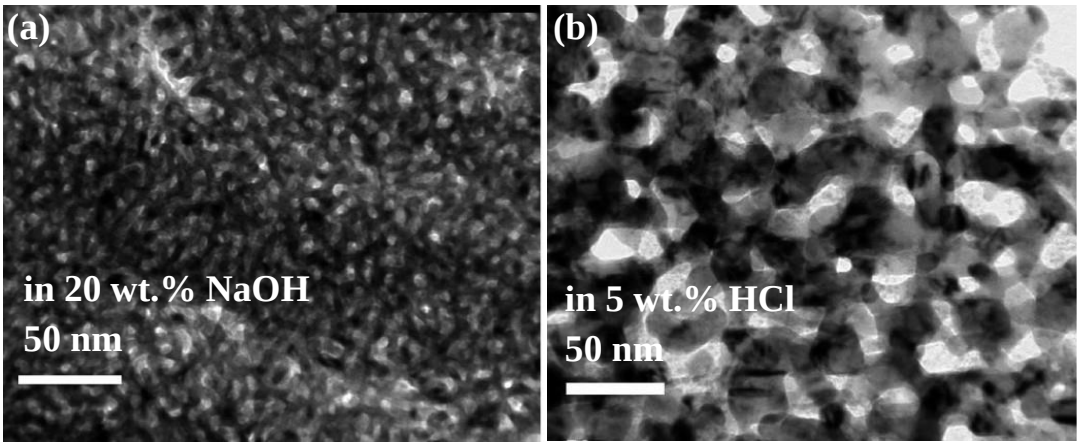

Fig. 2.14 TEM images showing the nanoporous structure of nanoporous Pd from the dealloying of $Al_{80}Pd_{20}$ ribbon samples in 20 wt.% NaOH (a) and 5 wt.% HCl (b) solutions [94].

The other method is called electrochemical dealloying in which a potential is applied to the sample to remove the less noble components. One advantage of this method is that it can be realized in neutral solutions (e.g. NaCl [87], $AgNO_3$ [97], etc.), which is desired from safety and green chemistry points of view. In addition, no effects from concentration changes can be observed during electrochemical dealloying process, leaving only the applied potential to control the final ligament size. By control of the applied potential, electrochemical dealloying can produce much finer microstructure features than chemical dealloying [98]. Hodge et al.

[98] compared the microstructures of nanoporous Au made from the chemical and electrochemical dealloying of $Al_{75}Au_{25}$ alloys and found that the electrochemical dealloying resulted in much finer microstructures (Fig. 2.15).

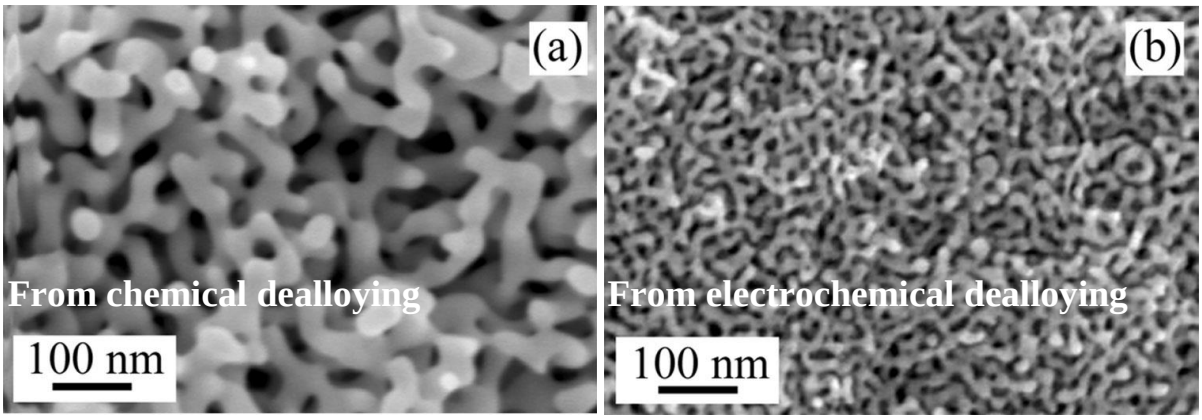

Fig. 2.15 SEM micrographs of dealloyed $Ag_{75}Au_{25}$ foam by (a) chemical dealloying and (b) electrochemical dealloying [98].

2.3.2 Precursor alloys for dealloying

2.3.2.1 Binary alloys

(i) Single solid solution

Single solid solution precursors have been confirmed to be good candidates as dealloying precursors for preparing uniform nanoporous metals. Ag-Au alloy is an ideal precursor because Au and Ag are completely miscible across the entire composition range (see Ag-Au phase diagram [99] in Fig. 2.16) and no phase separation occurs during selectively dissolving of Ag in concentrated HNO_3 solution. Dealloying of Ag-Au precursor alloys has been extensively studied since 1979 [100], when Forty presented electron micrographs for a free-standing nanoporous Au membrane material, which had a pore size of approximately 20 nm and was made by etching an Ag-Au alloy film in HNO_3 solution. Since the 1980s, Sieradzki and Newman and others [101-103] have systematically investigated the corrosion process of Ag-Au alloys. With advanced electrochemical techniques, such as electrochemical scanning tunnelling microscopy, they discussed in great detail about the two key parameters associated with dealloying: the *parting limit* and the *critical potential* (E_{crit}), where the parting limit defines the concentration of noble metal in an alloy above which dealloying does not occur, while the E_{crit} is empirically defined as a voltage threshold above which the dissolution current rises dramatically, resulting in substantial dealloying.

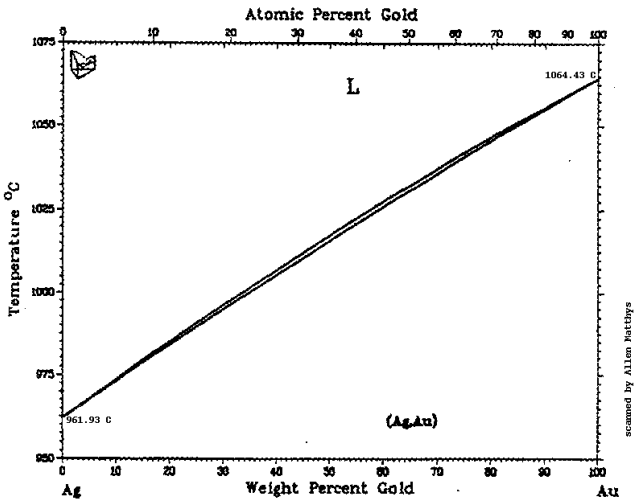

Fig. 2.16 Ag-Au phase diagram [99].

At the very beginning of this century, Erlebacher et al. [61] further clarified the underlying physical mechanism of dealloying of Ag-Au alloys using experimental approaches and computer simulation. After that, increasing interest has been paid to making nanoporous Au by dealloying of Ag-Au solid solution alloys. The four effects, namely extended immersion time of samples in HNO_3 solution (see Fig. 2.17) [104], annealing treatment pre and in the middle of dealloying treatment [93, 105], various applied potentials [74, 78], and different precursor types (films [106], ingots [107], particles [74], nanotubes [108] and nanowires [75]), on the nanoporous microstructure have been studied systematically. These studies also provided informative details about the dealloying using other possible precursor systems. In addition, nanoporous Au produced from the dealloying of single solid solution Ag-Au alloys are promising candidates in catalytic [66, 67, 69], optical [109], sensor [106] and actuation [68] applications.

Except the Ag-Au solid solution precursors, other solid solution precursors (e.g. Mn-Cu [110, 111], Ni-Cu [112], Pt-Cu [113]) have also been dealloyed to fabricate corresponding nanoporous metals.

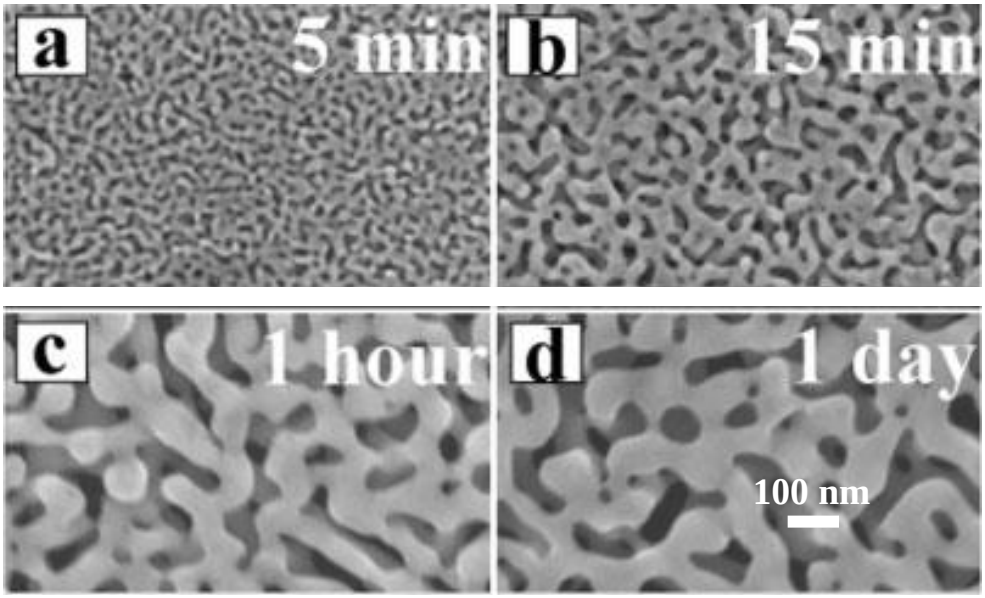

Fig. 2.17 Plan-view SEM images of nanoporous Au samples showing significant structure coarsening upon continued immersion in acid for an extended time (a-d: 5 min - 1 day) after the alloy is completely dealloyed (dealloying was completed after 5 min) [104].

(ii) Single intermetallic compound alloys

For some alloy systems which meet the two requirements for dealloying to occur, intermetallic compound alloys rather than solid solution are more common, like Au-Cu [64, 114-116], Al-Au [94, 117-119], Al-Cu [79] and Mg-Cu [85, 120] alloy systems.

Renner et al. [64, 114-116] have created nanoporous Au by dealloying of a single Cu_3Au intermetallic phase and systematically investigated its initial dealloying behaviour under various potentials and in various electrolytes. Zhang et al. created homogeneous nanoporous Au from the dealloying of a single Al_2Au [94, 117-119] intermetallic phase and a single AlAu [117] intermetallic phase, respectively. Fig. 2.18 shows the microstructure of nanoporous Au obtained from the dealloying of Al_2Au and AlAu. It implied an effect from the precursor composition on the microstructure, which shows that the average ligament-void size from the dealloying of AlAu intermetallic compound is larger than that from the dealloying of Al_2Au. The same authors also fabricated nanoporous Cu from the dealloying of a single Al_2Cu [79] phase and a single Mg_2Cu [85, 120] phase. However, it has been found that the dealloying of some single intermetallic compound alloys (e.g. Ag_2Al [121], AlCu [122], $MgCu_2$ [85]) can only happen on the surface of the sample without penetrating through the entire sample.

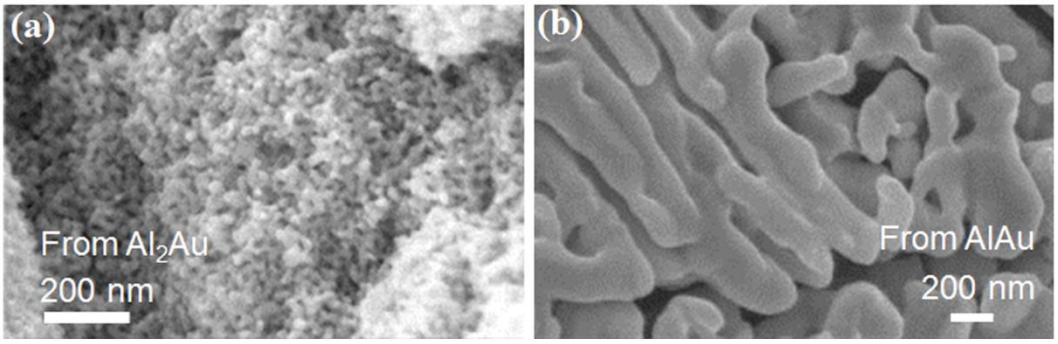

Fig. 2.18 SEM images showing the microstructure of nanoporous Au obtained through the electrochemical dealloying of a single Al_2Au phase (a) and a single AlAu phase (b) in the 10 wt.% NaCl solution at the potential of 1.5 V [117].

(iii) Multi-phase alloys

The coexistence of multi-phases in the matrix is typical of multi-component alloys. Researchers have studied the dealloying of multi-phases and found interactions between the coexistent phases summarized as follows.

a) As for a two-phase alloy, the dealloying of the less noble phase has a promoting effect on the dealloying of the nobler phase. This promoting effect exists in two-phase alloys consisting of solid solution and intermetallic compound, (e.g. $Al_{65}Ag_{35}$ alloy consisting of α-Al(Ag) and Ag_2Al [82, 121]) and two-phase alloys consisting of two intermetallic compounds (e.g. $Mg_{50}Cu_{50}$ alloy consisting of Mg_2Cu and $MgCu_2$ [85], $Al_{60}Cu_{40}$ consisting of Al_2Cu and AlCu [122]). For example [121]: for the $Al_{40}Ag_{60}$ (a single Ag_2Al phase), the dealloying only happened on the surface of the sample (Fig. 2.19(a, b)), while for the multi-phase $Al_{50}Ag_{50}$ sample (Ag_2Al + α-Al(Ag)), the dealloying was complete and resulted in homogeneous nanoporous microstructure throughout the thickness of the ribbon sample (Fig. 2.19(c and d)). The existence of a less noble phase can serve as penetration paths for the solution and promote the dealloying of the nobler phase.

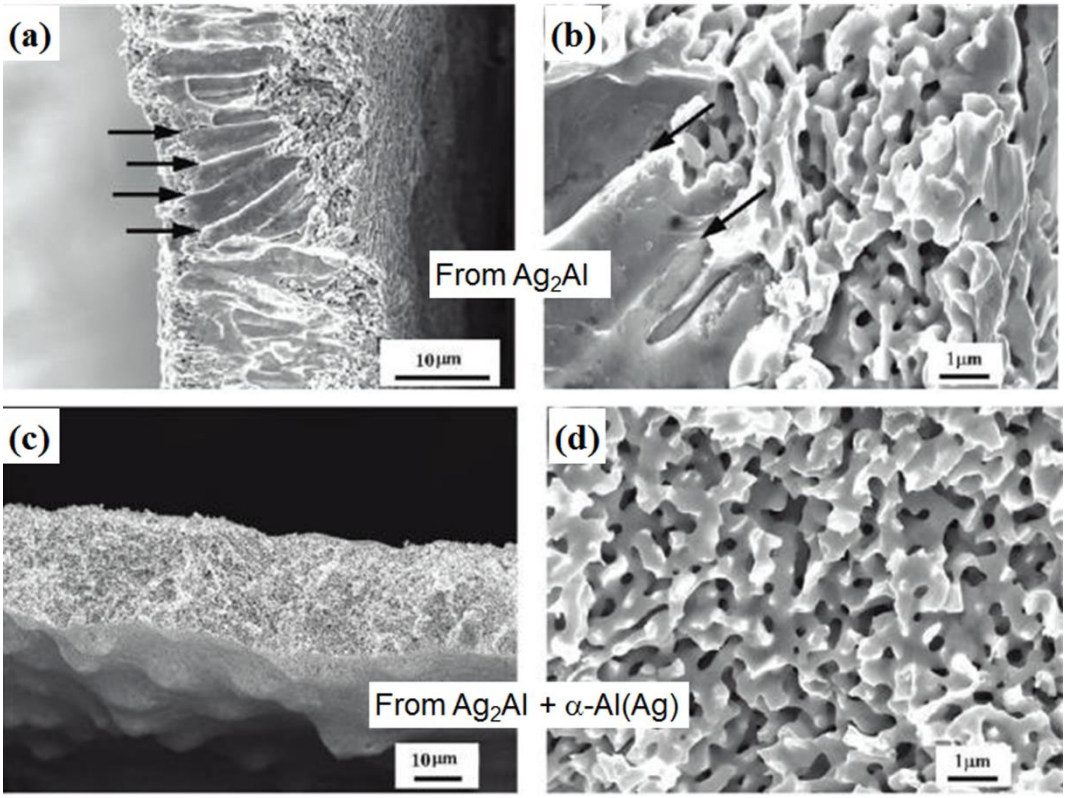

Fig. 2.19 Cross-sectional SEM images showing the microstructures of as-dealloyed $Al_{40}Ag_{60}$ (consisting of single Ag_2Al phase) ribbon sample (a, b) and $Al_{50}Ag_{50}$ (consisting of Ag_2Al and α-Al(Ag) phases) ribbon sample (c, d) [121].

(b) The dealloying of some two-phase alloys can result in hierarchical porous structures. The initial structure of such two-phase alloys can be inherited after the dealloying process which generates a nanoporous structure with a bimodal pore distribution. Zhang and co-workers developed nanoporous gold with bimodal channels by chemical dealloying rapidly solidified $Al_{80}Au_{20}$ (consisting of α-Al(Au) and Al_2Au) [123] and $Al_{60}Au_{40}$ (consisting of Al_2Au and AlAu) [118] ribbons. For the creation of bimodal porous Au through the dealloying of $Al_{60}Au_{40}$ which consists of Al_2Au and AlAu, Zhang showed a schematic illustration (see Fig. 2.20 [118]). The resulting microstructure is featured by 25-50 nm large sized channels due to dealloying of the Al_2Au phase and 10-20 nm small sized channels due to dealloying of the AlAu phase [118]. Fabrication of bimodal porous metals *via* dealloying of precursor alloys consisting of two phases were also presented in rapid solidified $Al_{73}Cu_{27}$ alloy (consisting of α-Al(Cu) and Al_2Cu) [124] and mechanical alloyed $Al_{80}Pd_{20}$ alloy (consisting of α-Al(Pd) and $PdAl_3$ phases) [96].

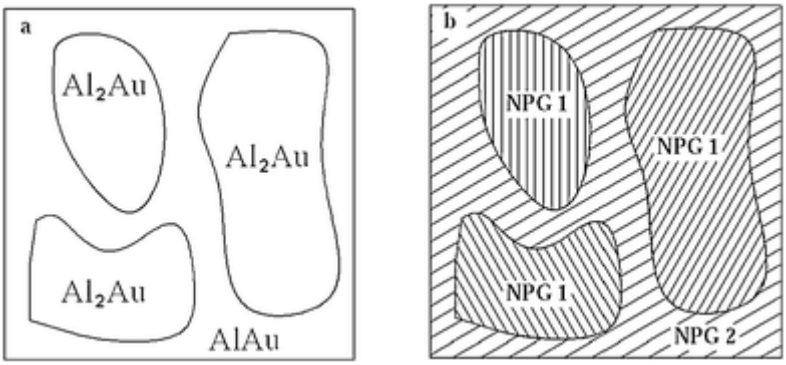

Fig. 2.20 Schematic illustrations showing the microstructure of (a) the starting $Al_{60}Au_{40}$ alloy and (b) nanoporous Au by chemical dealloying of $Al_{60}Au_{40}$. The starting $Al_{60}Au_{40}$ alloy is composed of Al_2Au and AlAu, and the primary Al_2Au is surrounded by AlAu. The resulting nanoporous structure comprises two kinds of microstructures: nanoporous Au1 (NPG 1) and nanoporous Au2 (NPG 2) with different length scales of ligaments/channels. The dealloying of Al_2Au and AlAu results in the formation of NPG 1 and NPG 2, respectively [118].

These studies indicate that it is possible to manipulate the resulting nanoporous structure *via* the design of the precursor alloy and the control of their microstructure.

2.3.2.2 Ternary or multicomponent alloys

Research on dealloying over the last decade has been largely focused on de-alloying of binary alloys (AB) with a view to producing nanoporous structures of essentially pure metal B, and to understanding the dealloying process. A few studies have also dealt with dealloying of alloys containing a third element such as $(Pt_{0.05}Au_{0.95})_{25}Ag_{75}$ [125], $Mg_{90-x}Cu_xY_{10}$ [88], $Al_{65}Ag_{22.75}Au_{12.25}$ [126], $Ag_{64}Au_{30}Pt_6$ [90], $Al_{75}Pt_{15}Au_{10}$ [91] and $Al_{66}Au_{27.2}X_{6.8}$ (X = Pt, Pd, PtPd, Ni, Co and NiCo) (in at.%) [92, 127]. However, it should be pointed out that in these ternary ABC alloys, the third element C introduced was normally a noble element, a slow diffuser. The purpose was to slow down the surface diffusivity of B, in order to decrease the ligament/channel size of the resulting nanoporous B and achieve high specific surface area. Fig. 2.21 [125] shows the refining effect of small amount of Pt in dealloying $Au_{25}Ag_{75}$ alloy. The $(Pt_{0.05}Au_{0.95})_{25}Ag_{75}$ was obtained by substituting 1.25 at.% of Au by Pt, and even such minor addition of Pt had reduced ligament size from ~30 nm to ~5 nm (Fig. 2.21). The doped third element C substituted the noble element B in the lattice of the precursor alloys. From this angle, dealloying of these deceptively ternary alloys was not different from the dealloying of binary alloys.

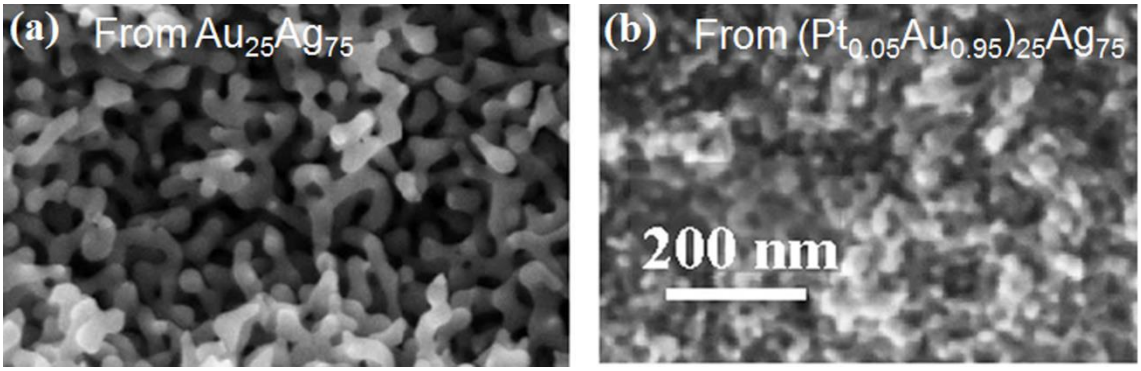

Fig. 2.21 SEM images of nanoporous samples dealloyed from (a) $Au_{25}Ag_{75}$ and (b) $(Pt_{0.05}Au_{0.95})_{25}Ag_{75}$ respectively. Both samples were dealloyed in 1 M $HClO_4$ aqueous solution at 1.03 V [125].

For dealloying of ternary alloys (ABC), which consist of three distinctly different phases, the only research reported to date appears to be from Feng et al [128]. Similar to dealloying of binary AB alloys which produces nanoporous structures of essentially pure metal B, dealloying of ternary ABC alloys has the potential to produce nanoporous composite structures with constituting elements B and C and with characteristics different from those dealloyed from binary alloys. In addition, dealloying of ternary alloys is expected to show different dissolution and diffusion behaviors due to the involvement of the third element. Understanding their dealloying characteristics is necessary for the fabrication of advanced nanoporous metal structures aside from enhancing the knowledge base of dealloying.

2.3.3 Dealloying conditions

The properties of nanoporous materials are closely related to their microstructure and especially the characteristic length scale of ligaments/channels. It is of great importance to control the microstructures of nanoporous metals. Some factors including the microstructure of precursors discussed in Section 2.2.2, the type of electrolytes, the applied dealloying potential, and the dealloying temperature and time, will affect the dealloying process and, in turn, the microstructure of nanoporous metals and their property.

2.3.3.1 Applied potentials

Compared to the less noble component's dissolution potential, dealloying always turns-on at a much higher over-potential, referred to as the critical potential (E_{crit}) [129]. Below this potential, dealloying is usually limited to a thin surface layer with the formation of a

passivation layer because of the enrichment of the nobler component [130]. Above the E_{crit}, dealloying behaves qualitatively like elemental metal dissolution but results in bi-continuous structures. A generalized polarization curve is illustrated in Fig. 2.22(a). At a low potential, the dissolution current is small but constant. Close to the E_{crit}, the dissolution current rises exponentially. Since the E_{crit} is sensitive to sweep rates and compositions of precursor alloys and electrolytes [129], it usually falls into a narrow range, rather than a well-defined value. Fig. 2.22(a) is for the single phase precursor alloy. Two individual phases normally have different E_{crit} values (see Tafel curves for single alpha-Mg and single Mg_2Cu in Fig. 2.22(b) [120]). And such issue should be taken into account when selecting the right applied potentials for dealloying of the multi-phase alloys (like Mg-Cu alloy consisting of alpha-Mg and Mg_2Cu).

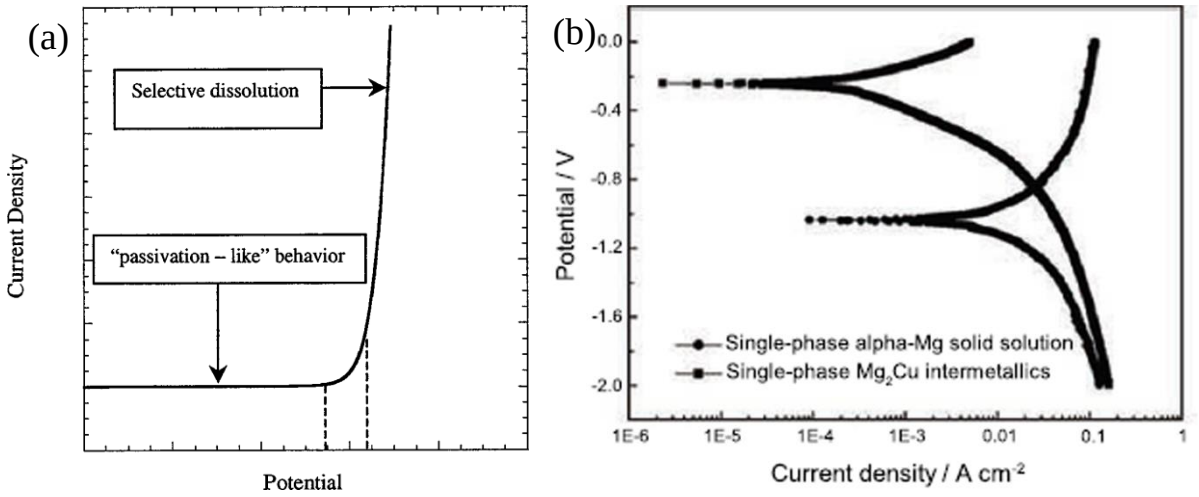

Fig. 2.22 (a) Schematic illustration shows the current/potential behavior of a single phase alloy undergoing selective dissolution. The critical potential (E_{crit}) corresponds to that associated with the knee in the curve and is not sharply defined. The shape of the knee is affected by sweep rate, alloy, and electrolyte composition. The dashed vertical lines indicate typical ambiguity in defining E_{crit} [129]. (b) Tafel polarization curves of single phase alpha-Mg solid solution and Mg_2Cu intermetallics in the HCl solution [120].

Dealloying potential has a strong influence on the formation of ligaments. Generally speaking, the higher the dealloying potential, the faster the dissolution of the active component and the faster the diffusion of the noble component as well [74, 78, 107, 119, 131]. As a result, a higher dealloying potential results in coarsened porous structure and a lower dealloying potential corresponds to a finer one (one such example is shown in Fig. 2.23 [78]). Meanwhile, it was suggested that the cracks formed during dealloying are highly dependent

on the applied dealloying potential [78]. Accordingly, it is important to pay sufficient attention to the potential selection during the investigation of electrochemical dealloying.

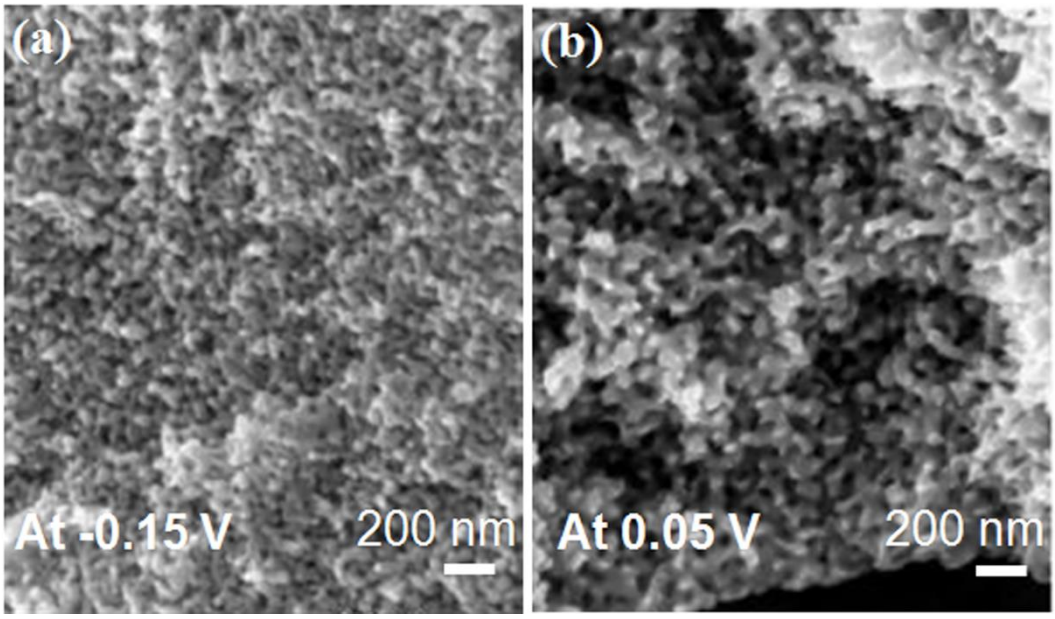

Fig. 2.23 SEM images showing the microstructure of nanoporous Au by electrochemical dealloying the Al_2Au alloy in the 1 M NaCl solution at the temperature of 273 K at the potential of -0.15 V (a) and 0.05 V (b) [78].

2.3.3.2 Temperatures

The resulting nanoporous microstructure can be manipulated through three temperature-based treatments or processes: pre-dealloying annealing, dealloying at different temperatures and post-dealloying annealing.

Pre-dealloying annealing: For ingot precursor samples, before dealloying, the samples can be annealed at a certain temperature for either homogenization or residual stress relief [125, 132, 133]. This is an important step to producing samples with a homogeneous nanoporous structure without the formation of microscale voids. Fig. 2.24 shows the effect of pre-dealloying annealing on the microstructure of as-dealloyed samples [133].

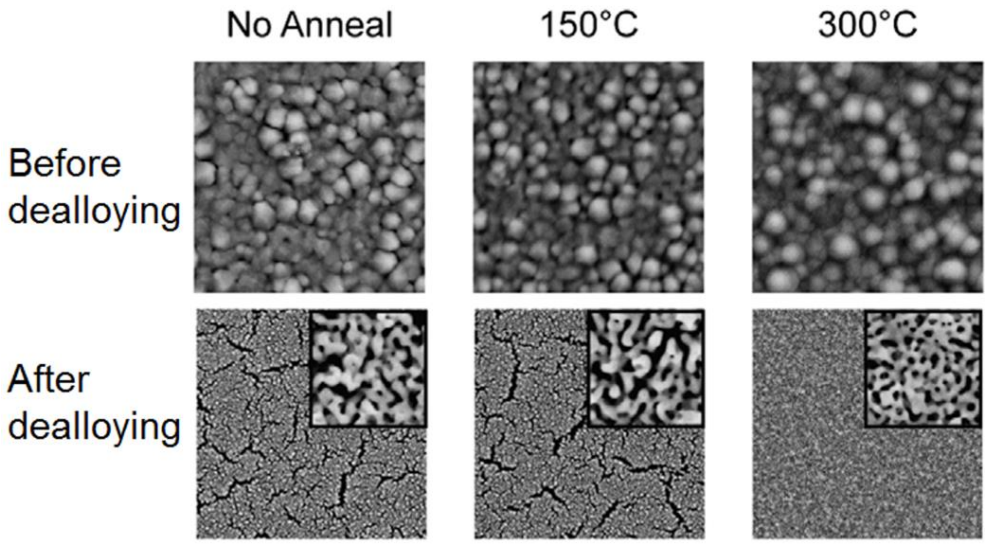

Fig. 2.24 Micrographs of $Au_{37.5}Ag_{62.5}$ films after annealing treatment and dealloying treatment showing that the annealing treatment of precursor alloy mitigates the formation of microscale voids during dealloying [133].

In addition, annealing is also effective to modify the phase constitution and distribution in the precursor alloy [134]. It offers an effective approach to design and control the microstructure of the as-dealloyed samples by modifying the precursor alloys.

Dealloying at different temperatures: The dealloying temperature affects the final ligaments scale. One can reduce the ligament size by using a lower temperature to slow down the surface diffusivity of the nobler component [119, 131, 135]. On the contrary, increasing the dealloying temperature can increase the ligament size. For safety reasons, the temperature for dealloying is usually not higher than 100 °C. Attention is normally required when selecting the appropriate dealloying temperature. For example, in the Cu-Sn system, the intermetallic formation is temperature-sensitive: below 60 °C, only Cu_6Sn_5 forms while at or above 60 °C both Cu_6Sn_5 and Cu_3Sn can develop [136].

Post-dealloying annealing: Post-dealloying annealing can increase the pore size and change the microstructure [137-139]. A typical example of tuning the ligament size by post-annealing is shown in Fig. 2.25 [137]. In addition, the hardness of the nanoporous structure was changed as well after the annealing treatment (see Fig. 2.25 (d)) [137].

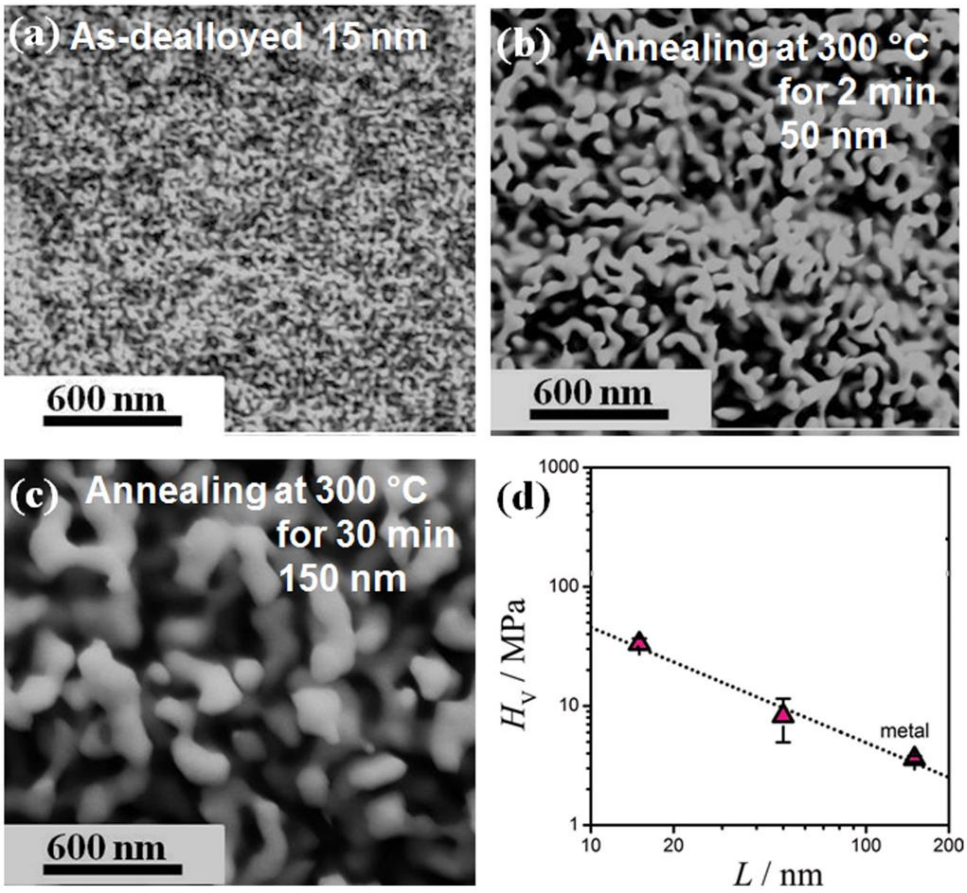

Fig. 2.25 Ligament size modulation by different annealing treatments: (a) as-dealloyed (15 nm), (b) after annealing at 300 °C for 2 min (50 nm), (c) after annealing at 300 °C for 30 min (150 nm) and (d) Vickers microhardness, H_v of nanoporous Au versus the ligament size, L [137].

2.3.4 Summary

Based on the significant influence of the precursor alloy on the final nanoporous microstructure, this thesis chooses to select three precursor alloy systems for dealloying: (i) the Al-Sn alloy system which is an immiscible system (see Fig. 2.26(a)), (ii) the Al-Cu-Sn alloy system which consists of three distinctly different elements and (iii) the Al-Cu alloy system which consists of multi-phases (either solid solution + intermetallic or two intermetallics, see Fig. 2.26(b)). The compositions and phase constitutions of each alloy precursor selected and to be investigated in this thesis are listed in Table 2.2. The influence of alloy compositions and dealloying conditions will be investigated in detail. The dealloying treatment will lead to porous Sn and Cu-Sn materials which can be used as anode materials and porous Cu which can be used as current collectors in LIBs.

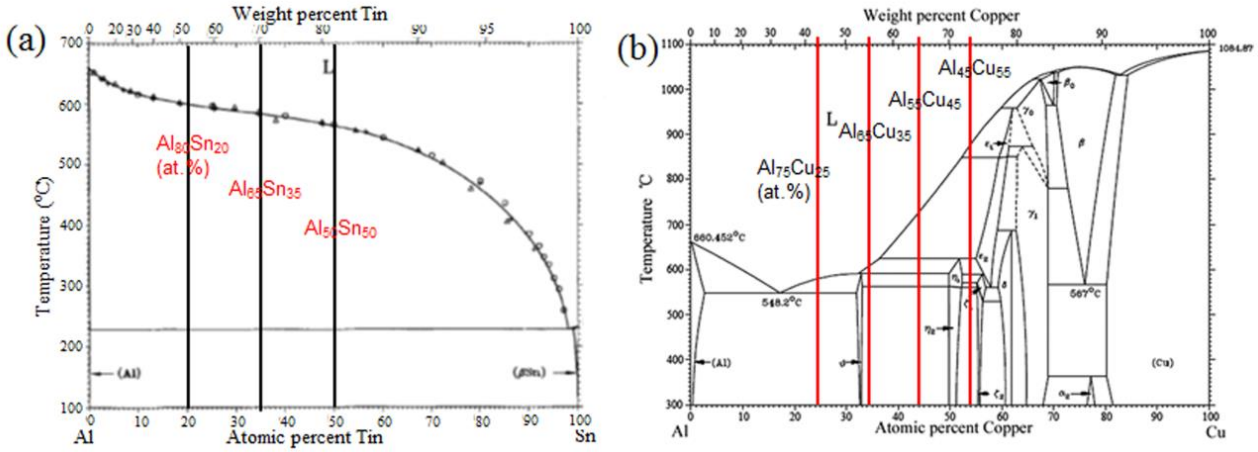

Fig. 2.26 Binary Al-Sn [140] and Al-Cu [141] phase diagram and the selection of compositions.

2.4 Dealloying mechanisms

2.4.1 History

Pickering [70] and Forty [100, 142, 143] has pioneered in the relevant research, and significant advances were made in understanding the electrochemical mechanism of dealloying since 1967. It is suggested that the basic procedure or any theoretical framework of dealloying should involve how the atoms are dissolved and how they move or transport at the alloy surface and within the solid state, during which, one or more of the following mechanisms are assumed to operate:

1) Both metals ionize followed by redeposition of nobler metal. It was first proposed by R.B. Brahms [144] in 1922 for the dezincification of brass where both Cu and Zn dissolve into the electrolyte at different rates followed by redeposition of Cu at more cathodic sites.

2) Only the less noble metal ionizes and enters the solution while the atoms of the nobler metal aggregate by surface diffusion. The surface diffusion model proposed first by H.Gerisher [145] involves the nucleation and growth of the pure, or almost pure, MN component via a surface diffusion process. The model, as it was originally proposed, assumes

that there is no transport of less noble atoms to the electrode surface via volume diffusion. As the less noble element is selectively dissolved from the surface of the alloy, the remaining nobler element, which is now in a highly disordered state, begins to reorder by surface diffusion, resulting in nucleation and growth of nobler-rich islands possibly at preferred surface sites such as structural fault boundaries, micro-twins and/or slip steps. Theoretically, it is expected that after removal of the less noble metal from the kink sites where atoms are least firmly bounded and from the terrace sites which requires a greater activation energy (overpotential), eventually the alloy becomes completely passivated when all the surface sites are occupied by the nobler metal. However, this is clearly contrary to practical experience and alternative mechanisms were suggested first by A.J. Forty [143] and later by K.Sieradzki [146].

3) Only the less noble metal ionizes and enters the solution, and atoms of both metals move in the solid phase by volume diffusion. The volume diffusion mechanism was first introduced by Pickering and Wagner [70]. The major concept of the volume diffusion mechanism is that by the injection of surface vacancies into the crystal volume below the surface, a large vacancy supersaturation beyond the thermodynamic equilibrium concentration is developed adjacent to the alloy/electrolyte interface, which results in an enhanced diffusion of the less noble element toward the surface and the nobler element away from the surface which is further owing to the compositional gradients created by the selective removal process. The inherent problem with this mechanism is that at room temperature the rate of transport of the less noble element to the surface is not sufficient to support the dealloying rate observed experimentally. Besides, neither of the diffusivity nor the mole fraction of divancies can meet the demand of experimentally observed dealloying rate. The needed diffusivity is many orders of magnitude higher than the bulk alloy diffusivity at 25 ºC while the needed

divacancy mole fraction is 100 times larger than the equilibrium mole fraction of monovacancies just below the melting point of a metal [147].

4) Synergetic volume and surface diffusion. A.J. Forty et al. [143] proposed that both volume and surface diffusion are of importance in the selective dissolution process. It is believed that the selective dissolution of the less noble species of an alloy should lead to the creation of surface vacancies. These vacancies can then migrate across the surface to form pits, steps and other surface roughening features, or they can assist the migration of the residual nobler atoms which subsequently leads to island growth. The coalescence of these islands by migration of nobler atoms exposes fresh alloy to the corrosive environment where further dissolution will occur, leading to the formation of deep pits and tunnels. These surface vacancies can also diffuse into the alloy inside to assist volume diffusion of the less noble metal to the corroding surface.

In addition, Forty et al. [100, 142, 143] proposed that the formation of the island-channel structure during dealloying of Ag-Au alloys can be explained in terms of a (corrosion and disordering) + (diffusion and reordering) model in which corrosion proceeds by selective dissolution of the less noble component, thereby creating a disordered surface layer which subsequently reorders by surface diffusion of gold atoms. In 1989, Sieradzki et al. [148] developed a new model to account for all the known features of dealloying based upon the percolation theory. Their Monte Carlo simulation results reproduced many of the features usually associated with dealloying in real binary noble-metal alloy systems, including the porous morphology of the dealloyed residue, coarsening of porosity, sharp dealloying thresholds or parting limits, and the development of intermediate compositions.

Table 2.2 The compositions and phase constitutions of alloy systems selected in this thesis [140, 141].

Requirement	Alloy system	at.%	Phases	Feature
Porous Sn (anode materials)	Al-Sn	$Al_{80}Sn_{20}$	α-Al + β-Sn	Immiscible
		$Al_{65}Sn_{35}$	α-Al + β-Sn	
		$Al_{50}Sn_{50}$	α-Al + β-Sn	
Porous Cu-Sn (anode materials)	Al-Cu-Sn	$Al_{67}Cu_{18}Sn_{15}$	α-Al + Al_2Cu + Sn	Ternary
Porous Cu (current collectors)	Al-Cu	$Al_{75}Cu_{25}$	α-Al + Al_2Cu	Two-phase
		$Al_{65}Cu_{35}$	Al_2Cu + AlCu	
		$Al_{55}Cu_{45}$	Al_2Cu + AlCu	
		$Al_{45}Cu_{55}$	AlCu + Al_4Cu_9	

In 2001, Erlebacher et al. [61] proposed a continuum model which is consistent with experiments and theoretical simulations of alloy dissolution. They demonstrated that nanoporosity in dealloyed metals is due to an intrinsic dynamical pattern formation process; that is, pores form because the nobler atoms are chemically driven to aggregate into two-dimensional clusters by a phase separation process (spinodal decomposition) at the solid-electrolyte interface, and the surface area continuously increases owing to etching. Fig. 2.27 shows the simulated nanoporosity evolution during dealloying. Moreover, the nanoporous structure of gold can be simulated using their model. In 2004, Erlebacher [149] further described the microscopic details of porosity formation during dealloying as illuminated by a kinetic Monte Carlo model, which incorporates site coordination-dependent surface diffusion of all alloy components, and site coordination-dependent dissolution of the less noble atoms. Their model can reproduce many of the characteristics of the dealloying process, particularly the porosity evolution and the phenomenology of an existing, parting limit and a composition-dependent E_{crit}.

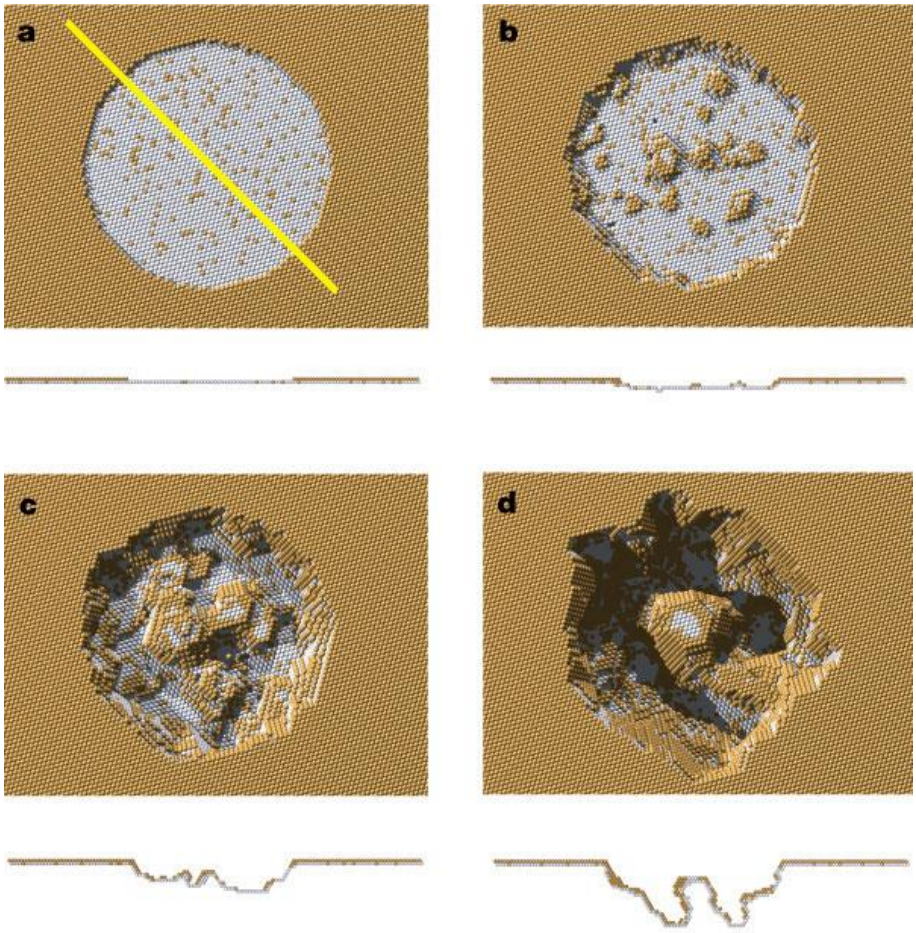

Fig. 2.27 Simulated evolution of an artificial pit in Au10%Ag90% (at.%), f = 1.8 eV. Cross-sections along the $(11\bar{1})$ plane defined by the yellow line in (a) are shown below each plan view. (a) The initial condition is a surface fully passivated with gold except within a circular region (the artificial pit). (b) After 1 s, the pit has penetrated a few monolayers into the bulk. There are fewer gold clusters near the side wall than at the centre of the pit. (c) After 10 s, a gold cluster has nucleated in the centre of the pit. (d) At 100 s, the pit has split into multiple pits; each will continue to propagate into the bulk to form a porous structure [61].

2.4.2 Current understanding

Given the importance of dealloying in producing advanced nanoporous Cu materials, much effort has been made to understand the underlying mechanism for the dealloying from the perspective of phase evolution. Zhang et al. [86, 87, 117, 131] managed to use electrochemical measurements (e.g. cyclic voltammetry (CV) measurements, potentiostat polarization measurements) to specify the phase transformation during dealloying. Fig. 2.28 shows an example of using the CV curves to trace the phase evolution of $Al_{60}Cu_{40}$ alloy (consisting of Al_2Cu and AlCu phases) [87]. By analyzing these CV loops, the authors

suggested that the dealloying of the Al_2Cu phase started first and then the AlCu phase received serious attack before the depletion of Al from the Al_2Cu phase [87]. This is an intricate approach and requires specialized knowledge in electrochemistry to interpret the CV curves [86, 87, 117, 131].

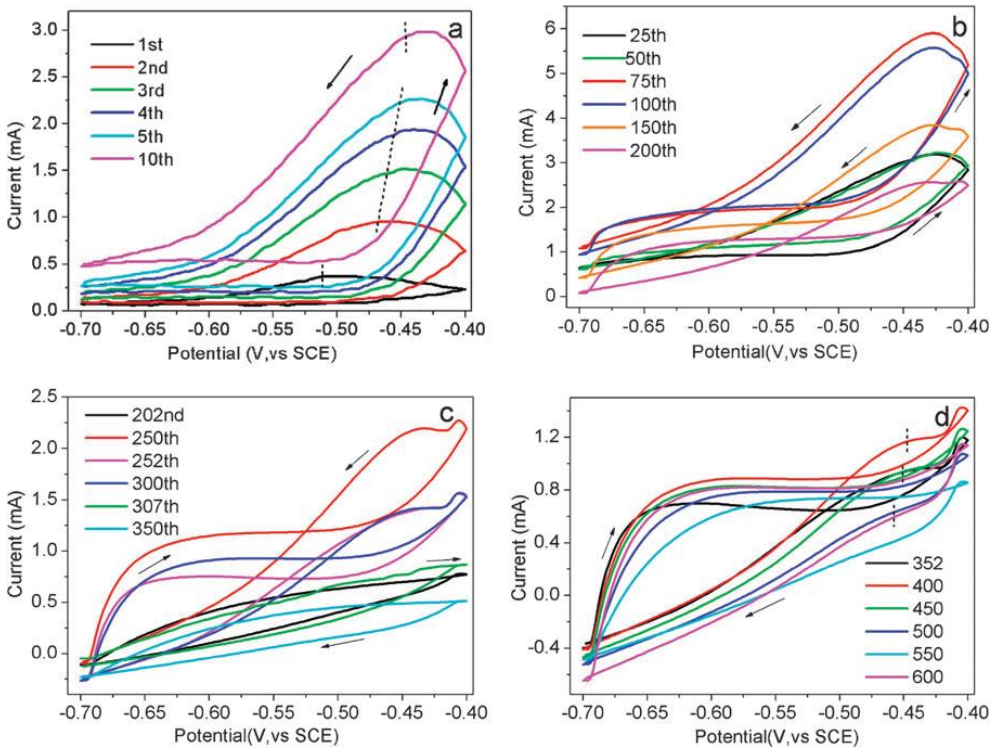

Fig. 2.28 The evolution of the cyclic voltammetry (CV) curves of the two-phase $Al_{60}Cu_{40}$ alloy subjected to 600 cycles of CV measurements and the position of current peaks is denoted by dashed lines. The alloy turned dark yellow after 600 cycles [87].

X-ray diffraction (XRD) has been commonly used to assist in understanding the underlying dealloying mechanism of Al-Cu alloys. The phase transformation during dealloying which consist of two intermetallics, however, still remains unclear for the following two reasons (take Al-Cu alloy system as an example): (a) there was only description of dissolution of Al from Al-Cu phases but without quantitative assessments and (b) there was no consideration of the formation of α-Cu(Al) solid solution during dealloying. The solubility of Al in Cu is up to 23.5 at.% [150]. Hence, there is a high probability for the formation of nanoporous α-Cu(Al) after dealloying. However, in the applications of nanoporous Cu especially when used as current collectors in LIBs, residual Al is undesired. The reason is that Al itself is an anode material in LIBs [10] and the presence of Al in a Cu current collector can result in reactions between lithium ions and α-Cu(Al), leading to severe safety issues. As a result, it is important

to clarify whether there is existence of α-Cu(Al) or not before employing the as-dealloyed nanoporous Cu for applications in LIBs. To date, neither issue has been clarified as yet, mainly because (a) the powder X-ray diffraction peaks of the involved phases (e.g. Al_2Cu, AlCu, Cu) are very similar to each other (they often overlap, see Fig. 2.29) and (b) the resolution of conventional lab XRD is inadequate to allow quantitative identification of the evolution process of these phases during dealloying.

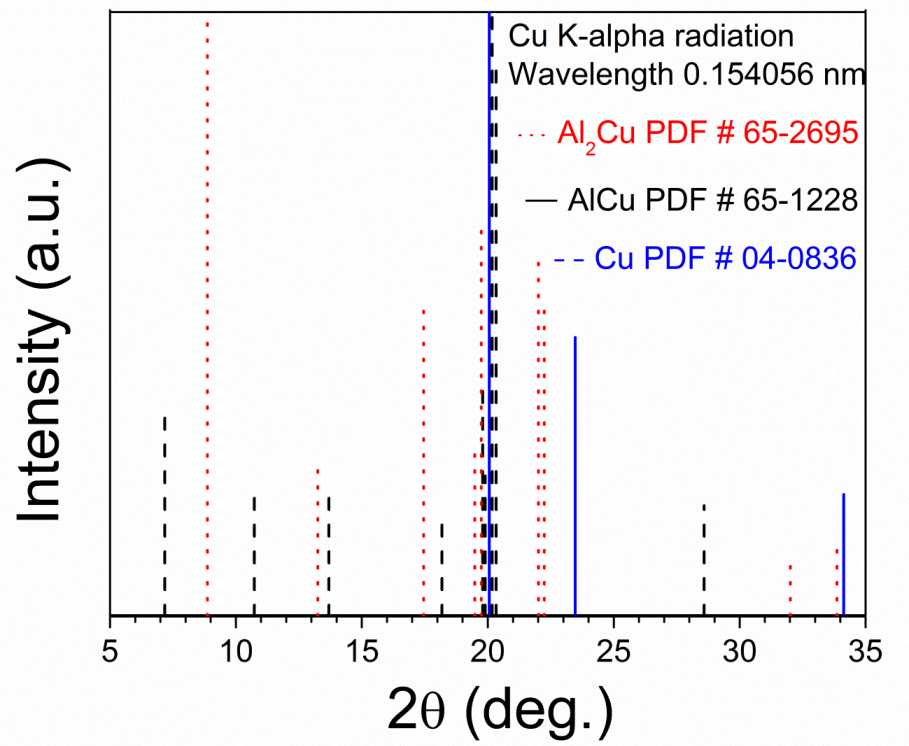

Fig. 2.29 Diffraction information (in 2θ range of 5-35° with Mo K-alpha radiation, λ = 0.70926 nm) for the phases (Al_2Cu, AlCu and Cu) involved in the dealloying of Al-Cu alloys in the International Crystal Diffraction Data (ICDD) database.

Synchrotron radiation provides a powerful tool to quantitatively analyse the dealloying process. Renner et al. [64] used synchrotron surface sensitive XRD to characterize the structure and composition evolution at the initial stages of corrosion of a $Cu_3Au(111)$ single crystal alloy. They revealed microscopic structural changes are associated with a general passivation phenomenon on the atomic scale. They also observed the formation of a gold-enriched single-crystal layer which is two to three monolayers thick and has an unexpected inverted (CBA-) stacking sequence. At higher potentials, the protective passivation layer dewets and pure gold islands are formed; such structures form the templates for the growth of nanoporous metals. Dotzler et al. [151] used Synchrotron XRD to investigate the nanoporous

structure formation and strain development during the dealloying of Ag-Au solid solution alloys. Synchrotron XRD is a potent tool for studying phase and crystal evolution. It can be expected that the use of Synchrotron XRD can help to clarify the dealloying mechanism from the perspective of crystal structure evolution.

2.4.3 Summary

Different precursor alloys (immiscible, two-phase and ternary alloys) as shown in Fig. 2.26 and Table 2.2 can be selected for dealloying. Based on the dealloying mechanism for the solid solution Ag-Au system obtained so far, this thesis will reveal the dealloying mechanisms of the selected alloy systems *via* both ex-situ and in-situ dealloying experiments under synchrotron powder diffraction. The outcomes are expected to significantly enhance the understanding of dealloying.

References

[1] J. Zhang, J. Wang, J. Ma, Porous structures of natural materials and bionic design, J. Zheijang Univ. Sci. A, 6 (2005) 1095-1099.

[2] M. Martín-Vivaldi, J.J. Soler, J.M. Peralta-Sánchez, L. Arco, A.M. Martín-Platero, M. Martínez-Bueno, M. Ruiz-Rodríguez, E. Valdivia, Special structures of hoopoe eggshells enhance the adhesion of symbiont-carrying uropygial secretion that increase hatching success, J. Anim. Ecol., 83 (2014) 1289-1301.

[3] http://www.trr141.de/index.php/research-areas-2/research-areas/.

[4] C.-P. Yang, Y.-X. Yin, S.-F. Zhang, N.-W. Li, Y.-G. Guo, Accommodating lithium into 3D current collectors with a submicron skeleton towards long-life lithium metal anodes, Nat. Commun., 6 (2015) 80581-80589.

[5] K.C. Chen, C.C. Wang, Performance improvement of high power liquid-cooled heat sink via non-uniform metal foam arrangement, Appl. Therm. Eng., 87 (2015) 41-46.

[6] H. Nakajima, *Porous Metals with Directional Pores*, Spring Japan (2013) 45, 242-243.

[7] B. Scrosati, J. Garche, Lithium batteries: Status, prospects and future, J. Power Sources, 195 (2010) 2419-2430.

[8] B. Xu, D. Qian, Z. Wang, Y.S. Meng, Recent progress in cathode materials research for advanced lithium ion batteries, Mat. Sci. Eng. R, 73 (2012) 51-65.

[9] A. Shukla, T. Prem Kumar, Materials for next-generation lithium batteries, Curr. Sci., 94 (2008) 314-331.

[10] M. Winter, J.O. Besenhard, M.E. Spahr, P. Novák, Insertion electrode materials for rechargeable lithium batteries, Adv. Mater., 10 (1998) 725-763.
[11] D. Larcher, S. Beattie, M. Morcrette, K. Edstrom, J.C. Jumas, J.M. Tarascon, Recent findings and prospects in the field of pure metals as negative electrodes for Li-ion batteries, J. Mater. Chem., 17 (2007) 3759-3772.
[12] M.N. Obrovac, V.L. Chevrier, Alloy negative electrodes for Li-ion batteries, Chem. Rev., 114 (2014) 11444-11502.
[13] J.H. Ryu, J.W. Kim, Y.-E. Sung, S.M. Oh, Failure modes of silicon powder negative electrode in lithium secondary batteries, Electrochem. Solid-State Lett., 7 (2004) A306-A309.
[14] L.Y. Beaulieu, K.W. Eberman, R.L. Turner, L.J. Krause, J.R. Dahn, Colossal reversible volume changes in lithium alloys, Electrochem. Solid-State Lett., 4 (2001) A137-A140.
[15] L.J. Gibson, M.F. Ashby, Energy absorption in cellular materials, in *Cellular Solids: Structure and Properties*, Cambridge University Press (1997) 309-343.
[16] C. Wu, J. Maier, Y. Yu, Sn-based nanoparticles Encapsulated in a porous 3D graphene network: Advanced anodes for high-rate and long life Li-ion batteries, Adv. Funct. Mater., 25 (2015) 3488-3496.
[17] H.Q. Wang, X.H. Zhang, J.B. Wen, Y.G. Huang, F.Y. Lai, Q.Y. Li, Preparation of spherical Sn/SnO_2/porous carbon composite materials as anode material for lithium-ion batteries, J. Mater. Eng. Perform., 24 (2015) 1856-1864.
[18] J. Liu, P. Kopold, P.A. van Aken, J. Maier, Y. Yu, Energy storage materials from nature through nanotechnology: A sustainable route from reed plants to a silicon anode for lithium-ion batteries, Angew. Chem., 127 (2015) 9768-9772.
[19] Z. Zhang, Y. Wang, W. Ren, Q. Tan, Z. Zhong, F. Su, Low-cost synthesis of porous silicon via ferrite-assisted chemical etching and their application as Si-based anodes for Li-ion batteries, Adv. Electron. Mater., 1 (2015) doi: 10.1002/aelm.201400059.
[20] T. Wada, T. Ichitsubo, K. Yubuta, H. Segawa, H. Yoshida, H. Kato, Bulk-Nanoporous-Silicon negative electrode with extremely high cyclability for lithium-ion batteries prepared using a top-down process, Nano Lett., 14 (2014) 4505-4510.
[21] C. Zhao, S. Li, X. Luo, B. Li, W. Pan, H. Wu, Integration of Si in a metal foam current collector for stable electrochemical cycling in Li-ion batteries, J. Mater. Chem. A, 3 (2015) 10114-10118.
[22] L. Huang, Z. Min, Q. Zhang, Research and analysis on electrochemical performances of α-Fe_2O_3 electrode in Li-ion battery with different current collectors, Mater. Res. Bull., 66 (2015) 39-44.

[23] H. Zhao, C. Jiang, X. He, J. Ren, A new process of preparing composite microstructure anode for lithium ion batteries, J. Power Sources, 184 (2008) 532-537.
[24] L. Liu, B.G. Choi, S.O. Tung, T. Hu, Y. Liu, T. Li, T. Zhao, N.A. Kotov, Low-current field-assisted assembly of copper nanoparticles for current collectors, Faraday Discuss., 181 (2015) 383-401.
[25] Y. Yu, L. Gu, X. Lang, C. Zhu, T. Fujita, M. Chen, J. Maier, Li storage in 3D nanoporous Au-supported nanocrystalline tin, Adv. Mater., 23 (2011) 2443-2447.
[26] Z. Xie, J. Zhao, Y. Wang, One-step solvothermal synthesis of Sn nanoparticles dispersed in ternary manganese-nickel-cobalt carbonate as superior anode materials for lithium ion batteries, Electrochim. Acta, 174 (2015) 1023-1029.
[27] Y. Chen, C. Liu, X. Sun, H. Ye, C. Cheung, L. Zhou, Recycled diesel carbon nanoparticles for nanostructured battery anodes, J. Power Sources, 275 (2015) 26-31.
[28] J. Yang, M. Wachtler, M. Winter, J.O. Besenhard, Sub-microcrystalline Sn and Sn-SnSb powders as lithium storage materials for lithium-ion batteries, Electrochem. Solid-State Lett., 2 (1999) 161-163.
[29] C.K. Chan, H. Peng, G. Liu, K. McIlwrath, X.F. Zhang, R.A. Huggins, Y. Cui, High-performance lithium battery anodes using silicon nanowires, Nat. Nano., 3 (2008) 31-35.
[30] J. Yang, M. Winter, J.O. Besenhard, Small particle size multiphase Li-alloy anodes for lithium-ion batteries, Solid State Ionics, 90 (1996) 281-287.
[31] X. Yan, Z. Wang, M. He, Z. Hou, T. Xia, G. Liu, X. Chen, TiO_2 Nanomaterials as anode materials for lithium-ion rechargeable batteries, Energy Technol., 3 (2015) 801-814.
[32] I.S. Kim, G.E. Blomgren, P.N. Kumta, Nanostructured Si/TiB_2 composite anodes for Li-ion batteries, Electrochem. Solid-State Lett., 6 (2003) A157-A161.
[33] A.D.W. Todd, P.P. Ferguson, J.G. Barker, M.D. Fleischauer, J.R. Dahn, Comparison of mechanically milled and sputter deposited Tin–Cobalt–Carbon alloys using small angle neutron scattering, J. Electrochem. Soc., 156 (2009) A1034-A1040.
[34] L.Y. Beaulieu, D. Larcher, R.A. Dunlap, J.R. Dahn, Reaction of Li with grain-boundary atoms in nanostructured compounds, J. Electrochem. Soc., 147 (2000) 3206-3212.
[35] M.L. Sui, K. Lu, W. Deng, L.Y. Xiong, S. Patu, Y.Z. He, Positron-lifetime study of polycrystalline Ni-P alloys with ultrafine grains, Phys. Rev. B, 44 (1991) 6466-6471.
[36] X. Zhu, R. Birringer, U. Herr, H. Gleiter, X-ray diffraction studies of the structure of nanometer-sized crystalline materials, Phys. Rev. B, 35 (1987) 9085-9090.

[37] M.M. Thackeray, L. Trahey, J.T. Vaughey, Multi-component intermetallic electrodes for lithium batteries, US Patent 8974959 B2 (Priority date: Jul 16, 2008) (2015).
[38] M. Zhang, T. Wang, G. Cao, Promises and challenges of tin-based compounds as anode materials for lithium-ion batteries, Int. Mater. Rev., 60 (2015) 330-352.
[39] X.J. Pang, C.H. Tan, X.H. Dai, X. Wang, G.W. Qi, S.Y. Zhang, Performance enhancement of Sn–Sb–Co alloy film anode for lithium-ion batteries via post electrodissolution treatment, J. Appl. Electrochem., 45 (2015) 115-122.
[40] D.H. Nam, R.H. Kim, C.L. Lee, H.S. Kwon, Highly reversible Sn-Co alloy anode using porous Cu foam substrate for Li-ion batteries, J. Electrochem. Soc., 159 (2012) A1822-A1826.
[41] L.M.L. Fransson, J.T. Vaughey, R. Benedek, K. Edström, J.O. Thomas, M.M. Thackeray, Phase transitions in lithiated Cu_2Sb anodes for lithium batteries: an in situ X-ray diffraction study, Electrochem. Commun., 3 (2001) 317-323.
[42] R. Goodall, A. Mortensen, Porous metals, in: D.E.L. Hono (Ed.) *Physical Metallurgy* (Fifth Edition), Elsevier, Oxford (2014) 2399-2595.
[43] Y. Conde, J.F. Despois, R. Goodall, A. Marmottant, L. Salvo, C. San Marchi, A. Mortensen, Replication processing of highly porous materials, Adv. Eng. Mater., 8 (2006) 795-803.
[44] J.W. Joachim Baumeister, Manufacuring processes for metal foams, in: N. Dukhan (Ed.) *Metal Foams: Fundamentals and Applications*, DEStech Publications (2013) 1-30.
[45] N. Kranzlin, M. Niederberger, Controlled fabrication of porous metals from the nanometer to the macroscopic scale, Mater. Horiz., 2 (2015) 359-377.
[46] P.J. Tan, S.R. Reid, J.J. Harrigan, On the dynamic mechanical properties of open-cell metal foams – A re-assessment of the 'simple-shock theory', Int. J. Solids Struct., 49 (2012) 2744-2753.
[47] V. Paserin, S. Marcuson, J. Shu, D.S. Wilkinson, CVD technique for inco nickel foam production, Adv. Eng. Mater., 6 (2004) 454-459.
[48] B. Ye, D.C. Dunand, Titanium foams produced by solid-state replication of NaCl powders, Mater. Sci. Eng. A, 528 (2010) 691-697.
[49] T. Guillén, A. Ohrndorf, G. Tozzi, J. Tong, H.-J. Christ, Compressive fatigue behavior of bovine cancellous bone and bone analogous materials under multi-step loading conditions, Adv. Eng. Mater., 14 (2012) B199-B207.

[50] W. Zhou, Y. Tang, R. Song, L. Jiang, K.S. Hui, K.N. Hui, Characterization of electrical conductivity of porous metal fiber sintered sheet using four-point probe method, Mater. Design, 37 (2012) 161-165.
[51] K.C. Leong, C.Y. Liu, G.Q. Lu, Characterization of sintered copper wicks used in heat pipes, J. Porous Mater., 4 (1997) 303-308.
[52] N. Lippitz, J. Rösler, B. Hinze, Potential of metal fibre felts as passive absorbers in absorption ailencers, Metals, 3 (2013) 150.
[53] A. Stein, F. Li, N.R. Denny, Morphological control in colloidal crystal templating of inverse opals, hierarchical structures, and shaped particles, Chem. Mater., 20 (2008) 649-666.
[54] J. Zhang, C.M. Li, Nanoporous metals: fabrication strategies and advanced electrochemical applications in catalysis, sensing and energy systems, Chem. Soc. Rev., 41 (2012) 7016-7031.
[55] J.R. Hayes, G.W. Nyce, J.D. Kuntz, J.H. Satcher, A.V. Hamza, Synthesis of bi-modal nanoporous Cu, CuO and Cu_2O monoliths with tailored porosity, Nanotechnology, 18 (2007) 275602.
[56] P. Jiang, J. Cizeron, J.F. Bertone, V.L. Colvin, Preparation of macroporous metal films from colloidal crystals, J. Am. Chem. Soc., 121 (1999) 7957-7958.
[57] X. Yu, Y.J. Lee, R. Furstenberg, J.O. White, P.V. Braun, Filling fraction dependent properties of inverse opal metallic photonic crystals, Adv. Mater., 19 (2007) 1689-1692.
[58] H. Liu, Q. Yang, Facile fabrication of nanoporous Au-Pd bimetallic foams with high catalytic activity for 2-nitrophenol reduction and SERS property, J. Mater. Chem., 21 (2011) 11961-11967.
[59] N.C. Bigall, A.K. Herrmann, M. Vogel, M. Rose, P. Simon, W. Carrillo-Cabrera, D. Dorfs, S. Kaskel, N. Gaponik, A. Eychmüller, Hydrogels and aerogels from noble metal nanoparticles, Angew. Chem. Int. Edit., 48 (2009) 9731-9734.
[60] M. Li, Y. Su, J. Zhao, H. Geng, J. Zhang, L. Zhang, C. Yang, Y. Zhang, One-pot preparation of thin nanoporous copper foils with enhanced light absorption and SERS properties, CrystEngComm, 17 (2015) 1296-1304.
[61] J. Erlebacher, M.J. Aziz, A. Karma, N. Dimitrov, K. Sieradzki, Evolution of nanoporosity in dealloying, Nature, 410 (2001) 450-453.
[62] H. Lechtman, Pre-Columbian surface metallurgy, Sci. Am., 250 (1984) 56-63154.
[63]http://www.banrepcultural.org/blaavirtual/publicacionesbanrep/bolmuseo/1998/endi4445/endi03d.htm.

[64] F.U. Renner, A. Stierle, H. Dosch, D.M. Kolb, T.L. Lee, J. Zegenhagen, Initial corrosion observed on the atomic scale, Nature, 439 (2006) 707-710.
[65] http://www.corrosion.org/wco_media/nowisthetime.pdf.
[66] Y. Ding, M. Chen, Nanoporous metals for catalytic and optical applications, MRS Bull., 34 (2009) 569-576.
[67] A. Wittstock, J. Biener, M. Baumer, Nanoporous gold: a new material for catalytic and sensor applications, Phys. Chem. Chem. Phys., 12 (2010) 12919-12930.
[68] H.-J. Jin, J. Weissmüller, Bulk nanoporous metal for actuation, Adv. Eng. Mater., 12 (2010) 714-723.
[69] A. Wittstock, M. Bäumer, Catalysis by unsupported skeletal gold catalysts, Acc. Chem. Res., 47 (2014) 731-739.
[70] H.W. Pickering, C. Wagner, Electrolytic dissolution of binary alloys containing a noble metal, J. Electrochem. Soc., 114 (1967) 698-706.
[71] D. Artymowicz, R. Newman, J. Erlebacher, Insights into the parting limit for de-alloying from reconsideration of atomistic considerations, ECS Trans., 3 (2007) 499-506.
[72] D.M. Artymowicz, J. Erlebacher, R.C. Newman, Relationship between the parting limit for de-alloying and a particular geometric high-density site percolation threshold, Philos. Mag., 89 (2009) 1663-1693.
[73] Z. Qi, U. Vainio, A. Kornowski, M. Ritter, H. Weller, H. Jin, J. Weissmüller, Porous gold with a nested-network architecture and ultrafine structure, Adv. Funct. Mater., 25 (2015) 2530-2536.
[74] X. Li, Q. Chen, I. McCue, J. Snyder, P. Crozier, J. Erlebacher, K. Sieradzki, Dealloying of noble-metal alloy nanoparticles, Nano Lett., 14 (2014) 2569-2577.
[75] L. Burr, I. Schubert, W. Sigle, C. Trautmann, M.E. Toimil-Molares, Surface enrichment in Au–Ag alloy nanowires and investigation of the dealloying process, J. Phys. Chem. C, 119 (2015) 20949-20956.
[76] Z. Yu, J. Zhang, Z. Liu, J.M. Ziegelbauer, H. Xin, I. Dutta, D.A. Muller, F.T. Wagner, Comparison between dealloyed $PtCo_3$ and $PtCu_3$ cathode catalysts for proton exchange membrane fuel cells, J. Phys. Chem. C, 116 (2012) 19877-19885.
[77] F.U. Renner, G.N. Ankah, A. Bashir, D. Ma, P.U. Biedermann, B.R. Shrestha, M. Nellessen, A. Khorashadizadeh, P. Losada-Pérez, M.J. Duarte, D. Raabe, M. Valtiner, Star-shaped crystallographic cracking of localized nanoporous defects, Adv. Mater., 2 (2015) 4877-4882.

[78] Y. Zhong, J. Markmann, H.-J. Jin, Y. Ivanisenko, L. Kurmanaeva, J. Weissmüller, Crack mitigation during dealloying of Au25Cu75, Adv. Eng. Mater., 16 (2014) 389-398.
[79] Z. Qi, C. Zhao, X. Wang, J. Lin, W. Shao, Z. Zhang, X. Bian, Formation and characterization of monolithic nanoporous copper by chemical dealloying of Al−Cu alloys, J. Phys. Chem. C, 113 (2009) 6694-6698.
[80] J. Li, H. Jiang, N. Yu, C. Xu, H. Geng, Fabrication and characterization of bulk nanoporous copper by dealloying Al–Cu alloy slices, Corros. Sci., 90 (2015) 216-222.
[81] M. Zhang, A.M. Jorge Junior, S.J. Pang, T. Zhang, A.R. Yavari, Fabrication of nanoporous silver with open pores, Scr. Mater., 100 (2015) 21-23.
[82] T.T. Song, Y.L. Gao, Z.H. Zhang, Q.J. Zhai, Microstructure and phase evolution during the dealloying of bi-phase Al–Ag alloy, Corros. Sci., 68 (2013) 256-262.
[83] N.T. Tuan, J. Park, J. Lee, J. Gwak, D. Lee, Synthesis of nanoporous Cu films by dealloying of electrochemically deposited Cu–Zn alloy films, Corros. Sci., 80 (2014) 7-11.
[84] Q. Zhang, Z.H. Zhang, On the electrochemical dealloying of Al-based alloys in a NaCl aqueous solution, Phys. Chem. Chem. Phys., 12 (2010) 1453-1472.
[85] C. Zhao, Z. Qi, X. Wang, Z. Zhang, Fabrication and characterization of monolithic nanoporous copper through chemical dealloying of Mg–Cu alloys, Corros. Sci., 51 (2009) 2120-2125.
[86] C. Zhao, X. Wang, Z. Qi, H. Ji, Z. Zhang, On the electrochemical dealloying of Mg–Cu alloys in a NaCl aqueous solution, Corros. Sci., 52 (2010) 3962-3972.
[87] Q. Zhang, Z.H. Zhang, On the electrochemical dealloying of Al-based alloys in a NaCl aqueous solution, Phys. Chem. Chem. Phys., 12 (2010) 1453-1472.
[88] X. Luo, R. Li, L. Huang, T. Zhang, Nucleation and growth of nanoporous copper ligaments during electrochemical dealloying of Mg-based metallic glasses, Corros. Sci., 67 (2013) 100-108.
[89] H. Ji, X. Wang, C. Zhao, C. Zhang, J. Xu, Z. Zhang, Formation, control and functionalization of nanoporous silver through changing dealloying media and elemental doping, CrystEngComm, 13 (2011) 2617-2628.
[90] J. Snyder, P. Asanithi, A.B. Dalton, J. Erlebacher, Stabilized nanoporous metals by dealloying ternary alloy precursors, Adv. Mater., 20 (2008) 4883-4886.
[91] Z. Zhang, Y. Wang, X. Wang, Nanoporous bimetallic Pt-Au alloy nanocomposites with superior catalytic activity towards electro-oxidation of methanol and formic acid, Nanoscale, 3 (2011) 1663-1674.

[92] Y. Wang, J. Xu, B. Wu, Electrochemical dealloying of Al_2(Au,X) (X = Pt, Pd, PtPd, Ni, Co and NiCo) alloys in NaCl aqueous solution, Phys. Chem. Chem. Phys., 15 (2013) 5499-5509.

[93] Z. Qi, U. Vainio, A. Kornowski, M. Ritter, H. Weller, H. Jin, J. Weissmüller, Porous gold with a nested-network architecture and ultrafine structure, Adv. Funct. Mater., (2015) 2530-2536.

[94] Z. Zhang, Y. Wang, Z. Qi, W. Zhang, J. Qin, J. Frenzel, Generalized fabrication of nanoporous metals (Au, Pd, Pt, Ag, and Cu) through chemical dealloying, J. Phys. Chem. C, 113 (2009) 12629-12636.

[95] R.C. Newman, K. Sieradzki, Metallic corrosion, Science, 263 (1994) 1708-1709.

[96] Q. Kong, L. Lian, Y. Liu, J. Zhang, L. Wang, W. Feng, Bulk hierarchical nanoporous palladium prepared by dealloying PdAl alloys and its electrochemical properties, Micropor. Mesopor. Mater., 208 (2015) 152-159.

[97] J. Snyder, K. Livi, J. Erlebacher, Dealloying silver/gold alloys in neutral silver nitrate solution: Porosity evolution, surface composition, and surface oxides, J. Electrochem. Soc., 155 (2008) C464-C473.

[98] A.M. Hodge, J.R. Hayes, J.A. Caro, J. Biener, A.V. Hamza, Characterization and mechanical behavior of nanoporous gold, Adv. Eng. Mater., 8 (2006) 853-857.

[99] R. Elliott, F. Shunk, The Ag−Au (silver-gold) system, Bull. Alloy Phase Diagr., 1 (1980) 45-47.

[100] A.J. Forty, Corrosion micromorphology of noble metal alloys and depletion gilding, Nature, 282 (1979) 597-598.

[101] K. Sieradzki, R.C. Newman, Micro- and nano-porous metallic structures, US patent 4977083 (Priority date: Apr 14, 1989) (1990).

[102] I.C. Oppenheim, D.J. Trevor, C.E.D. Chidsey, P.L. Trevor, K. Sieradzki, In situ scanning tunneling microscopy of corrosion of silver-gold alloys, Science, 254 (1991) 687-689.

[103] R.C. Newman, K. Sieradzki, Corrosion science, MRS Bull., 24 (1999) 12-15.

[104] Y. Ding, Y.J. Kim, J. Erlebacher, Nanoporous gold leaf: "Ancient technology"/advanced material, Adv. Mater., 16 (2004) 1897-1900.

[105] Y. Ding, J. Erlebacher, Nanoporous metals with controlled multimodal pore size distribution, J. Am. Chem. Soc., 125 (2003) 7772-7773.

[106] X. Ke, Z. Li, L. Gan, J. Zhao, G. Cui, W. Kellogg, D. Matera, D. Higgins, G. Wu, Three-dimensional nanoporous Au films as high-efficiency enzyme-free electrochemical sensors, Electrochim. Acta, 170 (2015) 337-342.
[107] E. Detsi, M. van de Schootbrugge, S. Punzhin, P.R. Onck, J.T.M. De Hosson, On tuning the morphology of nanoporous gold, Scr. Mater., 64 (2011) 319-322.
[108] X. Gu, L. Xu, F. Tian, Y. Ding, Au-Ag alloy nanoporous nanotubes, Nano Res., 2 (2009) 386-393.
[109] D. Garoli, E. Calandrini, S. Cattarin, S. Barison, P. Zilio, A. Bozzola, A. Toma, F. De Angelis, Engineered/tailored nanoporous gold structures for infrared plasmonics, Proc. SPIE, 9547 (2015) 95470K1-95470K6.
[110] L.-Y. Chen, J.-S. Yu, T. Fujita, M.-W. Chen, Nanoporous copper with tunable nanoporosity for SERS applications, Adv. Funct. Mater., 19 (2009) 1221-1226.
[111] X.-M. Zhang, Y.-X. Li, H.-W. Zhang, Y. Liu, Evolution of porous structure with dealloying corrosion on Gasar Cu–Mn alloy, Trans. Nonferrous Met. Soc. China, 25 (2015) 1200-1205.
[112] K. Koboski, E. Nelsen, J. Hampton, Hydrogen evolution reaction measurements of dealloyed porous NiCu, Nanoscale Res. Lett., 8 (2013) 1-7.
[113] K. Maruya, R. Yamauchi, T. Narushima, S. Miura, T. Yonezawa, Structure consideration of platinum nanoparticles constructing nanostructures obtained by electrochemical dealloying of a Cu-Pt alloy, J. Nanosci. Nanotechnol., 13 (2013) 2999-3003.
[114] F.U. Renner, G.N. Ankah, A. Bashir, D. Ma, P.U. Biedermann, B.R. Shrestha, M. Nellessen, A. Khorashadizadeh, P. Losada-Pérez, M.J. Duarte, D. Raabe, M. Valtiner, Star-shaped crystallographic cracking of localized nanoporous defects, Adv. Mater., 2 (2015) 4877-4882.
[115] G.N. Ankah, A. Pareek, S. Cherevko, A.A. Topalov, M. Rohwerder, F.U. Renner, The influence of halides on the initial selective dissolution of Cu_3Au (1 1 1), Electrochim. Acta, 85 (2012) 384-392.
[116] A. Pareek, S. Borodin, A. Bashir, G.N. Ankah, P. Keil, G.A. Eckstein, M. Rohwerder, M. Stratmann, Y. Gründer, F.U. Renner, Initiation and inhibition of dealloying of single crystalline Cu_3Au (111) surfaces, J. Am. Chem. Soc., 133 (2011) 18264-18271.
[117] Q. Zhang, X. Wang, Z. Qi, Y. Wang, Z. Zhang, A benign route to fabricate nanoporous gold through electrochemical dealloying of Al–Au alloys in a neutral solution, Electrochim. Acta, 54 (2009) 6190-6198.

[118] Z. Zhang, Y. Wang, Z. Qi, C. Somsen, X. Wang, C. Zhao, Fabrication and characterization of nanoporous gold composites through chemical dealloying of two phase Al-Au alloys, J. Mater. Chem., 19 (2009) 6042-6050.
[119] J. Xu, Y. Wang, Z. Zhang, Potential and concentration dependent electrochemical dealloying of Al_2Au in sodium chloride solutions, J. Phys. Chem. C, 116 (2012) 5689-5699.
[120] W. Liu, S. Zhang, N. Li, J. Zheng, Y. Xing, Fabrication and dealloying behavior of monolithic nanoporous copper ribbons with bimodal channel size distributions, J. Mater. Sci. Tech., 28 (2012) 693-699.
[121] X. Wang, Z. Qi, C. Zhao, W. Wang, Z. Zhang, Influence of alloy composition and dealloying solution on the formation and microstructure of monolithic nanoporous silver through chemical dealloying of Al−Ag alloys, J. Phys. Chem. C, 113 (2009) 13139-13150.
[122] W.B. Liu, S.C. Zhang, N. Li, J.W. Zheng, Y.L. Xing, Influence of phase constituent and proportion in initial Al–Cu alloys on formation of monolithic nanoporous copper through chemical dealloying in an alkaline solution, Corros. Sci., 53 (2011) 809-814.
[123] Z. Zhang, Y. Wang, Z. Qi, J. Lin, X. Bian, Nanoporous gold ribbons with bimodal channel size distributions by chemical dealloying of Al−Au alloys, J. Phys. Chem. C, 113 (2009) 1308-1314.
[124] W. Liu, L. Chen, J. Yan, N. Li, S. Shi, S. Zhang, Dealloying solution dependence of fabrication, microstructure and porosity of hierarchical structured nanoporous copper ribbons, Corros. Sci., 94 (2015) 114-121.
[125] X.-L. Ye, N. Lu, X.-J. Li, K. Du, J. Tan, H.-J. Jin, Primary and secondary dealloying of Au(Pt)-Ag: Structural and compositional evolutions, and volume shrinkage, J. Electrochem. Soc., 161 (2014) C517-C526.
[126] Y. Wang, B. Wu, Formation and evolution of nanoporous dendrites during dealloying of a ternary Al-Ag-Au precursor, CrystEngComm, 16 (2014) 479-485.
[127] Z. Zhang, C. Zhang, Y. Gao, J. Frenzel, J. Sun, G. Eggeler, Dealloying strategy to fabricate ultrafine nanoporous gold-based alloys with high structural stability and tunable magnetic properties, CrystEngComm, 14 (2012) 8292-8300.
[128] Y. Feng, S. Zhang, Y. Xing, W. Liu, Preparation and characterization of nanoporous Cu6Sn5/Cu composite by chemical dealloying of Al–Cu–Sn ternary alloy, J Mater. Sci, 47 (2012) 5911-5917.
[129] K. Sieradzki, N. Dimitrov, D. Movrin, C. McCall, N. Vasiljevic, J. Erlebacher, The dealloying critical potential, J. Electrochem. Soc., 149 (2002) B370-B377.

[130] K. Wagner, S.R. Brankovic, N. Dimitrov, K. Sieradzki, Dealloying below the critical potential, J. Electrochem. Soc., 144 (1997) 3545-3555.
[131] C. Zhang, J. Sun, J. Xu, X. Wang, H. Ji, C. Zhao, Z. Zhang, Formation and microstructure of nanoporous silver by dealloying rapidly solidified Zn–Ag alloys, Electrochim. Acta, 63 (2012) 302-311.
[132] E. Seker, J.T. Gaskins, H. Bart-Smith, J. Zhu, M.L. Reed, G. Zangari, R. Kelly, M.R. Begley, The effects of annealing prior to dealloying on the mechanical properties of nanoporous gold microbeams, Acta Mater., 56 (2008) 324-332.
[133] E. Seker, M.L. Reed, M.R. Begley, A thermal treatment approach to reduce microscale void formation in blanket nanoporous gold films, Scr. Mater., 60 (2009) 435-438.
[134] S. Chattopadhyay, C.M. Sellars, Kinetics of pearlite spheroidisation during static annealing and during hot deformation, Acta Metall., 30 (1982) 157-170.
[135] L.H. Qian, M.W. Chen, Ultrafine nanoporous gold by low-temperature dealloying and kinetics of nanopore formation, Appl. Phys. Lett., 91 (2007) 083105.
[136] K.N. Tu, R.D. Thompson, Kinetics of interfacial reaction in bimetallic Cu-Sn thin films, Acta Metall., 30 (1982) 947-952.
[137] K. Wang, J. Weissmüller, Composites of nanoporous gold and polymer, Adv. Mater., 25 (2013) 1280-1284.
[138] H.J. Qiu, Y. Ito, M.W. Chen, Hierarchical nanoporous nickel alloy as three-dimensional electrodes for high-efficiency energy storage, Scr. Mater., 89 (2014) 69-72.
[139] T. Fujita, Y. Kanoko, Y. Ito, L. Chen, A. Hirata, H. Kashani, O. Iwatsu, M. Chen, Nanoporous metal papers for scalable hierarchical electrode, Adv. Sci., 2 (2015) doi: 10.1002/advs.201500086.
[140] A.J. McAlister, D.J. Kahan, The Al−Sn (aluminum-tin) system, Bull. Alloy Phase Diagr., 4 (1983) 410-414.
[141] Y. Funamizu, K. Watanabe, Interdiffusion in the Al-Cu System, T. Jpn. I. Met., 12 (1971) 147-152.
[142] A.J. Forty, P. Durkin, A micromorphological study of the dissolution of silver-gold alloys in nitric acid, Philos. Mag. A, 42 (1980) 295-318.
[143] A.J. Forty, Micromorphological studies of the corrosion of gold alloys, Gold bull. 14 (1981) 25-35
[144] R.B. Abrams, The dezincification of brass, Trans. Am. Chem. Soc, 42 (1922) 39-55.
[145] K. Deutsche, in Korrosion XIV: Korrosionsschutz durch Legieren, Verlag Chemie, Weinheim (1962).

[146] K. Sieradzki, Curvature effects in alloy dissolution, J. Electrochem. Soc., 140 (1993) 2868-2872.

[147] A. Dursun, Nanoporosity formation in Au-Ag alloys, Ph. D. Dissertation, (2003).

[148] K. Sieradzki, R.R. Corderman, K. Shukla, R.C. Newman, Computer simulations of corrosion: Selective dissolution of binary alloys, Philos. Mag. A, 59 (1989) 713-746.

[149] J. Erlebacher, An atomistic description of dealloying: Porosity evolution, the critical potential, and rate-limiting behavior, J. Electrochem. Soc., 151 (2004) C614-C626.

[150] N. Kuwano, T. Doi, T. Eguchi, Period of antiphase and tetragonality in the α_2 phase of Cu-Al alloys, T. Jpn. I. Met., 18 (1977) 807-815.

[151] C.J. Dotzler, B. Ingham, B.N. Illy, K. Wallwork, M.P. Ryan, M.F. Toney, In situ observation of strain development and porosity evolution in nanoporous gold foils, Adv. Funct. Mater., 21 (2011) 3938-3946.

Chapter 3 A dealloying approach to synthesizing micro-sized porous tin (Sn) from immiscible alloy system

Tin (Sn) metal is featured by higher specific capacity (994 mA·h g^{-1}) than that of commercialized graphite (372 mA·h g^{-1}). However, it undergoes a large volume expansion (360%) as an anode in lithium ion batteries (LIBs). Porous forms of Sn are expected to be able to cope with the volume change (see Section **2.1 Porous materials in lithium ion batteries**). Dealloying is a capable approach to producing micro/nanoporous metallic materials and has been applied to the synthesis of porous noble metals such as Au, Ag, Pt and Pd from various forms of precursor materials, e.g. amorphous, solid solution, or intermetallic compound alloys (see Section **2.3.1 Introduction to dealloying**).

This chapter deals with the dealloying of immiscible Al-Sn alloys and evaluates the effects of precursor alloy composition on the phase distribution in the precursor alloy and the pore size in the as-dealloyed porous structures (see Section **2.3.2.1 Binary alloys**). In addition, the performance of the as-dealloyed porous Sn as an anode in LIBs is also assessed (see Section **2.1 Porous materials in lithium ion batteries**).

(Paper 1)

A dealloying approach to synthesizing micro-sized porous tin (Sn) from immiscible alloy systems for potential lithium-ion battery anode applications

Tingting Song, Ming Yan, Ma Qian

Journal of Porous Materials, (2015) 1-7

J Porous Mater (2015) 22:713–719
DOI 10.1007/s10934-015-9944-6

A dealloying approach to synthesizing micro-sized porous tin (Sn) from immiscible alloy systems for potential lithium-ion battery anode applications

Tingting Song[1] · Ming Yan[1,2] · Ma Qian[1]

Published online: 24 March 2015

Abstract Dealloying is a useful approach to producing micro/nanoporous metallic materials and has been applied to the synthesis of porous noble metals such as Au, Ag, Pt and Pd from various forms of precursor materials (e.g. amorphous, solid solution, or intermetallic compound). This study shows that dealloying can also be used to fabricate porous non-noble metals like tin (Sn) from immiscible Al–Sn alloys of Al80Sn20, Al65Sn35 and Al50Sn50 (in at.% throughout the paper). The as-dealloyed porous Sn samples showed a three-dimensionally continuous porous structure throughout each sample and sufficient mechanical integrity for assembly in lithium ion battery cells as anodes. The average pore size depends on the size of the Al phase in each precursor alloy and falls in the range of 1.58 ± 0.26 to 4.09 ± 0.85 μm with respect to the three precursor alloys used. The resulting porous Sn structures can be controlled through changing the microstructure of the precursor alloy. The as-dealloyed porous Sn anode showed an outstanding initial charging-discharging capacity and a high coulombic efficiency in lithium ion battery performance tests.

✉ Ma Qian
ma.qian@rmit.edu.au

[1] School of Aerospace, Mechanical and Manufacturing Engineering, Centre for Additive Manufacturing, RMIT University, Melbourne, VIC 3001, Australia

[2] Department of Materials Science and Engineering, South University of Science and Technology of China, Shenzhen 518055, Guangdong, China

Keywords Dealloying · Immiscible alloys · Al–Sn alloys · Porous tin · Anode

1 Introduction

With the increasing demand for advanced electrical vehicles and mobile electronic devices, researchers working on lithium-ion batteries (LIBs) are being challenged to develop high performance electrodes with superior energy density [1]. Tin (Sn), as a metal based candidate anode material, has attracted much attention for its higher theoretical specific capacity ($\sim$994 mA h g^{-1}) than that of the traditional graphite electrodes during the Li^+ storage process [see Eq. (1)] [2].

$$4.4Li + Sn \rightarrow Li_{4.4}Sn \quad (1)$$

However, the large atomic uptake during lithiation [a rise by 440 % in the amount of atoms according to Eq. (1)] can induce large volume changes to the Sn anode material and this may lead to pulverization and therefore a short cycle life of the cell [2]. In this regard, making the Sn anode into a three-dimensionally porous structure may offer a promising solution as the porous structure has the potential to serve as a strain buffer to mitigate the detrimental impact from the large volume changes [3]. To date, much effort has been made to fabricate such porous Sn anodes using electrodeposition [3, 4], magnetic sputtering [5], and sol–gel [6]. However, none of these methods has received wide acceptance as yet. Hence, it is necessary to develop a simpler and more competent approach to the fabrication of porous Sn with micro-sized or even nano-sized porosity.

Dealloying, which is essentially a selective corrosion process [7], can be such a potential solution. During dealloying, the less noble component leaves the precursor alloy

and dissolves into the electrolyte, while the remaining nobler element diffuses and develops into a three-dimensionally continuous nano-sized and/or micro-sized porous structure. Novel mechanical [8] and optical [9] properties have been reported for such porous structures and potential applications (e.g. as catalysts [10] and sensors [11]) were recommended. A number of alloy systems have been dealloyed so far to fabricate porous metal structures, including Al–Zn (solid solution) [12], Si–Pt (amorphous) [13], Al–Ag (solid solution + intermetallic compound) [14], and Al–Cu (consisting of two intermetallic compounds without solid solution phases) alloys [15]. However, no dealloying effort has been made of immiscible alloy systems.

In this study, we selected three immiscible Al–Sn alloys as the precursors to investigate the dealloying process of immiscible alloy systems. The standard electrode potentials of Al and Sn are $E_{Al3+/Al} = -1.66$ V, and $E_{Sn2+/Sn} = -0.13$ V. Al is thus more active than Sn and is expected to be dealloyed from the Al–Sn alloys. Experiments confirmed this deduction and the phase constitution and microstructure of the as-dealloyed porous Sn foil samples were studied. In addition, an as-dealloyed porous Sn foil was assembled into a LIB unit as the anode for evaluation of its electrochemical performance.

2 Experimental

Ingots of Al50Sn50, Al65Sn35 and Al80Sn20 (in at.%) alloys were prepared from Al (purity, 99.99 %) and Sn (purity, 99.999 %) metals using an arc melting furnace under an argon atmosphere. The ingots were remelted four times at least to ensure chemical homogeneity. The molten alloy was sucked into a copper mould (~ϕ 8 mm × 30 mm) by the pressure differential between the sample chamber and the melting chamber. The as-cast rod samples were cut, ground and polished into foils (~ϕ 8 mm × ~0.15 mm).

Dealloying of the Al–Sn foil samples was carried out in a 5 wt% HCl aqueous solution at 70 ± 2 °C for 120 min. The samples were then rinsed in distilled water and dehydrated alcohol. The mass and thickness of each foil sample were recorded both before and after dealloying. X-ray diffraction (XRD, Bruker D8 with Cu Kα radiation) was used for phase identification in both the precursor alloys and their as-dealloyed samples. Powder samples (−200 mesh or <74 μm), crushed from Al–Sn precursor foils (~ϕ 8 mm × 0.15 mm), were used for the XRD of the precursor alloys. The microstructure was examined using scanning electron microscopy (SEM: JEOL 7001

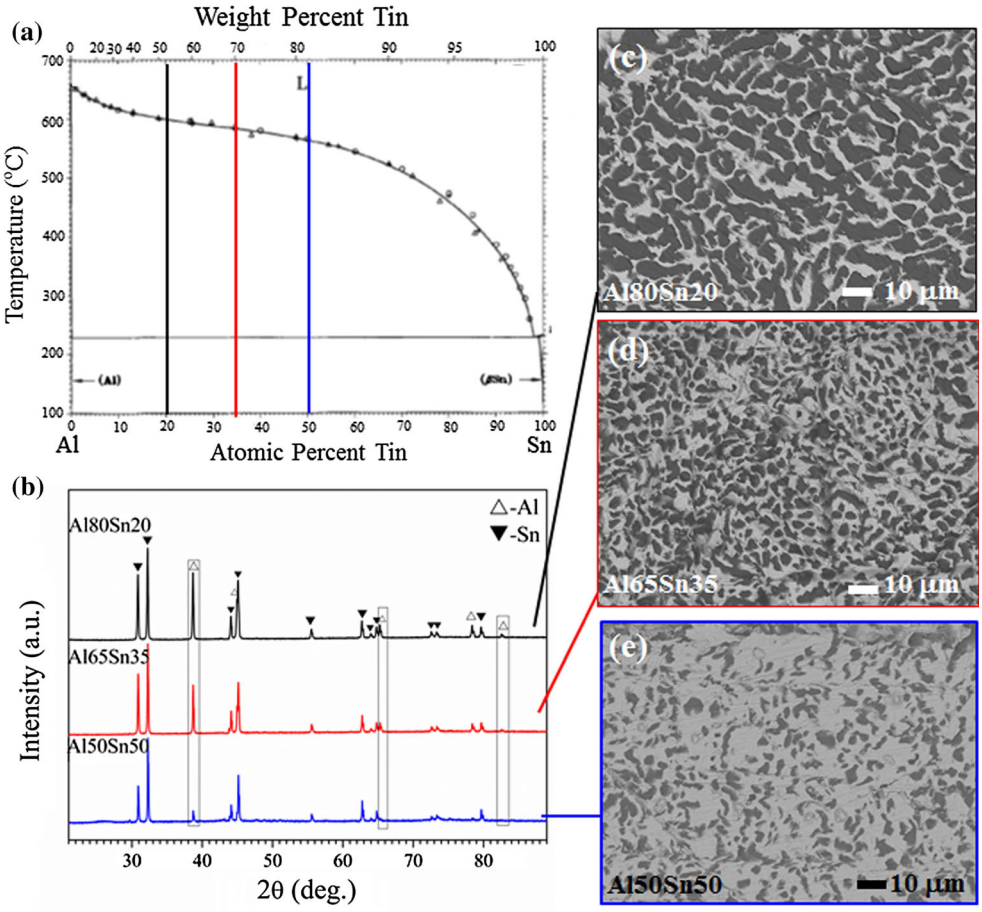

Fig. 1 Binary Al–Sn phase diagram (**a**) and XRD spectra of the three precursor Al–Sn alloys (8 mm diameter rods **b**). The corresponding SEM-BSE images (**c**–**e**) show the presence of the Al (*dark contrast*) and Sn (*light contrast*) phases in each microstructure

operated at 15 keV), assisted with energy-dispersive X-ray spectroscopy (EDX).

The electrochemical performance of the as-dealloyed samples was tested using a LAND galvanostatic charge–discharge cycle instrument after being assembled into a stainless steel coin cell (Brand 2032). The cells were cycled at room temperature at a 0.2 °C rate and between 0.01 V and 2.1 V.

3 Results and discussion

3.1 Phase constitution of the precursor alloys

Figure 1 shows the Al–Sn phase diagram [16], XRD results and SEM backscattered electron (BSE) images of the three precursor alloys of Al50Sn50, Al65Sn35 and Al80Sn20. Al and Sn are immiscible in each alloy (Fig. 1a). As expected, the intensity of the XRD peaks for the Al phase increased with increasing Al content (Fig. 1b). However, the Al peaks were found to be weaker than the Sn peaks even for the Al80Sn20 alloy (Fig. 1b) due likely to the high X-ray scattering factor of the heavy element Sn. The corresponding SEM-BSE images shown in Fig. 1c–e revealed the distribution of the Sn phase (light contrast) in the Al matrix (dark contrast). The average width of the Al phases, measured from at least 70 particles, was found to increase from 2.14 ± 0.82 (Al50Sn50) to 2.66 ± 0.61 μm (Al65Sn35), and then to 4.42 ± 0.93 μm (Al80Sn20) with increasing Al content.

The standard electrode potentials of Al and Sn are known to be $E_{Al3+/Al} = -1.66$ V, and $E_{Sn2+/Sn} = -0.13$ V. This distinct difference can readily lead to the formation of micro-galvanic corrosion cells between the Al and Sn phases shown in Fig. 1c–e [17] thereby leading to the preferential corrosion of the Al anode and the protection of the Sn cathode in the electrolytes. Table 1 lists the mass of each sample recorded before and after dealloying together with the actual mass of Sn in respective Al–Sn precursor alloys. The mass of each as-dealloyed sample (i.e. the leftover) was consistently lower than the actual mass of Sn in respective precursor alloys. This implies that there was some dissolution of Sn during dealloying. However, no consequences were observed from the limited dissolution of Sn as yet. It is possible to avoid the small dissolution of Sn by using a different acid solution as Sn responds differently to different acid solutions [18].

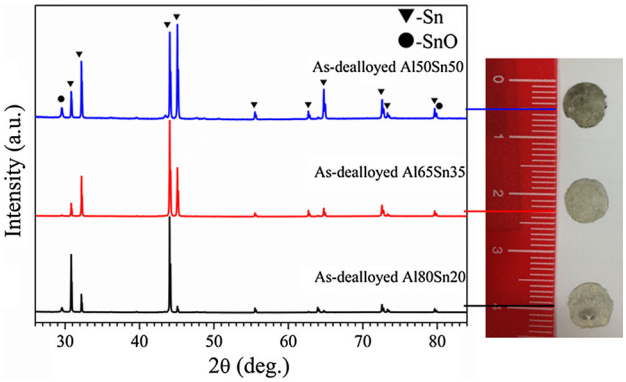

Fig. 2 XRD spectra of as-dealloyed Al–Sn foil samples together with photos showing the mechanical integrity of the as-dealloyed samples

3.2 Phase constitution and microstructure of as-dealloyed samples

Figure 2 shows the XRD results of the as-dealloyed Al–Sn foil samples together with three images showing the physical status of each sample. After dealloying, the Al phase disappeared in each precursor alloy and the as-dealloyed samples consisted of essentially the single Sn phase. A small presence of SnO was detected, but since SnO is a high capacity lithium ion storage material [19], its presence in the as-dealloyed material is not necessarily negative. Zhang et al. [20] fabricated porous Sn by dealloying of Mg70Sn30 (at.%). However, their samples lost mechanical integrity after dealloying; the original ribbons were not preserved but pulverized into mud-like powders according to the authors. As shown in Fig. 2, the as-dealloyed porous Sn in this study all showed good mechanical integrity. No problems were encountered in assembling them into batteries as anodes for performance testing (the results are shown in Fig. 5). The good mechanical integrity of the as-

Table 1 Mass and thickness of Al–Sn alloy samples before and after dealloying, together with the actual mass of Sn in respective precursor alloys

	Mass of sample before dealloying (mg)	Mass of sample after dealloying (mg)	Mass of Sn in the precursor (mg)	Sample thickness before dealloying (t_1, μm)	Sample thickness after dealloying (t_2, μm)	$[(t_1 - t_2) \times 100]/t_1$ (%)
Al80Sn20	8.7	4.2	4.5	97	67	30.9
Al65Sn35	22.3	15.4	15.8	177	120	32.2
Al50Sn50	13.9	10.2	11.2	149	96	35.5

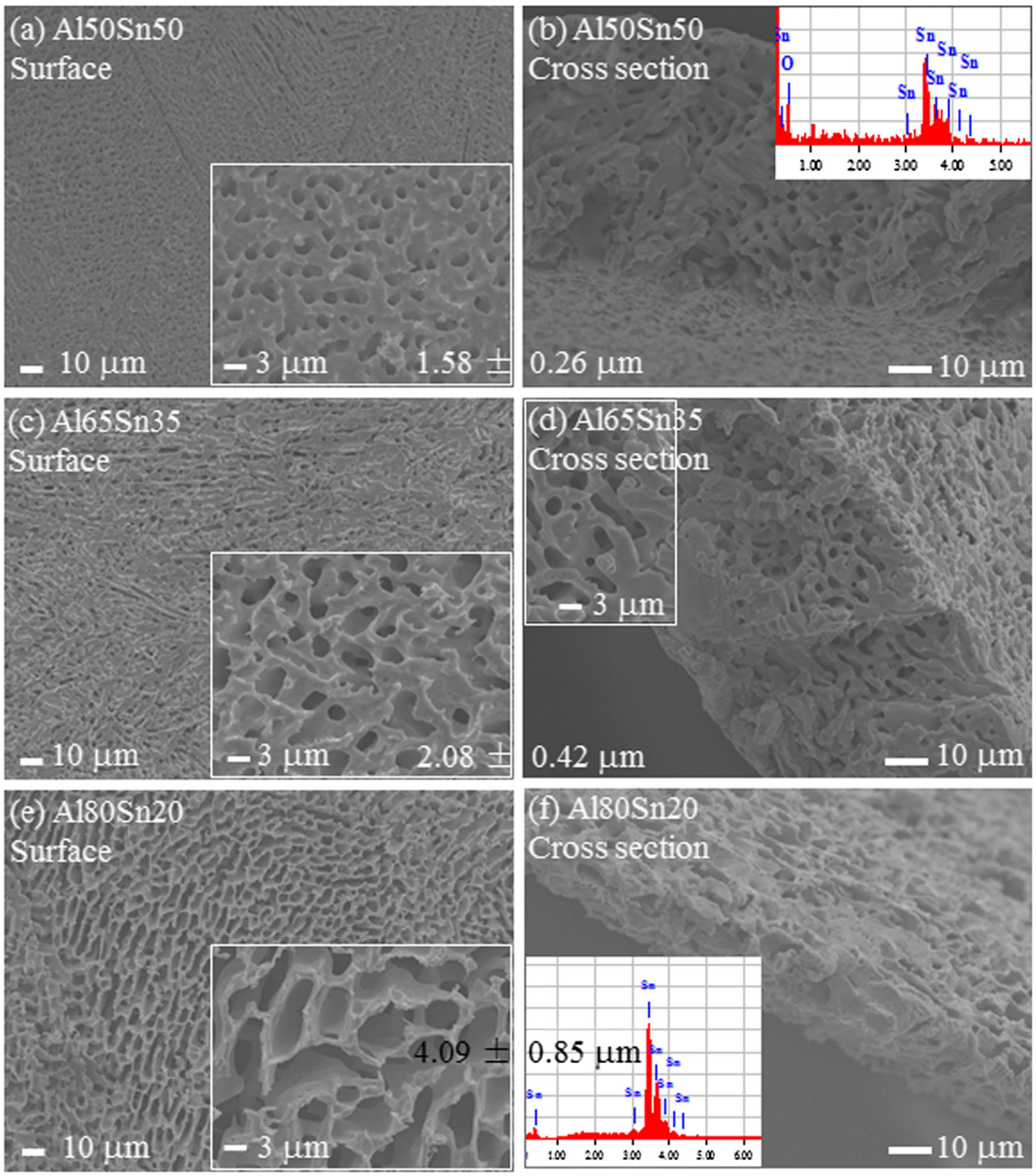

Fig. 3 SEM images and representative EDX results for porous Sn made from dealloying of Al50Sn50 (**a**, **b**), Al65Sn35 (**c**, **d**) and Al80Sn20 (**e**, **f**)

dealloyed porous Sn foil samples obtained from this study is critical to their application.

Figure 3 shows the microstructure of the as-dealloyed Al–Sn foil samples. Homogeneous porous structures were created from the surface (Fig. 3a, c, e) and across different sections (Fig. 3b, d, f) in each as-dealloyed sample. No Al was detected by the SEM-EDX analyses (see inset in Fig. 3b) in the dealloyed samples, indicative of complete dealloying, which is consistent with the XRD results shown in Fig. 2 (i.e. the absence of XRD peaks for Al). The average pore size was measured in each as-dealloyed porous Sn structure. It is 1.58 ± 0.26 μm in the porous Sn sample dealloyed from Al50Sn50, 2.08 ± 0.42 μm in that dealloyed from Al65Sn35 and 4.09 ± 0.85 μm in that dealloyed from Al80Sn20 (see Fig. 4). This is very close to the size of the Al phase in respective precursor alloys (Fig. 1c–e), suggesting that the porous structure was created by excavating the Al phase directly from each Al–Sn precursor alloy. This is supported by the observation that the resulting porous structure and the Sn ligament

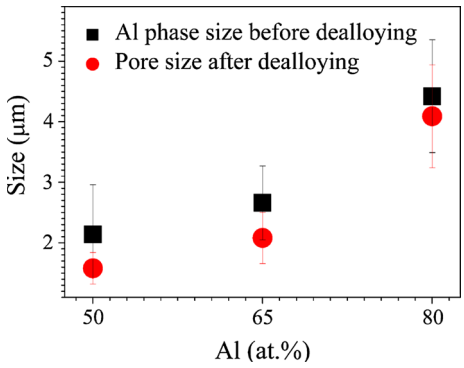

Fig. 4 Dependence of pore size in the as-dealloyed microstructure on the average size of the Al phases in corresponding precursor alloys

morphology are similar to the distribution of the Al phase and the morphology of the Sn phase, respectively, in each Al–Sn precursor alloy (Fig. 1c–e). This means that it is possible to manipulate the length scale of the porous Sn structure via the design of the precursor alloy and control of their microstructure. This concept has recently been applied to the dealloying of Al–Cu precursor alloys [21]. It differs from the mechanism by which a porous structure is created in a classical dealloying process, which comprises leaching of the non-noble element and diffusion of the noble element along the electrolyte/solid interface [7]. The resulting porous structures have no direct correspondences to the starting microstructure.

Also listed in Table 1 are the sample thickness values before and after dealloying. The sample thickness showed a reduction of more than 30 % after dealloying. This can be attributed to the volume shrinkage effect caused by dealloying due to the removal of the Al atoms (the main constituting element) from the precursor alloys as well as the limited dissolution of Sn discussed earlier. A similar degree of dealloying-induced volume contraction has been reported for dealloying of Au–Ag alloys [22].

3.3 Electrochemical performance of porous Sn anode

Three as-dealloyed porous Sn foil samples were assembled into lithium ion batteries as anodes for performance testing. Figure 5 shows a typical example of the electrochemical

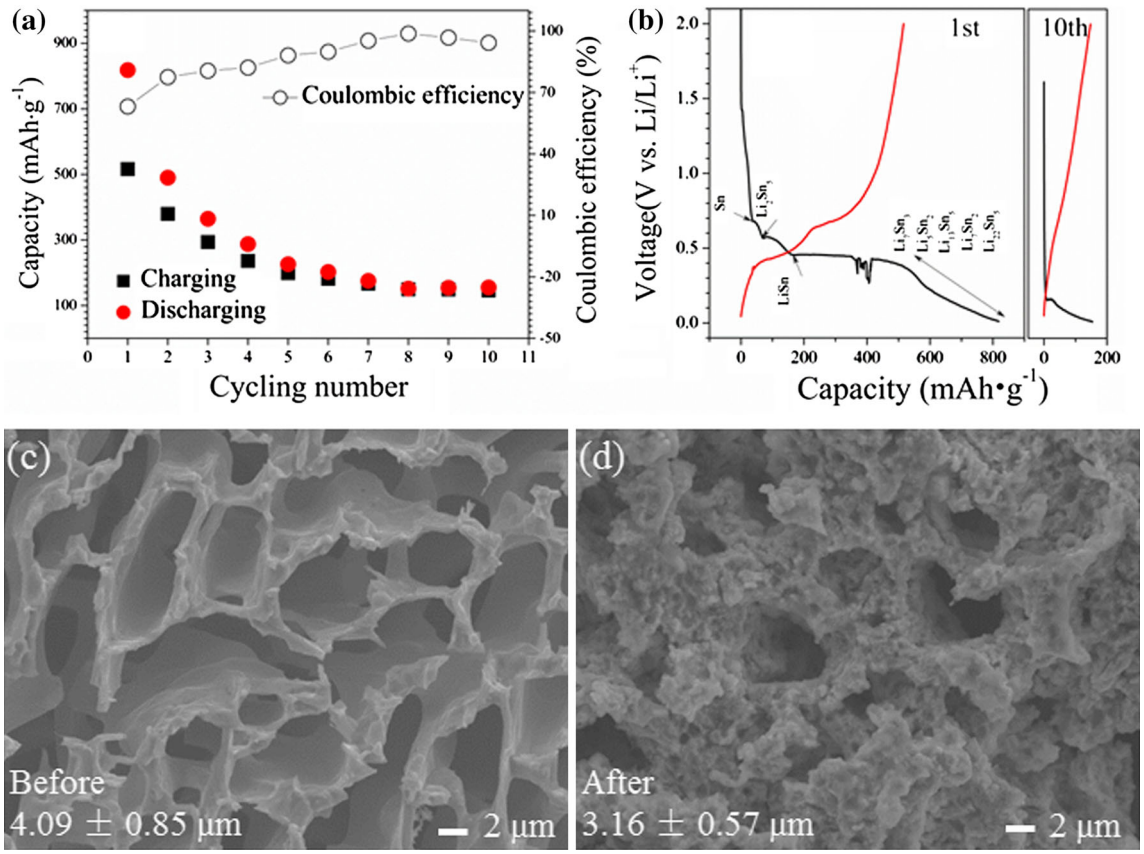

Fig. 5 Electrochemical performances (cycling performance together with coulombic efficiency) of the porous Sn dealloyed from Al80Sn20 (**a**, **b**), and SEM images of the porous Sn structure before (**c**) and after (**d**) the lithiation/delithiation process

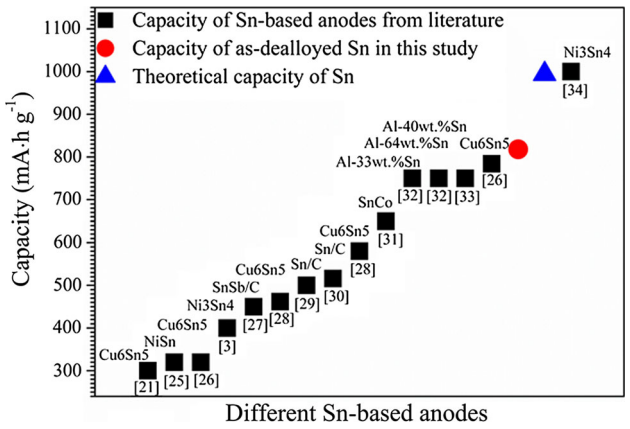

Fig. 6 Initial capacity of the porous Sn anode made in this study and literature data on Sn-based anodes

performance of one such porous Sn anode dealloyed from the Al80Sn20 alloy. It exhibited a high initial capacity of ~818 mA h g^{-1}, although the capacity declined to ~200 mA h g^{-1} after 10 cycles. In addition, each charge–discharge process showed a nearly 100 % coulombic efficiency. It was noted that some small departures occurred around 400 mA h g^{-1} on the 1st charging curve shown in Fig. 5b. This may arise from some contact issues between the Sn foil anode and the stainless steel substrate in the coin cell (Brand 2032). The 1st charging curve (Fig. 5b) is typical of the charging curves reported for Sn anodes [23], featured by the development of four voltage platforms due to the formation of Li_xSn_y intermetallics.

Figure 5c, d shows the porous Sn structure before Fig. 5c and after Fig. 5d the lithiation/delithiation processes. The average pore size decreased from 4.09 ± 0.85 to 3.16 ± 0.57 μm after lithiation/delithiation. In addition, EDX analyses revealed that after the battery performance tests the surface layers of the porous Sn samples contained about 57 at.% O and 43 at.% Sn, indicative of surface oxidation, which may result from the reaction between the porous Sn anode and the electrolyte and/or the pick-up of oxygen during dealloying. The surface Sn oxide layers have lower electrical conductivity than the underneath Sn metal [24]. This change in electrical conductivity may have served as another reason for the noise signals observed on the charge–discharge curves.

Figure 6 shows the initial capacity of the porous Sn anode made in this study and literature data on Sn-based anodes [3, 25–35] including the theoretical capacity of pure Sn. The porous Sn anode made in this study displayed an outstanding initial capacity. This shows the promise of employing the as-dealloyed porous Sn as anodes in lithium ion batteries. One remaining challenge is, however, its short cycle life due to the lack of sufficient ductility and strength. In other words, the porous Sn structures produced via dealloying were still inadequate to buffer the strain during lithiation/delithiation for the expected long cycle life. A possible remedy is to introduce an immiscible inactive ductile constituent M (which forms no intermetallics with Al or Sn) into the Al–Sn alloys to produce a more ductile porous Sn–M composite anode after dealloying of Al. This may represent an important future direction in the design of Sn-containing precursor alloys.

4 Conclusions

- Porous structures can be produced in the non-noble Sn metal through dealloying of Al from a variety of immiscible Al–Sn alloys in hydrochloric acid (HCl) solutions. The as-dealloyed porous Sn structures showed an average pore size in the range of 1.58 ± 0.26 to 4.09 ± 0.85 μm. The morphology and size of these pores are dependent on the morphology and size of the Al phase in respective precursor Al–Sn alloys. As a result, the resulting porous Sn structures can be manipulated through control of the composition and microstructure of the precursor alloy.
- The as-dealloyed porous Sn anode was assessed in a lithium ion battery and showed an outstanding initial capacity of 818 mA h g^{-1} and a coulombic efficiency in the range of 65–99 %. However, the cycle life was limited due to the lack of sufficient ductility and strength.

Acknowledgments T. Song acknowledges the support of the China Scholarship Council (CSC) for a CSC PhD Scholarship and the support of RMIT University for a fee waiver scholarship. The battery performance tests were carried out in the College of Materials Science and Engineering of Sichuan University, China. The authors thank Professor Yungui Chen for the provision of the experimental facilities. Useful comments and suggestions from the reviewers are acknowledged.

References

1. B. Scrosati, J. Hassoun, Y.K. Sun, Energy Environ. Sci. **4**, 3287 (2011)
2. W.J. Zhang, J. Power Sources **196**, 13 (2011)
3. H.C. Shin, M. Liu, Adv. Funct. Mater. **15**, 582 (2005)
4. L. Huang, Y. Yang, L.J. Xue, H.-B. Wei, F.S. Ke, J.T. Li, S.G. Sun, Electrochem. Commun. **11**, 6 (2009)
5. A.D.W. Todd, P.P. Ferguson, J.G. Barker, M.D. Fleischauer, J.R. Dahn, J. Electrochem. Soc. **156**, A1034 (2009)
6. N. Li, C.R. Martin, J. Electrochem. Soc. **148**, A164 (2001)
7. J. Erlebacher, M.J. Aziz, A. Karma, N. Dimitrov, K. Sieradzki, Nature **410**, 450 (2001)
8. J. Biener, A.M. Hodge, A.V. Hamza, Appl. Phys. Lett. **87**, 121908 (2005)
9. T. Song, Y. Gao, Z. Zhang, Q. Zhai, CrystEngComm **13**, 7058 (2011)
10. C. Xu, Y. Zhang, L. Wang, L. Xu, X. Bian, H. Ma, Y. Ding, Chem. Mater. **21**, 3110 (2009)

11. A. Abburi, N. Abrams, W. Yeh, J. Porous Mater. **19**, 543 (2012)
12. O.M. Surez, E.G. Estremera, R. Soler, A. Declet, A.J. Hernndez-Maldonado, Adv. Mater. Sci. Eng. **2014**, 1 (2014)
13. J.C. Thorp, K. Sieradzki, L. Tang, P.A. Crozier, A. Misra, M. Nastasi, D. Mitlin, S.T. Picraux, Appl. Phys. Lett. **88**, 033110 (2006)
14. I.C. Cheng, A.M. Hodge, J. Porous Mater. **21**, 467 (2014)
15. M. Li, Y. Zhou, H. Geng, J. Porous Mater. **19**, 791 (2012)
16. A.J. McAlister, D.J. Kahan, Bull. Alloy Phase Diagr. **4**, 410 (1983)
17. Q. Zhang, Z. Zhang, Phys. Chem. Chem. Phys. **12**, 1453 (2010)
18. A.M. Russel, K.L. Lee, *Si, Ge, Sn and Pb, Structure-Property Relations in Nonferrous Metals* (Wiley, New Jersey, 2005), pp. 392–418
19. Y. Idota, T. Kubota, A. Matsufuji, Y. Maekawa, T. Miyasaka, Science **276**, 1395 (1997)
20. Z. Zhang, Y. Wang, Y. Wang, J. Nanosci. Nanotechnol. **13**, 1503 (2013)
21. T. Song, M. Yan, Z. Shi, A. Atrens, M. Qian, Electrochim. Acta **164**, 288 (2015)
22. S. Parida, D. Kramer, C.A. Volkert, H. Rösner, J. Erlebacher, J. Weissmüller, Phys. Rev. Lett. **97**, 035504 (2006)
23. M. Winter, J. Besenhard, Electrochim. Acta **45**, 31 (1999)
24. M.V. Reddy, G.V. Subba Rao, B.V.R. Chowdari, Chem. Rev. **113**, 5364 (2013)
25. K. Nishikawa, K. Dokko, K. Kinoshita, S.W. Woo, K. Kanamura, J. Power Sources **189**, 726 (2009)
26. B.D. Polat, N. Sezgin, O. Keles, K. Kazmanlı, J. Alloys Compd. **553**, 204 (2013)
27. J. Hassoun, S. Panero, P. Simon, P.L. Taberna, B. Scrosati, Adv. Mater. **19**, 1632 (2007)
28. H. Zhao, C.Y. Jiang, X. He, J. Ren, J. Power Sources **184**, 532 (2008)
29. X.Y. Fan, Q.C. Zhuang, G.Z. Wei, L. Huang, Q.F. Dong, S.G. Sun, J. Appl. Electrochem. **39**, 1323 (2009)
30. G. Derrien, J. Hassoun, S. Panero, B. Scrosati, Adv. Mater. **19**, 2336 (2007)
31. J. Hassoun, G. Derrien, S. Panero, B. Scrosati, Adv. Mater. **20**, 3169 (2008)
32. D.H. Nam, R.H. Kim, C.L. Lee, H.S. Kwon, J. Electrochem. Soc. **159**, A1822 (2012)
33. R. Hu, M. Zeng, C.Y.V. Li, M. Zhu, J. Power Sources **188**, 268 (2009)
34. R. Hu, Q. Shi, H. Wang, M. Zeng, M. Zhu, J. Phys. Chem. C **113**, 18953 (2009)
35. L. Huang, H.B. Wei, F.-S. Ke, X.Y. Fan, J.T. Li, S.G. Sun, Electrochim. Acta **54**, 2693 (2009)

Supplementary Information for Chapter 3

Battery Performance Characterization

CR2032 coin cells were assembled in the glove box using the as-dealloyed foil sample as the working electrode, lithium metal as the counter and reference electrode, Celgard 2400 as the separator and a solution of 1 mol/L LiPF6 in ethylene carbonate (EC)/diethyl carbonate (DEC) (1:1 by volume) as the electrolyte. Galvanostatic charging/discharging was carried out at a 0.2 C rate in the voltage range of 0.01~2.1 V on a LAND testing system.

Chapter 4 Dealloying of a ternary $Al_{67}Cu_{18}Sn_{15}$ alloy and the fabrication of Cu-Sn composites

Nanoporous-structured Cu-Sn composites are promising candidate anodes for lithium ion batteries (LIBs) where both of the non-active component Cu and the nanoporous structure are expected to accommodate the large volume change compared to the use of Sn anode alone (see Section **2.1.3.3 Nanoporous composite anode materials**).

This chapter introduces a newly designed ternary $Al_{67}Cu_{18}Sn_{15}$ alloy, which, unlike traditional binary alloys used for dealloying; consists of three distinctly different composing elements (Section **2.3.2.2 Ternary alloys**). The chemical dealloying of this alloy and the creation of nanoporous Cu-Sn composites by dealloying are studied. In addition, its electrochemical dealloying is also studied and compared with chemical dealloying (Section **2.3.1 Introduction to dealloying** and Section **2.3.3 Dealloying conditions**).

4.1 (Paper 2)

Concurrence of de-alloying and re-alloying in a ternary $Al_{67}Cu_{18}Sn_{15}$ alloy and the fabrication of 3D nanoporous Cu-Sn composite structures

Tingting Song, Ming Yan, Yulai Gao, Andrej Atrens, Ma Qian

RSC Advances, 5(2015) 9574-9580.

RSC Advances

PAPER

View Article Online
View Journal | View Issue

Cite this: *RSC Adv.*, 2015, **5**, 9574

Concurrence of de-alloying and re-alloying in a ternary $Al_{67}Cu_{18}Sn_{15}$ alloy and the fabrication of 3D nanoporous Cu–Sn composite structures

T. Song,[a] M. Yan,[a] Y. Gao,[b] A. Atrens[c] and M. Qian*[a]

Received 2nd December 2014
Accepted 5th January 2015

DOI: 10.1039/c4ra15622f

www.rsc.org/advances

We report the concurrence of de-alloying and re-alloying in a ternary $Al_{67}Cu_{18}Sn_{15}$ alloy (at.%) de-alloyed in a 5 wt% hydrochloric acid (HCl) solution at 70 ± 2 °C, and the fabrication of three-dimensional (3D) nanoporous Cu_3Sn–Cu–Cu_6Sn_5 composites in the form of self-supporting foils. Re-alloying occurred in $Al_{67}Cu_{18}Sn_{15}$ compared to de-alloying alone in binary Al–Cu alloys. Both Cu_3Sn and Cu_6Sn_5 phases formed through an accompanied re-alloying process. This finding further proves the temperature sensitivity of phase formation in the Cu–Sn system established from Cu–Sn diffusion couple studies, and demonstrates the capability of designing and creating nanoporous composite materials *via* de-alloying a multicomponent alloy.

1. Introduction

De-alloying is the selective dissolution of one or more components from an alloy, leaving behind a material enriched in the nobler or less active alloy component. This approach was used as early as during the Incan civilization to dissolve the more active element Cu from dilute AuCu alloys to create the illusion of a pure gold artefact.[1] The last decade has seen a renewed interest in this approach due to its capability of producing nanoporous structures, which holds promise for applications as sensors[2,3] and catalysts based on their high specific surface areas.[4]

There are two prerequisites for an alloy to undergo de-alloying:[5–7] (i) the constituting elements in the alloy should have different electrochemical activities (*e.g.* A is less noble whilst B is nobler in a binary AB alloy);[5] and (ii) the concentration of the nobler element B is below a critical composition, referred to as parting limit, beyond which de-alloying does not take place due to surface passivation by the nobler element B.[6,7] Many binary alloys meet these two requirements, including single solid-solution alloys of Au–Ag,[8] Pt–Co,[9,10] and Au–Cu,[11] and two-phase alloys of Al–Cu,[12,13] Al–Ag,[14] Zn–Cu[15] and Mg–Cu.[12,16] They have been de-alloyed to produce nanoporous pure metals, and the mechanisms that control the nanoporosity and pattern formation have been investigated.[6,7,9,10,12–19] De-alloying of a binary AB alloy involves the dissolution of A, and the diffusion of B.[17] Both the rate of dissolution of A, and the surface diffusivity of B, have a significant influence on the formation of the nanoporous structure, including the size of the ligaments/channels in the nanoporous B.[20]

Research on de-alloying over the last decade has been largely focused on de-alloying of binary alloys (AB) with a view to producing nanoporous structures of essentially pure metal B, and understanding the de-alloying process. Only a few studies have dealt with de-alloying of alloys containing a third element such as $Mg_{90-x}Cu_xY_{10}$,[21] $Mg_{77}Ag_{18.4}Pd_{4.6}$,[22] $Ag_{64}Au_{30}Pt_6$,[23] $Al_{75}Pt_{15}Au_{10}$ [24] and $Al_{66}Au_{27.2}X_{6.8}$ (X = Pt, Pd, PtPd, Ni, Co and NiCo) (in at.%).[25,26] However, it should be pointed out that in these ternary ABC alloys, the third element C introduced was similar to the nobler element B, a slow diffuser. The purpose was to slow down the surface diffusivity of B, in order to decrease the ligament/channel size of the resulting nanoporous B.[21–23,26] The small amount of this third element C substituted for the noble element B in the lattice of the precursor alloys.[21–23,26] Accordingly, de-alloying of these deceptively ternary alloys was no different from the de-alloying of binary alloys.

For de-alloying of ternary alloys (ABC), which consist of three distinctly different elements, the only research reported to date appears to be that by Feng *et al.*[27] As with de-alloying of binary AB alloys, which produces nanoporous structures of essentially pure metal B, de-alloying of ternary ABC alloys has the potential to produce nanoporous composite structures with constituting elements B and C and with characteristics different from those de-alloyed from binary alloys for various applications. In addition, de-alloying of ternary alloys is expected to show different dissolution and diffusion behaviors due to the involvement of the third distinctly element. Understanding their de-alloying characteristics is necessary for the fabrication of more

[a]*RMIT University, School of Aerospace, Mechanical and Manufacturing Engineering, Centre for Additive Manufacturing, Melbourne, VIC 3001, Australia. E-mail: ma.qian@rmit.edu.au*

[b]*Shanghai Key Laboratory of Modern Metallurgy and Materials Processing, Shanghai University, 200072 Shanghai, P.R. China*

[c]*The University of Queensland, Division of Materials, School of Mechanical and Mining Engineering, Brisbane, QLD 4072, Australia*

complex nanoporous metal structures aside from enhancing the knowledge base of de-alloying.

This paper studied the de-alloying of a ternary $Al_{67}Cu_{18}Sn_{15}$ alloy at 70 ± 2 °C in a selected acid solution. The rationale for the selection of an AlCuSn ternary alloy is given as follows. First, dense nanostructured intermetallic Cu_6Sn_5 anodes outperform pure Sn anodes in lithium ion batteries, where the inactive Cu matrix can act as a stress buffer to accommodate the large volume change caused by lithiation/delithiation during battery operation.[28–30] The use of a nanoporous structure has proved to be effective to absorb the volume change of the anode material in lithium ion batteries, such as nanoporous SnO_2 anodes[31] and nanoporous Ge–C anodes.[32] Nanoporous Cu–Sn based composites, if they can be created by de-alloying of a ternary AlCuSn alloy, may have the potential to show desired strain-accommodation capabilities due to their nanoporous structure. In addition, they may offer some good composite strain buffer ability too, like the Sn–Cu composites.[28–30] Second, Al is electrochemically more active than both Cu and Sn.[5] This allows the creation of various Cu–Sn based nanostructures *via* the de-alloying of AlCuSn alloys. Third, both Cu and Sn have fast self-diffusion rates,[33] which are in favour of complete de-alloying of the entire sample. Additionally, Cu atoms can diffuse interstitially into Sn even at room temperature to enable intermetallic formation.[34,35] These characteristics imply that AlCuSn alloys are promising candidate ternary precursors for the creation of a Cu–Sn based nanoporous structure *via* de-alloying of the Al. The composition of the ternary $Al_{67}Cu_{18}Sn_{15}$ alloy was determined as follows. The concentration of 67 at.% Al was chosen to be close to the parting limit of Al[6,7] whilst the relative concentrations of Cu and Sn were chosen to match the ratio of 1.2 : 1 for Cu to Sn in Cu_6Sn_5.[30] The selection of the de-alloying temperature (70 ± 2 °C) is based on the phase formation sequence in the Cu–Sn system established from Cu–Sn diffusion couple studies,[35] which identified that below 60 °C only Cu_6Sn_5 forms while at or above 60 °C both Cu_6Sn_5 and Cu_3Sn can develop.[35] Feng *et al.*[27] have recently reported the formation of Cu_6Sn_5 by de-alloying of an $Al_{10}Cu_3Sn$ alloy at 60 °C but no formation of Cu_3Sn was observed. The selection of 70 ± 2 °C is expected to lead to the formation of Cu_3Sn and this will allow us to compare the phase formation in de-allying with the observations made from diffusion couple studies.

2. Experimental

The $Al_{67}Cu_{18}Sn_{15}$ alloy was prepared from 99.99% purity Al, 99.99% purity Cu and 99.999% purity Sn using arc melting under argon. The alloy was remelted four times to ensure chemical homogeneity. The molten alloy from the fourth remelting was sucked into a water-cooled copper mould with a cavity of 8 mm in diameter and 30 mm in length, by the pressure differential between the mould and melting chamber. Disc samples were cut from the rod, ground and polished into 0.6 mm thick foils (8 mm in diameter).

De-alloying of the foil samples was carried out at 70 ± 2 °C in 200 ml of 5 wt% HCl aqueous solution. A hot plate and a mercurial thermometer were used to control the temperature. According to the preliminary tests performed on three disc samples, it was found that complete de-alloying of each sample required about 480 min. On this basis, samples were de-alloyed for various durations from 60 min to 480 min. This permitted a systematic study of the de-alloying process. De-alloyed samples were removed from the acid solution, rinsed in distilled water and dehydrated with alcohol.

The phase constitution and microstructure were characterized using X-ray diffraction (XRD, Bruker D8 instrument, with Cu Kα radiation, with a scanning rate of 1° min^{-1}), scanning electron microscopy (SEM) in both the second electron (SE) imaging and backscattered electron (BSE) imaging modes (JEOL 7001, operated at 15 keV equipped with energy dispersive X-ray spectroscopy (EDX) made by INCA). Transmission electron microscopy (TEM) and selected area electron diffraction (SAED) (from JEOL 2100, operated at 200 kV) were also employed to study the microstructure and phase constitution. Samples for TEM analysis were prepared by grinding the as-dealloyed foils into powder, followed by dispersing the powder in ethanol by ultrasonic, and finally releasing just a few drops of the particles-containing ethanol solution on a 3 mm diameter carbon film supported on a copper grid. After drying in air for 20 min, the powder samples were ready for TEM analysis.

3. Results

3.1 Phase constitution of precursor

Fig. 1 presents the XRD patterns and a typical SEM micrograph of the precursor $Al_{67}Cu_{18}Sn_{15}$ alloy, which consisted of three phases: α-Al(Cu, Sn) solid solution, β-Sn(Al, Cu) solid solution, and the Al_2Cu intermetallic. At room temperature, the solubility limits of Cu and Sn in Al are 5.5 wt%[36] and 0.12 wt%,[37] respectively, whilst β-Sn(Al, Cu) contains only up to 0.06 wt% Al and 0.005 wt% Cu.[38] Hence, the solid solutions are essentially α-Al(Cu) and metallic β-Sn. Fig. 1 shows the α-Al(Cu) phase (dark contrast), the Al_2Cu phase (grey contrast), and the Sn phase (bright contrast, enveloping the Al_2Cu phase), using the BSE imaging mode. These observations are consistent with the Al–Cu–Sn ternary phase diagram.[39]

3.2 Phase constitution and morphology evolution during dealloying

The following observations are notable after various durations of de-alloying from 60 to 480 min according to the XRD patterns shown in Fig. 2a and b.

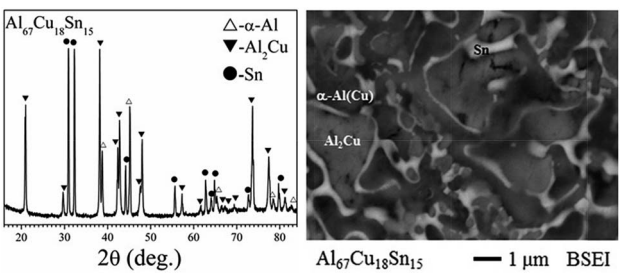

Fig. 1 XRD pattern and SEM BSE microstructure of the $Al_{67}Cu_{18}Sn_{15}$ precursor.

(i) The α-Al(Cu) had disappeared after the first 60 min de-alloying, and there were new phases, identified to be Cu_3Sn, Cu and Cu_6Sn_5 with a preponderance of the Cu_3Sn phase. In addition, there was a noticeable decrease in the intensity of the XRD peaks for both Al_2Cu and Sn. Fig. 3 shows the microstructures after 60 min, 120 min and 180 min de-alloying. The preferential de-alloying of α-Al(Cu) can be seen from Fig. 3a. Fig. 3b shows remnants of Sn and a surface nanoporous structure (with an average ligament width of 40 ± 8 nm) on the Al_2Cu substrate, which is interpreted to be Cu_3Sn and/or Cu according to the XRD results in Fig. 2a and c. With the progress of de-alloying, the nanoporous structure on the Al_2Cu substrate became increasingly coarser (see Fig. 3c and d) while the amount of Cu_3Sn and/or Cu continued to increase (see Fig. 2a).

(ii) No Sn was detected by XRD after 240 min de-alloying, and there was a noticeable decrease in the intensity of the XRD peaks for Al_2Cu. The SEM BSE image in Fig. 4a confirmed the absence of Sn. The surface nanoporous structure after the first 180 min de-alloying (Fig. 3b–d) had further developed after 240 min de-alloying as shown in Fig. 4b. TEM selected area electron diffraction (SAED) identified the presence of both Cu_3Sn and Cu_6Sn_5 (Fig. 4d), consistent with the XRD results.

(iii) The Al_2Cu phase remained after 300 min de-alloying but had disappeared after 480 min de-alloying (Fig. 2b), indicative of complete de-alloying of the Al_2Cu phase. This was confirmed by the microstructures shown in Fig. 5a and b, in which no Al_2Cu was observed. The three strongest XRD lines in the 2θ range of 23–47° for each of the Cu_3Sn (JSPDS reference no. 03-065-4653), Cu (00-004-0836) and Cu_6Sn_5 (01-076-2703) phases in the International Centre for Diffraction Data (ICDD) database are shown in Fig. 2c to assist in phase identification.

The microstructure of the final dealloyed product is shown in Fig. 5. A nanoporous microstructure with an average ligament width of 170 ± 50 nm was obtained on the surface (Fig. 5a and b) and throughout the longitudinal section (Fig. 5c and d). The inhomogeneous microstructure observed after 240 min (Fig. 4c) and 300 min de-alloying (Fig. 4e and f) had evolved into a homogenous nanoporous structure (Fig. 5c). TEM examination confirmed the nanoporous nature of the product (Fig. 5e). Also, the existence of Cu_3Sn and Cu_6Sn_5 was identified by SAED and high resolution TEM images (Fig. 5f), consistent

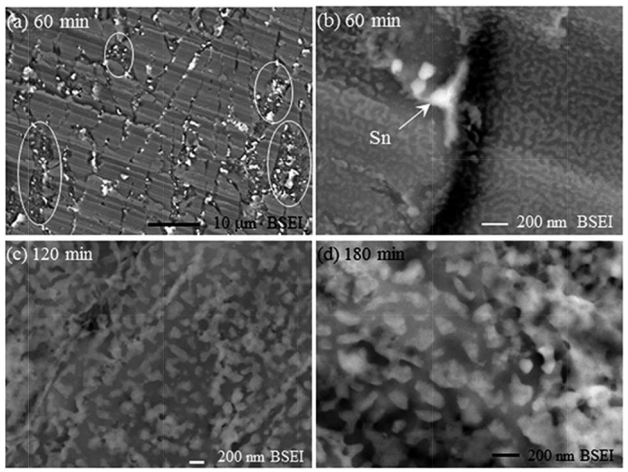

Fig. 3 (a) SEM image showing preferential de-alloying of α-Al(Cu) (circled); (b) remnants of Sn (arrowed) and nanoporous Cu_3Sn and Cu on Al_2Cu substrate; (c) and (d) surface nanoporous structures after 120 min and 180 min de-alloying.

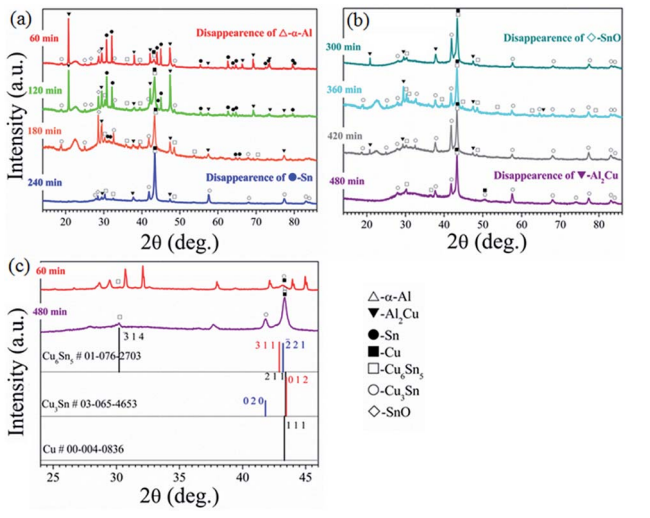

Fig. 2 (a and b) XRD patterns of $Al_{67}Cu_{18}Sn_{15}$ alloy after de-alloying in a 5 wt% HCl solution for up to 480 min; and (c) three strongest diffraction lines (in 2θ range of 23–47°) for each of the Cu_3Sn, Cu and Cu_6Sn_5 phases in the ICDD database together with XRD patterns obtained from samples after 60 and 480 min de-alloying.

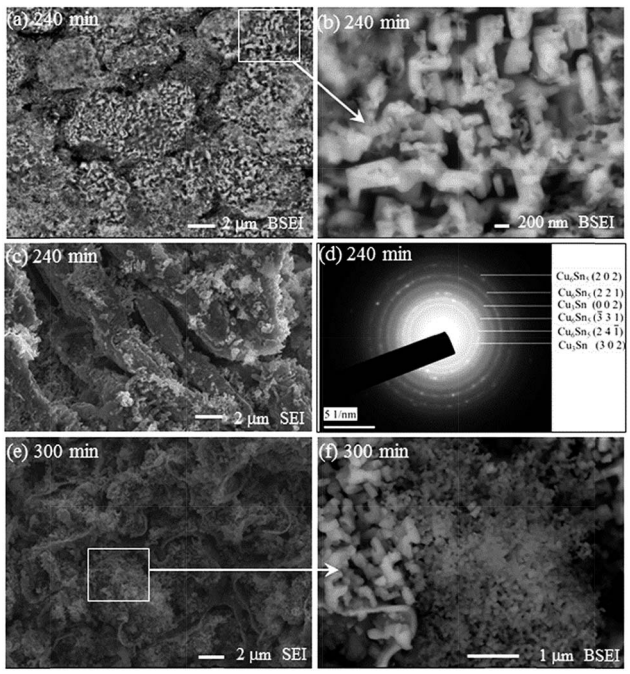

Fig. 4 (a) and (b) surface nanoporous structures of Cu_3Sn–Cu–Cu_6Sn_5; (c) inhomogeneous microstructure on cross section; (d) TEM SAED results of Cu_3Sn and Cu_6Sn_5 after 240 min de-alloying; and (e) and (f) inhomogeneous microstructure after 300 min of de-alloying.

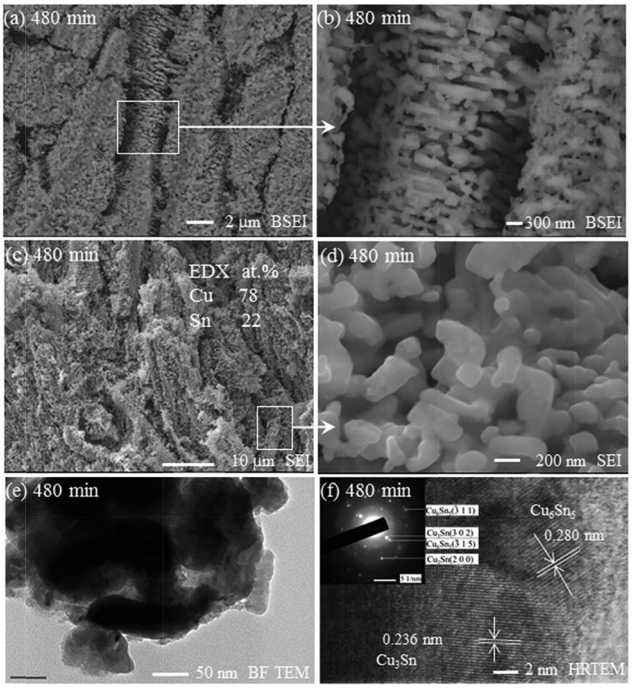

Fig. 5 Nanoporous structures of Cu_3Sn–Cu–Cu_6Sn_5 produced after 480 min de-alloying: (a) and (b) surface; (c) and (d) cross section; (e) bright field (BF) TEM image confirming the nanoporous structure; and (f) HRTEM image and TEM SAED results of Cu_3Sn and Cu_6Sn_5 phases. The nanoporous Cu_3Sn–Cu–Cu_6Sn_5 composite is produced in the form of self-supporting foils (0.6 mm thick and 8 mm in diameter).

with the XRD results. EDX analyses detected no Al but did detect Cu and Sn (as presented in the inset in Fig. 5c). In addition, the atomic ratio of Cu : Sn detected by EDX analyses is around 78 : 22, which is clearly greater than the ratio of Cu to Sn in either Cu_3Sn (3 : 1) or Cu_6Sn_5 (1.2 : 1.0). This supports the detection of free Cu in the de-alloyed sample by XRD. The nanoporous Cu_3Sn–Cu–Cu_6Sn_5 composite is produced in the form of self-supporting foils (0.6 mm thick and 8 mm in diameter).

4. Discussion

4.1 De-alloying of ternary AlCuSn alloys

α-Al(Cu) has a large volume fraction in the precursor ternary $Al_{67}Cu_{18}Sn_{15}$ alloy (Fig. 1). De-alloying of the $Al_{67}Cu_{18}Sn_{15}$ alloy started with the preferential dissolution of α-Al(Cu), as evidenced by its quick disappearance after 60 min de-alloying (Fig. 2a). This is similar to the observations made from the de-alloying of other Al-based alloys (binary $Al_{65}Ag_{35}$,[14] AlCu,[12,13,40,41] or ternary $Al_{66}Au_{27.2}X_{6.8}$ (X = Pt, Pd, PtPd, Ni, Co and NiCo)[26]). It was noticed that there was release of hydrogen (H_2) as gas bubbles during de-alloying. Hence the de-alloying process of the α-Al(Cu) phase may be described as follows

$$2\alpha\text{-Al(Cu)(s)} + 6\text{HCl(l)} \rightarrow 2\text{Cu(s)} + 2\text{AlCl}_3\text{(l)} + 3\text{H}_2\text{(g)} \quad (1)$$

where the Cu atoms released from this process are limited to the solubility of Cu in α-Al.

De-alloying of the Al_2Cu phase also occurred in this process, as informed by the notable decrease in the intensity of the Al_2Cu XRD peaks. Considering both the release of H_2 and the presence of free Cu in the final de-alloyed product, the de-alloying process of Al_2Cu may be described by eqn (2) below

$$\text{Al}_2\text{Cu(s)} + 6\text{HCl(l)} \rightarrow 2\text{AlCl}_3\text{(l)} + \text{Cu(s)} + 3\text{H}_2\text{(g)} \quad (2)$$

As mentioned previously, the only other study of de-alloying of ternary AlCuSn alloys was that by Feng *et al.*[27] Table 1 lists the distinct differences between this study and Feng *et al.*'s work.[27]

(i) Different precursors. The precursor used in ref. 27 was based on Cu_3Sn while this study is based on Cu_6Sn_5 (18 : 15 = 6 : 5) aiming to obtain a nanoporous Cu_6Sn_5, as the Cu_6Sn_5 compound has proved to outperform pure Sn as anode material.[28,29]

(ii) Different electrolyte solutions. Both NaOH and HCl solutions are able to dissolve Al from Al-based alloys for de-alloying.[12–14,24,40,41] The selection of HCl solutions is complementary to the selection of NaOH solutions for the de-alloying of AlCuSn alloys[27] and it can also show the influence of electrolyte on the de-alloying of AlCuSn alloys.

(iii) Different de-alloying temperatures. Detailed Cu–Sn diffusion couple studies have indicated that below 60 °C only Cu_6Sn_5 forms while at or above 60 °C both Cu_6Sn_5 and Cu_3Sn can form.[35] Indeed, Feng *et al.*[27] selected 60 °C and confirmed only the formation of Cu_6Sn_5 although the ratio of Cu : Sn of their precursor was designed to be 3 : 1. In contrast, by selecting 70 ± 2 °C, both Cu_6Sn_5 and Cu_3Sn formed during de-alloying, consistent with Cu–Sn diffusion couple studies.[35]

As a result of the differences discussed above, Feng *et al.* obtained nanoporous Cu–Cu_6Sn_5 (ref. 27) while this study attained nanoporous Cu_3Sn–Cu–Cu_6Sn_5. These two different studies are complementary to each other and together they show the significances of precursor composition, electrolyte type, and de-alloying temperature in the de-alloying process of ternary AlCuSn alloys. Also noticed from the XRD results shown in Fig. 2a and b is a small presence of the SnO phase in the samples de-alloyed for 60–300 min. This can be attributed to oxidation in the de-alloying solution. However, no SnO phase was detected after de-alloying for 300 min (Fig. 2b). The consumption of Sn by oxidation could be one of the reasons responsible for the lower Sn content in the final product of Cu_3Sn–Cu–Cu_6Sn_5 than in the precursor alloy.

4.2 Re-alloying of Cu and Sn among de-alloying

The XRD results together with the ICDD information (Fig. 2) revealed that, there was formation of both Cu_3Sn and Cu_6Sn_5

Table 1 De-alloying of ternary AlCuSn alloys

De-alloying system	Feng *et al.*'s paper[27]	This study
Precursor composition (at.%)	$Al_{10}Cu_3Sn$	$Al_{67}Cu_{18}Sn_{15}$
Electrolyte solution	20 wt% NaOH	5 wt% HCl
De-alloying temperature (°C)	60	70 ± 2
De-alloyed product	Cu–Cu_6Sn_5	Cu_3Sn–Cu–Cu_6Sn_5

during de-alloying at 70 ± 2 °C from the early stages (60 min) of de-alloying to the end (480 min). This means that there has been re-alloying that occurred between the Cu atoms released from reactions (1) and (2) and the Sn atoms in the precursor. These re-alloying processes may be described by eqn (3) and (4) below.

$$3Cu(s) + Sn(s) \rightarrow Cu_3Sn(s) \quad (3)$$

$$6Cu(s) + 5Sn(s) \rightarrow Cu_6Sn_5(s) \quad (4)$$

It has long been established that at room temperature, Cu atoms can diffuse fast (interstitially) into the lattice of Sn, particularly along the *c*-axis direction in the lattice of Sn,[34] and then react with Sn to form Cu_6Sn_5.[35,42,43] This occurs at room temperature and from the formation of many other intermetallic compounds which typically occurs at a much higher temperature. The free Cu atoms released by de-alloying according to eqn (1) and (2) were expected to be chemically reactive, as would also be the newly exposed Sn atoms in the precursor alloy. In addition, the de-alloying or removal of the Al atoms from the ternary precursor alloy $Al_{67}Cu_{18}Sn_{15}$ naturally left Cu and Sn atoms in contact. This enables the formation of Cu_6Sn_5 and Cu_3Sn during de-alloying at 70 ± 2 °C. The formation of Cu_3Sn and Cu_6Sn_5 is based on the interactions between Cu and Sn atoms, similar to the recent study of dealloying of ternary Al–Au–M (M = Ni, Co or NiCo) alloys by Zhang *et al.*,[25] who discussed the importance of the interactions between Au and other atoms. Our study supports Tu's observation[35] that "the ordered ε-phase (Cu_3Sn) was found only in those specimens that had been annealed above 60 °C", although no experimental data were given by Tu. It has been found that there was formation of just Cu_6Sn_5 during de-alloying of a ternary $Al_{10}Cu_3Sn$ alloy in a 20 wt% NaOH solution at 60 °C.[27]

Table 2 lists the detailed literature data on intermetallic formation in the Cu–Sn system under various conditions together with the experimental observations of this study. Previous Cu–Sn diffusion couple studies have established that Cu_6Sn_5 can form over a wide range of temperatures[3,27,35,42–44,46,47] down to −2 °C (Table 2) while Cu_3Sn forms mainly at temperatures above 100 °C.[35,42–44,46,47] Dreyer *et al.*[3] reported that Cu_3Sn nucleated at the temperature of 87 °C in their Cu/Cu_6Sn_5 thin film diffusion couple study. It is clear from Table 2 that the formation of Cu_3Sn at 70 ± 2 °C observed in this study is the lowest temperature reported to date for the intermetallic formation of Cu_3Sn with solid experimental data. This improves the knowledge base of phase formation in the Cu–Sn system. Experimental studies have further established that once nucleated, the apparent activation energy (E_a) for the growth of Cu_3Sn (70.28 kJ mol^{-1}), determined over the temperature range of 120–200 °C, is smaller than that for the growth of Cu_6Sn_5 (84.3 kJ mol^{-1} determined over the temperature range of 70–200 °C).[48] This implies that Cu_3Sn tends to grow easier than Cu_6Sn_5. The preponderance of Cu_3Sn over Cu_6Sn_5 in the de-alloyed product can be attributed to this reason.

After the disappearance of Sn, de-alloying of Al_2Cu continued to release free Cu atoms by reaction (2). However, because of the absence of Sn, reactions (3) and (4) no longer occurred. The Cu–Sn diffusion couple studies at temperatures above 100 °C have identified another reaction, described by reaction (5) below,[35,45,49] for the formation and continued growth of Cu_3Sn in Cu–Sn diffusion couples.

$$\frac{1}{5}Cu_6Sn_5(s) + \frac{9}{5}Cu(s) \rightarrow Cu_3Sn(s) \quad (5)$$

It is plausible that the same reaction may have also occurred in the de-alloying process studied contributing to the preponderance of Cu_3Sn over Cu_6Sn_5 in the final de-alloyed nanoporous Cu_3Sn–Cu–Cu_6Sn_5 structures. However, the noticeable presence of both Cu and Cu_6Sn_5 detected by XRD after 480 min

Table 2 Intermetallic formation in the Cu–Sn system

Diffusion couple	Temperature (°C)	Duration	Intermetallic compounds	Ref.
Cu/Sn	−2[a]	NA	Cu_6Sn_5	42
Cu/Sn	Room temperature	15 days	Cu_6Sn_5	42
Cu/Sn	Room temperature	One year	Cu_6Sn_5	42 and 43
Cu/Sn	Room temperature	10 days	Cu_6Sn_5	35
Cu/Sn	60[a]	NA	Cu_6Sn_5 and Cu_3Sn	42
Cu/Sn (de-alloying of $Al_{10}Cu_3Sn$)	60	8 h	Cu_6Sn_5	27
Cu/Sn (de-alloying of $Al_{67}Cu_{18}Sn_{15}$)	70 ± 2	60 min	Cu_6Sn_5 and Cu_3Sn	This study
Sn–5Bi–3.5Ag solder/Cu	70, 100 and 120	30 days	Cu_6Sn_5	44
Cu/Sn	87	NA	Cu_3Sn nucleation	3
Cu/Sn	100	36 h	Cu_6Sn_5 and Cu_3Sn	42 and 43
Cu/Sn	100	60 h	Cu_6Sn_5 and Cu_3Sn	42
SnPb solder/Cu_6Sn_5/Cu_3Sn/Cu	100, 125 and 150	80 days	Cu_6Sn_5 and Cu_3Sn	45
Lead-free solder/Cu	100, 125, 150 and 170	>50 h	Cu_6Sn_5 and Cu_3Sn	46
Cu/Cu_6Sn_5	115–150	10 min	Cu_6Sn_5 and Cu_3Sn	35
Lead-free solder/Cu	150	NA	Cu_6Sn_5 and Cu_3Sn	47
Sn–5Bi–3.5Ag solder/Cu	150, 170 and 200	30 days	Cu_6Sn_5 and Cu_3Sn	44
Cu/Sn	200	10 min	Cu_3Sn	35 and 43
SnPb solder/Cu	220	3–4 min	Cu_6Sn_5 and Cu_3Sn	45

[a] Without experimental data. NA: not available.

de-alloying suggests that reaction (5) may have only occurred to a small extent by the end of the 480 min de-alloying process. The two predominant reasons are: (i) reaction (5) is slow; it has been found that a large amount of residual Cu_6Sn_5 and Cu still remained after even 80 days of annealing at 150 °C,[45] and (ii) the de-alloying temperature (70 ± 2 °C) used is inadequate to completely overcome the large energy barrier (95.5 kJ mol^{-1}, determined over the temperature range of 115–150 °C [35]) required for reaction (5) to occur. In fact, it is ideal to have a noticeable presence of Cu in the as-dealloyed product as Cu offers better thermal and electrical conductivities than both Cu_6Sn_5 and Cu_3Sn,[35,42] in addition to the much needed ductility to hold Cu_6Sn_5 and Cu_3Sn together. In this regard, it is desired that reaction (5) is slow.

5. Conclusions

A ternary $Al_{67}Cu_{18}Sn_{15}$ alloy has been designed and de-alloyed in a 5 wt% hydrochloric acid solution at 70 °C. Unlike de-alloying of binary alloys, de-alloying of the ternary $Al_{67}Cu_{18}Sn_{15}$ alloy was accompanied by a re-alloying process. Together they have enabled the fabrication of a nanoporous Cu_3Sn–Cu–Cu_6Sn_5 composite with an average ligament width of 170 ± 50 nm. The formation of Cu_3Sn and Cu_6Sn_5 intermetallics and the reaction between Cu_6Sn_5 and Cu during de-alloying at 70 ± 2 °C are discussed in detail in relation to the experimental findings obtained from the Cu–Sn diffusion couple studies. This finding further proves the temperature sensitivity of phase formation in the Cu–Sn system established from Cu–Sn diffusion couple studies. De-alloying of multicomponent alloys offers an effective approach to the fabrication of nanoporous composite materials including the formation of new phases through the accompanied re-alloying process.

Acknowledgements

T. Song is financially supported by a China Scholarship Council (CSC) Scholarship and a RMIT fee waiver scholarship. Y. Gao acknowledges the Program for Professor of Special Appointment (Eastern Scholar) at Shanghai Institutions of Higher Learning (no. TP2014042).

Notes and references

1 H. Lechtman, *Sci. Am.*, 1984, **250**, 63156.
2 Y. Wang, J. Cao, S. Wang, X. Guo, J. Zhang, H. Xia, S. Zhang and S. Wu, *J. Phys. Chem. C*, 2008, **112**, 17804.
3 K. F. Dreyer, W. K. Neils, R. R. Chromik, D. Grosman and E. J. Cotts, *Appl. Phys. Lett.*, 1995, **67**, 2795.
4 T. Déronzier, F. Morfin, L. Massin, M. Lomello and J.-L. Rousset, *Chem. Mater.*, 2011, **23**, 5287.
5 H. W. Pickering and C. Wagner, *J. Electrochem. Soc.*, 1967, **114**, 698.
6 D. Artymowicz, R. Newman and J. Erlebacher, *ECS Trans.*, 2007, **3**, 499.
7 D. M. Artymowicz, J. Erlebacher and R. C. Newman, *Philos. Mag.*, 2009, **89**, 1663.
8 K. Zhang, X. Tan, J. Zhang, W. Wu and Y. Tang, *RSC Adv.*, 2014, **4**, 7196.
9 L. Liu, E. Pippel, R. Scholz and U. Gosele, *Nano Lett.*, 2009, **9**, 4352.
10 Z. Yu, J. Zhang, Z. Liu, J. M. Ziegelbauer, H. Xin, I. Dutta, D. A. Muller and F. T. Wagner, *J. Phys. Chem. C*, 2012, **116**, 19877.
11 A. Pareek, G. N. Ankah, S. Cherevko, P. Ebbinghaus, K. J. J. Mayrhofer, A. Erbe and F. U. Renner, *RSC Adv.*, 2013, **3**, 6586.
12 W. B. Liu, S. C. Zhang, N. Li, J. W. Zheng, S. S. An and Y. L. Xing, *Corros. Sci.*, 2012, **58**, 133.
13 W. B. Liu, S. C. Zhang, N. Li, J. W. Zheng and Y. L. Xing, *Corros. Sci.*, 2011, **53**, 809.
14 T. T. Song, Y. L. Gao, Z. H. Zhang and Q. J. Zhai, *Corros. Sci.*, 2013, **68**, 256.
15 J. F. Li, P. A. Agyakwa and C. M. Johnson, *Acta Mater.*, 2011, **59**, 1198.
16 C. Zhao, X. Wang, Z. Qi, H. Ji and Z. Zhang, *Corros. Sci.*, 2010, **52**, 3962.
17 J. Erlebacher, M. J. Aziz, A. Karma, N. Dimitrov and K. Sieradzki, *Nature*, 2001, **410**, 450.
18 I. C. Oppenheim, D. J. Trevor, C. E. D. Chidsey, P. L. Trevor and K. Sieradzki, *Science*, 1991, **254**, 687.
19 F. U. Renner, A. Stierle, H. Dosch, D. M. Kolb, T. L. Lee and J. Zegenhagen, *Nature*, 2006, **439**, 707.
20 Z. Zhang, Y. Wang, Y. Wang, X. Wang, Z. Qi, H. Ji and C. Zhao, *Scr. Mater.*, 2010, **62**, 137.
21 X. Luo, R. Li, L. Huang and T. Zhang, *Corros. Sci.*, 2013, **67**, 100.
22 H. Ji, X. Wang, C. Zhao, C. Zhang, J. Xu and Z. Zhang, *CrystEngComm*, 2011, **13**, 2617.
23 J. Snyder, P. Asanithi, A. B. Dalton and J. Erlebacher, *Adv. Mater.*, 2008, **20**, 4883.
24 Z. Zhang, Y. Wang and X. Wang, *Nanoscale*, 2011, **3**, 1663.
25 Z. Zhang, C. Zhang, Y. Gao, J. Frenzel, J. Sun and G. Eggeler, *CrystEngComm*, 2012, **14**, 8292.
26 Y. Wang, J. Xu and B. Wu, *Phys. Chem. Chem. Phys.*, 2013, **15**, 5499.
27 Y. Feng, S. Zhang, Y. Xing and W. Liu, *J. Mater. Sci.*, 2012, **47**, 5911.
28 H. C. Shin and M. Liu, *Adv. Funct. Mater.*, 2005, **15**, 582.
29 D. Reyter, S. Rousselot, D. Mazouzi, M. Gauthier, P. Moreau, B. Lestriez, D. Guyomard and L. Roué, *J. Power Sources*, 2013, **239**, 308.
30 S. Wang, W. Zhao, X. Liu and L. Li, *RSC Adv.*, 2013, **3**, 18339.
31 Z. P. Guo, G. D. Du, Y. Nuli, M. F. Hassan and H. K. Liu, *J. Mater. Chem.*, 2009, **19**, 3253.
32 J. Cheng, J. Wang, W. Li, X. Liu and Y. Yu, *RSC Adv.*, 2014, **4**, 37746.
33 E. G. Seebauer and C. E. Allen, *Prog. Surf. Sci.*, 1995, **49**, 265.
34 B. F. Dyson, T. R. Anthony and D. Turnbull, *J. Appl. Phys.*, 1967, **38**, 3408.
35 K. N. Tu and R. D. Thompson, *Acta Metall.*, 1982, **30**, 947.
36 Y. Kim and R. Buchheit, *Corrosion and Protection of Light Metal Alloys: Proceedings of the International Symposium*, 2004, vol. 23, p. 19.

37 A. J. McAlister and D. J. Kahan, *Bull. Alloy Phase Diagrams*, 1983, **4**, 410.
38 I. Isaichev, *Zh. Tekh. Fiz.*, 1939, **9**, 1867–1872.
39 J. Andrew and C. Edwards, *J. Inst. Met.*, 1909, **11**, 29.
40 W. B. Liu, S. C. Zhang, N. Li, J. W. Zheng and Y. L. Xing, *Microporous Mesoporous Mater.*, 2011, **138**, 1.
41 W. Liu, S. Zhang, N. Li, J. Zheng and Y. Xing, *J. Electrochem. Soc.*, 2010, **157**, D666.
42 K. N. Tu, *Acta Metall.*, 1973, **21**, 347.
43 K. N. Tu, *Mater. Chem. Phys.*, 1996, **46**, 217.
44 J. W. Yoon, C. B. Lee and S. B. Jung, *Mater. Sci. Technol.*, 2003, **19**, 1101.
45 K. Zeng, R. Stierman, T.-C. Chiu, D. Edwards, K. Ano and K. N. Tu, *J. Appl. Phys.*, 2005, **97**, 0245081.
46 Y. G. Lee and J. G. Duh, *J. Mater. Sci.: Mater. Electron.*, 1999, **10**, 33.
47 Y. G. Lee and J. G. Duh, *J. Mater. Sci.*, 1998, **33**, 5569.
48 J.-W. Yoon, C.-B. Lee and S.-B. Jung, *Mater. Sci. Technol.*, 2003, **19**, 1101.
49 C. N. Liao and C. T. Wei, *J. Electron. Mater.*, 2004, **33**, 1137.

4.2 (Paper 3)

Electrochemical dealloying of a ternary $Al_{67}Cu_{18}Sn_{15}$ alloy compared with that of a binary $Al_{75}Cu_{25}$ alloy

Tingting Song, Ming Yan, Zhiming Shi, Andrej Atrens, Ma Qian

ECS Transactions, 66(2015) 23-30.

ECS Transactions, 66 (40) 23-30 (2015)
10.1149/06640.0023ecst ©The Electrochemical Society

Electrochemical Dealloying of a Ternary $Al_{67}Cu_{18}Sn_{15}$ Alloy Compared with That of a Binary $Al_{75}Cu_{25}$ Alloy

T. Song[a], M. Yan[b], Z. Shi[c], A. Atrens[c], and M. Qian[a]

[a] RMIT University, School of Aerospace, Mechanical and Manufacturing Engineering, Center for Additive Manufacturing, Melbourne, Victoria 3053, Australia
[b] South University of Science and Technology of China, Department of Materials Science and Engineering, Shenzhen, Guangdong 518055, China
[c] The University of Queensland, Division of Materials, School of Mechanical and Mining Engineering, Brisbane, Queensland 4072, Australia

This paper reports on the electrochemical dealloying of a ternary $Al_{67}Cu_{18}Sn_{15}$ (in at.% throughout the paper) alloy consisting of α-Al, Al_2Cu and Sn using potentiodynamic and potentiostatic polarization measurements. When the applied potential (-0.5 V) was below the critical potential of the Al_2Cu phase (-0.41 V), complete electrochemical dealloying of the binary $Al_{75}Cu_{25}$ alloy (consisting of α-Al and Al_2Cu) occurred, leading to the formation of a nanoporous (52 ± 10 nm) copper (Cu) structure. However, under the same condition dealloying only occurred partially to the α-Al phase in the ternary $Al_{67}Cu_{18}Sn_{15}$ alloy due to the suppressing influence of Sn. The electrochemical dealloying of the ternary $Al_{67}Cu_{18}Sn_{15}$ alloy was potential dependent and involved the concurrence of dealloying and realloying as evidenced by the formation of Cu_6Sn_5.

Introduction

Dealloying is a selective corrosion process, during which the less noble component leaves the precursor alloy and dissolves into the electrolyte, while the remaining nobler element diffuses and develops into a nano-sized and/or micro-sized porous structure (1). The resulting porous surfaces or porous bulk materials are of high specific surface area, holding promise for applications including energy storage, and catalyzing medium with high activity (2). Research on dealloying over the last decade has largely focused on dealloying of binary alloys (i.e. AB type) to produce nanoporous pure metal B, and to understand the dealloying process. There are only a few studies which dealt with dealloying of alloys containing a third element such as $Mg_{90-x}Cu_xY_{10}$ and $Al_{66}Au_{27.2}X_{6.8}$ (X = Pt, Pd, PtPd, Ni, Co and NiCo) (in at.%) (3, 4). This minor third element, which substitutes the nobler element, was introduced to slow down the diffusivity of the nobler element. Accordingly, dealloying of these deceptively ternary alloys was essentially dealloying of binary alloys. Chemical dealloying of ternary alloys consisting of three distinctly different elements were reported only by Feng et al. and Song et al. (5, 6). Compared to the chemical dealloying of binary $Al_{75}Cu_{25}$ alloys, the chemical dealloying of $Al_{67}Cu_{18}Sn_{15}$ alloys was accompanied by a realloying process due to the impact of Sn (6, 7). However, no detailed studies seem to be available on electrochemical dealloying of ternary alloys consisting of three distinctly different elements.

This paper studies the electrochemical dealloying of the $Al_{67}Cu_{18}Sn_{15}$ alloy in a 1 M NaCl solution at room temperature. We employed the same dealloying conditions (-0.2 V and -0.5 V) used for the $Al_{75}Cu_{25}$ alloy to dealloy the $Al_{67}Cu_{18}Sn_{15}$ alloy, in order to investigate the influences of Sn on the electrochemical dealloying behavior (7). The differences between electrochemical and chemical dealloying of $Al_{67}Cu_{18}Sn_{15}$ are discussed. In addition, it has been reported that in Cu-Sn diffusion couples only Cu_6Sn_5 can form at room temperature while both Cu_6Sn_5 and Cu_3Sn intermetallics form at temperatures above 60 °C (8). This study also provides complementary information on phase formations in the Cu-Sn binary system at room temperature (8).

Experimental Methods

Alloy preparation

The $Al_{67}Cu_{18}Sn_{15}$ alloy was prepared from 99.99% purity Al, 99.99% purity Cu and 99.999% purity Sn using arc melting under argon. The alloy was remelted four times to ensure chemical homogeneity. The molten alloy from the fourth remelting was sucked into a water-cooled copper mould with a cavity of 8 mm in diameter and 30 mm in length, by the pressure differential between the mould chamber and the melting chamber. Disc samples were cut from the rod, then ground and polished into 0.6 mm thick foils (8 mm in diameter).

Electrochemical dealloying

Electrochemical experiments, including potentiodynamic polarization and potentiostatic polarization, were performed in a standard three-electrode cell using an electrochemical workstation (Parstat 2273, Princeton). The Ag/AgCl electrode (in a saturated KCl solution) was the reference electrode. A platinum plate was the counter electrode. Samples made from the $Al_{67}Cu_{18}Sn_{15}$ and as-cast Al_2Cu alloys, 99.99% purity Al and 99.999% purity Sn were the working electrodes. The geometric area (S_g) of the sample immersed below the electrolyte/air interface was used as the actual surface area in the calculation of the electrochemical parameters such as current density and charge density. All measurements were made in solutions exposed to air at room temperature. The electrolyte was a 1 M NaCl aqueous solution prepared using analytical-grade reagents and distilled water. The scanning rates were 5 mV/s for the potentiodynamic polarization. The applied potentials for electrochemical dealloying of the $Al_{67}Cu_{18}Sn_{15}$ alloy were determined according to the potentiodynamic polarization measurements and our previous work (7). The chronoamperometric (current response) curves were obtained during potentiostatic polarizations. All potentials quoted were on the Ag/AgCl scale unless otherwise stated.

Phase and morphology characterization

The phase constitution and microstructure in typical samples before and after electrochemical dealloying were characterized using X-ray diffraction (XRD, Bruker D8 instrument, with Cu Kα radiation and a scanning rate of 1°/min) and scanning electron microscopy (SEM) in both the second electron (SE) imaging and backscattered electron (BSE) imaging modes (JEOL 7001, operated at 15 keV equipped with energy dispersive X-ray spectroscopy (EDX) made by INCA.

Results and Discussion

Phase constitution of precursor

Figure 1(a) presents the XRD pattern and Figure 1(b) a typical SEM micrograph of the precursor $Al_{67}Cu_{18}Sn_{15}$ alloy, which consisted of three phases: α-Al solid solution phase, Al_2Cu intermetallic phase and β-Sn solid solution phase. The $Al_{67}Cu_{18}Sn_{15}$ alloy solidifies in a sequence of pre-eutectic Al_2Cu (grey contrast), lamellar eutectic α-Al and Al_2Cu (lamellar dark contrast and grey contrast), and then Sn phase (bright contrast). The phase constitution indicated that the $Al_{67}Cu_{18}Sn_{15}$ alloy was essentially a mixture of $Al_{67}Cu_{18}$ alloy (= α-Al + Al_2Cu) and Sn metal. The EDX results shown in Figure 1(c,d) confirmed the phase distribution in Figure 1(b), where area I is for Al_2Cu and area II is for lamellar structure of α-Al and Al_2Cu.

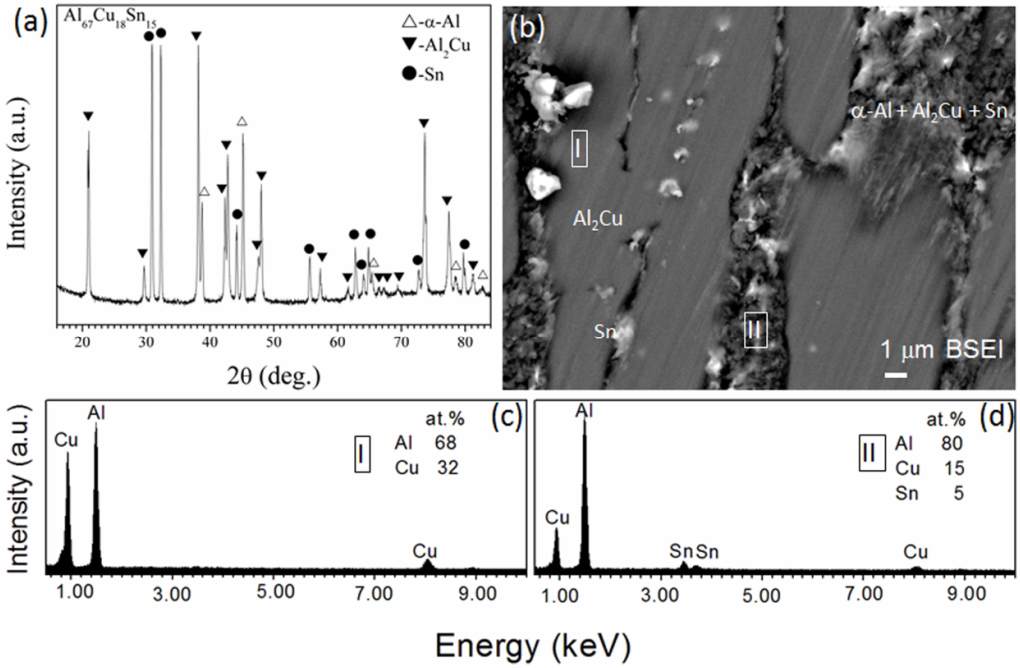

Figure 1. (a) XRD pattern and (b) SEM BSE microstructure of the $Al_{67}Cu_{18}Sn_{15}$ precursor consisting of α-Al, Al_2Cu and Sn; (c) and (d) EDX spectra of the Al_2Cu (I) and the mixture of three phases (II) marked in (b), respectively.

Electrochemical activities of $Al_{67}Cu_{18}Sn_{15}$ alloy in NaCl solution

The electrochemical property of the $Al_{67}Cu_{18}Sn_{15}$ alloy was determined using the potentiodynamic polarization (Tafel) approach shown in Figure 2(a). In addition, pure Al, pure Sn and as-cast Al_2Cu samples were analyzed as references. The potential corresponding to the tip of the Tafel curve (at the intersection of the anodic and cathodic branches) was defined as the critical potential (E_{crit}) (9). Figure 2(b) summarizes the critical potential (E_{crit}) values determined for the $Al_{67}Cu_{18}Sn_{15}$ alloy, pure Al, pure Sn and as-cast Al_2Cu. The $Al_{67}Cu_{18}Sn_{15}$ alloy exhibited a E_{crit} value (-0.82 V) which was more negative than that of pure Al (-0.66 V) (Figure 3(b)). This negative value offers more flexibility and wider processing window for the electrochemical dealloying.

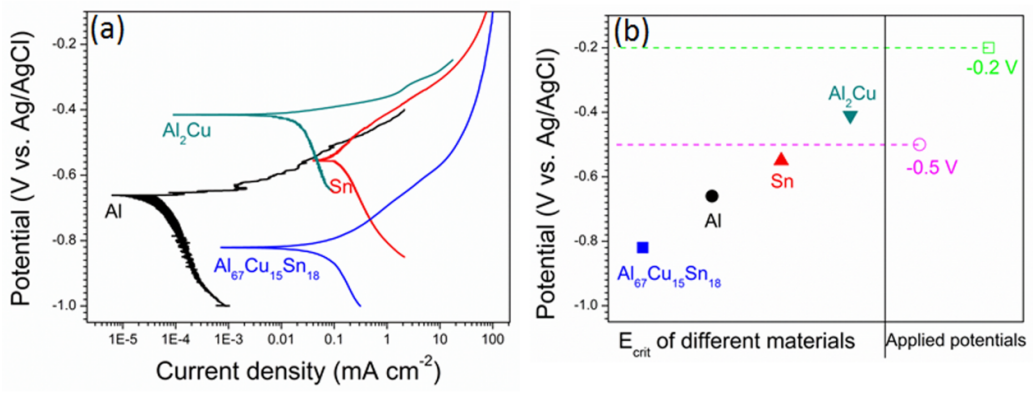

Figure 2. (a) Polarization curves that define the E_{crit} values for the $Al_{67}Cu_{18}Sn_{15}$ precursor (-0.82 V), pure Al (-0.66 V), pure Sn (-0.55 V) and as-cast Al_2Cu (-0.41 V). (b) The E_{crit} values for each material and the two applied potentials selected for electrochemical dealloying.

Electrochemical dealloying

To compare the dealloying behavior of the $Al_{67}Cu_{18}Sn_{15}$ alloy and $Al_{75}Cu_{25}$ (Ref. (7)) and to study the influence of the Sn phase, we selected electrochemical dealloying conditions similar to those used for $Al_{75}Cu_{25}$. One condition was to dealloy $Al_{67}Cu_{18}Sn_{15}$ at -0.5 V, a potential above the critical values of both the $Al_{67}Cu_{18}Sn_{15}$ alloy and pure Al, but below that of the Al_2Cu phase. The other was to dealloy at -0.2 V, a potential above the critical values of the $Al_{67}Cu_{18}Sn_{15}$ alloy, pure Al and the as-cast Al_2Cu. These selected applied potentials were above the critical value of Sn and were plotted in Figure 2(b).

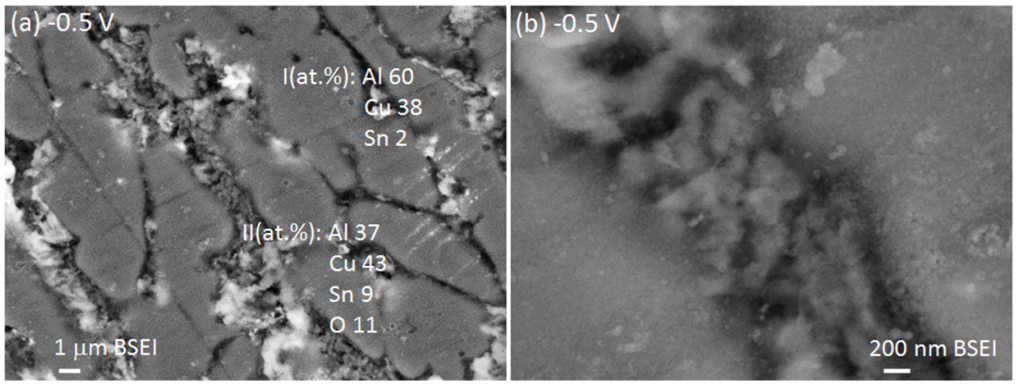

Figure 3. (a) Phase distribution of the $Al_{67}Cu_{18}Sn_{15}$ sample electrochemically dealloyed at -0.5 V with EDX information for resultant I and II phases (see Figure 1(b)); (b) high-magnified SEM image of (a) showing preferential dealloying of α-Al.

Electrochemical dealloying at -0.5 V. The microstructure resulting from dealloying at -0.5 V is shown in Figure 3. The sample (Figure 3(a)) shows the same phase distribution as the precursor (see Figure 1(b)). Figure 3(b) shows the preferential dealloying of α-Al in the lamellar eutectic α-Al and Al_2Cu, which can be described by Eq. [1]. There was no observable change in the morphology and the composition of the pre-eutectic Al_2Cu (Figure 3(a)). The distribution of bright contract Sn did not change much compared with that of precursor (Figure 1(b)). There was some oxygen

in the area II which might be from passivation of Sn via the following equations [2, 3] (10):

$$\alpha\text{-Al(Cu)} \rightarrow Al^{3+} + Cu + 3e^- \quad [1]$$
$$Sn + 2OH^- \rightarrow SnO + H_2O + 2e^- \quad [2]$$
$$Sn(OH)_2 + 2OH^- \rightarrow SnO_2 + 2H_2O + 2e^- \quad [3]$$

This was different from the dealloying of $Al_{75}Cu_{25}$ (α-Al and Al_2Cu), where both dealloying of α-Al and Al_2Cu occurred and nanoporous copper was created with an average ligament width of 52 ± 10 nm (7). Apparently, the presence of the Sn phase modified the phase constitution and electrochemical activities of $Al_{67}Cu_{18}Sn_{15}$ compared to $Al_{75}Cu_{25}$. Furthermore, it can be proposed that the presence of the Sn phase suppressed the dealloying of Al_2Cu, and as a result, a fresh surface full of Cu atoms was unavailable for the realloying of Cu and Sn and unavailable for the formation of any Cu-Sn composites at -0.5 V.

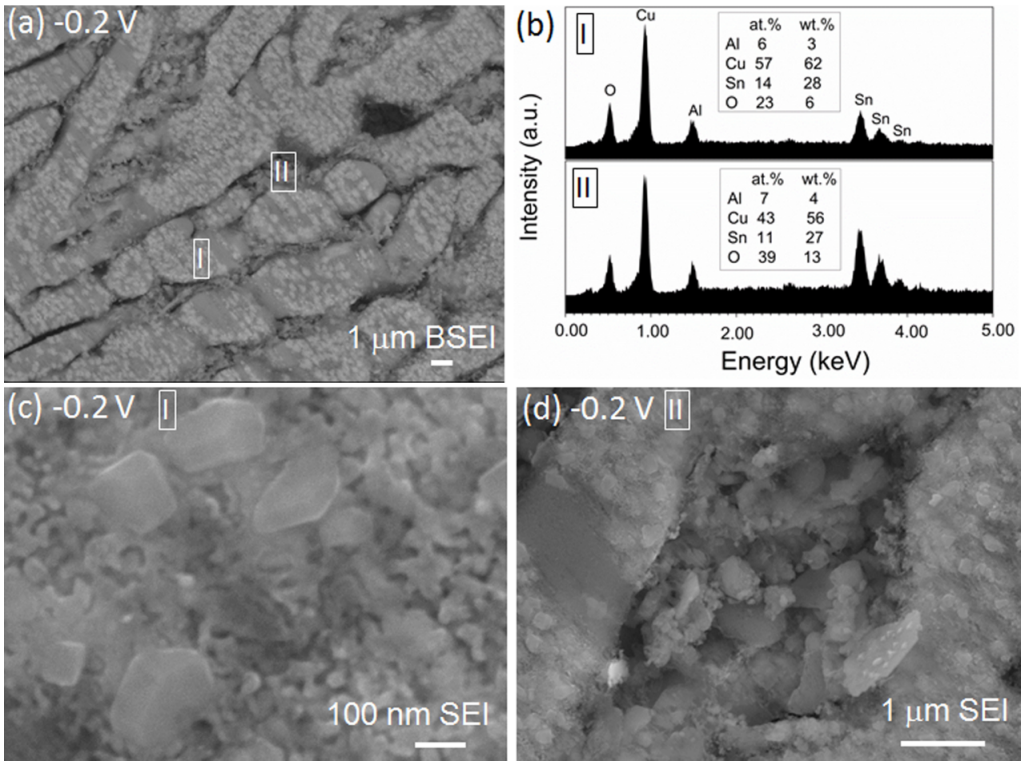

Figure 4. (a) SEM BSE image of the sample electrochemically dealloyed at -0.2 V showing two types of morphologies; (b) EDX results showing similar composition for the two types of structure in (a); (c) nanoporous Cu with an average width of 29 ± 7 nm and scallop-type Cu_6Sn_5 phase on the substrate of nanoporous Cu in I; (d) inhomogeneous and coarsened porous structure in II.

Electrochemical dealloying at -0.2 V. The microstructure resulting from dealloying at -0.2 V is shown in Figure 4. The applied potential (-0.2 V) was above the E_{crit} values of α-Al and Al_2Cu, and dealloying of both phases occurred leading to two types of porous structures (Figure 4(a,c,d)) with similar compositions (Figure 4(b)). The dealloying of pre-eutectic Al_2Cu resulted in fine nanoporous structure with an average ligament width of 29 ± 7 nm on the surface (Figure 4(c)), while the dealloying of lamellar eutectic of α-Al and Al_2Cu resulted in an inhomogeneous and coasened porous structure on the surface (Figure 4(d)). In addition, the Sn contents in

area I and area II were similar (27-28 wt.%) but were different from the precursor (Figure 1(b)). There were scallop-type structures, with an average width of 158 ± 30 nm, on the substrate of Al_2Cu and α-Al in Figure 4(a). The bright contrast in the SEM BSE image implies they were Sn-containing phases. It has been stated that only Cu_6Sn_5 can develop at room temperature in Cu/Sn diffusion couples (8). In addition, the Cu_6Sn_5 phase forming in either the solder joints (Sn-based solder/Cu interface) or Cu/Sn diffusion couples are uniquely featured by a scallop-type morphology (11, 8). The scallop-type morphology observed here may therefore be of a nano-sized Cu_6Sn_5 phase.

The results of dealloying the $Al_{67}Cu_{18}Sn_{15}$ alloy may be attributed to the following. (i) The applied potential of -0.2 V was able to realize the dealloying of α-Al and Al_2Cu via Eq. [1] and [4], releasing fresh Cu phase in the same manner as during the dealloying of Al-Cu binary alloys. (ii) The dealloying potential of -0.2 V, being more positive than -0.5 V, improved the diffusion of Sn atoms from the Sn phase. (iii) The large diffusion coefficient of Cu into Sn at room temperature enabled the formation of the Cu_6Sn_5 phase (8). Once the fresh Cu atoms described by Eq.[1, 4] contact Sn atoms diffusing from the Sn phase, Cu atoms could diffuse interstitially into Sn to form the Cu_6Sn_5 phase via the Eq. [5].

$$Al_2Cu \rightarrow 2Al^{3+} + Cu + 6e^- \quad [4]$$

$$Cu + Sn \rightarrow Cu_6Sn_5 \quad [5]$$

On the electrochemical dealloying of AlCu and AlCuSn. Figure 5(a) shows the current response curves of the $Al_{67}Cu_{18}Sn_{15}$ alloy dealloyed at -0.2 V and -0.5 V, plotted on double logarithmic coordinates. The current response curves of the $Al_{75}Cu_{25}$ alloy from our previous work are also shown for comparison (7). At -0.5 V, it took ~60 seconds for the current density (= current I divided by S_g) to reach a steady state of 6.7 mA·cm^{-2}. At -0.2 V, the current density reached a steady state (~ 55 mA·cm^{-2}) at the beginning (within 5 seconds) of the electrochemical dealloying. The current density at -0.5 V lower than that at -0.2 V was due to the dealloying of α-Al (Eq.(1)) alone without concurrent dealloying of the Al_2Cu phase (Eq.(4)).

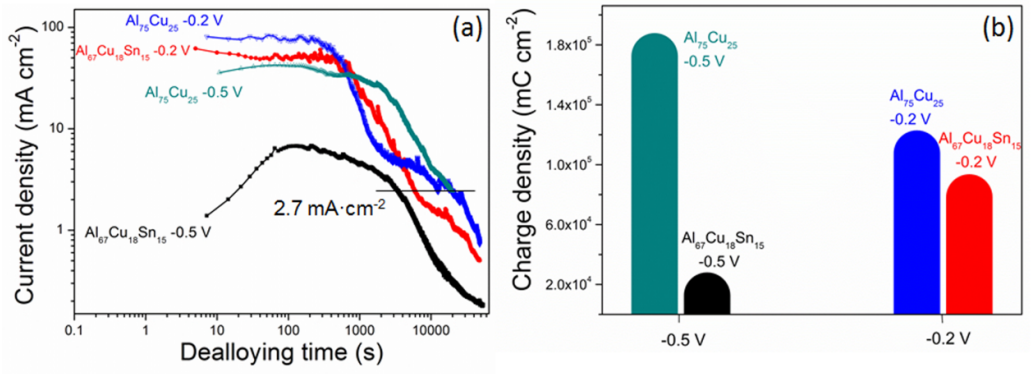

Figure 5. (a) Current responses of the $Al_{67}Cu_{18}Sn_{15}$ alloy and the $Al_{75}Cu_{25}$ alloy during electrochemical dealloying; (b) charge density values when the current density decreased to 2.7 mA cm^{-2} at each applied potential. The data related to $Al_{75}Cu_{25}$ alloy is from Ref (7).

For each specimen, the charge density (σ_q) transferred through the working electrode was evaluated according to the following definition (12):

$$\sigma_q = \int J dt = \int \frac{I}{S_g} dt \quad [6]$$

where J is the electrochemical dealloying current density, t is time and S_g (the geometric area of the sample immersed below the electrolyte/air interface) is the area under the electrochemical dealloying current density curves in Figure 5(a). Figure 5(b) compares the charge densities when the current density decreased to 2.7 mA cm^{-2} at each electrochemical dealloying treatment. Dealloying of the $Al_{67}Cu_{18}Sn_{15}$ alloy at -0.5 V resulted in the smallest charge density, which was noticeably smaller than that achieved from dealloying of $Al_{67}Cu_{18}Sn_{15}$ at -0.2 V or dealloying of $Al_{75}Cu_{25}$. The lowest charge density further confirms the dissolution of the smallest amount of Al from α-Al. In addition, the charge density from dealloying of $Al_{67}Cu_{18}Sn_{15}$ was lower than that of $Al_{75}Cu_{25}$, which can be due to the incomplete dealloying of $Al_{67}Cu_{18}Sn_{15}$ at -0.2 V (see the residual Al phase in Figure 4(b)).

Conclusion

We studied the electrochemical dealloying of a ternary $Al_{67}Cu_{18}Sn_{15}$ alloy, which consisted of three phases of α-Al, Al_2Cu and Sn. The presence of the Sn phase suppressed the dealloying of Al-based phases in the $Al_{67}Cu_{18}Sn_{15}$ alloy at the potential of -0.5 V, which is above the critical potential (E_{crit}) of the α-Al but below that of the Al_2Cu phase. This was different from the complete dealloying of Al_2Cu observed in the dealloying of the binary $Al_{75}Cu_{25}$ at -0.5 V for the production of nanoporous Cu. At -0.2 V, two types of nanoporous structure resulted from the dealloying of Al_2Cu and α-Al, respectively, in the ternary $Al_{67}Cu_{18}Sn_{15}$. In addition, there was formation of scallop-type Cu_6Sn_5 on the as-dealloyed products at -0.2 V, indicative of the occurrence of realloying during the electrochemical dealloying of the ternary $Al_{67}Cu_{18}Sn_{15}$ alloy.

Acknowledgments

T. Song is financially supported by a China Scholarship Council (CSC) scholarship and a RMIT fee waiver scholarship. T. Song acknowledges the High Degree by Research Travel Grant (HDRTG) of RMIT University.

References

1. R.C. Newman and K. Sieradzki, *Science*, **263**, 1708 (1994).
2. Y. Ding and M. Chen, *MRS Bull.*, **34**, 569 (2009).
3. X. Luo, R. Li, L. Huang and T. Zhang, *Corros. Sci.*, **67**, 100 (2013).
4. Y. Wang, J. Xu and B. Wu, *Phys. Chem. Chem. Phys.*, **15**, 5499 (2013).
5. Y. Feng, S. Zhang, Y. Xing and W. Liu, *J. Mater. Sci.*, **47**, 5911 (2012).
6. T. Song, M. Yan, Y. Gao, A. Atrens and M. Qian, *RSC Adv.*, **5**, 9574 (2015).
7. T. Song, M. Yan, Z. Shi, A. Atrens and M. Qian, *Electrochim. Acta*, **164**, 288 (2015).
8. K. N. Tu, *Mater. Chem. Phys.*, **46**, 217 (1996).
9. J. Snyder, K. Livi and J. Erlebacher, *J. Electrochem. Soc.*, **155**, C464 (2008).
10. U. S. Mohanty and K. L. Lin, *Corros. Sci.*, **48**, 662 (2006).

11. J. O. Suh, K. N. Tu, G. V. Lutsenko and A.M. Gusak, *Acta Mater.*, **56**, 1075 (2008).
12. F. C. Strong, *J. Chem. Educ.*, **38**, 98 (1961).

Chapter 5 Creation of bimodal porous copper materials by an annealing-electrochemical dealloying approach

Nanoporous copper (Cu) as a current collector in lithium ion batteries (LIBs) can provide unique advantages in mass transport including easier diffusion of electron and lithium ions, higher electrode-electrolyte interfacial contact area and better accommodation of structural strain during lithiation-delithiation reactions (see Section **2.1.3.2 Nanoporous metal current collector or anode structures**).

This chapter chooses to use a two-phase $Al_{75}Cu_{25}$ alloy as the precursor for dealloying (Section **2.3.2.1 Binary alloys: Multi-phases**) and employs an innovative approach based on the combination of annealing treatment and electrochemical dealloying to produce hierarchical porous Cu materials (Section **2.3.3.2 Temperatures: Pre-dealloying annealing** and Section **2.3.3.1 Applied potentials**).

(Paper 4)

Creation of bimodal porous copper materials by an annealing-electrochemical dealloying approach

Tingting Song, Ming Yan, Zhiming Shi, Andrej Atrens, Ma Qian

Electrochimica Acta, 164(2015) 288-296

Electrochimica Acta 164 (2015) 288–296

Contents lists available at ScienceDirect

Electrochimica Acta

journal homepage: www.elsevier.com/locate/electacta

Creation of bimodal porous copper materials by an annealing-electrochemical dealloying approach

T. Song [a], M. Yan [a,b], Z. Shi [c], A. Atrens [c], M. Qian [a,*]

[a] RMIT University, School of Aerospace, Mechanical and Manufacturing Engineering, Centre for Additive Manufacturing, Melbourne, VIC 3001, Australia
[b] South University of Science and Technology of China, Department of Materials Science and Engineering, Shenzhen, Guangdong 518055, China
[c] The University of Queensland, Queensland Centre for Advanced Materials Processing and manufacturing (AMPAM), School of Mechanical and Mining Engineering, Brisbane, QLD 4072 Australia

ARTICLE INFO

Article history:
Received 15 December 2014
Received in revised form 16 February 2015
Accepted 26 February 2015
Available online 26 February 2015

Keywords:
Annealing
Dealloying
Bimodal
Nanoporous
Microporous

ABSTRACT

Hierarchical (bimodal) porous copper (Cu) materials with micro- and nano-sized pores are desired for a wide variety of important applications. This study proposes an annealing-electrochemical dealloying approach for the creation of bulk bimodal porous Cu materials from an as-cast hypereutectic $Al_{75}Cu_{25}$ (at.%) precursor alloy, which consists of pre-eutectic $CuAl_2$ and lamellar eutectic α-Al(Cu)-$CuAl_2$. Annealing of the precursor alloy plays a critical role in the subsequent electrochemical dealloying for the creation of bimodal porous Cu. It decouples the lamellar eutectic structure and substantially increases the size of the α-Al(Cu) phase which determines the size of the subsequently produced micropores. In addition, it reduces the solubility of Cu in α-Al(Cu) and noticeably decreases the critical potential of the $Al_{75}Cu_{25}$ alloy thereby enabling more flexible electrochemical dealloying. A variety of bimodal porous Cu structures were produced using the proposed approach. The most homogeneous bimodal porous Cu structure with the average ligament width of 52 nm was produced by electrochemical dealloying of the annealed $Al_{75}Cu_{25}$ alloy at the applied potential of -0.5 V, which is above the critical potential of the α-Al (Cu) but below that of the $CuAl_2$ phase. The influence of annealing on the microstructure and the subsequent electrochemical dealloying behaviours of the $Al_{75}Cu_{25}$ alloy was characterised and discussed in detail.

1. Introduction

Dealloying is a selective dissolution process which dissolves one or more active components from a binary or multicomponent alloy, leaving behind a material enriched in the nobler or less active alloy component(s). The resulting nanoporous bulk materials or nanoporous surfaces hold promise for applications including energy storage [1–3], substrates against bacteria [4], catalyzing medium with high activity [5,6], environmental detectors [7,8], and heat-transfer with high efficiency [9]. To date, a variety of precursor alloys have been dealloyed to produce nanoporous metals (e.g. copper [3,9], silver [10], gold [7,11], platinum [12,13], palladium [6]) or alloys [14] in the form of small ingots, foils, ribbons, films and powder. However, the pore size distribution (PSD) produced by a normal dealloying process is often limited to a narrow- or single-sized range, for instance, 200 nm for nanoporous Cu [15], 225 ± 53 nm for nanoporous Ag [10], and 13 nm for nanoporous Au [7].

Unlike single-sized porous materials, a hierarchical (bimodal) porous structure can impart enhanced or novel properties to the porous materials. For example, large pores can favour increased mass transport while fine pores can improve activity due to their high specific surface area [16,17]. One such development was that made by Tsubaki et al. [18], who showed that cobalt-deposited hierarchical porous silica exhibited remarkably high activity as an catalyst due to the high specific surface area from the fine pores in addition to the improved diffusion efficiency because of the large pores. Another development is that nanoporous gold (Au) with a dual microscopic scale of porosity showed a charge-induced strain response amplified by two orders of magnitude [16,17].

Hierarchical porous metals can be produced by different approaches [19–21]. Zhang and co-workers [19,20] developed nanoporous gold with bimodal channels by chemical dealloying rapidly solidified Al-Au ribbons. The large-sized channels were hundreds of nanometers wide in one case [19] and 25–50 nm wide in another case [20] with the corresponding small-sized channels being 10–20 nm wide [19] and 10–25 nm wide [20]. Dan et al. [21]

* Corresponding author at: RMIT University, School of Aerospace, Mechanical and Manufacturing Engineering, Melbourne VIC 3001 Australia. Tel.: +61 3 9925 4491.
E-mail address: ma.qian@rmit.edu.au (M. Qian).

http://dx.doi.org/10.1016/j.electacta.2015.02.217
0013-4686/

reported the fabrication of bimodal nanoporous Ni (with 150–440 nm large-sized and 70–130 nm small sized ligaments) via electrochemical dealloying of Ni-Mn alloys. In another development, Renner et al. [22] observed bimodal nanoporosity on the surface of the $CuAu_3$ sample in the beginning of its dealloying process. In neither case, the size difference is distinct enough. Ding et al. [23] adopted a dealloying-plating-annealing-dealloying approach and produced bimodal porous gold from Ag–Au precursors with 1–2 μm large pores and 8 nm fine pores. This approach, however, involved the use of long plating, expensive chemicals and repeated high temperature annealing (500 °C). Dealloying has also been applied to rapidly solidified $Al_{85}Cu_{15}$ (at.% throughout the paper) ribbons consisting of α-Al(Cu) and $CuAl_2$ phases [24]. Bimodal porous Cu ribbons with micro- and nano-sized pores were produced [24]. However, because of the low Cu content in the $Al_{85}Cu_{15}$ precursor alloy and the use of ribbon forms of $Al_{85}Cu_{15}$, the resulting bimodal porous Cu ribbons are fragile and prone to fragmentation [25,26].

This paper aims to produce bimodal porous Cu with distinctly different pore sizes and good mechanical integrity using a simple process free of toxic chemicals. To achieve this, we propose an annealing-dealloying approach and apply it to $Al_{75}Cu_{25}$ ingot samples rather than foils or ribbons. The rest of the paper first discusses the rationales for the precursor selection as well as the proposed annealing-dealloying approach, followed by experimental description and results. The bimodal porous structures and their formation mechanism are discussed in Section 5. The last section summarizes the major findings of this study.

2. The selection of the precursor alloy and the annealing-dealloying approach

The rationales for the selection of the $Al_{75}Cu_{25}$ precursor alloy are given below.

(i) The presence of 25 at.%Cu (equivalent to 44 wt.%Cu) in the precursor can physically ensure the production of bulk nanoporous Cu with good integrity after complete removal of the Al by dealloying [25,27]. Such bulk nanoporous Cu materials can be used as current collectors in batteries [3], substrates against bacteria [4], heat transfer [9] and other applications due to their high specific surface area and good mechanical integrity.

(ii) Another consideration is from the dealloying perspective. $Al_{75}Cu_{25}$ solidifies as pre-eutectic $CuAl_2$ and lamellar eutectic α-Al (Cu)-$CuAl_2$ [27]. Dealloying of such a two-phase precursor alloy offers the possibility for the creation of a porous material with two-length scale hierarchy, especially when the two phases show different dealloying behaviors. The two-phase $Al_{75}Cu_{25}$ is a good fit in this regard. For instance, dealloying of $CuAl_2$ can result in nanoporous Cu [24,28] while due to the limited solubility of Cu in α-Al(Cu), it is expected that dealloying of α-Al(Cu) is equivalent to removing Al atoms from the α-Al(Cu) phase until it leaves behind a cavity of the same size of the α-Al(Cu) phase [24,29]. This offers a chance of producing large pores with the same size and distribution of the α-Al(Cu) phase.

The introduction of annealing and the section of electrochemical dealloying over chemical dealloying are based on the following grounds. The uniform lamellar eutectic structure in the as-cast $Al_{75}Cu_{25}$ alloy is undesired for the production of a bimodal porous structure, in addition to the small size (≤500 nm thick) of the lamellar eutectic α-Al(Cu) phase. Similar to the well-established spheroidisation annealing treatment of lamellar pearlite (eutectoid) in carbon steel [30], it is expected that annealing of the as-cast $Al_{75}Cu_{25}$ alloy can effectively decouple its lamellar eutectic structure and increase the α-Al(Cu) phase size. Also, annealing can reduce the solubility of Cu in the α-Al(Cu) phase and this favours subsequent dealloying of the α-Al(Cu) phase. As regards the dealloying process, chemical dealloying is capable of realizing the designed hierarchical porous structures. However, compared to chemical dealloying, electrochemical dealloying can produce much finer microstructural features (e.g. ~4 nm of ligament size or 2–5 nm pore size [6]) through control of the applied potential than chemical alloying. Another contrast is that chemical dealloying is always performed in aggressive solutions, e.g. HNO_3 [31], HCl [10], NaOH [32] while electrochemical dealloying can be realized in neutral salt solutions (e.g. NaCl [10,29], $AgNO_3$ [33], etc.), which are pollution-free, non-toxic, and inexpensive. Electrochemical dealloying is thus preferred. In this study, we selected a 1 M NaCl aqueous solution as the electrolyte, where the existence of chloride ion (Cl^-) is able to prevent the passivation of Al or Cu occurring in neutral solutions [34,35].

These considerations constitute the conceptual framework for the annealing-and-electrochemical-dealloying approach to be presented and discussed below.

3. Experimental Section

The selected precursor alloy $Al_{75}Cu_{25}$ was prepared from 99.99% purity Al and Cu using arc melting under a protective argon atmosphere. Also prepared was an $Al_{67}Cu_{33}$ alloy, which is equivalent to the $CuAl_2$ phase. Each alloy was remelted four times to ensure chemical homogeneity. Samples were made by sucking the molten alloy into a copper mould with a cavity of Φ8 mm × 10 mm. Annealing of the as-cast $Al_{75}Cu_{25}$ ingot samples was performed at 490 °C for 24 h under argon (heated at 20 °C/min to temperature), followed by furnace cooling. The annealing temperature was selected to be about 60 °C below the eutectic temperature of the alloy for pronounced coarsening of the α-Al (Cu) phase. Disc samples were cut from the as-annealed rods, and thinned into Φ8 mm × 0.6 mm thick foils.

Electrochemical experiments, including potentiodynamic polarization, cyclic voltammetry (CV) and potentiostatic polarization, were performed in a standard three-electrode cell using an electrochemical workstation (Parstat 2273, Princeton). The Ag/AgCl electrode (in a saturated KCl solution) was used as the reference electrode, along with a platinum plate as the counter electrode. Samples made from the as-annealed $Al_{75}Cu_{25}$ and as-cast $Al_{67}Cu_{33}$ (i.e. $CuAl_2$) alloys and 99.99% purity Al were used as the working electrodes. In this study, the geometric area (S_g) of the sample immersed below the electrolyte/air interface was used as the actual surface area in the calculation of the electrochemical parameters such as current density and charge density. All measurements were performed in solutions exposed to air at 25 ± 2 °C. The electrolyte was a 1 M NaCl aqueous solution prepared using analytical-grade reagents and distilled water. The scanning rates were 5 mV/s for potentiodynamic polarization and 50 mV/s for CV measurements. A total of 600 cycles of CV curves were recorded for as-annealed $Al_{75}Cu_{25}$. The applied potentials for electrochemical dealloying of the as-annealed $Al_{75}Cu_{25}$ alloy were determined according to potentiodynamic polarization measurement. The chronoamperometric (current response) curves were obtained during potentiostatic polarizations. All potentials quoted are on the Ag/AgCl scale unless otherwise stated.

The phase constitution and microstructure in selected samples before and after electrochemical dealloying were characterized using scanning electron microscopy (SEM, JEOL 7001 equipped with energy dispersive X-ray spectroscopy (EDX) made by INCA, operated at 15 kV) and transmission electron microscopy (TEM, JEOL 2100, operated at 200 kV). Samples for TEM analysis were prepared by grinding specially dealloyed foils into powder, followed by dispersing the powder in ethanol. Then a few drops of the particles-containing ethanol solution were released on a

3 mm diameter carbon film placed on a copper grid support. After drying in air for 20 min, the powder samples were ready for TEM analysis.

4. Results

4.1. Phase constitution of the as-cast and as-annealed hypereutectic $Al_{75}Cu_{25}$ alloy

Fig. 1(a) shows the positions of the selected $Al_{75}Cu_{25}$ and $Al_{67}Cu_{33}$ alloys in the Al-Cu phase diagram. The $Al_{67}Cu_{33}$ alloy is equivalent to $CuAl_2$ in composition and Fig. 1(b) shows the XRD spectrum obtained from the $Al_{67}Cu_{33}$ ingot sample, confirming that it is essentially $CuAl_2$. The $Al_{75}Cu_{25}$ alloy solidifies as pre-eutectic $CuAl_2$ and lamellar eutectic α-Al(Cu)-$CuAl_2$, shown in Fig. 1(c,d). After annealing at 490 °C for 24 h, the lamellar eutectic structure disappeared and evolved into α-Al(Cu) and $CuAl_2$ (see Fig. 2(a)). The annealed α-Al(Cu) contained 1.8 at.%Cu by EDX, Fig. 2(b), consistent with the solubility of Cu in α-Al at 490 °C (1.6 at.%Cu, Fig. 1(a)). The annealed $CuAl_2$ phase had a Cu:Al ratio close to 1:2 by EDX (Fig. 2(c)). As expected, after annealing the Cu-depleted α-Al(Cu) was much coarser than the original lamellar eutectic α-Al(Cu). Both the increased α-Al(Cu) phase size and its reduced solubility of Cu are in favour of the creation of a large sized porous structure by subsequent dealloying.

4.2. Electrochemical activities of as-cast and as-annealed $Al_{75}Cu_{25}$ alloy in NaCl solutions

The electrochemical properties of the $Al_{75}Cu_{25}$ alloy in both the as-cast and the as-annealed states were determined using the potentiodynamic polarization (Tafel) approach shown in Fig. 3(a). In addition, pure Al, pure Cu and as-cast $CuAl_2$ samples were analysed as a point of reference. The potential corresponding to the tip of the Tafel curve (intersection point of anodic and cathodic branches) was defined as the critical potential (E_{crit}) [32,36]. Fig. 3(b) summarizes the critical potential (E_{crit}) values determined for the as-cast $Al_{75}Cu_{25}$, as-annealed $Al_{75}Cu_{25}$, pure Al, pure Cu and as-cast $CuAl_2$. The as-cast $Al_{75}Cu_{25}$ showed an E_{crit} value between the respective values of Al and $CuAl_2$ while the as-annealed $Al_{75}Cu_{25}$ exhibited a much lower E_{crit} value which was even smaller than that of pure Al (Fig. 3(b)). Annealing decreased the critical potential value of the $Al_{75}Cu_{25}$ from −0.61 V to −0.77 V. This noticeable decline offers more flexibility in electrochemical dealloying and was an unexpected benefit of annealing. In addition, an inflexion point was observed on the Tafel curves for both the as-cast and as-annealed $Al_{75}Cu_{25}$ alloy at about -0.39 V, close to the E_{crit} value (-0.41 V) of the $CuAl_2$ phase shown in Fig. 3(a). This is important for the selection of applied potentials for electrochemical dealloying in the following section as it affects the dealloying behaviours.

4.3. Electrochemical dealloying and the resulting bimodal porous Cu

The as-annealed $Al_{75}Cu_{25}$ alloy was potentiostatically dealloyed under two circumstances according to the E_{crit} values shown in Fig. 3(b) for each material. One was to dealloy it at potentials above the critical values of the as-annealed $Al_{75}Cu_{25}$, pure Al and the as-cast $Al_{67}Cu_{33}$ (i.e. $CuAl_2$). The applied potential thus selected were -0.1 V and -0.2 V. The other was to dealloy it at a potential above the critical values of both the as-annealed $Al_{75}Cu_{25}$ and pure Al, but below that of the $CuAl_2$ phase. This resulted in the selected potential of -0.5 V. These selected applied potentials are also plotted into Fig. 3(b) for comparison.

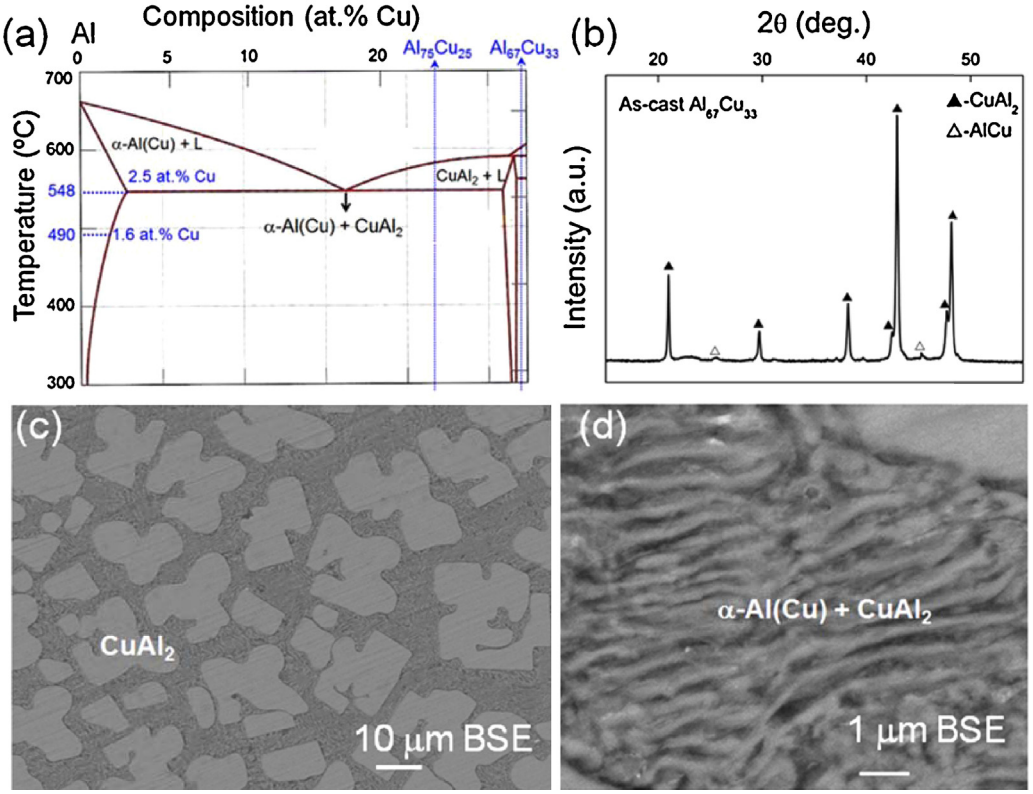

Fig. 1. (a) Al-Cu phase diagram showing the phase constitution information of $Al_{75}Cu_{25}$ and $Al_{67}Cu_{33}$ alloys and the solubility of Cu in α-Al at both the eutectic temperature and 490 °C. (b) XRD pattern of the as-cast $Al_{67}Cu_{33}$ alloy confirming that the alloy is composed of essentially the $CuAl_2$ phase. (c) Back scattered electron (BSE) image showing the microstructure of the as-cast $Al_{75}Cu_{25}$ consisting of pre-eutectic $CuAl_2$ and eutectic α-Al(Cu)-$CuAl_2$. (d) The lamellar eutectic α-Al(Cu)-$CuAl_2$.

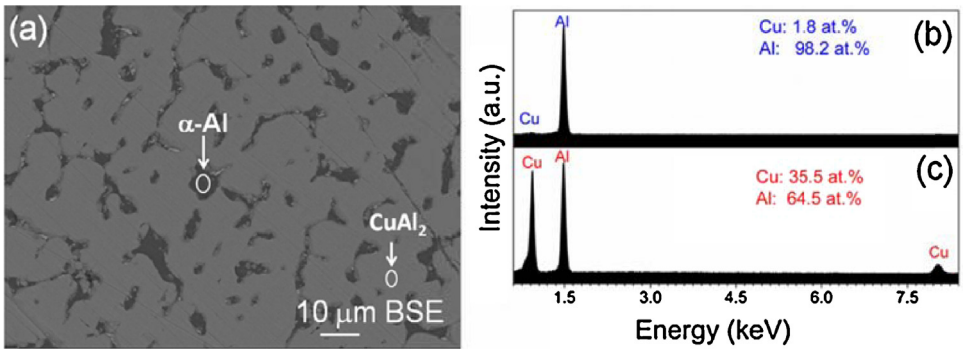

Fig. 2. (a) Microstructure of the annealed $Al_{75}Cu_{25}$ alloy consisting of the α-Al(Cu) and $CuAl_2$ phases. The lamellar eutectic α-Al(Cu)-$CuAl_2$ structure disappeared after annealing. (b) and (c) are EDX spectra of the α-Al(Cu) and $CuAl_2$ phases circled in (a), respectively.

The microstructures resulted from dealloying at -0.1 V and -0.2 V are shown in Fig. 4. Bimodal porous structures were obtained at each applied potential. Large pores up to tens of micrometres were produced (see Fig. 4(a,c)) while nanoporosity was produced in the larger ligaments (see Fig. 4(b,d)). However, there are still notable differences in the microstructure due to the difference in driving force for dealloying (greater at -0.1 V). The microstructure resulted from dealloying at -0.1 V is coarser (average ligament width, 204 ± 85 nm, Fig. 4(b)) than that resulted from dealloying at -0.2 V (average ligament width, 196 ± 48 nm, Fig. 4(d)). In addition, it was found from comparing Fig. 4(c) with Fig. 2(a) that the large pores produced from dealloying at -0.2 V resemble the α-Al(Cu) phase in the as-annealed alloy (see Fig. 2(a)) in terms of their size, morphology and distribution. In contrast, the large pores produced from dealloying at -0.1 V (Fig. 4(a)) are less similar due to coarsening caused by the large driving force. Hence dealloying at -0.2 V resulted in a more homogeneous microstructure than dealloying at -0.1 V. EDX analyses of the sample dealloyed at -0.1 V detected no signals of Al but overwhelming signals of Cu (see inset in Fig. 4(b)).

The microstructure resulted from dealloying at -0.5 V is shown in Fig. 5. Although the applied potential (-0.5 V) was only above the critical potential of pure Al (reference for α-Al(Cu)), dealloying of both α-Al(Cu) and $CuAl_2$ phases occurred leading to a bimodal porous structure as shown in Fig. 5(a,b) with a much smaller average ligament width (52 ± 10 nm). EDX analyses (see inset in Fig. 5(c)) showed the presence of 2 at.% (1 wt.%) of residual Al. TEM selected area electron diffraction (SAED) patterns, shown in Fig. 5(d), revealed that Cu was the only remaining phase, indicative complete dealloying of both the α-Al(Cu) and $CuAl_2$ phases. High resolution TEM (HRTEM) observations also revealed the presence of twinning structures in the Cu ligaments (Fig. 5(e,f)).

4.4. Cyclic voltammetry (CV) measurements

Fig. 6(a) shows the CV loop of the as-annealed $Al_{75}Cu_{25}$ between the applied potentials of -0.8 V, which is 0.03 V below the E_{crit} value of the as-annealed $Al_{75}Cu_{25}$, and -0.3 V, which is 0.110 V above the E_{crit} value of the $CuAl_2$ phase. Also shown are the CV loops of pure Al and the $CuAl_2$ phase for comparison. The CV loop of pure Al has a reverse scan density higher than the current density during the forward scan (see dotted arrows in Fig. 6(a)). And there was a crossover (marked by an open triangle) in the CV loop of $CuAl_2$ which separated the loop into two sections. In the higher potential section, the current of the reverse scan was higher than that of the forward scan (Al-type). In the lower potential section, the observation was opposite (Fig. 6(a)).

Fig. 6(b,c) shows the CV loops of the annealed $Al_{75}Cu_{25}$ alloy up to 600 cycles. In the initial 12 cycles (Fig. 6(b)), the CV curves are of the Al-type. From then on, there was a crossover (marked by an open triangle) similar to that of $CuAl_2$ shown in Fig. 6(a). In the 600th cycle, the crossover disappeared and the current of the reverse scan was lower than that of the forward scan, which is typical of the CV loop for Cu [29]. The CV loops of the annealed

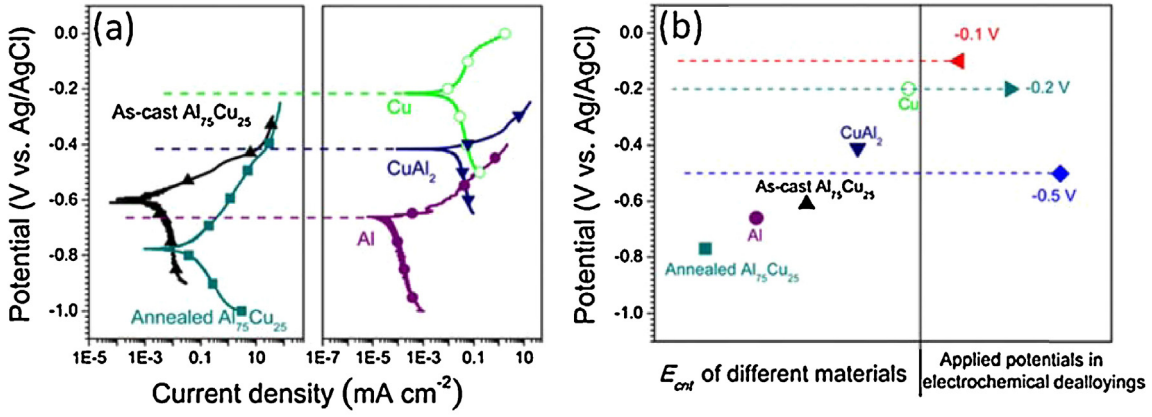

Fig. 3. (a) Tafel curves that define the E_{crit} values for as-cast $Al_{75}Cu_{25}$ (-0.61 V), as-annealed $Al_{75}Cu_{25}$ (-0.77 V), pure Al (-0.66 V), pure Cu (-0.20 V) and as-cast $CuAl_2$ (-0.41 V) (see Fig. 1(a)). (b) Distribution of the E_{crit} values for each material and the three applied potentials selected for electrochemical dealloying.

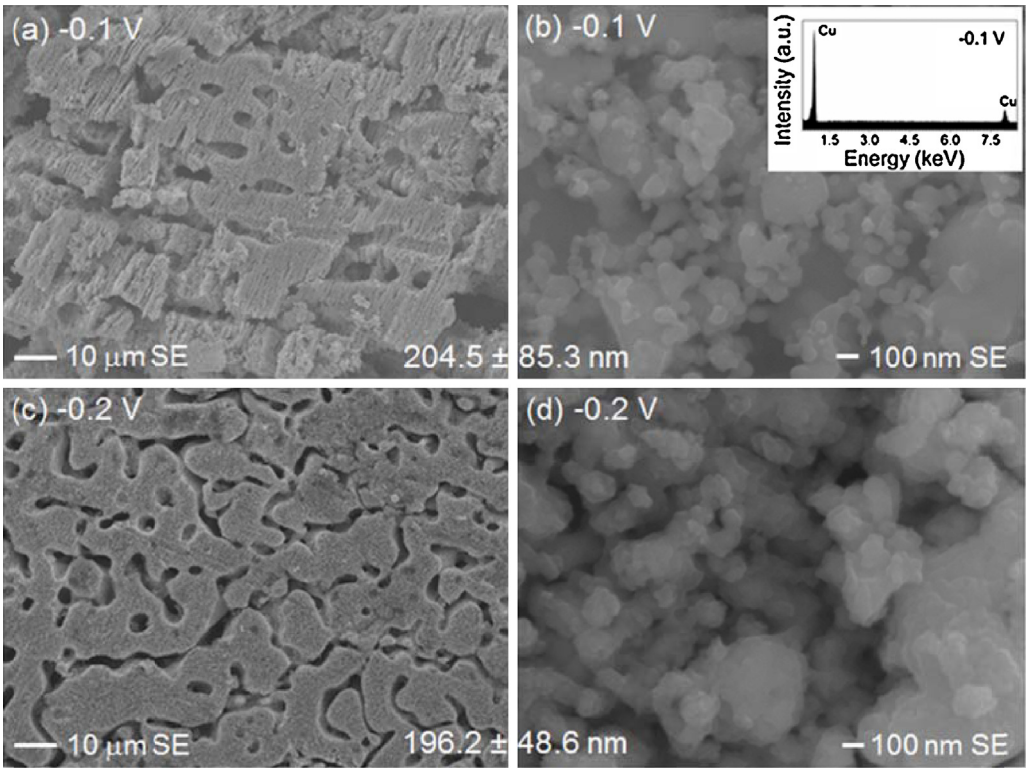

Fig. 4. Bimodal porous structures of Cu electrochemically dealloyed at -0.1 V (a, b) with an EDX spectrum inset in (b) and -0.2 V (c, d). All the images are from second electron (SE) imaging mode.

$Al_{75}Cu_{25}$ alloy evolved from the Al-type to the $CuAl_2$ type and finally to the Cu-type as the dealloying process went on.

4.5. Current and charge responses during electrochemical dealloying

Fig. 7(a) shows the current response curves of the annealed $Al_{75}Cu_{25}$ alloy dealloyed at -0.1 V, -0.2 V and -0.5 V, plotted on double logarithmic coordinates. At each applied potential, the current density (current I divided by S_g) quickly reached a steady state indicating dissolution of Al atoms into the solution. The higher the applied potential, the higher the resulting current density, and the higher the dissolution rate of Al. In addition, reducing the applied potential from -0.1 V to -0.5 V led to an extended steady state, which is preferred. The current response curves showed two relatively steady stages when dealloyed at -0.1 V and -0.2 V and each steady stage is indicative of continuous and fast dissolution of Al atoms. In contrast, the current response curve when dealloyed at -0.5 V exhibited only one single segment. In each case the current density showed a sharp fall at the end of the response. For each specimen, the charge density (σ_q) transferred through the work electrode was evaluated according to the definition below [37],

$$\sigma_q = \int J dt = \int \frac{I}{S_g} dt \quad (1)$$

where J is the electrochemical dealloying current density, t is time and S_g (the geometric area of the sample immersed below the electrolyte/air interface) is the area under respective electrochemical dealloying current density curves shown in Fig. 7(a). The curves of charge density vs. time are shown in Fig. 7(b). At each applied potential of -0.1 V and -0.2 V, the charge density increased sharply in the beginning, followed by a gradual increase, especially at -0.1 V, while at -0.5 V the initial stage showed a fairly gentle development. Fig. 7(c) compares the charge densities when the current density decreased to 2.7 mA cm^{-2} at each applied potential. Dealloying at -0.5 V resulted in the largest charge density, which is noticeably higher than that achieved from dealloying at either -0.1 V or -0.2 V. This is related to the surface area used in the evaluation of the current density and will be discussed in Section 5.3.

5. Discussion

5.1. The critical roles of annealing in the creation of bimodal porous structures

The as-solidified hypereutectic $Al_{75}Cu_{25}$ alloy consists of only two phases, pre-eutectic $CuAl_2$ and lamellar eutectic $CuAl_2$ and α-Al(Cu). As pointed out earlier, dealloying of the $CuAl_2$ phase can lead to nanoporous Cu [28]. Hence to produce a hierarchical porous Cu material with two distinctly different pore sizes from the $Al_{75}Cu_{25}$ alloy, it depends on how to produce desired large pores via dealloying of the eutectic lamellar α-Al(Cu) phase. The rationales for the introduction of annealing prior to dealloying have been specified previously. As shown in Fig. 2(a), after annealing at 490 °C for 24 h, the lamellar eutectic structure disappeared and the α-Al(Cu) phase grew to about 5 μm in size. The change is driven by the reduction in the interfacial free energy of the lamellar α-Al(Cu)-$CuAl_2$ eutectic and realised through the fast diffusion of Cu in α-Al(Cu) [38]. In addition, annealing decreased the solubility of Cu from 2.5 at.% at the eutectic temperature to about 1.8 at.% at 490 °C. The Cu-depleted coarse α-Al(Cu) phase makes it easier for micro-sized pores to form via excavation of the Al atoms by dealloying. In fact, as can be seen from comparing Fig. 4(c) and Fig. 2(a), the size and distribution of the large pores produced by electrochemical dealloying generally inherited the size and distribution of the Cu-depleted coarse α-Al

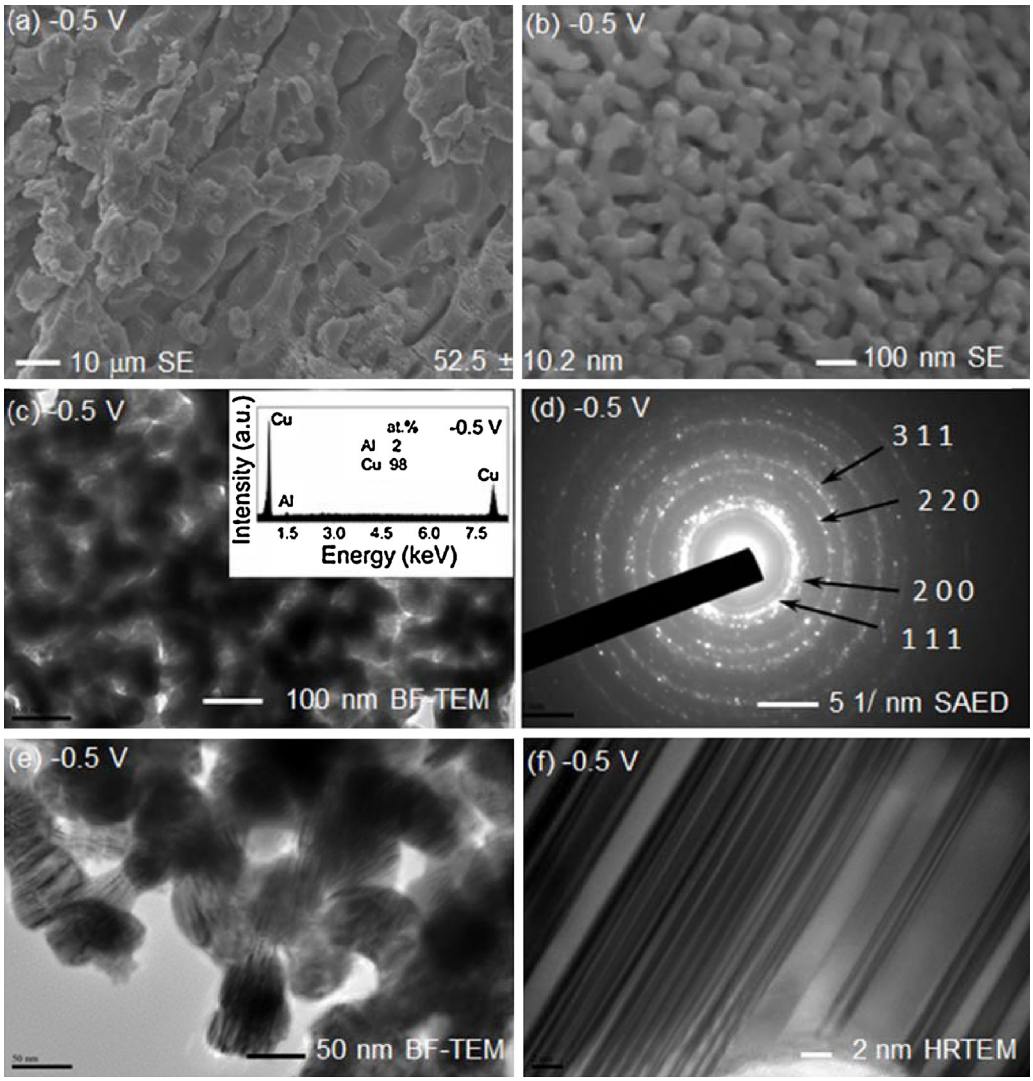

Fig. 5. Bimodal nanoporous structure resulted from dealloying at -0.5 V: (a, b) SEM images; (c, e) Bright field (BF) TEM images confirming the nanoporous structure (an EDX spectrum inset is shown in (c)); (d) TEM SAED results confirming the final crystal structure of Cu (the remaining phase after complete dealloying); and (f) HRTEM image from (e) showing twins in Cu ligaments.

(Cu) phase. This means that the size and distribution of the large pores can be effectively controlled via control of the size and distribution of the α-Al(Cu) phase by annealing.

An unexpected advantage resulted from annealing the as-cast alloy is that annealing noticeably decreased the E_{crit} value of the $Al_{75}Cu_{25}$. As a result, the E_{crit} value of the annealed $Al_{75}Cu_{25}$ is even clearly lower than that of pure Al (see Fig. 3(b)). This provides great flexibility for the selection of the applied potential for electrochemical dealloying. This is important especially when a homogenous bimodal porous structure with fine ligaments is desired (see Fig. 5). We have shown that hierarchical porous structures can be created by complete dealloying of the annealed $Al_{75}Cu_{25}$ alloy at -0.1 V, -0.2 V and -0.5 V (see Figs. 4 and 5) and dealloying at -0.5 V resulted in the most homogeneous microstructure.

In summary, the critical roles of annealing the as-cast $Al_{75}Cu_{25}$ precursor alloy prior to dealloying include (i) it decouples the lamellar eutectic structure and substantially increases the α-Al (Cu) phase size; (ii) it reduces the solubility of Cu in the α-Al(Cu) phase; and (iii) it decreases the E_{crit} value of the as-annealed $Al_{75}Cu_{25}$ precursor alloy and enables the creation of a homogenous bimodal porous structure with fine ligaments.

5.2. The electrochemical dealloying behaviour in NaCl solutions

The results obtained from dealloying at -0.1 V, -0.2 V and -0.5 V indicate that decreasing the applied potential decreases the average ligament size leading to an increasingly homogeneous porous structure. This is consistent with the study of Detsi et al. [39] on electrochemical dealloying of Ag-Au. The twinning structure observed in the Cu ligaments of the dealloyed sample at -0.5 V is also consistent with the other work on electrochemical dealloying and is due likely to the external potential applied [40].

The applied potential of -0.1 V is not only above the critical values of the as-annealed $Al_{75}Cu_{25}$, pure Al and $CuAl_2$, but also above that of Cu (Fig. 3). Accordingly, during dealloying at -0.1 V, apart from the dissolution of Al through Reaction (2) below, there should also be the dissolution of Cu, which, as suggested by Ref. [41], can occur through Reaction (3) below.

$$Al \rightarrow Al^{3+} + 3e^{-} \quad (2)$$

$$Cu + 2Cl^{-} \rightarrow CuCl_2^{-} + e^{-} \quad (3)$$

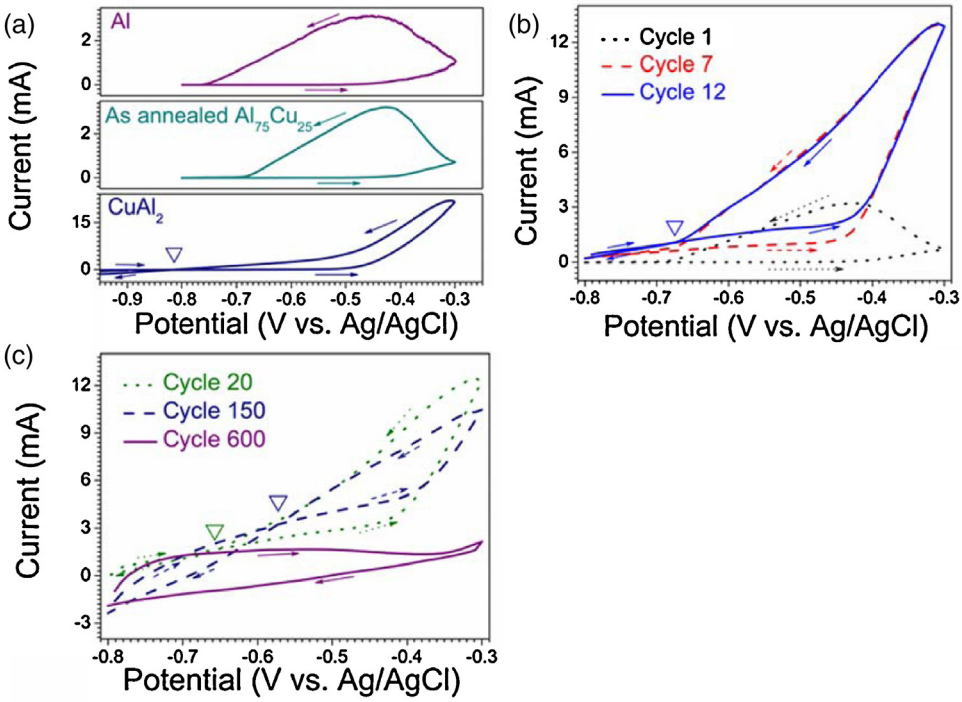

Fig. 6. (a) Cyclic Voltammetry (CV) curves for pure Al, as-annealed $Al_{75}Cu_{25}$ and $CuAl_2$. (b) and (c) show the evolution of the CV curves for as-annealed $Al_{75}Cu_{25}$ subjected to 600 cycles of CV measurements.

The development of Reaction (3) enhances the actual diffusion rate of Cu during dealloying [42]. As a result, the process led to inhomogeneous and coarse microstructures shown in Figs. 3 and 4. According to Faraday's law [37], the total charge passed during corrosion corresponds to the amount of metal corroded. Reactions of (2) and (3) are the prime dealloying reactions in the beginning. Hence they contribute to the majority of the increased charge density observed in the initial stage of dealloying leading to a sharp increase on the charge density-time curve shown in Fig. 7(b).

At the applied potential of -0.2 V, which is close to the critical potential of Cu (see Fig. 3), Reaction (3) occurs to a much lesser extent than at -0.1 V. The small quick initial increase in charge density in the beginning of electrochemical dealloying (see Fig. 7(b)) can be attributed to the limited contribution of Reaction (3). At the applied potential of -0.5 V, Reaction (3) no longer occurs and the charge density-time curve displays a gentle and slow development in the beginning of electrochemical dealloying (Fig. 7(b)).

Although the potential applied (-0.5 V) was below the E_{crit} value of the $CuAl_2$ phase in the precursor alloy, complete dealloying of both the $CuAl_2$ phase and the α-Al(Cu) occurred and a bimodal porous structure was produced. This differs from other electrochemical dealloying studies of two-phase precursor alloys when the applied potential is above the E_{crit} value of one phase while below that of the other phase [29,43,44]. In those cases, complete dealloying of the more active phase occurs but the less active one is often preserved [29,43,44]. The complete dealloying of the $CuAl_2$ and α-Al(Cu) phases in the annealed $Al_{75}Cu_{25}$ alloy at -0.5 V may be attributed to (i) Galvanic corrosion. The distinctly different E_{crit} of the Cu-depleted eutectic α-Al(Cu) and $CuAl_2$ phases in the annealed precursor alloy will naturally lead to the formation of many micro-galvanic corrosion cells [29,45]. In these galvanic corrosion cells, α-Al(Cu) would act as an anode while $CuAl_2$ would act as a cathode leading to a galvanic corrosion, which means the galvanic corrosion can promote the entire dissolution of Al to a certain extent. (ii) The self-acidifying effect of Al atoms in NaCl solutions. The Al^{3+} ions released from Reaction (2) in NaCl solution, either due to electrochemical corrosion or galvanic corrosion, leads to the enrichment of positive charges and, in turn, attraction to anions for charge balance. The anions (OH^- from H_2O and Cl^-) in the electrolyte migrate to the Al^{3+} rich zone and react with them through Reaction (4) leading to a lower pH value of the solution [46]. The released H^+ can accelerate the dealloying process of $Al_{75}Cu_{25}$ chemically through Reaction (5) given below [47].

$$Al^{3+} + H_2O + Cl^- \rightarrow [Al(OH)Cl]^+ + H^+ \quad (4)$$

$$2Al + 6H^+ + 4Cl^- \rightarrow 3H_2 + 2AlCl_2^+ \quad (5)$$

(iii) The promoting effect arising from dealloying the Al atoms from the α-Al(Cu) phase. The dissolution of the Al atoms from the α-Al(Cu) phase offers numerous penetration pathways for the electrolyte to interact with the Al atoms in the neighbouring $CuAl_2$ phase and therefore promotes dealloying of the $CuAl_2$ phase at the applied potential. Similar promoting effects were observed in chemical dealloying of Al-Ag alloys [25,48].

Compared to dealloying at -0.1 V and -0.2 V, the transient stage shown on the current response curve at the applied potential of -0.5 V was delayed, indicating a longer initial interaction time with the electrolyte for the Al atoms in the α-Al(Cu) and $CuAl_2$ phases and the formation of a porous network. However, a notable advantage of using a low applied potential such as -0.5 V is that it provides only a mild driving force for diffusion. Consequently, the resulting microstructure is finer and more homogeneous without undergoing significant coarsening. The proposed annealing-electrochemical dealloying approach is expected to be applicable to other alloy systems for the creation of bimodal porous metals.

5.3. Influence of surface area on the electrochemical dealloying

According to the discussion in 5.2, the total charge passed during the electrochemical dealloying of the sample at -0.5 V was

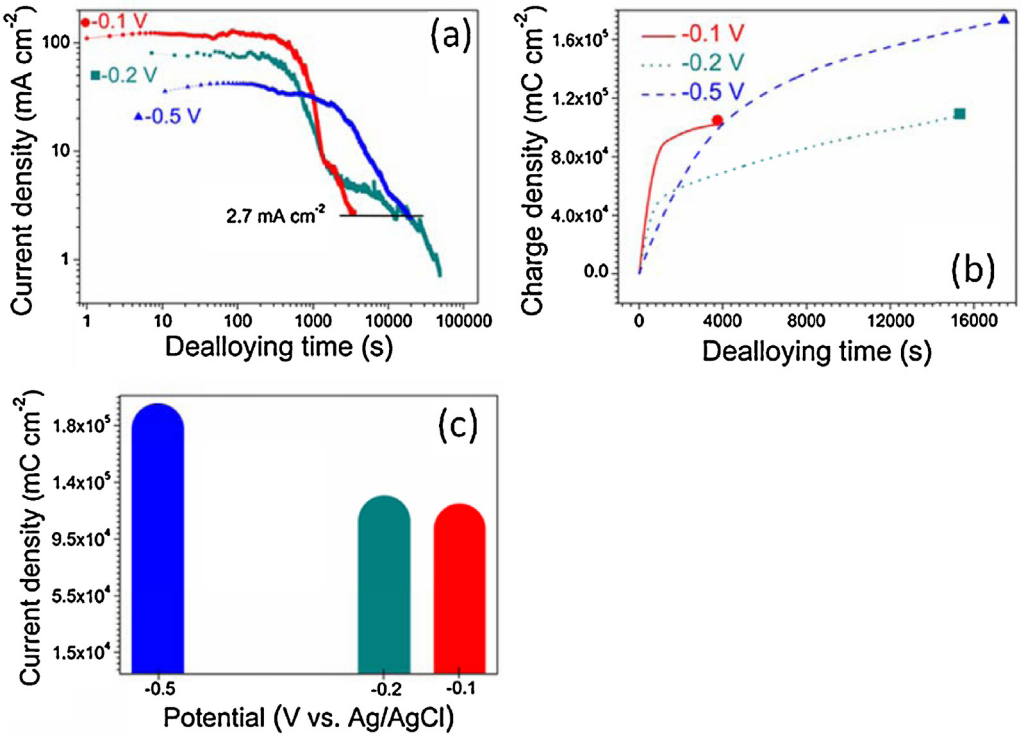

Fig. 7. (a) Current responses of as-annealed $Al_{75}Cu_{25}$ alloy during electrochemical dealloying; (b) charge density *vs.* time curves derived from (a); and (c) charge density values when the current density decreased to 2.7 mA cm^{-2} at each applied potential.

expected to be smaller than that passed during its electrochemical dealloying at -0.1 V or -0.2 V because of the lack of dissolution of Cu at -0.5 V (Eq. (3)). So was the charge density. However, Fig. 7(c) showed that the charge density passed during the electrochemical dealloying at -0.5 V is the largest, compared to a much smaller charge density at either -0.1 V or -0.2 V. This can be explained as follows.

With the formation of nanoporous structure during dealloying, the specific surface area (S_{sp}) of the sample can increase appreciably [49]. In the evaluation of charge density based on the definition of Eq. (1), we used the parameter of geometric area (S_g), which is much smaller than the actual S_{sp}. Consequently, the nominal final charge density calculated from $\frac{Q}{S_g}$ (Q: charge for the dissolution of metallic atoms) can be much smaller than its actual charge density, which should be calculated from $\frac{Q}{S_{sp}}$. As shown in Figs. 3 and 4, the microstructure resulted from dealloying at -0.5 V is finer and more homogeneous than the microstructure obtained from dealloying at either -0.1 V or -0.2 V. This implies that the bimodal nanoporous Cu produced from dealloying at -0.5 V is featured by an S_{sp} that is even larger than the S_{sp} for the bimodal nanoporous Cu produced from dealloying at either -0.1 V or -0.2 V. As a result, the actual charge density for electrochemical dealloying at -0.5 V is the largest (Fig. 7(c)). To our knowledge [10,29,34], there is yet to be any method for in-situ measurements of S_{sp} during an electrochemical corrosion process.

6. Conclusions

- An annealing + electrochemical dealloying approach has been proposed for the creation of bimodal porous Cu materials and the approach has proved to be efficient and flexible in producing hierarchical porous Cu consisting of micro- and nano-sized (50–200 nm) porous structures from an as-cast $Al_{75}Cu_{25}$ precursor alloy.
- The critical roles of annealing the as-cast $Al_{75}Cu_{25}$ precursor alloy in the proposed approach include (i) it decouples the lamellar eutectic structure and substantially increases the α-Al(Cu) phase size; both developments are essential for the production of the desired large porous structure; (ii) it reduces the solubility of Cu in the α-Al(Cu) phase and makes the subsequent dealloying of the α-Al(Cu) phase easier; and (iii) it decreases the E_{crit} value of the as-annealed $Al_{75}Cu_{25}$ precursor alloy and allows flexible selection of the applied potential for electrochemical dealloying, which is important for the creation of a homogenous hierarchical porous structure with fine ligaments (e.g. 52 nm).
- The most homogeneous bimodal porous Cu with the average ligament width of 52 nm was produced by electrochemical dealloying of the annealed $Al_{75}Cu_{25}$ alloy at the applied potential of -0.5 V, which is above the critical potential (E_{crit}) of the α-Al (Cu) but below that of the $CuAl_2$ phase. The complete dealloying of the $CuAl_2$ phase is attributed to the beneficial effect of the dissolution of the Al atoms from the α-Al(Cu) phase, which offers penetration pathways for the electrolyte to interact with the Al atoms in the neighbouring $CuAl_2$ phase and therefore promotes dealloying of the $CuAl_2$ phase even at a low applied potential.

Acknowledgements

T. Song acknowledges the support of the China Scholarship Council (CSC) for a CSC PhD Scholarship and the support of RMIT University for a fee waiver scholarship. Constructive and in-depth comments and suggestions from the reviewers are acknowledged.

References

[1] H.J. Qiu, J.L. Kang, P. Liu, A. Hirata, T. Fujita, M.W. Chen, Fabrication of large-scale nanoporous nickel with a tunable pore size for energy storage, J. Power Sources 247 (2014) 896–905.

[2] J. Kang, A. Hirata, H.J. Qiu, L. Chen, X. Ge, T. Fujita, M. Chen, Self-Grown oxy-hydroxide@ nanoporous metal electrode for high-performance supercapacitors, Adv. Mater. 26 (2014) 269–272.

[3] S. Zhang, Y. Xing, T. Jiang, Z. Du, F. Li, L. He, W. Liu, A three-dimensional tin-coated nanoporous copper for lithium-ion battery anodes, J. Power Sources 196 (2011) 6915–6919.

[4] S. Varghese, S. ElFakhri, D. Sheel, P. Sheel, F. Bolton, H. Foster, Antimicrobial activity of novel nanostructured Cu-SiO_2 coatings prepared by chemical vapour deposition against hospital related pathogens, AMB Express 3 (2013) 1–8.

[5] T. Kou, C. Si, Y. Gao, J. Frenzel, H. Wang, X. Yan, Q. Bai, G. Eggeler, Z. Zhang, Large-scale synthesis and catalytic activity of nanoporous Cu-O system towards CO oxidation, RSC Adv. 4 (2014) 65004–65011.

[6] Z. Dan, F. Qin, T. Wada, G. S.-i. Yamaura, Xie, Y. Sugawara, I. Muto, A. Makino, N. Hara, Nanoporous palladium fabricated from an amorphous $Pd_{42.5}Cu_{30}Ni_{7.5}P_{20}$ precursor and its ethanol electro-oxidation performance, Electrochim. Acta 108 (2013) 512–519.

[7] J. Zeng, F. Zhao, M. Li, C. Li, T. Lee, W. Shih, Morphological control and plasmonic tuning of nanoporous gold disks by surface modifications, J. Mater. Chem. C 3 (2015) 247–252.

[8] S. Dawan, R. Wannapob, P. Kanatharana, W. Limbut, A. Numnuam, S. Samanman, P. Thavarungkul, One-step porous gold fabricated electrode for electrochemical impedance spectroscopy immunosensor detection, Electrochim. Acta 111 (2013) 374–383.

[9] C. Li, Z. Wang, P.-I. Wang, Y. Peles, N. Koratkar, G.P. Peterson, Nanostructured copper interfaces for enhanced boiling, Small 4 (2008) 1084–1088.

[10] C. Zhang, J. Sun, J. Xu, X. Wang, H. Ji, C. Zhao, Z. Zhang, Formation and microstructure of nanoporous silver by dealloying rapidly solidified Zn–Ag alloys, Electrochim. Acta 63 (2012) 302–311.

[11] G.N. Ankah, A. Pareek, S. Cherevko, J. Zegenhagen, F.U. Renner, Hierarchical nanoporous films obtained by surface cracking on Cu-Au and ethanethiol on Au(001), Electrochim. Acta 140 (2014) 352–358.

[12] S. Supansomboon, A. Porkovich, A. Dowd, M.D. Arnold, M.B. Cortie, Effect of precursor stoichiometry on the morphology of nanoporous platinum sponges, ACS Appl. Mater. Interfaces 6 (2014) 9411–9417.

[13] Y. Wang, J. Xu, B. Wu, Electrochemical dealloying of Al_2(Au,X) (X=Pt, Pd, PtPd, Ni, Co and NiCo) alloys in NaCl aqueous solution, Phys, Chem. Chem. Phys. 15 (2013) 5499–5509.

[14] A.A. Vega, R.C. Newman, Nanoporous metals fabricated through electrochemical dealloying of Ag-Au-Pt with systematic variation of Au:Pt ratio, J. Electrochem. Soc. 161 (2014) C1–C10.

[15] X. Luo, R. Li, L. Huang, T. Zhang, Nucleation and growth of nanoporous copper ligaments during electrochemical dealloying of Mg-based metallic glasses, Corros. Sci. 67 (2013) 100–108.

[16] E. Detsi, S. Punzhin, J. Rao, P.R. Onck, J.T.M. De Hosson, Enhanced strain in functional nanoporous gold with a dual microscopic length scale structure, ACS Nano 6 (2012) 3734–3744.

[17] Z. Qi, J. Weissmüller, Hierarchical nested-network nanostructure by dealloying, ACS Nano 7 (2013) 5948–5954.

[18] N. Tsubaki, Y. Zhang, S. Sun, H. Mori, Y. Yoneyama, X. Li, K. Fujimoto, A new method of bimodal support preparation and its application in Fischer-Tropsch synthesis, Catal. Commun. 2 (2001) 311–315.

[19] Z. Zhang, Y. Wang, Z. Qi, J. Lin, X. Bian, Nanoporous gold ribbons with bimodal channel size distributions by chemical dealloying of Al-Au alloys, J. Phys. Chem. C 113 (2009) 1308–1314.

[20] Z. Zhang, Y. Wang, Z. Qi, C. Somsen, X. Wang, C. Zhao, Fabrication and characterization of nanoporous gold composites through chemical dealloying of two phase Al-Au alloys, J. Mater. Chem. 19 (2009) 6042–6050.

[21] Z. Dan, F. Qin, Y. Sugawara, I. Muto, N. Hara, Bimodal nanoporous nickel prepared by dealloying $Ni_{38}Mn_{62}$ alloys, Intermetallics 31 (2012) 157–164.

[22] F.U. Renner, G.N. Ankah, A. Pareek, In-situ surface-sensitive X-ray diffraction study on the influence of iodide over the selective electrochemical etching of Cu_3Au (111), Surf. Sci. 606 (2012) L37–L40.

[23] Y. Ding, J. Erlebacher, Nanoporous metals with controlled multimodal pore size distribution, J. Am. Chem. Soc. 125 (2003) 7772–7773.

[24] W.B. Liu, S.C. Zhang, N. Li, J.W. Zheng, Y.L. Xing, Facile one-pot synthesis of nanoporous copper ribbons with bimodal pore size distributions by chemical dealloying, J. Electrochem. Soc. 158 (2011) D611–D615.

[25] X. Wang, Z. Qi, C. Zhao, W. Wang, Z. Zhang, Influence of alloy composition and dealloying solution on the formation and microstructure of monolithic nanoporous silver through chemical dealloying of Al-Ag alloys, J. Phys. Chem. C 113 (2009) 13139–13150.

[26] E. Seker, J. Gaskins, M.R. Begley, H. Bart-Smith, G. Zangari, R.G. Kelly, M.L. Reed, Relationships between morphology and stress-state of Gold-Silver alloys and nanoporous gold blanket films, ECS Trans. 11 (2008) 43–48.

[27] T.B. Massalski, The Al-Cu (Aluminum-Copper) system, Bull. Alloy Phase Diagr. 1 (1980) 27–33.

[28] W.B. Liu, S.C. Zhang, N. Li, J.W. Zheng, Y.L. Xing, A facile one-pot route to fabricate nanoporous copper with controlled hierarchical pore size distributions through chemical dealloying of Al–Cu alloy in an alkaline solution, Micropor. Mesopor. Mater. 138 (2011) 1–7.

[29] Q. Zhang, Z.H. Zhang, On the electrochemical dealloying of Al-based alloys in a NaCl aqueous solution, Phys. Chem. Chem. Phys. 12 (2010) 1453–1472.

[30] S. Chattopadhyay, C.M. Sellars, Kinetics of pearlite spheroidisation during static annealing and during hot deformation, Acta Metall. 30 (1982) 157–170.

[31] J. Erlebacher, M.J. Aziz, A. Karma, N. Dimitrov, K. Sieradzki, Evolution of nanoporosity in dealloying, Nature 410 (2001) 450–453.

[32] K. Sieradzki, N. Dimitrov, D. Movrin, C. McCall, N. Vasiljevic, J. Erlebacher, The dealloying critical potential, J. Electrochem. Soc. 149 (2002) B370–B377.

[33] J. Snyder, K. Livi, J. Erlebacher, Dealloying Silver/Gold alloys in neutral silver nitrate solution: Porosity evolution, surface composition, and surface oxides, J. Electrochem. Soc. 155 (2008) C464–C473.

[34] Q. Zhang, X. Wang, Z. Qi, Y. Wang, Z. Zhang, A benign route to fabricate nanoporous gold through electrochemical dealloying of Al-Au alloys in a neutral solution, Electrochim. Acta 54 (2009) 6190–6198.

[35] A.M. Alfantazi, T.M. Ahmed, D. Tromans, Corrosion behavior of copper alloys in chloride media, Mater. Des. 30 (2009) 2425–2430.

[36] A. Dursun, D.V. Pugh, S.G. Corcoran, A steady-state method for determining the dealloying critical potential, Electrochem. Solid-State Lett. 6 (2003) B32–B34.

[37] F.C. Strong, Faraday's laws in one equation, J. Chem. Educ. 38 (1961) 98.

[38] S. Mader, S. Herd, Formation of second phase particles in aluminum-copper alloy films, Thin Solid Films 10 (1972) 377–389.

[39] E. Detsi, M. van de Schootbrugge, S. Punzhin, P.R. Onck, J.T.M. De Hosson, On tuning the morphology of nanoporous gold, Scripta Mater. 64 (2011) 319–322.

[40] S. Parida, D. Kramer, C.A. Volkert, H. Rösner, J. Erlebacher, J. Weissmüller, Volume change during the formation of nanoporous Gold by dealloying, Phys. Rev. Lett. 97 (2006) 0355041–0355044.

[41] A.L. Bacarella, J.C. Griess, The anodic dissolution of Copper in flowing sodium chloride solutions between 25° and 175 °C, J Electrochem. Soc. 120 (1973) 459–465.

[42] Z. Zhang, Y. Wang, Z. Qi, W. Zhang, J. Qin, J. Frenzel, Generalized fabrication of nanoporous metals (Au, Pd, Pt, Ag, and Cu) through chemical dealloying, J. Phys. Chem. C 113 (2009) 12629–12636.

[43] J. Jayaraj, B.J. Park, D.H. Kim, W.T. Kim, E. Fleury, Nanometer-sized porous Ti-based metallic glass, Scripta Mater. 55 (2006) 1063–1066.

[44] A. Gebert, A.A. Kündig, L. Schultz, K. Hono, Selective electrochemical dissolution in two-phase La–Zr–Al–Cu–Ni metallic glass, Scripta Mater. 51 (2004) 961–965.

[45] W.B. Liu, S.C. Zhang, N. Li, J.W. Zheng, S.S. An, Y.L. Xing, A general dealloying strategy to nanoporous intermetallics, nanoporous metals with bimodal, and unimodal pore size distributions, Corros. Sci. 58 (2012) 133–138.

[46] T. Hagyard, J.R. Williams, Potential of aluminium in aqueous chloride solutions. Part 1, Trans. Faraday Soc. 57 (1961) 2288–2294.

[47] Z. Szklarska-Smialowska, Pitting corrosion of aluminum, Corros. Sci. 41 (1999) 1743–1767.

[48] T. Song, Y. Gao, Z. Zhang, Q. Zhai, Dealloying behavior of rapidly solidified Al-Ag alloys to prepare nanoporous Ag in inorganic and organic acidic media, CrystEngComm 13 (2011) 7058–7067.

[49] G. Pia, M. Mascia, F. Delogu, Kinetics of nanoporous Au formation by chemical dealloying, Scripta Mater. 76 (2014) 57–60.

Chapter 6 Synchrotron-based understanding of the dealloying of Al-Cu and Al-Cu-Sn alloys

Given the potential commercial importance of nanoporous Cu-based materials, it is necessary to understand the dealloying mechanisms of Al-Cu and Al-Cu-Sn alloys in terms of the phase transformation and/or crystal structure evolution involved. Relevant details have been absent in the context of dealloying because of the inadequate resolution of conventional X-ray diffraction (XRD) and the very similar powder diffraction peaks of the various phases involved in Al-Cu and Cu-Sn system (Section **2.4.2 Current understanding**).

This chapter employs high-resolution synchrotron XRD to analyse the detailed dealloying process of the selected Al-Cu and Al-Cu-Sn system investigated in this thesis. The purpose is to enhance the understanding of the dealloying behaviour based on the understanding derived from the dealloying of Ag-Au solid solution alloys (Section **2.4 Dealloying mechanisms**).

6.1 Towards a complete understanding of dealloying of Al-Cu by in-situ and ex-situ synchrotron X-ray diffraction

(Paper 5)

Tingting Song, Ming Yan, Nathan A.S. Webster, Mark J. Styles, Justin A. Kimpton, Ma Qian

(Ready for submission)

Towards a complete understanding of dealloying of Al-Cu by in-situ and ex-situ synchrotron X-ray diffraction

T. Song[1], M. Yan[2], N.A.S. Webster[3], M.J. Styles[4], J.A. Kimpton[5], M. Qian[1,*]

Nanoporous copper (Cu) structures have important potential applications. Dealloying of inexpensive dual-phase Al-Cu alloys offers a simple and flexible approach to the fabrication of affordable nanoporous Cu structures in various product forms. However, the pathways to the dealloying of these alloys and the mechanisms behind each dealloying pathway remain unclear. This hinders the design and fabrication of novel high-performance nanoporous Cu structures. Here we demonstrate, through quantitative in-situ and ex-situ high-resolution synchrotron X-ray diffraction studies, that, the dealloying of dual-phase (Al_2Cu and AlCu) Al-Cu alloys occurs in sequence from Al_2Cu to AlCu, which collectively results in a hierarchical nanoporous Cu structure. In addition, we show that the formation of the Cu phase undergoes an incubation stage and a subsequent two-stage kinetic process governed by different mechanisms. These findings provide a fundamental basis for the design and fabrication of novel nanoporous Cu or Cu-AlCu composite structures for various applications.

Dealloying is the selective dissolution process of the less noble element/component out of an alloy, producing a nanoporous structure of the nobler element/component[1, 2, 3]. The process has received significant attention over the last 15 years as a novel approach to the fabrication of nanoporous metals. To date, a large number of precursor alloys, including Ag-Au[2, 4, 5, 6], Co-Pt[7], Cu-Au[8, 9, 10], Al-X (X=Au, Pd, Pt, Ag, and Cu)[11], Mg-Cu[12], Mn-Cu[13], Zn-X (X =

[1] RMIT University, School of Engineering, Centre for Additive Manufacturing, Melbourne, VIC 3000, Australia.
[2] South University of Science and Technology of China, Department of Materials Science and Engineering, Shenzhen, Guangdong 518055, China.
[3] CSIRO Mineral Resources, Private Bag 10, Clayton South, VIC 3169, Australia.
[4] CSIRO Manufacturing, Private Bag 10, Clayton South, VIC 3169, Australia.
[5] Australian Synchrotron, 800 Blackburn Road, Clayton, VIC 3168, Australia.
Correspondence and requests for materials should be addressed to M.Q. (email: ma.qian@rmit.edu.au).

Cu[14, 15], Ag[16]), and Al-Cu-Sn[17] have been dealloyed to produce nanoporous copper[11, 12, 13, 14, 15], silver[11, 16], gold[2, 4, 5, 6, 8, 9, 10], platinum[7, 11], palladium[11] or alloys[17]. Owing to its notable technological importance, nanoporous Cu with its enormous specific surface area remains to be one of the most important nanoporous metals produced by dealloying and holds promise for a wide variety of important applications. For instance, they can be used as in industrial applications that deal with efficient heat conduction, mass transformation and easy accommodation of volumetric expansion. For instance, silicon particles (~4 μm) deposited and sealed on a nanoporous Cu current collector in lithium ion batteries (LIBs) showed better cyclic performance and higher charge capacity than using a solid Cu foil current collector[18].

Nanoporous Cu can be dealloyed from single-phase solid solution Mn-Cu[13] alloys, the single-phase intermetallic Al_2Cu alloy[19, 20] and dual-phase X-Cu (X = Al[11,19, 20], Mg[12], Zn[14, 15]) alloys. In general, dealloying of single-phase solid solution alloys can be regarded as a simple dissolution and diffusion process[21] where there is no change in lattice structure before and after dealloying and the lattice parameters are often similar[22]. However, dealloying of dual-phase X-Cu (X = Al, Mg, Zn) alloys and the single-phase intermetallic Al_2Cu alloy deal with crystal structural changes. Of these precursor alloys, dual-phase precursor alloys are most attractive for the following reasons: (1) Dealloying of such a dual-phase precursor alloy offers the possibility for the creation of a porous material with two- length scale hierarchy, especially when the two phases show different dealloying behaviors. Song et al.[23] fabricated hierarchical porous Cu consisting of micro- and nano-sized (50-200 nm) porous structures from dual-phase Al75Cu25 precursor alloy consisting of α-Al(Cu) and Al_2Cu. Zhang et al. developed nanoporous gold with bimodal channels (large-size: 25-50 nm; small-size: 10-25 nm) by dealloying of dual-phase Al60Au40 consisting of AlAu and Al_2Au. (2) Dealloying of such dual-phase precursor alloy provides with the possibility for the creation of nanoporous-

bulk composites. Wang et al.[24] developed nanoporous Ag-bulk $AlAg_2$ from dealloying of Al-Ag alloys consisting of α-Al(Ag) and $AlAg_2$. As a result, dealloying of dual-phase precursor alloys advances the designable dealloying approach offering more advanced functional materials.

However, the identification and understanding of the dealloying pathways and kinetics of such dual-phase alloys remain unclear. Zhang et al.[12, 25] studied the dealloying process of dual-phase Al-Cu and Mg-Cu alloys and suggested that dealloying of the AlCu phase occurred before the dealloying of Al_2Cu based on indirect evidence obtained from electrochemical measurements (e.g. cyclic voltammetry, potentiostat polarization)[25]. In contrast, Liu et al.[26] reported synergetic dealloying of Al_2Cu and AlCu in a 5 wt.% HCl solution based on laboratory X-ray diffraction (XRD) studies and attributed the reasons to the similar electrochemical potentials of Al_2Cu (-374.59 mV) and AlCu (-345.90 mV) in HCl solutions. However, it should be pointed out that Al_2Cu, AlCu and Cu have overlapping laboratory XRD peaks (see ~20° 2θ in Fig. 1a) and characterisation of the dealloying process of dual-phase Al-Cu alloys based on laboratory XRD data can be problematic. To address that challenge for the clarification of dealloying pathways, high-resolution synchrotron XRD[27, 28] is a powerful tool.

In addition, understanding the kinetic process that dictates the rate of dealloying is also essential to control the dealloying process in terms of both pattern formation and ligament coarsening[29, 30, 31]. Few studies have investigated the fundamental aspects of the kinetics especially for dealloying of precursor alloys consisting of intermetallics, mainly due to the lack of appropriate characterization techniques. In-situ synchrotron XRD is a powerful tool in this regard as well. It monitors abundant time-resolved reaction information to allow a

statistical investigation into the kinetic process. Renner et al.[8, 9, 10] have reported in-situ synchrotron surface-sensitive XRD studies providing crucial information on the initial stages of the dealloying of Cu-Au but did not address the phase formation kinetics among the long-term dealloying. We employ both in-situ and ex-situ synchrotron XRD in this study to clarify the dealloying mechanisms and phase transformation kinetics.

In this study, we aim to clarify the dealloying mechanisms of dual-phase Al65Cu35 and Al55Cu45 precursor alloys which consist of Al_2Cu and AlCu[32] through quantitative in-situ and ex-situ synchrotron XRD experiments. The two alloys selected are easy to cast and their high Cu content (55 wt.% and 66 wt.%) can ensure the production of bulk nanoporous Cu structures with expected good mechanical integrity for practical applications. We conclude from the quantitative in-situ and ex-situ synchrotron XRD results that the dealloying of Al_2Cu and AlCu phases in each alloy occurs in a clear sequence and the sequential dealloying process eventually results in a hierarchical nanoporous Cu structure. We argue for that the crystal structure transition is an integral part of the sequential dealloying process. We further propose that the identification of the sequential dealloying process offers a new approach to the design of hierarchical nanoporous Cu structures or Cu-AlCu composite structures. In addition, based on the in-situ dataset, we present evidence to reveal an incubation + two-stage formation kinetic for the development of Cu phase by dealloying. These quantitative in-situ and ex-situ synchrotron XRD results provide new insights into dealloying of dual-phase alloys for either design of novel precursor alloys or control of the dealloying process. In addition, it enriches the current knowledge base of the pathways of dealloying from dealloying of single solid solution precursor alloys.

Results

Creation of hierarchical nanoporous Cu. Fig. 1a shows the laboratory XRD pattern of the as-cast Al65Cu35 alloy consisting of Al_2Cu and AlCu phases. The corresponding microstructure confirmed the dual-phase Al_2Cu-AlCu intermetallic structure (Fig. 1b). After dealloying in a 10 vol.% HCl solution at 70 ± 2 °C for 120 min, most of the diffraction peaks for Al_2Cu and AlCu disappeared with the predominant phase becoming the Cu phase (Fig. 1a). A hierarchical nanoporous microstructure, shown in Fig. 1c, resulted from the dealloying process. The hierarchical nanoporous structure is characterized by two types of ligaments, those dealloyed from the AlCu phase, which is 116 ± 20 nm wide (Fig. 1c), and those dealloyed from the Al_2Cu phase, which is 50 ± 7 nm wide (Fig. 1d).

Sequential dealloying of Al_2Cu and AlCu. We employed synchrotron XRD to investigate the in-situ phase evolution during the creation of hierarchical nanoporous Cu from dealloying of the Al65Cu35 alloy consisting of Al_2Cu and AlCu phases in the dilute HCl solution. The experimental set-up is shown in Fig. 2a. The mounted as-cast Al65Cu35 plate sample was placed in the cavity located on the top of the cell body and the diffraction data was collected while the preheated HCl solution was recirculated through the cell. As the as-cast plate sample has preferred grain orientation and large grain size effects, only a few diffraction peaks with high intensity can be observed[21]. We rocked the sample stage ± 2° about its axis during the in-situ measurement to increase the number of illuminated grains to improve the data quality. The detailed experimental procedure can be found as Supplementary Methods 1 and Supplementary Movie 1. Synchrotron XRD dataset, obtained in situ as a function of dealloying time, of the as-cast Al65Cu35 alloy, is shown in Fig. 2b. Rocking the sample stage caused fluctuations in intensity of, for example, the Al_2Cu peak at ~10°2θ, observed in Fig. 2b. As in-situ dealloying proceeded, the intensity of some synchrotron XRD peaks for the

Al_2Cu phase decreased (the Al_2Cu (112) and (312) peaks were indicated by arrows) and one diffraction peak for Cu emerged after ~14 min of dealloying, while the diffraction peaks for AlCu showed only minor variations among the in-situ dealloying measurements. Our in-situ data provided solid experimental data that there is no concurrent formation of synchrotron detectable Cu phase when the dissolution of Al occurred. We described the dealloying period before the emergence of the first Cu diffraction peak as incubation stage and the dealloying time for the first detection of Cu as incubation time (t_0). In addition, among the in-situ dealloying process, no intermediate phase was detected. As plate sample for in-situ experiments is not an ideal powder sample for powder diffraction, the in-situ data might be not of sufficient quality for quantitative analysis. This in-situ synchrotron XRD dataset suggests that dealloying of the Al_2Cu and AlCu phases appears to have occurred in sequence.

To quantitatively clarify the dealloying behavior of Al_2Cu and AlCu, Al65Cu35 powder samples, before and after different durations of dealloying in HCl solutions, were loaded into capillaries (0.3 mm in diameter) for ex-situ synchrotron XRD measurements. Fig. 3a shows the synchrotron XRD results (18°-23.5°, X-ray wavelength = 0.6891 Å) obtained from each sample. The intensity of all four synchrotron XRD peaks for the Al_2Cu phase decreased as dealloying went on and diffraction peak for Cu emerged after 20 min. In contrast, the intensity of the diffraction peaks for the AlCu phase remained almost unchanged. Using the Rietveld method[33] (see Fig. 3b, Supplementary Figs. 1-3a), the phase concentration at different stages of the dealloying process was estimated. However, it should be pointed out that an unidentified phase was detected in analyzing the ex-situ synchrotron data (Fig. 3c). As no intermediate phase was detected from the in-situ measurements, this unidentified phase could be introduced during the powder sample preparation. The existence of unidentified

peaks might affect the final fitting and increase the weight percentage R (R_{wp}) value. Such phenomenon occurred in previous studies including Ref.[34].

The Cu content, as a proportion of the total Cu available, in each of the Al_2Cu, AlCu, and the newly formed Cu phase were determined as a function of dealloying time using the quantitative information obtained from the Rietveld analysis of the ex-situ synchrotron XRD data (Table 1). The results are plotted in Fig. 3d. After 40 minutes of dealloying, the content of Cu in the Al_2Cu phase declined, accompanied by an increase in the newly formed Cu phase, while the Cu content in the AlCu phase showed only small fluctuations with no clear trend, consistent with in-situ synchrotron XRD data.

The SEM and EDX results of the Al65Cu35 powder sample after 40 minutes of dealloying are shown in Fig. 3e and f. Compared to the microstructure of the precursor alloy (Fig. 1a), the Al_2Cu phase has been dealloyed into a nanoporous microstructure while the AlCu phase only exhibited some surface roughening. No Al was detected in the dealloyed Al_2Cu phase by the EDX analysis, indicative of complete dealloying of this region after 40 min. By comparison, the atomic ratio of Cu : Al in the AlCu phase after 40 minutes of dealloying was found to be 56 : 44, close to its original 1 : 1 ratio prior to dealloying. It is clear that dealloying of Al_2Cu and AlCu in the as-cast Al65Cu35 alloy occurred in distinct sequence and that the hierarchical nanoporous Cu structure, shown in Fig. 1c, is a result of this sequential dealloying behavior.

To further demonstrate the sequential dealloying process of Al_2Cu and AlCu identified during dealloying of Al65Cu35, the dealloying of another Al_2Cu-AlCu dual-phase Al-Cu alloy, Al55Cu45, which contains more AlCu than Al65Cu35 alloy[32], was studied using both in-situ

and ex-situ synchrotron XRD. Fig. 4a shows the in-situ synchrotron XRD results of the as-cast Al55Cu45 plate sample while the ex-situ synchrotron dealloying results are shown in Fig. 4b, obtained from ex-situ dealloying measurements of Al55Cu45 powder samples from 10 min to 60 min. Fig. 4c shows the changes of the Cu content in each of the Al_2Cu, AlCu phases and the newly formed Cu phase obtained from the ex-situ synchrotron XRD (see Supplementary Figs. 4-8a and Table 2). The observations are all similar to those shown in Fig. 3. The major difference noticed was the incubation time for the emergence of the four diffraction peaks for Cu (960 s) compared to 840s for the dealloying of the Al65Cu35 alloy.

Discussion

The in-situ and ex-situ synchrotron XRD studies, presented above, identified the sequential dealloying mode of Al_2Cu and AlCu phases in dual-phase Al65Cu35 and Al55Cu45 alloys. This was not expected as the electrochemical activities or corrosion potential values of Al_2Cu (-374.59 mV) and AlCu (-345.90 mV) are similar in the HCl solutions[26]. Hence, in principle, dealloying of these two phases in as-cast Al65Cu35 and Al55Cu45 alloys is expected to occur simultaneously, rather than in a sequence. In this regard, we propose that the crystal structure including the interatomic bonding has played a more decisive role in dictating the selective dissolution of Al from Al_2Cu and AlCu. Al_2Cu has a tetragonal (I4/mcm) structure (see Fig. 5) in which 6 Al atoms and 4 Cu atoms surround each Al atom[32] while AlCu has a monoclinic (C2/m) structure in which 6 Al atoms and 8 Cu atoms surround each Al atom[32]. Complete dealloying of AlCu thus needs to break up four extra Al-Cu binding pairs compared to that of Al_2Cu. The binding energy of the Al-Cu pair (-2.2 eV) is nearly 1.6 times of the Al-Al pair (-1.4 eV)[35]. In other words, it is much more difficult to dealloy Al from an Al-Cu binding pair than from an Al-Al binding pair or the former is the controlling process to completely dealloy Al_xCu_y intermetallic compound. Another potentially important

reason can be attributed to the transition of crystal structure at the end of dealloying. By the time when most Al atoms are removed or dealloyed from each Al_xCu_y phase, it is reasonable to expect that the residual Cu atoms may instantly inherit the crystal structure of their parent phase. For Al_2Cu, it is tetragonal while for AlCu it is monoclinic (see Fig. 5). The subsequent transition from a tetragonal lattice to an fcc lattice (Cu) requires only limited shrinkage of the tetragonal lattice. However, the transition from a monoclinic lattice to an fcc lattice requires not only shrinkage of the lattice but also a significant distortion of the lattice as illustrated in Fig. 5. The sequential dealloying of Al_2Cu and AlCu phases can be ascribed to these two fundamental differences. Unlike a solid solution phase, intermetallic phases typically show different crystalline facets[36]. Similar to sequential dealloying, the surface roughening observed during the early stages of dealloying of the AlCu phase (Fig. 3e) can be regarded as another type of sequential dealloying where different crystalline facets of the same intermetallic phase display different dissolution rates, like the AlCu (111) peak marked in Fig. 4a (in-situ synchrotron XRD data). Similar anisotropic dissolution behavior has been reported in other systems including Fe-Cr[37] and Au[38].

The solubility of Al in Cu is up to 19.4 at.%[32]. During dealloying, intermediate α-Cu(Al) phases are thus expected to form. However, this potential development has been overlooked in previous studies due in part to the lack of perception of this development and in part to the insufficient resolution of laboratory XRD. In this research, the refined lattice parameter (*a*) values for the newly formed Cu phase were determined to be in the range of 3.617 Å (30min-dealloyed sample) to 3.621 Å (10min-dealloyed sample) based on the ex-situ synchrotron XRD data (see Tables 1-2). This confirms that α-Cu(Al) has clearly formed during the dealloying process and its Al content decreased from 2.0 at.%Al to 0.74 at.%Al with increasing dealloying time from 10 min to 30 min. This also gives a general indication of the

rate of dealloying Al from α-Cu(Al). The clarification of the formation of α-Cu(Al) is important to ensure proper use of the as-dealloyed nanoporous Cu as current collectors because the presence of Al in Cu can cause severe safety issues[39]. In that regard, it is necessary to realize complete dealloying of Al from α-Cu(Al). As the Al content decreases, the dealloying rate is expected to decrease because Al enhances the intrinsic self-diffusion of Cu[40], which can expose Al atoms to the HCl solution to facilitate the dealloying process. Complete dealloying can thus be sluggish.

The formation of crystalline Cu showed an incubation period of ~960 seconds during the in-situ dealloying of each Al-Cu alloy. We employed the atomic-scale observation of the initial stages of dealloying of Cu_3Au[8, 9, 10, 41] to illustrate the incubation stage here. Among the incubation period, the dissolution of Al atoms commenced with the concurrent two-dimensional (2D) process of enrichment and clustering of Cu atoms. And such process occurred within an ultrathin layer (several monolayers) on the surface of the sample so that no Cu phase was synchrotron detectable. After the incubation stage, we calculated the area of the Cu(111) peak in the in-situ synchrotron XRD spectrum and plotted it as a function of dealloying time for both Al65Cu35 (Fig. 6a) and Al55Cu45 (Fig. 6b). The fluctuations originated from the operations of rocking the sample stage ± 2° around its axis during in-situ synchrotron XRD experiments. In both cases, the increase in the area of the Cu(111) peak showed two different stages, suggesting two potentially different kinetic processes. To gain new insight into each potential process, the data in Fig. 6a and b were fitted to the Avrami-Erofe'ev equation[42]:

$$\alpha = 1 - exp[-(k(t - t_0)^n)] \quad (1)$$

or

$$ln(-\ln(1 - \alpha)) = nln(t - t_0) + k \quad (2)$$

where α is the amount of material transformed, t is the reaction time, t_0 is the incubation time, k is the rate constant, and n is a parameter that describes how the transformation propagates through the material[42]. Fig. 6c,d shows the plots of $ln(-\ln(1-\alpha))$ versus $ln(t-t_0)$ for dealloying of Al65Cu35 and Al55Cu45. Two distinctly different stages of dealloying were revealed for each alloy and the corresponding values of n were obtained from the lines of best fit, which resulted in 0.38 and 1.13 for dealloying of Al65Cu35 (see Fig. 6c) and 0.36 and 1.96 for dealloying of Al55Cu45 (see Fig. 6d). It has been proposed that a process characterised by $n < 1$ proceeds by a diffusion-controlled mechanism while a process with $1 < n < 2$ is dictated by a nucleation-and-growth-controlled mechanism[54]. These mechanims can reasonally explain the formation of Cu from dealloying process of each alloy, where the first satge, featured by $n < 1$ (n = 0.36 or 0.38), referes to the transformation from ultrathin Cu enrichment or clusters in the incubation stage to thicker Cu islands with nanoporous structure by diffusion, and the second stage, featured by $1 < n < 2$ (n = 1.13 or 1.96), occurs via nucleation of nanoporous Cu on thicker Cu islands, followed by growth.

Diffusion of the nobler element in the alloy plays a decisive role in the creation of the final nanoporous structure by dealloying[2, 29, 43, 44], including crystalline defects. For instance, diffusion-induced twinning due to diffusion of the nobler atoms[45, 46] has been reported previously during dealloying of Al-Cu[23, 47] and Au-Ag[30, 48]. The twinning defects can contribute to the overall stability of the structure and have exhibited favorable effects either in mechanical properties[45] or in catalytic performances[48]. In this research, we have found that the Cu ligaments are full of diffusion-induced twins in the as-dealloyed state. Fig. 7a, b shows one such example. Fine crystallite size, lattice deformations (inhomogeneous strain) and planar lattice defects can broaden diffraction peaks while twin faults can significantly contribute to the X-ray line broadening of certain peaks more than others[49]. In applying the

Rietveld refinement analysis to the synchrotron XRD data, we found that the analysis resulted in no good fitting unless we took into account the anisotropic broadening issue of the Cu (002) diffraction peak (see Fig. 7c, Supplementary Figs. 3b, 6-8c). This indicates that the existence of massive twins in the Cu ligaments caused by the diffusion of Cu has contributed to the anisotropic broadening phenomena observed.

To conclude, using in-situ and ex-situ synchrotron X-ray diffraction experiments in conjunction with the Rietveld refinement analysis, we have identified the sequential dealloying behavior of Al_2Cu and AlCu phases in HCl solutions. These two intermetallic phases have overlapping diffraction peaks beyond the resolution of laboratory XRD measurements and similar corrosion potential values in HCl solutions. We proposed that the difference in the proportion of the Al-Cu bonding in the Al_2Cu and AlCu phases, which has much higher binding energy than the Al-Al bonding, and the difference in the potential transition of each crystal structure to fcc Cu, played a decisive role rather than the corrosion potential of each phase. The sequential dealloying process resulted in the formation of hierarchical nanoporous Cu structures. In addition, we demonstrated the incubation + two-stage formation process for the development of Cu phase from dealloying of Al-Cu by analyzing the in-situ synchrotron X-ray diffraction data. The formation of synchrotron detectable Cu phase did not concur with the dissolution of Al but emerged after an incubation stage. And the Cu phase from dealloying of Al-Cu was developed firstly diffusion-controlled and then nucleation-growth controlled, both revealing the fundamental role of the diffusion of Cu atoms. The identification of the sequential dealloying in conjunction with the phase formation kinetics from the new experimental findings extends the perspective on dealloying of Al-Cu alloys and opens up a new avenue to the creation of a wide variety of nanoporous

Cu or Cu-AlCu composite structures via the design of the precursor alloys and control of each dealloying step.

Methods

Sample preparation. Ingot samples of Al65Cu35 and Al55Cu45 (at.%) alloys were prepared by arc melting of 99.99 wt.% Al and 99.99 wt.% Cu in a Ti-gettered argon atmosphere. Each ingot (~30 grams) was remelted four times to ensure homogeneity. Samples with approximate dimensions of 10 mm × 10 mm×3 mm were cut from the ingot, ground and polished to about 1 mm thick disks. Dealloying of the disk samples was carried out at 70 ± 2 °C in a 200 ml of 10 vol.% HCl aqueous solution on a hot plate and the temperature was monitored using a mercurial thermometer. The dealloyed sample was removed from the acid solution, rinsed in distilled water and dehydrated with alcohol.

Laboratory characterization. The phase constitution of each sample before and after dealloying was characterized using laboratory X-ray diffraction (XRD, CPS120 by INEL, with a position-sensitive detector covering 120° in 2θ, Mo Kα radiation, with a collection time of 60 s). The microstructures were examined using scanning electron microscopy (SEM) (FEI Nova NanoSEM, operated at 15 keV equipped with energy dispersive X-ray spectroscopy (EDX) made by Oxford Instrument) and transmission electron microscopy (TEM, JEOL 2100, operated at 200 kV). To evaluate the Cu ligament size in as-dealloyed Al_2Cu and AlCu, a total of 100 Cu ligaments were analyzed from SEM images taken from each dealloyed sample using Image-Pro Plus software.

Synchrotron X-ray diffraction measurements. The in-situ synchrotron X-ray diffraction (SXRD) measurements were performed using the powder diffraction beamline at the

wavelength of 0.7745 Å at the Australian Synchrotron. Samples cut from the ingot were mounted, ground and polished to 4.9-5.0 mm thick disks, which were then placed in the cavity located on the top of the cell in the synchrotron. A detailed description of the cell can be found from Ref.[50]. XRD data were collected continuously throughout each dealloying experiment with individual data sets collected at every 1 min at each of the two detector positions P1 and P2 (the Mythen-II microstrip detector[51] contains 0.2° gaps every 5° 2θ; data were collected at two detector positions 0.5° apart in order to cover the entire 2θ range). The data were collected in asymmetric diffraction geometry with cell rocking. The experimental set-up is shown in Fig. 2a and the detailed in-situ SXRD experimental procedure can be found from Supplementary Methods 1 and Supplementary Movie 1.

The ex-situ SXRD measurements were performed using the same beamline at the wavelength of 0.6891 Å at Australian Synchrotron. Powder samples (< 74 μm) of each alloy were crushed from the ingot and dealloyed at 90 ± 2 °C in the 5 wt.% HCl solution for different durations. The powder samples were loaded into borosilicate capillaries (0.3 mm in diameter) for characterization by SXRD both before and after each dealloying experiment. SXRD data were collected from each sample in Debye-Scherrer geometry using the Mythen-II microstrip detector[51] in the 2θ range of 4-84°. Individual data sets were collected for 5 min at each of the two detector positions P1 and P2.

For visualization of the phase evolution process during dealloying, individual data sets collected from the P1 and P2 detector positions were merged using PDVIPER software (Powder Diffraction Beamline, Australian Synchrotron) to remove the detector gaps. The merged data sets were used for the Rietveld refinement analysis[33]. The Rietveld refinement was performed using TOPAS-Academic (Version 5)[52].

References

1. Pickering, H.W. & Wagner, C. Electrolytic dissolution of binary alloys containing a noble metal. *J. Electrochem. Soc.* **114**, 698-706 (1967).
2. Erlebacher, J., Aziz, M.J., Karma A., Dimitrov N. & Sieradzki K. Evolution of nanoporosity in dealloying. *Nature* **410**, 450-453 (2001).
3. Geslin, P.A., McCue, I., Gaskey, B., Erlebacher, J. & Karma, A. Topology-generating interfacial pattern formation during liquid metal dealloying. *Nat. Commun.* **6:** 8887, (2015).
4. Xue, Y., Markmann, J., Duan, H., Weissmüller, J. & Huber, P. Switchable imbibition in nanoporous gold. *Nat Commun* **5:** 4237, (2014).
5. Zeng, J., Zhao, F., Li, M., Li, C.H., Lee, T.R., Shih, W.C. Morphological control and plasmonic tuning of nanoporous gold disks by surface modifications. *J. Mater. Chem. C* **3**, 247-252 (2015).
6. Ankah, G.N., Pareek, A., Cherevko, S., Zegenhagen, J., Renner, F.U. Hierarchical nanoporous films obtained by surface cracking on Cu-Au and ethanethiol on Au(001). *Electrochim. Acta* **85**, 384-392 (2012).
7. Liu, L., Pippel E., Scholz, R. & Gösele, U. Nanoporous Pt−Co alloy nanowires: Fabrication, characterization, and electrocatalytic properties. *Nano Lett.* **9**, 4352-4358 (2009).
8. Renner, F.U., *et al.* Star-Shaped crystallographic cracking of localized nanoporous defects. *Adv. Mater.* **27**, 4877-4882 (2015).
9. Pareek, A., *et al.* Initiation and inhibition of dealloying of single crystalline Cu_3Au (111) surfaces. *J. Am. Chem.l Soc.* **133**, 18264-18271 (2011).
10. Renner, F.U., Stierle, A., Dosch, H., Kolb, D.M., Lee, T.L. & Zegenhagen, J. Initial corrosion observed on the atomic scale. *Nature* **439**, 707-710 (2006).

11. Zhang, Z., Wang, Y., Qi, Z., Zhang, W., Qin, J. & Frenzel, J. Generalized fabrication of nanoporous metals (Au, Pd, Pt, Ag, and Cu) through chemical dealloying. *J. Phys. Chem. C* **113**, 12629-12636 (2009).

12. Zhao, C., Wang, X., Qi, Z., Ji, H. & Zhang, Z. On the electrochemical dealloying of Mg–Cu alloys in a NaCl aqueous solution. *Corros. Sci.* **52**, 3962-3972 (2010).

13. Chen, L.Y., Fujita, T., Ding, Y. & Chen, M.W. A three-dimensional gold-decorated nanoporous copper core–shell composite for electrocatalysis and nonenzymatic biosensing. *Adv. Funct. Mater.* **20**, 2279-2285 (2010).

14. Cheng, I.C. & Hodge, A.M. Strength scale behavior of nanoporous Ag, Pd and Cu foams. *Scr. Mater.* **69**, 295-298 (2013).

15. Zhang, S.J., Zheng, Y.X., Yuan, L.S. & Zhao, L.H. Ni–B amorphous alloy nanoparticles modified nanoporous Cu toward ethanol oxidation in alkaline medium. *J. Power Sources* **247**, 428-436 (2014).

16. Zhang, C., *et al.* Formation and microstructure of nanoporous silver by dealloying rapidly solidified Zn–Ag alloys. *Electrochim. Acta* **63**, 302-311 (2012).

17. Song, T., Yan, M., Gao, Y., Atrens, A., Qian, M. Concurrence of de-alloying and re-alloying in a ternary Al67Cu18Sn15 alloy and the fabrication of 3D nanoporous Cu-Sn composite structures. *RSC Adv.* **5**, 9574-9580 (2015).

18. Zhao, C., Li, S., Luo, X., Li, B., Pan, W. & Wu, H. Integration of Si in a metal foam current collector for stable electrochemical cycling in Li-ion batteries. *J. Mater. Chem. A* **3**, 10114-10118 (2015).

19. Qi, Z., *et al.* Formation and characterization of monolithic nanoporous copper by chemical dealloying of Al−Cu alloys. *J. Phys. Chem. C* **113**, 6694-6698 (2009).

20. Liu, W.B., Zhang, S.C., Li, N., Zheng, J.W., Xing, Y.L.. Influence of phase constituent and proportion in initial Al–Cu alloys on formation of monolithic

nanoporous copper through chemical dealloying in an alkaline solution. *Corros. Sci.* **53**, 809-814 (2011).

21. Petegem, S.V., *et al.* On the microstructure of nanoporous gold: An X-ray diffraction study. *Nano Lett.* **9**, 1158-1163 (2009).

22. Elliott, R. & Shunk, F. The Ag−Au (silver-gold) system. *Bull. Alloy Phase Diagr.* **1**, 45-47 (1980).

23. Song, T., Yan, M., Shi, Z., Atrens, A. & Qian, M. Creation of bimodal porous copper materials by an annealing-electrochemical dealloying approach. *Electrochim. Acta* **164**, 288-296 (2015).

24. Wang, X., Qi, Z., Zhao, C., Wang, W., Zhang, Z. Influence of alloy composition and dealloying solution on the formation and microstructure of monolithic nanoporous silver through chemical dealloying of Al−Ag alloys. *J. Phys. Chem. C* **113**, 13139-13150 (2009).

25. Zhang, Q. & Zhang, Z.H. On the electrochemical dealloying of Al-based alloys in a NaCl aqueous solution. *Phys. Chem. Chem. Phys.* **12**, 1453-1472 (2010).

26. Liu, W., Zhang, S., Li, N., Zheng & J., Xing, Y. Microstructure evolution of monolithic nanoporous copper from dual-phase Al-35atom%Cu alloy. *J. Electrochem. Soc.* **157**, D666-D670 (2010).

27. Hess, M., Sasaki, T., Villevieille, C. & Novak, P. Combined operando X-ray diffraction-electrochemical impedance spectroscopy detecting solid solution reactions of $LiFePO_4$ in batteries. *Nat. Commun.* **6:** 8169 (2015).

28. Luo, Q., *et al.* Hierarchical densification and negative thermal expansion in Ce-based metallic glass under high pressure. *Nat. Commun.* **6:** 5703 (2015).

29. Fujita, T., Qian, L.H., Inoke, K., Erlebacher, J. & Chen, M.W. Three-dimensional morphology of nanoporous gold. *Appl. Phys. Lett.* **92**, 251902 (2008).

30. Parida, S., Kramer, D., Volkert, C.A., Rösner, H., Erlebacher, J. & Weissmüller, J. Volume change during the formation of nanoporous gold by dealloying. *Phys. Rev. Lett.* **97**, 035504 (2006).

31. Kosinova, A., Wang, D., Schaaf, P., Kovalenko, O., Klinger, L., Rabkin, E. Fabrication of hollow gold nanoparticles by dewetting, dealloying and coarsening. *Acta Mater.* **102**, 108-115 (2016).

32. Massalski, T.B. The Al−Cu (aluminum-copper) system. *Bull. Alloy Phase Diagr.* **1**, 27-33 (1980).

33. Von Dreele, R.B. Chapter 9 Rietveld Refinement. In: *Powder Diffraction: Theory and Practice* (ed^(eds). The Royal Society of Chemistry (2008).

34. Du, G., Sharma, N., Peterson, V.K., Kimpton, J.A., Jia, D., Guo, Z. Br-doped Li4Ti5O12 and composite TiO2 anodes for Li-ion batteries: Synchrotron X-ray and in situ neutron diffraction studies. *Adv. Funct. Mater.* **21**, 3990-3997 (2011).

35. Liu, C.L., Liu, X.Y., Borucki, L.J.. Defect generation and diffusion mechanisms in Al and Al–Cu. *Appl. Phys. Lett.* **74**, 34-36 (1999).

36. Trainor, A., Bartlett, B.E. A possible mechanism of crystal growth from the melt and its application to the problem of anomalous segregation at crystal facets. *Solid-State Electron.* **2**, 106-114 (1961).

37. Janik-Czachor, M. & Szklarska-Smialowska, Z. Pitting corrosion of single crystals of the Fe-16 Cr alloy in solutions containing Cl^- ions. *Corros. Sci.* **8**, 215-220 (1968).

38. Ye, S., Ishibashi, C. & Uosaki, K. Anisotropic dissolution of an Au(111) electrode in perchloric acid solution containing chloride anion investigated by in situ STM: The important role of adsorbed chloride anion. *Langmuir* **15**, 807-812 (1999).

39. Ji, L., Lin, Z., Alcoutlabi, M., Zhang, X. Recent developments in nanostructured anode materials for rechargeable lithium-ion batteries. *Energy Environ. Sci.* **4**, 2682-2699 (2011).

40. Kučera, J. & Million, B. Self-diffusion of copper in Cu−Al solid solutions. *Mater. Trans.* **1**, 2599-2602 (1970).

41. Moffat, T.P., Fan, F.R.F., Bard, A.J. Electrochemical and scanning tunneling microscopic study of dealloying of Cu3Au. *J. Electrochem. Soc.* **138**, 3224-3235 (1991).

42. Avrami, M. Kinetics of phase change. I general theory. *J. Chem. Phys.* **7**, 1103-1112 (1939).

43. Erlebacher, J., Sieradzki, K. Pattern formation during dealloying. *Scr. Mater.* **49**, 991-996 (2003).

44. Erlebacher, J. An atomistic description of dealloying: Porosity evolution, the critical potential, and rate-limiting behavior. *J. Electrochem. Soc.***151**, C614-C626 (2004).

45. Lu, L., Chen, X., Huang, X., Lu, K. Revealing the maximum strength in nanotwinned copper. *Science* **323**, 607-610 (2009).

46. Chen, K.C., Wu, W.W., Liao, C.N., Chen, L.J., Tu, K.N. Observation of atomic diffusion at twin-modified grain boundaries in copper. *Science* **321**, 1066-1069 (2008).

47. Liu, W.B., Zhang, S.C., Li, N., Zheng, J.W., Xing, Y.L. A facile one-pot route to fabricate nanoporous copper with controlled hierarchical pore size distributions through chemical dealloying of Al–Cu alloy in an alkaline solution. *Micropor. Mesopor. Mater.* **138**, 1-7 (2011).

48. Fujita T, *et al.* Atomic observation of catalysis-induced nanopore coarsening of nanoporous gold. *Nano Lett.* **14**, 1172-1177 (2014).

49. Paterson, M.S. X-ray diffraction by face-centered cubic crystals with deformation faults. *J. Appl. Phys.* **23**, 805-811 (1952).

50. Clancy, M., *et al.* In situ synchrotron X-ray diffraction investigation of the evolution of a $PbO_2/PbSO_4$ surface layer on a copper electrowinning Pb anode in a novel electrochemical flow cell. *J. Synchrotron Radiat.* **22**, 366-375 (2015).

51. Schmitt, B., *et al.* Mythen detector system. *Nucl. Instrum. Meth. A* **501**, 267-272 (2003).

52. Coelho, A. TOPAS Academic: General Profile and Structure Analysis Software for Powder Diffraction Data. *Bruker AXS, Karlsruhe, Germany,* (2007).

Acknowledgements

The synchrotron XRD experiments were performed at the Australian Synchrotron Powder Diffraction Beamline (Proposal ID: PD/7953 and PD/8856). T. Song acknowledges the China Scholarship Council (CSC) for a CSC Scholarship, the support of RMIT University for a fee waiver scholarship and the experimental assistance of Dr. Y.F. Yang and Miss Y. Sun of RMIT University.

Author Contributions

T.S. prepared all the samples and conducted laboratory characterization. T.S., N.A.S.W., M.J.S., and M.Y. conducted the synchrotron experiments with the guidance of J.A.K. T.S. conducted the refinement analysis with the guidance of N.A.S.W., M.J.S. and J.A.K. T.S. and M.Q. wrote the manuscript. T.S., M.Y. and M.Q. are responsible for the project direction and planning. All authors contributed to the discussions of the results and manuscript.

Figures for

Towards a complete understanding of dealloying of Al-Cu by in-situ and ex-situ synchrotron X-ray diffraction

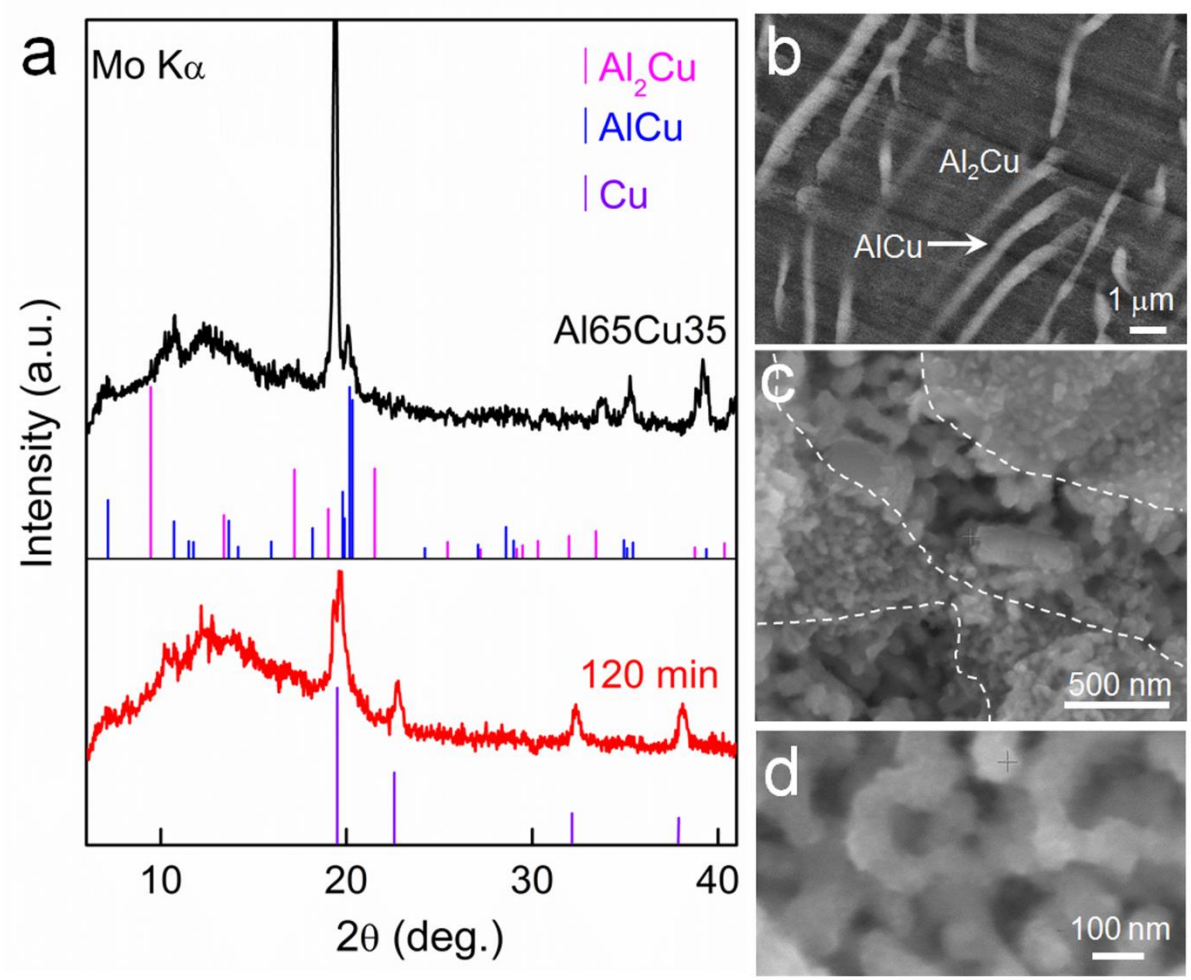

Figure 1 Creation of hierarchical nanoporous Cu from dealloying of two-phase Al65Cu35. (a) Laboratory XRD patterns of the Al65Cu35 alloy before and after 120 min dealloying in a 10 vol.% HCl solution. The tick marks indicate the position and intensity of Bragg peaks of Al_2Cu (PDF#65-2695), AlCu (PDF#65-1228) and Cu (PDF#04-0836) phases. (b) Backscattered electron (BSE) image of the microstructure of the as-cast Al65Cu35 precursor alloy consisting of primary AlCu and Al_2Cu matrix. (c) Hierarchical nanoporous structures of Cu from dealloying of AlCu (surrounded by dash lines) and Al_2Cu phases in Al65Cu35 alloy respectively. (d) High magnification SEM image of the nanoporous structure from the dealloying of Al_2Cu phase.

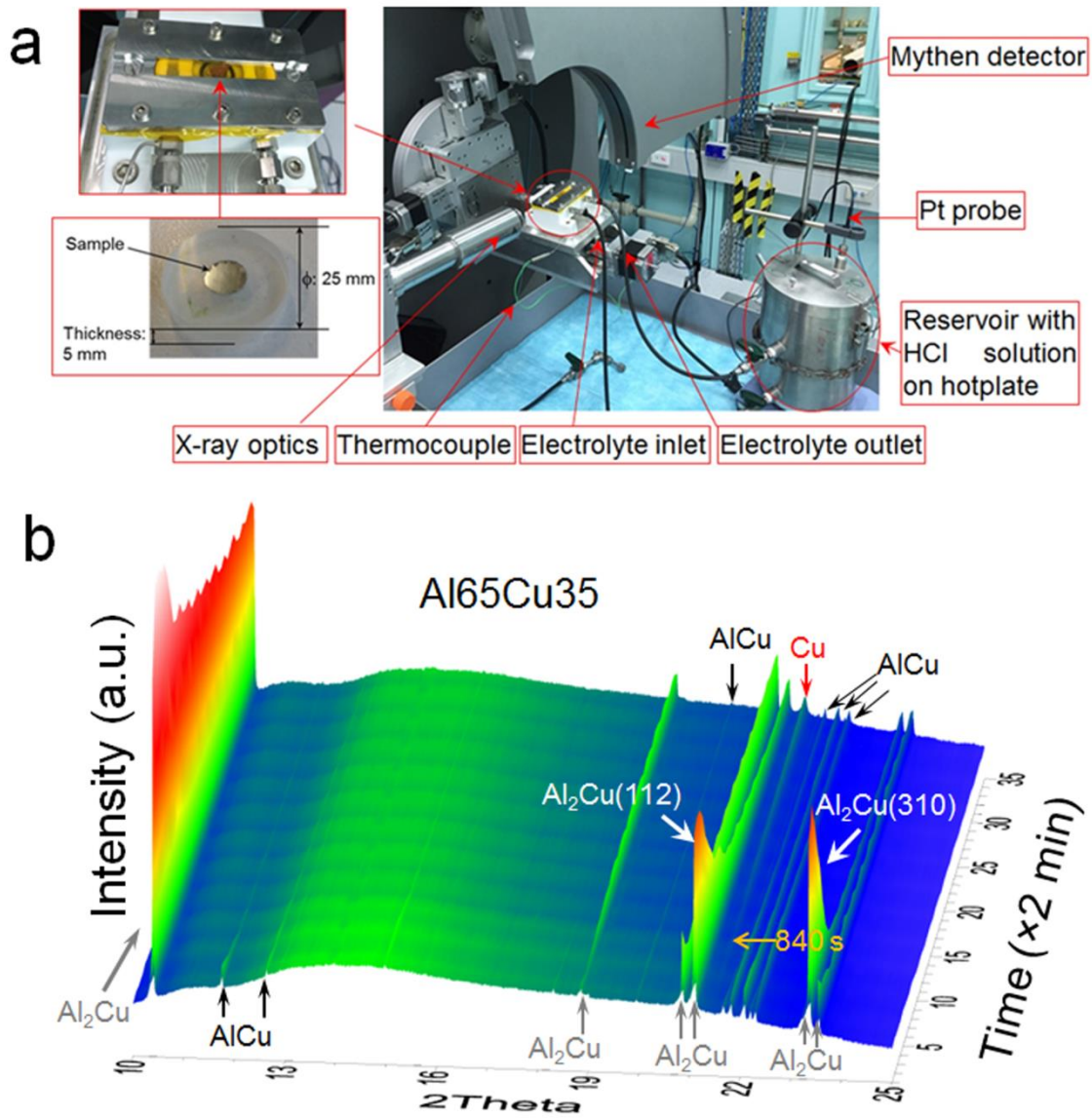

Figure 2 Experimental set-up for synchrotron in-situ dealloying and time-resolved sequential evolution of Al_2Cu and AlCu in Al65Cu35. (a) The synchrotron data is collected continuously while the heated electrolyte solution is re-circulated through the mounted alloy sample in the cell. (b) In-situ phase evolution for the dealloying of the Al65Cu35 alloy, which consists of Al_2Cu and AlCu, in a 5 wt.% HCl solution at 70 °C (X-ray wavelength = 0.7745 Å) (the fluctuations in intensity of, for example, the Al_2Cu peak at ~10°2θ, is caused by rocking of the sample stage ± 2° about its axis for improvement of data quality).

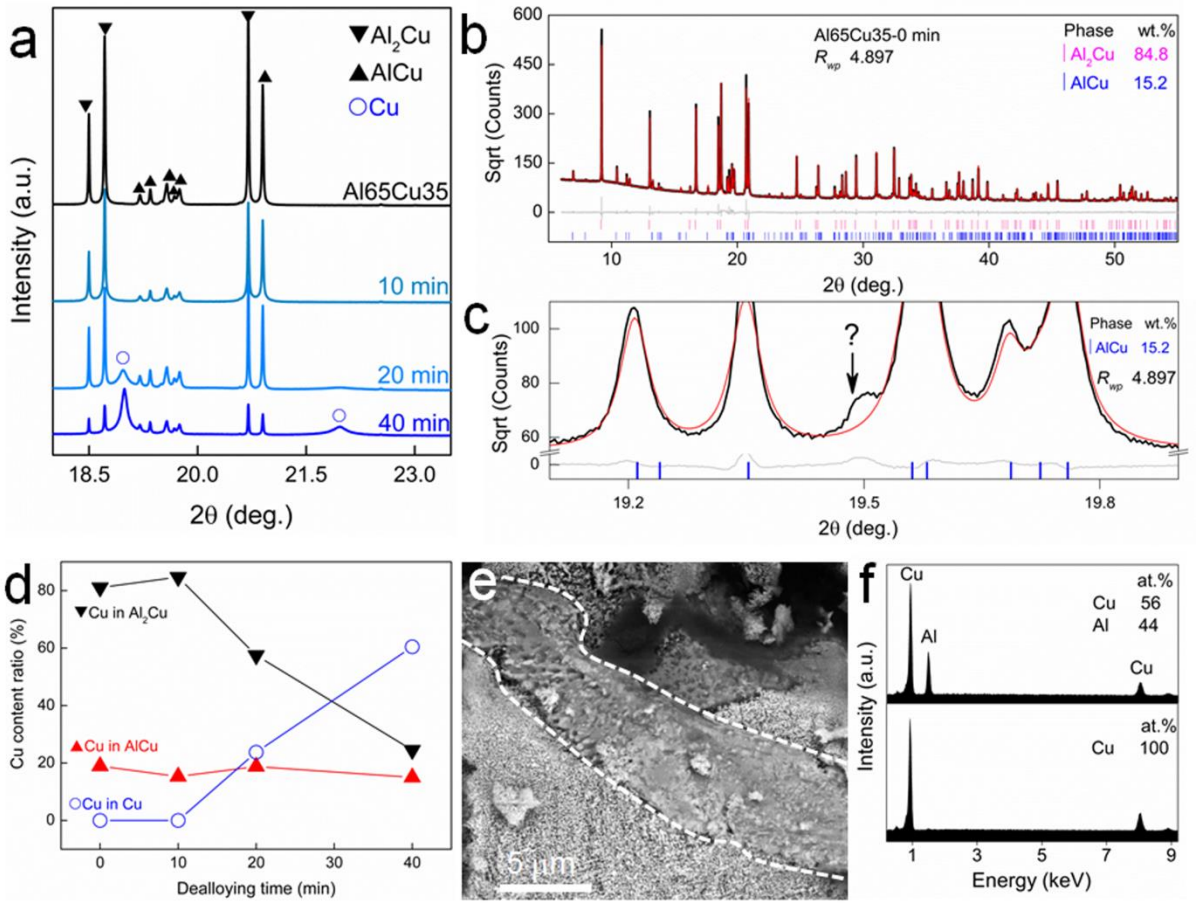

Figure 3 Quantified sequential evolution of Al_2Cu and AlCu in Al65Cu35. (a) Ex-situ SXRD patterns of Al65Cu35 alloy powders after dealloying in a 10 vol.% HCl solution from 10 min to 40 min (X-ray wavelength = 0.6891 Å). (b) Rietveld refinement output of the Al65Cu35 precursor powder sample data using the TOPAS-Academic software. The black, red and grey solid lines indicate the observed and calculated patterns and their difference, respectively. The tick marks indicate the position of the Bragg reflection markers for Al_2Cu (upper) and AlCu (lower). (c) An expanded region of the fit in (b) between $19.1° \leq 2\theta \leq 19.9°$ showing the unidentified phase in the sample which can affect the fitting. (d) evolution of the Cu content, as a proportion of the total Cu available, in each of the Al_2Cu, AlCu and Cu phases from refinement analysis of each pattern in (a). (e) The microstructure of the as-dealloyed Al65Cu35-40 min sample consisting of the nanoporous structure from the

dealloying of Al_2Cu and the un-dealloyed AlCu with just a rough surface. (f) and (g) EDX spectra of the as-dealloyed AlCu and Al_2Cu phases in (e), respectively.

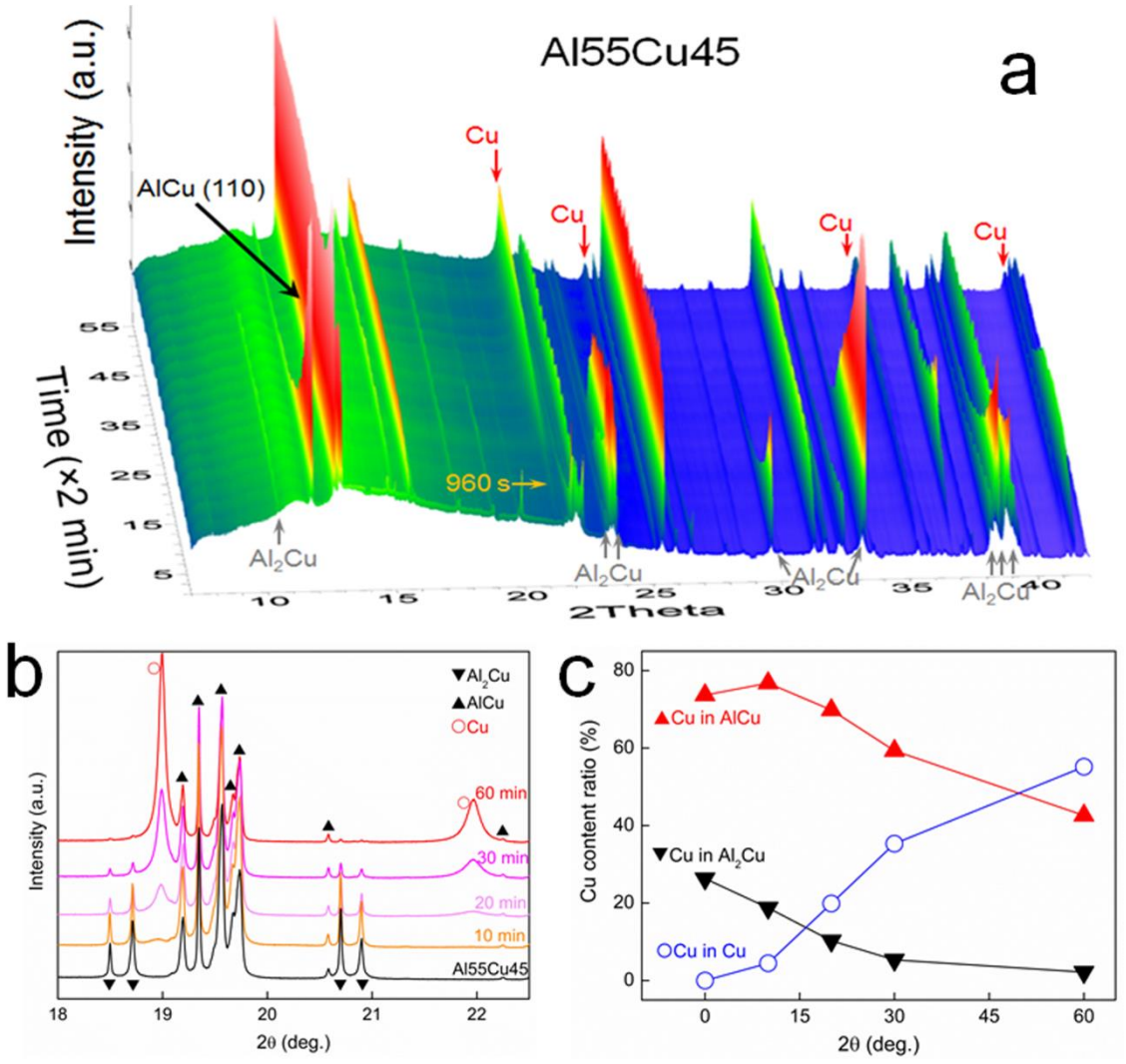

Figure 4 Sequential evolution of Al_2Cu and AlCu in Al55Cu45. (a) In-situ phase evolution for the dealloying of the Al55Cu45 alloy, which consists of Al_2Cu and AlCu, in a 5 wt.% HCl solution at 70 °C (X-ray wavelength = 0.7745 Å). (b) Ex-situ SXRD patterns of Al55Cu45 alloy powders after dealloying in a 10 vol.% HCl solution from 10 min to 60 min (X-ray wavelength = 0.6891 Å); (c) Evolution of the Cu content, as a proportion of the total Cu available, in each of the Al_2Cu, AlCu and Cu phases from refinement analysis of each pattern in (b).

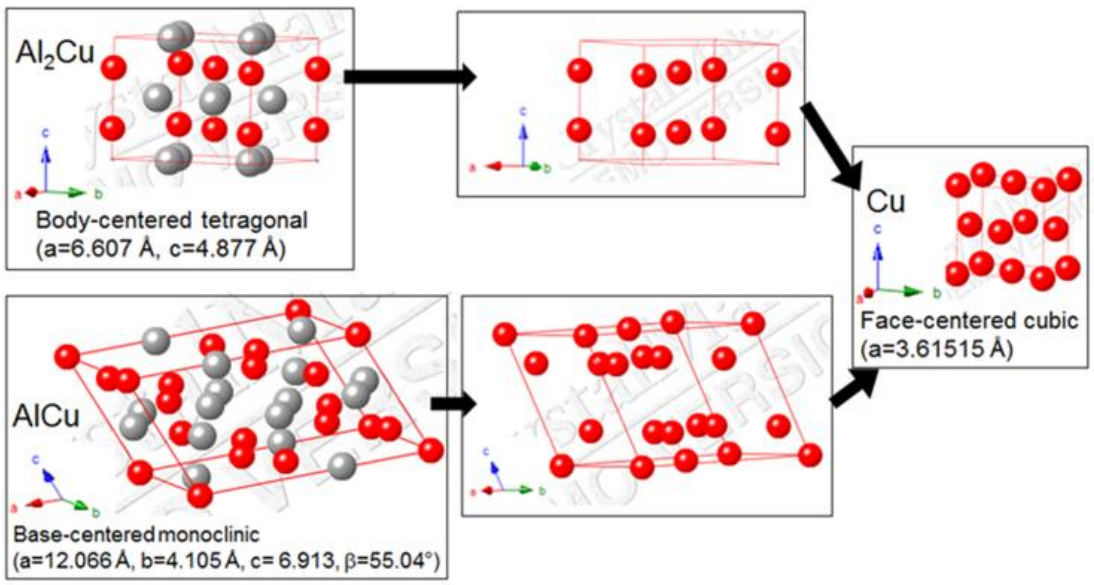

Figure 5 Schematic maps showing the unit cell evolution. The smaller red ball represents the Cu atom and the larger grey ball represents the Al atom. During dealloying of body-centered tetragonal Al_2Cu and base-centered monoclinic AlCu, once all Al atoms are removed, the residual Cu atoms may temporarily assume a precursor crystal structure and then evolve into a face-centered cubic crystal structure.

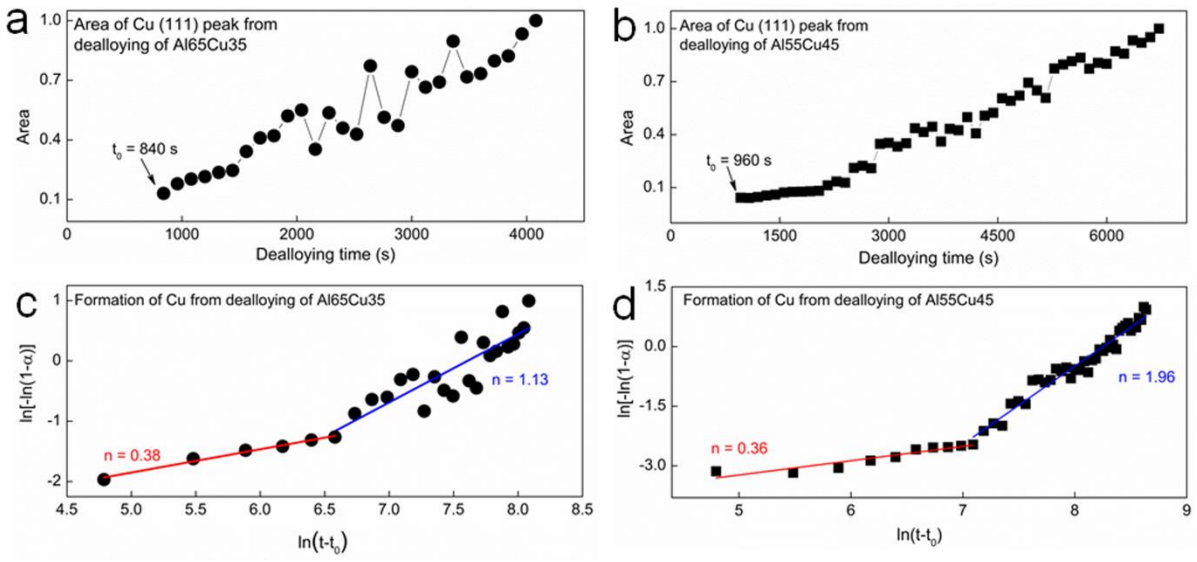

Figure 6 Formation kinetics of Cu phase. (a) The development of the peak area of the Cu (111) diffraction peak as a function of dealloying time from the in-situ dealloying of Al65Cu35 in Figure 2(b). (b) The plot of Avrami-Erofe'ev equation to determine the value of the *n* parameter for the formation of Cu from dealloying of Al65Cu35. (c) The development of the peak area of the Cu (111) diffraction peak as a function of dealloying time from the in-situ dealloying of Al55Cu45 in Figure 4(a). (d) The plot of Avrami-Erofe'ev equation to determine the value of the *n* parameter for the formation of Cu from dealloying of Al55Cu45. The time of 840 s and 960 s for the observation of first Cu (111) peak in Figure 2(b) and Figure 4(a) is considered as the induction time t_0 for the formation of Cu. The area of Cu (111) diffraction peak was normalized considering the area in the final pattern of the in-situ dataset as one. The Cu (111) peak area fluctuations in both cases (Figure 6(a,c)) are due to the rocking the sample stage ± 2° about its axis during the in-situ experiments. The two *n* values for both cases (Figure 6(b,d)) indicates two kinetics during the formation of Cu from dealloying approach. A full discussion of the data is presented in the text.

Figure 7 Consequences of diffusion of Cu. (a) Bright field (BF) TEM image of Al65Cu35-40 min sample with twins in the ligaments. (b) Corresponding HRTEM image showing twins in Cu ligaments. (c) Rietveld refinement output of Al65Cu35-40 min sample considering the isotropic broadening of Cu peaks and (d) anisotropic broadening of Cu (002) peak. The better fitting of (d) clarifies the anisotropic broadening in Cu diffraction peaks as a result of the presence of twins in the as-dealloyed samples.

Tables for

Towards a complete understanding of dealloying of Al-Cu alloys by in-situ and ex-situ synchrotron X-ray diffraction

Table 1 R_{wp} – weight profile *R* value, lattice parameter *a* of as-created Cu phase, the weight percentage of each phase before and after dealloying of Al65Cu35 alloy, obtained from Rietveld refinement.

Sample	R_{wp}	a_{Cu} (Å)	Al_2Cu (wt.%)	$\frac{Cu_{Al_2Cu}}{Cu_{Al_2Cu}+Cu_{AlCu}+Cu_{Cu}}$	AlCu (wt.%)	$\frac{Cu_{AlCu}}{Cu_{Al_2Cu}+Cu_{AlCu}+Cu_{Cu}}$	Cu (wt.%)	$\frac{Cu_{Cu}}{Cu_{Al_2Cu}+Cu_{AlCu}+Cu_{Cu}}$
Al65Cu35	4.897	NA	84.7	81.1%	16	18.9%	0	0
10 min	4.043	NA	87.7	84.6%	13	15.3%	0	0
20 min	5.968	3.618	67.8	57.5%	21	18.8%	15.0	23.7%
40 min	4.868	3.617	35.7	24.5%	21	15.0%	47.5	60.5%

Table 2 R_{wp} – weight profile *R* value, lattice parameter *a* of as-created Cu phase, the weight percentage of each phase before and after dealloying of Al55Cu45 alloy, obtained from Rietveld refinement.

Sample	R_{wp}	a_{Cu} (Å)	Al_2Cu (wt.%)	$\frac{Cu_{Al_2Cu}}{Cu_{Al_2Cu}+Cu_{AlCu}+Cu_{Cu}}$	AlCu (wt.%)	$\frac{Cu_{AlCu}}{Cu_{Al_2Cu}+Cu_{AlCu}+Cu_{Cu}}$	Cu (wt.%)	$\frac{Cu_{Cu}}{Cu_{Al_2Cu}+Cu_{AlCu}+Cu_{Cu}}$
Al55Cu45	8.236	NA	31.4	26.3%	67.7	73.6%	0	0
10 min	9.345	3.621	19.1	15.2%	77.7	80.0%	3.1	4.5%
20 min	8.390	3.617	13.7	10.3%	71.9	69.8%	14.4	19.9%
30 min	8.212	3.617	7.6	5.3%	65.1	59.3%	27.2	35.3%
60 min	7.184	3.617	3.4	2.2%	50.6	42.6%	46.0	55.2%

Supplementary Information for

Towards a complete understanding of dealloying of Al-Cu by in-situ and ex-situ synchrotron X-ray diffraction

Supplementary Methods 1:

In-situ Synchrotron X-Ray Diffraction (SXRD) dealloying experiments

For the in-situ experiments, we used a special cell. The design of the cell was based on a previous cell described by Webster et al.[1] and the details of the cell have been described in Clancy et al.[2] The Al65Cu35 and Al55Cu45 alloy ingot sample were cut to 5 mm thick disks, then centered in a 25 mm-diameter mold and mounted in epoxy resin. Once cured, the surface of the mounted samples was ground and polished until the thickness of the mounted disk was in the 4.9-5.0 mm range. The mounted samples were then placed in the cavity located on the top of the cell body (see Fig. 2a).

In-situ SXRD experiments were performed on the powder diffraction beamline at the Australian Synchrotron, equipped with a Mythen microstrip detector spanning 80° 2θ. The 500 ml of the 5 wt.% HCl electrolyte solution was heated to 70 °C and stirred within a covered 3 L stainless-steel reservoir using a digital hotplate and a magnetic stirrer. The cell was connected to the XYZ stage of the diffractometer and aligned to the X-ray beam. A Polyvinyl chloride (PVC) spill tray was bolted to the top of the end-station table. The solution was re-circulated from the reservoir, through the cell and then back to the reservoir through Viton® tubing using a peristaltic pump. The temperature of the electrolyte entering the cell was recorded to be 70 °C.

XRD data were collected throughout each dealloying experiment with individual data sets collected at every 1 min at each of two detector positions P1 and P2 (the Mythen detector[3] contains 0.2° gaps every 5° 2θ; data were collected at two detector positions 0.5° apart in order to cover the entire 2θ range). The data were collected in asymmetric diffraction geometry with the cell rocking, over the range 4°≤2θ≤84°. The X-ray wavelength was 0.7745 Å, which was calibrated using NIST Standard Reference Material LaB_6 660b collected in a capillary in Debye-Scherrer geometry. The height of the plate sample was calibrated with Y_2O_3 contained in the cell.

Supplementary Figures:

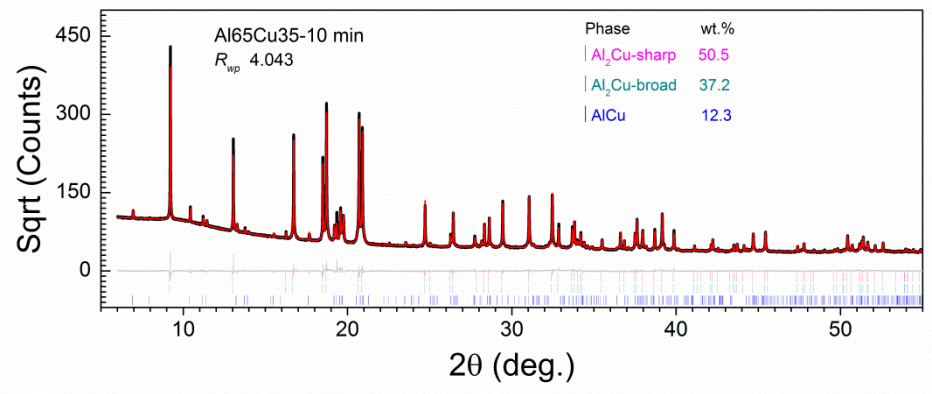

Supplementary Figure 1 (a) Rietveld plot of the Al65Cu35-10 min sample and (b) the peak broadening of Al_2Cu phase due to the uneven particle sizes.

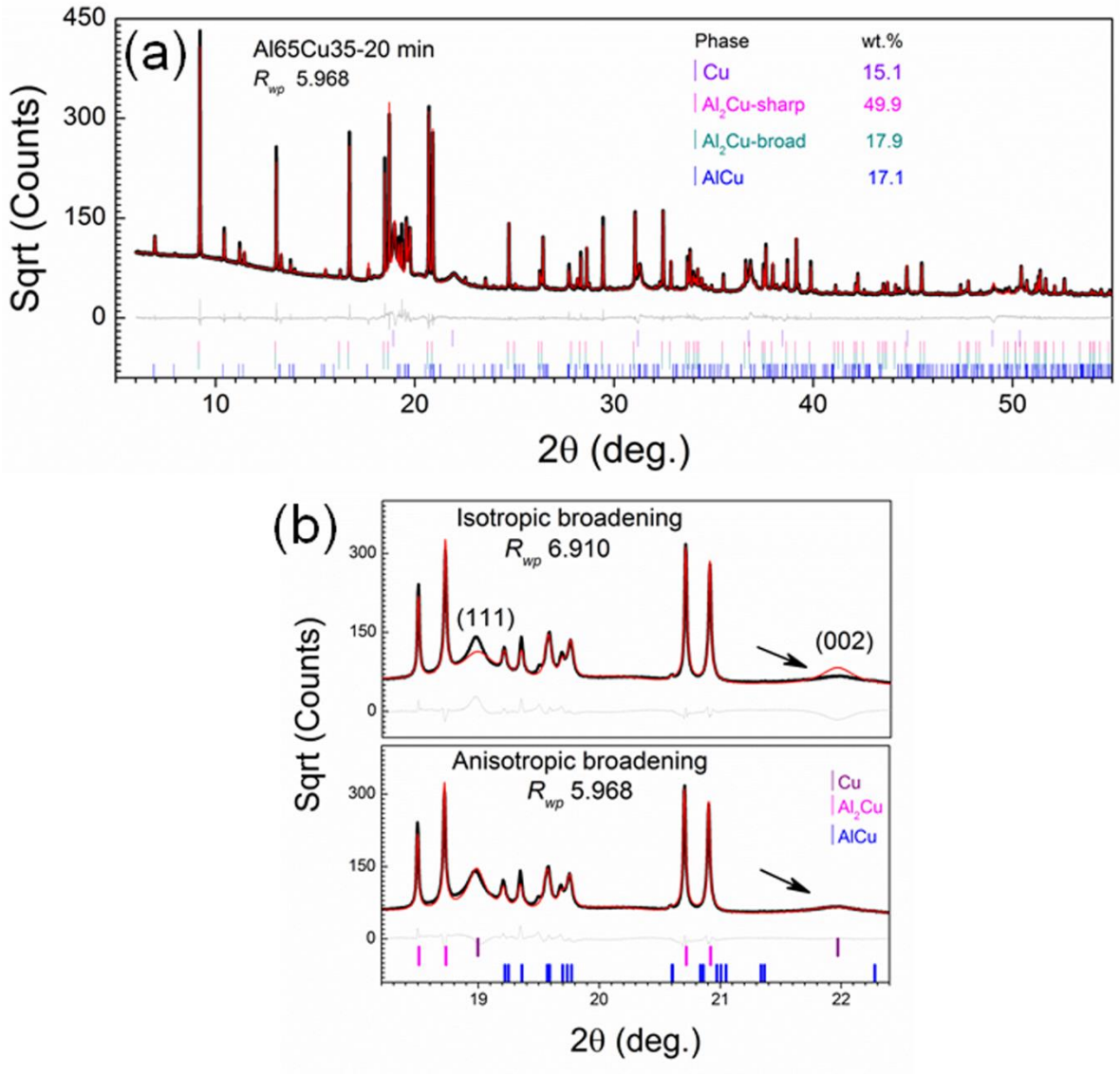

Supplementary Figure 2 (a) Rietveld plot of the Al65Cu35-20 min sample and (b) evidence of anisotropic broadening of (002) diffraction peak.

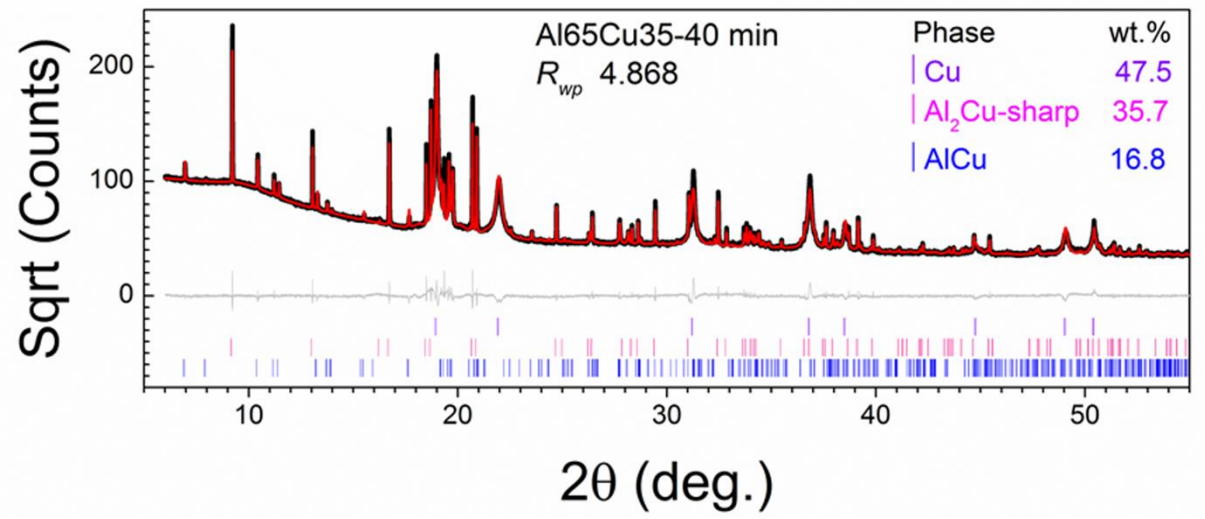

Supplementary Figure 3 Rietveld plot of the Al65Cu35-40 min sample.

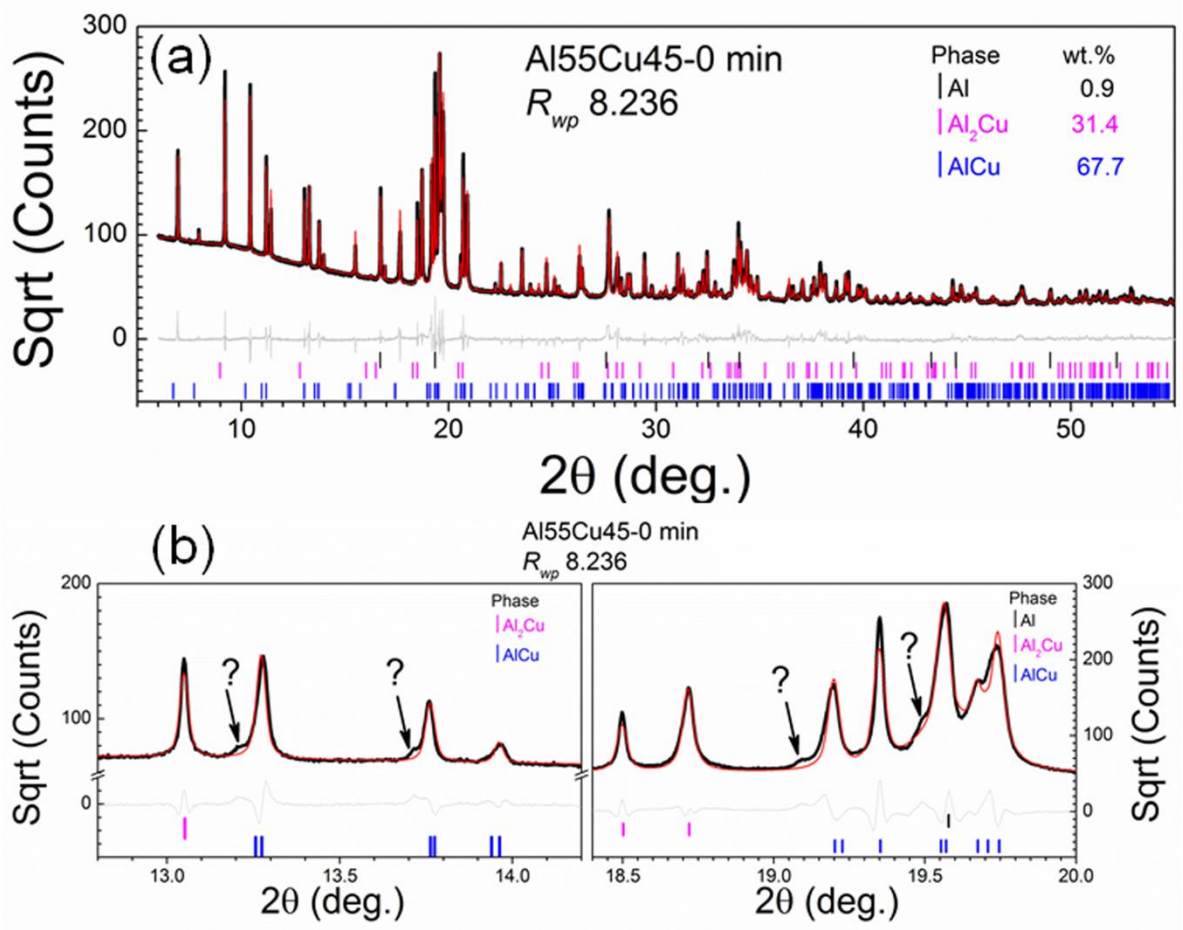

Supplementary Figure 4 (a) Rietveld plot of the Al55Cu45-0 min sample and (b) expanded regions showing unidentified phases.

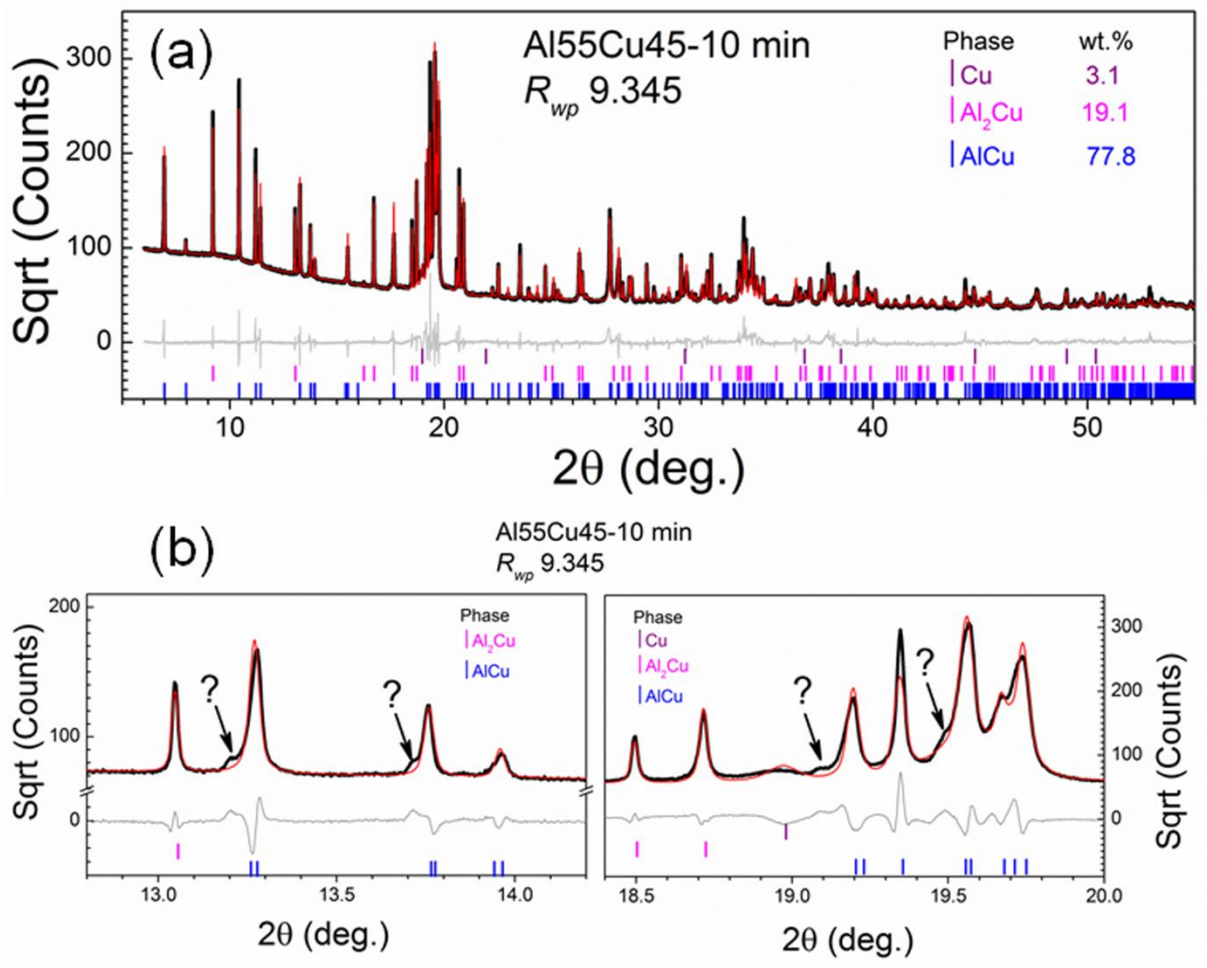

Supplementary Figure 5 (a) Rietveld plot of the Al55Cu45-10 min sample and (b) expanded regions showing unidentified phases.

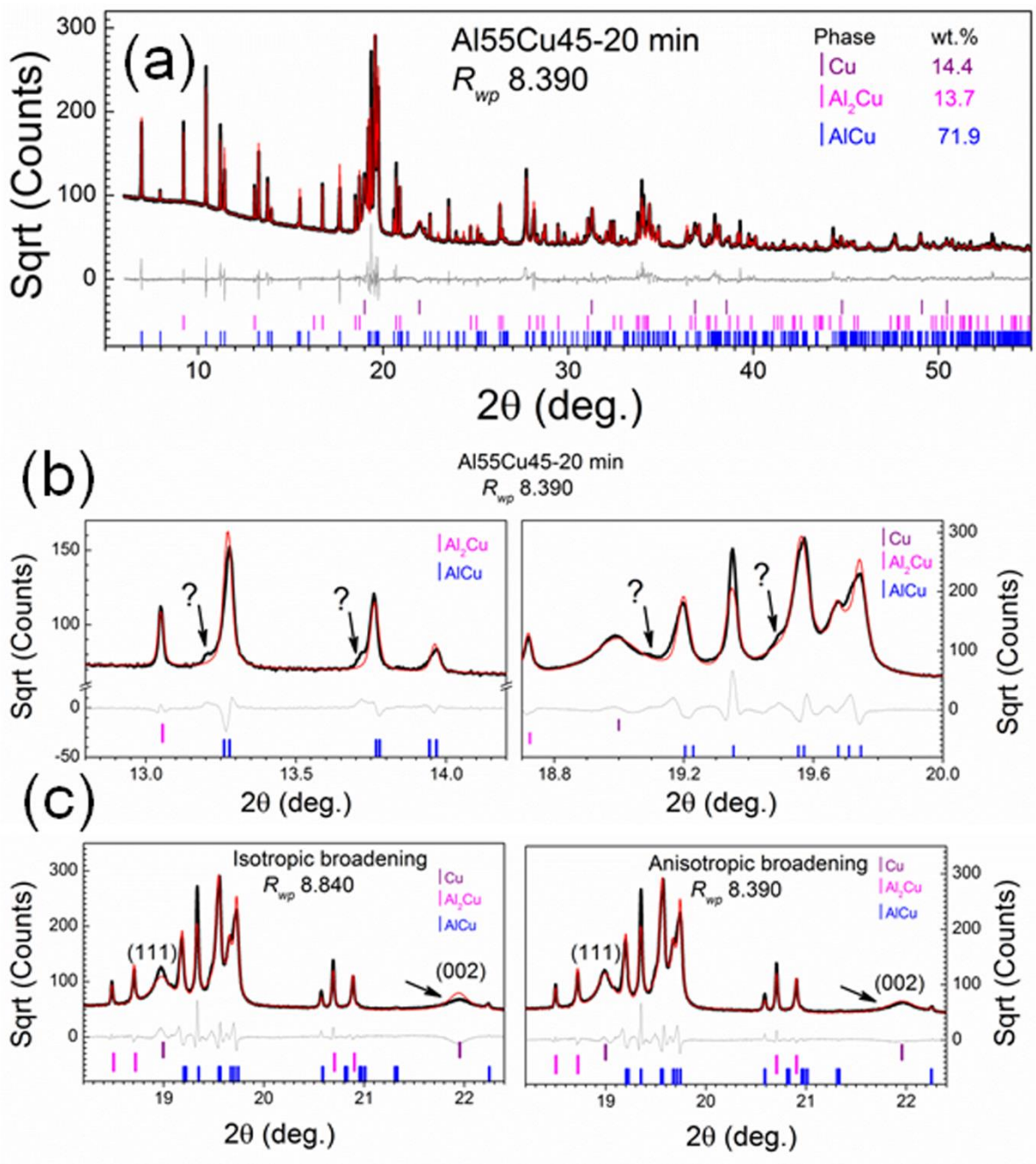

Supplementary Figure 6 (a) Rietveld plot of the Al55Cu45-20 min sample, (b) expanded regions showing unidentified phases and (c) evidence of anisotropic broadening of (002) diffraction peak.

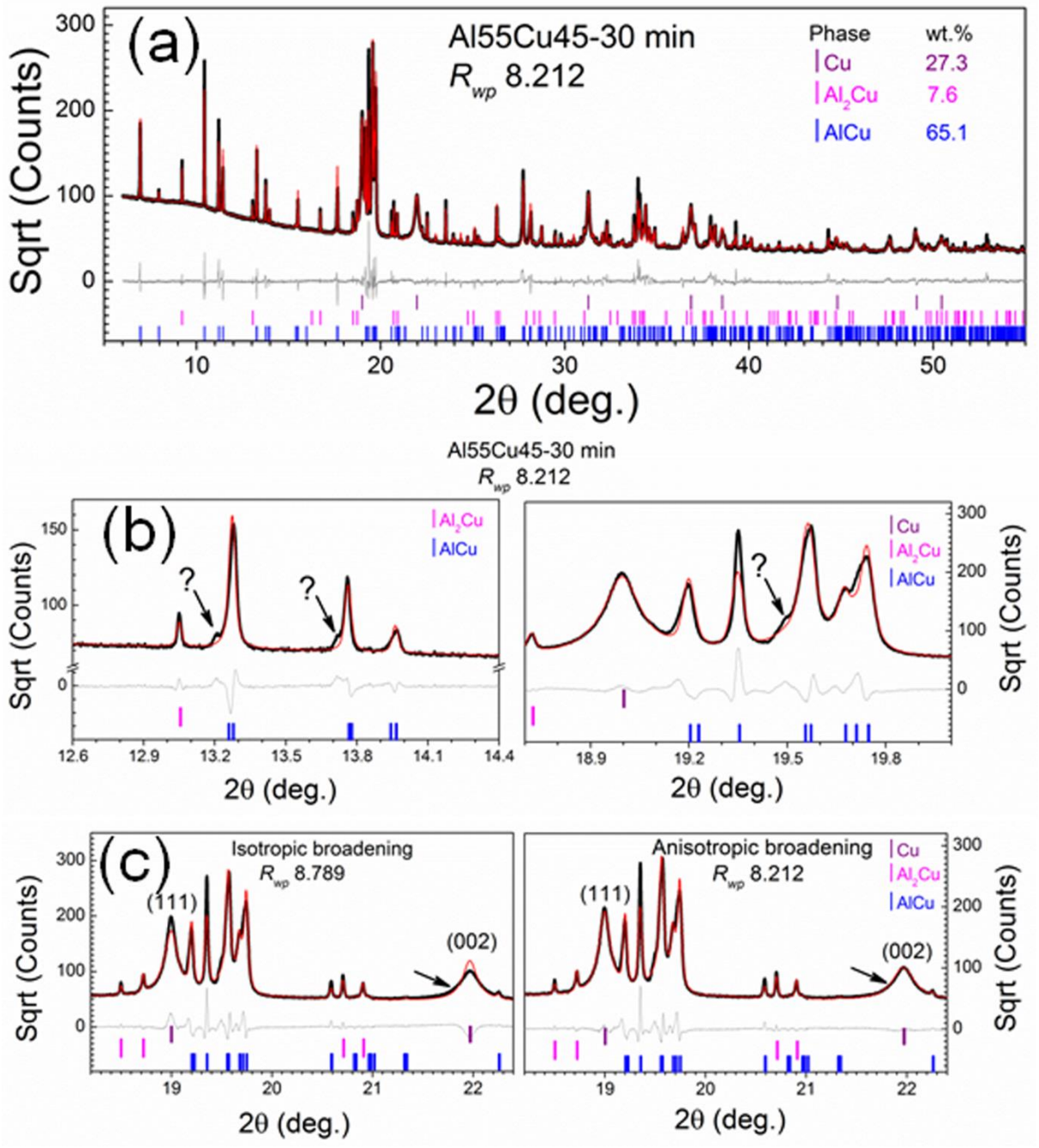

Supplementary Figure 7 (a) Rietveld plot of the Al55Cu45-30 min sample, (b) expanded regions showing unidentified phases and (c) evidence of anisotropic broadening of (002) diffraction peak.

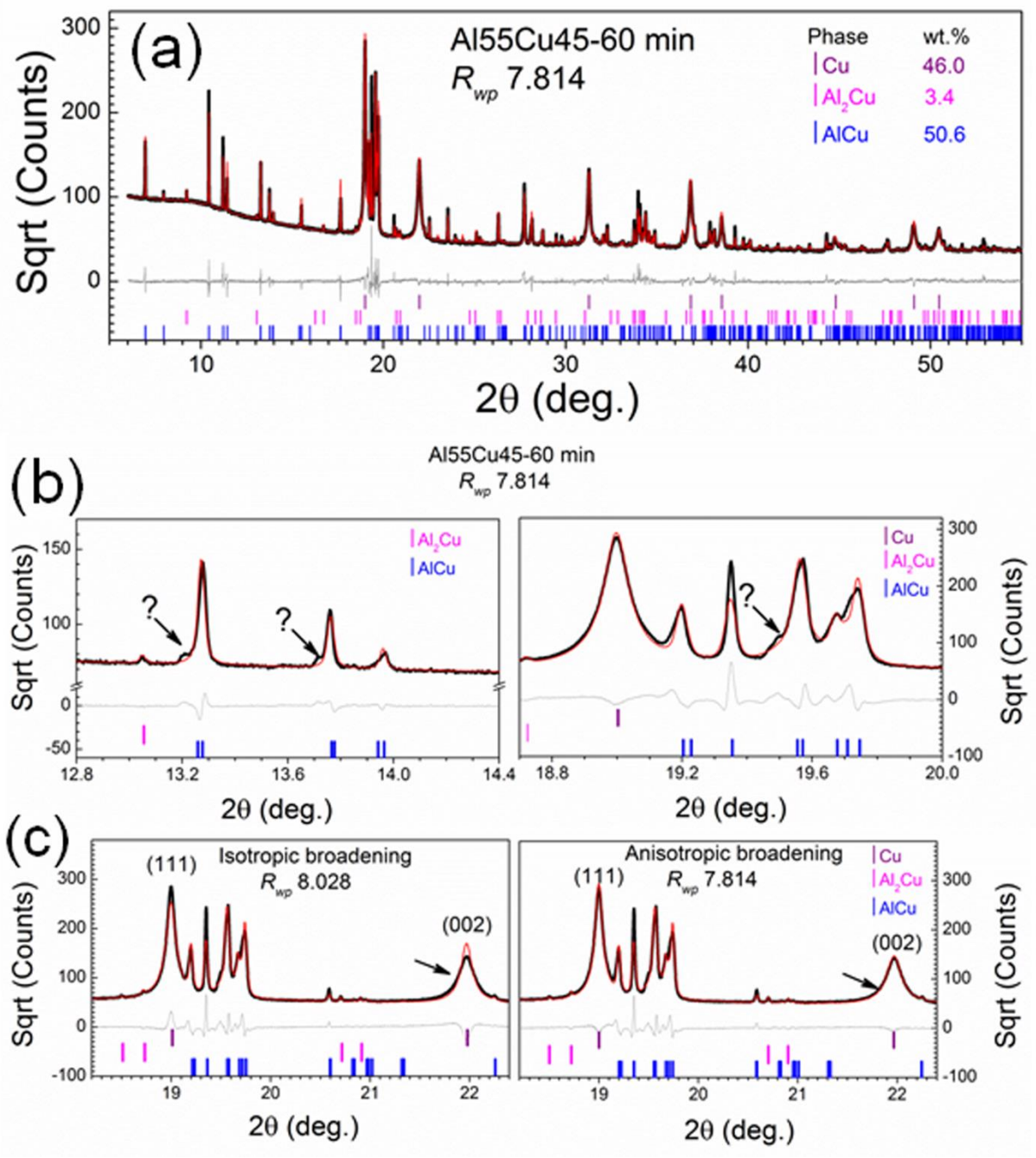

Supplementary Figure 8 (a) Rietveld plot of the Al55Cu45-60 min sample, (b) expanded regions showing unidentified phases and (c) evidence of anisotropic broadening of (002) diffraction peak.

References

1. Webster, N.A.S., Madsen, I.C., Loan, M.J., Scarlett, N.V.Y., Wallwork, K.S. A flow cell for in situ synchrotron x-ray diffraction studies of scale formation under Bayer processing conditions. *Rev. Sci. Instrum.* **80**, 084102 (2009).
2. Clancy, M., *et al.* In situ synchrotron X-ray diffraction investigation of the evolution of a $PbO_2/PbSO_4$ surface layer on a copper electrowinning Pb anode in a novel electrochemical flow cell. *J. Synchrotron Radiat.* **22**, 366-375 (2015).
3. Schmitt, B., *et al.* Mythen detector system. *Nucl. Instrum. Meth. A* **501**, 267-272 (2003).

6.2 In-situ and ex-situ synchrotron studies on the dealloying of Al-Cu and Al-Cu-Sn alloys

6.2.1 Introduction

During the dealloying of Ag-Au, the face centred cubic (fcc) Ag-Au solid-solution changes to fcc Au without changing the crystal structure. Dealloying occurs *via* a simple change in composition in this case. In many dealloyable systems, it is common that the precursor alloy consists of phases with different crystal structures. Hence, it is necessary to kinetically clarify the significance of crystal structure evolution during the creation of nanoporous metals *via* the dealloying approach.

Taking the Al-Cu alloy system as an example: the Al-Cu precursor alloys can consist of different phases with various crystal structures as well as different compositions (see the phase diagram in Fig. 2.26, and the composition and crystallographic data in Table 6.2.1). The Al-Cu alloy system thus offers an informative model system to study the significance of crystal structure evolution for the dealloying process.

Table 6.2.1 Composition and crystallographic data of Al-Cu phases [1].

Phase	at.% Cu	Crystal system structure	Space group
α-Al(Cu)	0-2.84	Cubic	Fm-3m
Al_2Cu	31.9-33.0	Tetragonal	I4/mcm
AlCu	49.8-52.3	Monoclinic	I12/m1
Cu_4Al_3	55.2-56.3	Hexagonal	P6/mmm
Cu_3Al_2	59.3-61.9	Trigonal	P-3m1
Cu_9Al_4	62.5-69.0	Cubic	P-43m
α-Cu(Al)	80.3-100	Cubic	Fm-3m

For the Al-Cu-Sn alloy system: in the Cu-Sn system, the intermetallic formation is temperature-sensitive: below 60 °C only Cu_6Sn_5 forms while at or above 60 °C both Cu_6Sn_5 and Cu_3Sn can develop [2]. The concurrent dealloying and realloying process observed in this alloy system (see **Chapter 4**) is also supposed to be temperature dependent. Hence, it is useful to use temperature as a variant to either better understand the dealloying-realloying mechanism or to better manipulate the fabrication of nanoporous Cu-Sn composites. In

particular, when the dealloyed nanoporous Cu-Sn composites are used as anode materials in LIBs, the non-active Cu content can decrease the specific capacities. In this regard, it is important to form pure Cu_6Sn_5 or Cu_3Sn or their mixture in the final nanoporous microstructure than the pure Cu phase. Ex-situ and in-situ synchrotron radiation can help clarify and further understand the various stages of the dealloying process.

6.2.2. Experimental procedure

The in-situ and ex-situ synchrotron experimental procedures are the same as that described in **Section 6.1**.

6.2.3. Results

6.2.3.1 In-situ and ex-situ synchrotron study of the dealloying process of Al-Cu alloy systems

(1) Dealloying of the $Al_{75}Cu_{25}$ (α-Al(Cu) + Al_2Cu)

Fig. 6.2.1 presents the time evolution of in-situ Synchrotron XRD patterns for phase evolution during dealloying of the $Al_{75}Cu_{25}$ alloy, which consists of α-Al(Cu) and Al_2Cu, in a 5 wt.% HCl solution at 70 °C. The following observations are notable:

(i) For α-Al(Cu): There was a progressive decrease in the intensity of the Synchrotron XRD peaks for the α-Al(Cu) until the α-Al(Cu) disappeared after the first 40 min dealloying, while most of the diffraction peaks for Al_2Cu were still there, indicating sequential dealloying responses of α-Al(Cu) and Al_2Cu.
(ii) For Cu phase: As dealloying proceeded, small peaks corresponding to the Cu phase began to emerge after almost 6 min dealloying and they progressively intensify over time. The diffraction peaks for the Cu phase are broad, indicative of the formation of nanoporous Cu phase in small crystallites.
(iii) For Al_2Cu phase: There was a noticeable decrease in the intensity of the diffraction peaks for Al_2Cu, due to its dealloying of Al_2Cu into Cu. By the end of the in-situ dealloying experiment conducted, some Al_2Cu phase still remained due to incomplete dealloying. There were fluctuations in peak intensity for certain peaks of Al_2Cu. This is due to the orientation effect in the as-cast alloy plate sample. Another reason is that the penetration depth of synchrotron X-ray is larger than the penetration of the HCl solution.

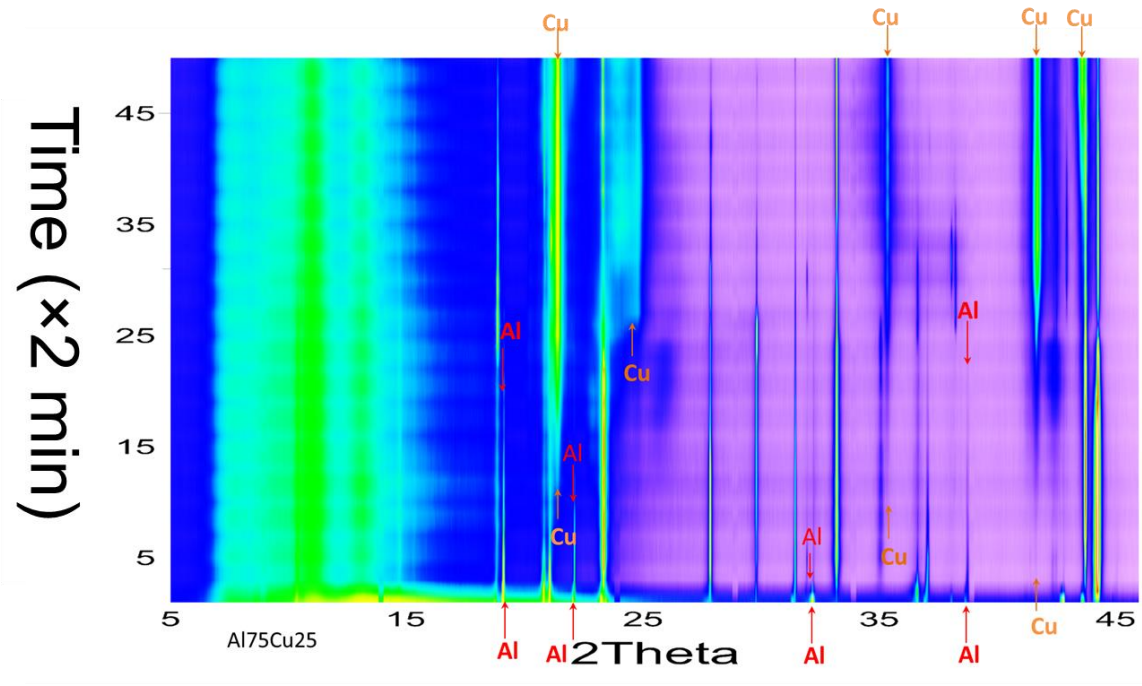

Fig. 6.2.1 In-situ phase evolution during the dealloying of the $Al_{75}Cu_{25}$ alloy, which consists of α-Al(Cu) and Al_2Cu, in a 5 wt.% HCl solution at 70 °C (the unlabelled peaks all correspond to the Al_2Cu phase).

(2) Dealloying of the $Al_{45}Cu_{55}$ (AlCu + Al_4Cu_9)

It has been suggested that the composition of $Al_{50}Cu_{50}$ (at.%) represents the parting limit [3] for the Al-Cu alloy system to undergo dealloying. For the dealloying of Al-Cu alloys, containing more than 50 at.%Cu, the only two studies reported to date appear to be those by Wang et al. [4] and Kong et al [5]. However, both studies were based on the results from conventional XRD [4, 5]. Since the PDF information for Al-Cu based intermetallic compounds is very similar (see Fig. 2.29), more detailed and accurate investigations are necessary for a robust conclusion.

Fig. 6.2.2 shows the Synchrotron XRD spectra obtained from in-situ dealloying of the $Al_{45}Cu_{55}$ alloy, which consists of AlCu and Al_4Cu_9, in a 5 wt.% HCl solution at 70 °C. It can be observed that:

- Both AlCu and Al_4Cu_9 are dealloyable leading to the formation of Cu diffraction peaks. As a result, it can be concluded $Al_{50}Cu_{50}$ (at.%) is not the parting limit for Al-Cu alloy system.
- The intensity of some of the diffraction peaks for both phases decreased from the beginning of dealloying without preferential dissolution of each phase. During dealloying

of Al_4Cu_9, which contains more Cu than the reported parting limit composition of $Al_{50}Cu_{50}$ (at.%) [3], the cubic Al_4Cu_9 changes into cubic Cu [1]. Apart from alloy composition, the crystal structure evolution may play another significant role in dictating if one phase is dealloyable or not.

- The variation of diffraction peaks for both AlCu and Al_4Cu_9 (i.e. some peaks decrease noticeably in intensity while other peaks remain their intensity) confirms that different crystal facets have different dealloying rates.

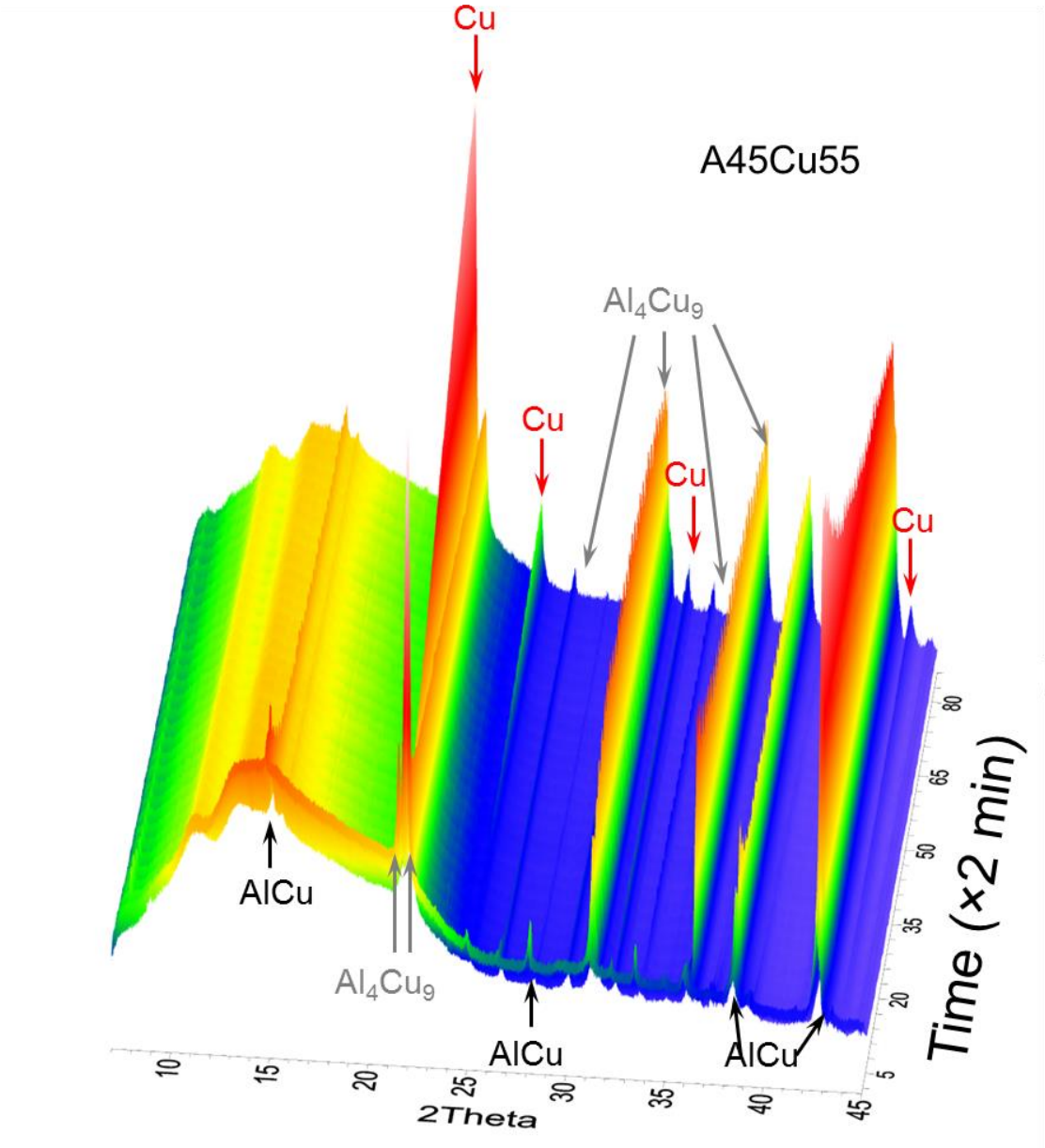

Fig. 6.2.2 In-situ phase evolution for the dealloying of the $Al_{45}Cu_{55}$ alloy, which consists of AlCu and Al_4Cu_9, in a 5 wt.% HCl solution at 70 °C.

6.2.3.2 In-situ and ex-situ synchrotron study of the dealloying process of the $Al_{67}Cu_{18}Sn_{15}$ precursor alloys

It has been reported that the intermetallic formation in the Cu-Sn system is temperature-sensitive: below 60 °C, only Cu_6Sn_5 forms while at or above 60 °C both Cu_6Sn_5 and Cu_3Sn can develop [2]. In **Chapter 4**, it was shown that the lowest temperature for the formation of Cu_3Sn is 60 °C. In this section, more studies, based on both in-situ and ex-situ synchrotron experiments on dealloying of $Al_{67}Cu_{18}Sn_{15}$ precursor alloys at different temperatures, are performed to clarify this temperature sensitivity issue.

(1) Dealloying of the $Al_{67}Cu_{18}Sn_{15}$ at 55 °C

Fig. 6.2.3 shows the phase evolution during the dealloying of $Al_{67}Cu_{18}Sn_{15}$ at 55 °C. A decrease of intensity in diffraction peaks for Al, Al_2Cu and Sn was observed with increasing dealloying time. Surprisingly, not only Cu_6Sn_5 but also Cu_3Sn has formed. As a result, the lowest temperature for the formation of Cu_3Sn in the Cu-Sn system now stands at 55 °C supported by solid experimental data thanks to in-situ synchrotron studies.

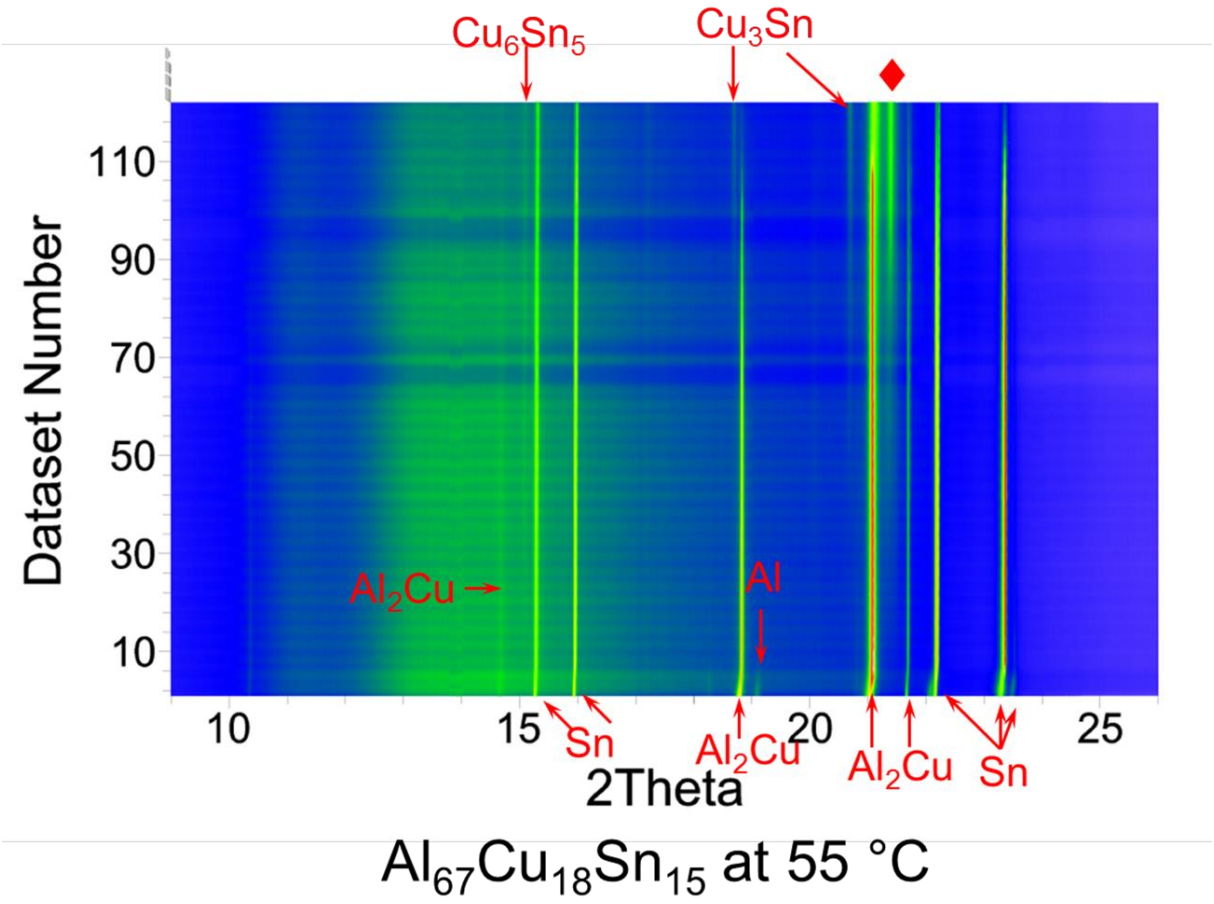

Fig. 6.2.3 In-situ phase evolution during dealloying of the $Al_{67}Cu_{18}Sn_{15}$ alloy in a 5 wt.% HCl solution at 55 °C (♦: a mixture of Cu_6Sn_5 and Cu_3Sn).

(2) Dealloying of the $Al_{67}Cu_{18}Sn_{15}$ at 70 °C

Fig. 6.2.4 shows the phase evolution during the dealloying of the $Al_{67}Cu_{18}Sn_{15}$ at 70 °C. Similarly, a decrease of intensity in diffraction peaks for Al, Al_2Cu and Sn was observed with increasing dealloying time. The final as-dealloyed product is a Cu_6Sn_5-Cu-Cu_3Sn composite. This is consistent with the ex-situ results obtained from conventional XRD presented in **Chapter 4**, but differs from the as-dealloyed product of Cu_6Sn_5-Cu_3Sn composite resulted from dealloying at 55 °C. More detailed analysis is needed to identify the fundamental mechanism that dictates intermetallic formation in the Cu-Sn system.

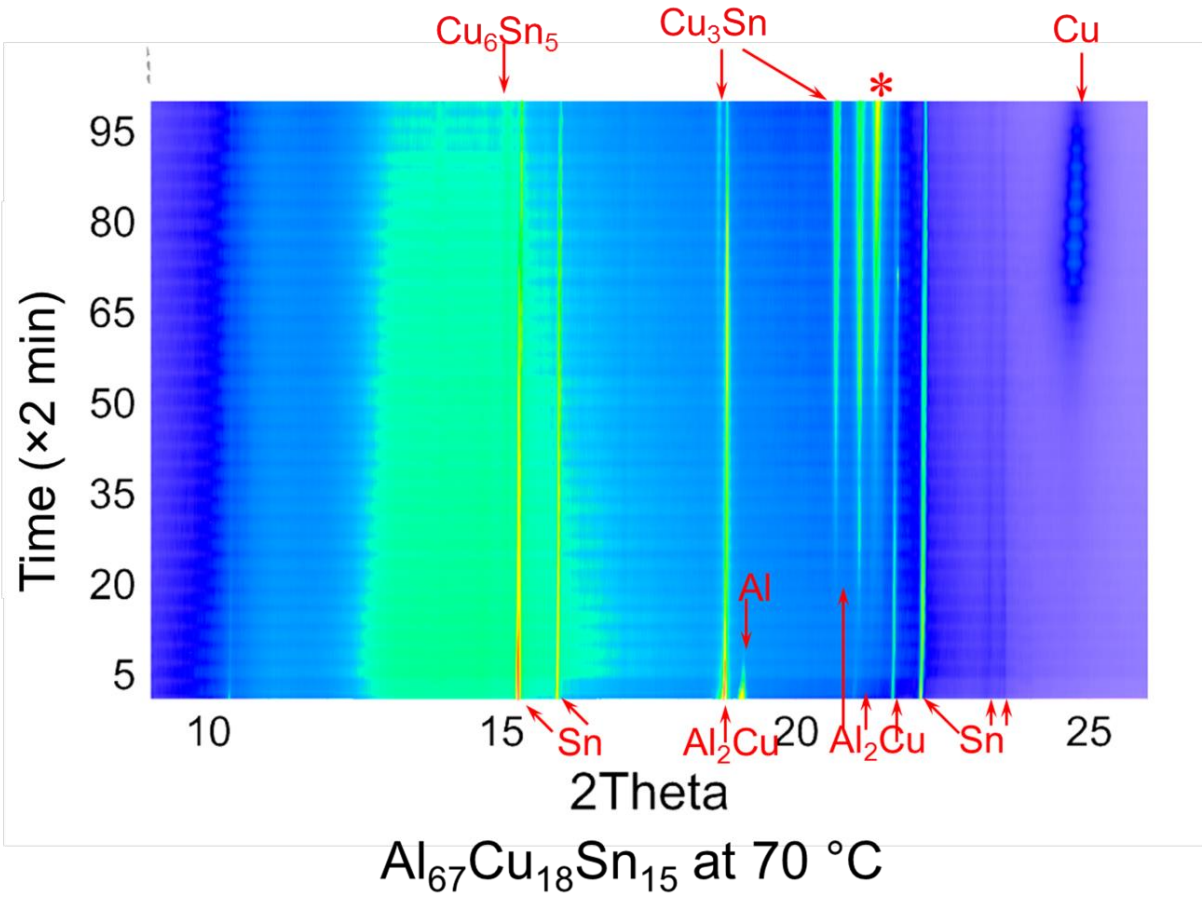

Fig. 6.2.4 In-situ phase evolution during the dealloying of the $Al_{67}Cu_{18}Sn_{15}$ alloy in a 5 wt.% HCl solution at 70 °C (∗: a mixture of Cu_6Sn_5, Cu_3Sn and Cu).

(3) Dealloying of the $Al_{67}Cu_{18}Sn_{15}$ at 90 °C

Figs. 6.2.5 and 6.2.6 present the results obtained from dealloying of the $Al_{67}Cu_{18}Sn_{15}$ alloy at 90 °C. The ex-situ synchrotron spectra are of good quality for quantitative analysis. The final as-dealloyed product at 90 °C is Cu_6Sn_5-Cu_3Sn with residual Al_2Cu (Fig. 6.2.6(a)). During dealloying of the $Al_{67}Cu_{18}Sn_{15}$ alloy at 90 °C, Cu_6Sn_5 formed first (Fig. 6.2.6(b)) and then Cu_3Sn emerged with the progress of dealloying. Based on the Rietveld refinement analysis in Fig. 6.2.7(a-c), the composition evolution for each phase is shown in Fig. 6.2.7(d), corresponding to the dissolution of Al and Al_2Cu (equations (1, 2)) and the formation of Cu_6Sn_5 and Cu_3Sn (equations (1, 2)). The Cu-Sn diffusion couple studies performed at temperatures above 100 °C have identified another reaction, described by reaction (5) below [2, 6, 7], for the formation and the continuing growth of Cu_3Sn in Cu-Sn diffusion couples. This reaction remains unclear from the conventional XRD results in **Chapter 4** and the in-

situ synchrotron results above. After 30 min dealloying at 90 °C, there is no more Sn phase left, indicating that neither equation (3) nor (4) should continue. However, the content of Cu_3Sn increased while that of Cu_6Sn_5 decreased (Fig. 6.2.7(d)). This quantitative analysis verifies the existence of mechanism (5) for the first time in the dealloying of $Al_{67}Cu_{18}Sn_{15}$ alloy at 90 °C.

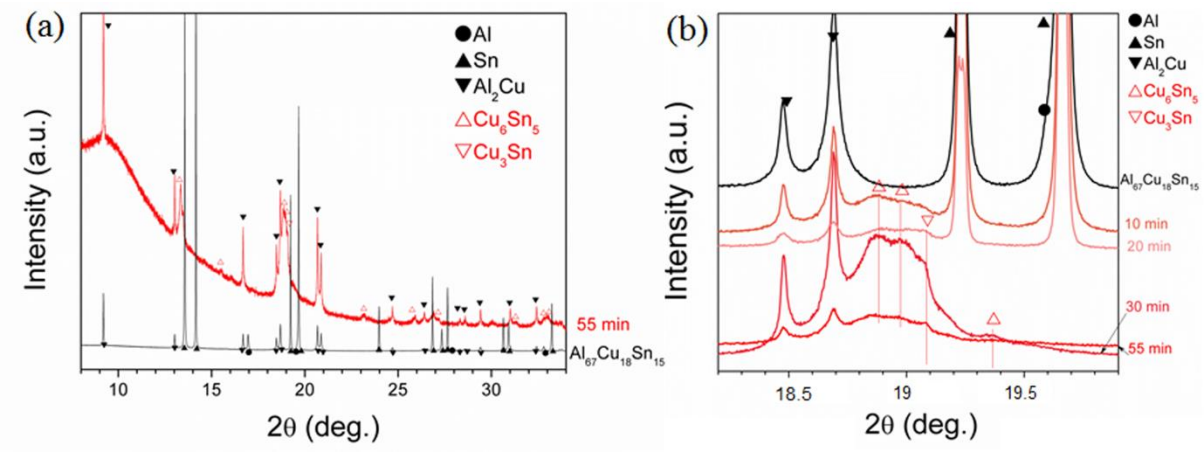

Fig. 6.2.5 Ex-situ phase evolution during the dealloying-realloying of the $Al_{67}Cu_{18}Sn_{15}$ alloy in a 10 vol.% HCl at 90 °C.

$$2\alpha\text{-Al(Cu)(s)} + 6HCl(l) \rightarrow 2Cu(s) + 2AlCl_3(l) + 3H_2(g) \quad (1)$$

$$Al_2Cu(s) + 6HCl(l) \rightarrow 2AlCl_3(l) + Cu(s) + 3H_2(g) \quad (2)$$

$$3Cu(s) + Sn(s) \rightarrow Cu_3Sn(s) \quad (3)$$

$$6Cu(s) + 5Sn(s) \rightarrow Cu_6Sn_5(s) \quad (4)$$

$$\frac{1}{5}Cu_6Sn_5(s) + \frac{9}{5}Cu(s) \rightarrow Cu_3Sn(s) \quad (5)$$

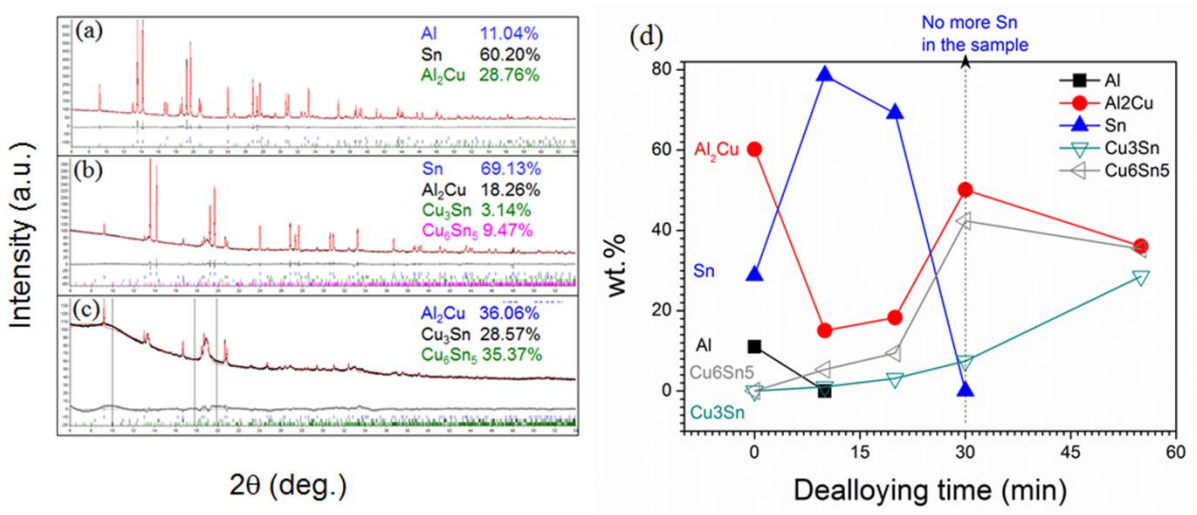

Fig. 6.2.6 (a-c) Examples of refinement analysis of synchrotron spectra with phase compositions, and (d) the evolution of phase compositions with increasing dealloying time.

6.2.4 Summary

A number of new experimental findings have been derived from the ex-situ and in-situ synchrotron studies of various Al-Cu and Al-Cu-Sn alloys. They will form an important experimental basis for both understanding the dealloying process of these alloys and designing new alloys to achieve desired nanoporous Cu or Cu-based composite structures.

References

[1] Y. Funamizu, K. Watanabe, Interdiffusion in the Al-Cu System, T. Jpn. I. Met., 12 (1971) 147-152.

[2] K.N. Tu, R.D. Thompson, Kinetics of interfacial reaction in bimetallic Cu-Sn thin films, Acta Metall., 30 (1982) 947-952.

[3] W.B. Liu, S.C. Zhang, N. Li, J.W. Zheng, Y.L. Xing, Influence of phase constituent and proportion in initial Al-Cu alloys on formation of monolithic nanoporous copper through chemical dealloying in an alkaline solution, Corros. Sci., 53 (2011) 809-814.

[4] Y. Wang, Y. Wang, C. Zhang, T. Kou, Z. Zhang, Tuning the ligament/channel size of nanoporous copper by temperature control, CrystEngComm, 14 (2012) 8352-8356.

[5] Q. Kong, L. Lian, Y. Liu, J. Zhang, Hierarchical porous copper materials: fabrication and characterisation, Micro Nano Lett., 8 (2013) 432-435.

[6] C.N. Liao, C.T. Wei, Effect of intermetallic compound formation on electrical properties of Cu/Sn interface during thermal treatment, J. Electron. Mater., 33 (2004) 1137-1143.

[7] K. Zeng, R. Stierman, T.C. Chiu, D. Edwards, K. Ano, K.N. Tu, Kirkendall void formation in eutectic SnPb solder joints on bare Cu and its effect on joint reliability, J. Appl. Phys., 97 (2005) 024508.

Chapter 7 Summary and future work

7.1 Summary

This thesis focused on two major issues on dealloying: (a) dealloyable precursor alloy systems and (b) dealloying mechanisms. The dealloyable alloy systems have been systematically extended from solid solution alloys to immiscible Al-Sn, ternary Al-Cu-Sn and two-phase Al-Cu alloy systems. A variety of products including porous Sn, porous Cu-Sn composites and porous Cu have been created as potential candidate materials for LIBs. In addition, with the effort of this thesis, the dealloying mechanisms for various precursor alloys studied have been clarified from the phase evolution perspective using advanced analytical means, especially ex-situ and in-situ synchrotron powder diffraction. The major conclusions are summarised as follows.

- Porous structures can be produced in the non-noble Sn metal through dealloying of Al from a variety of immiscible Al-Sn alloys in hydrochloric acid (HCl) solutions. The as-dealloyed porous Sn structures showed an average pore size in the range of 1.58 ± 0.26 μm to 4.09 ± 0.85 μm. The morphology and size of these pores are dependent on the morphology and size of the Al phase in respective precursor Al-Sn alloys. As a result, the resulting porous Sn structures can be manipulated through control of the composition and microstructure of the precursor alloy. The as-dealloyed porous Sn anode was assessed in a lithium ion battery and showed an outstanding initial capacity of 818 mA·h g^{-1} and a coulombic efficiency in the range of 65-99%. However, the cycle life was limited due to the lack of sufficient ductility and strength.
- A ternary $Al_{67}Cu_{18}Sn_{15}$ (at.%) alloy has been designed and dealloyed in a 5 wt% hydrochloric acid solution at 70 °C. Unlike dealloying of binary alloys, dealloying of the ternary $Al_{67}Cu_{18}Sn_{15}$ alloy was accompanied by a realloying process. Together they have enabled the fabrication of a nanoporous Cu_3Sn-Cu-Cu_6Sn_5 composite with an average ligament width of 170 ± 50 nm. The formation of Cu_3Sn and Cu_6Sn_5 intermetallics and the reaction between Cu_6Sn_5 and Cu during dealloying at 70 ± 2 °C are discussed in detail in relation to the experimental findings obtained from the Cu-Sn diffusion couple studies. This finding further proves the temperature sensitivity of phase formation in the Cu-Sn system established from Cu-Sn diffusion couple studies. Dealloying of multicomponent alloys offers an effective approach to the fabrication of

nanoporous composite materials including the formation of new phases through the accompanied realloying process.

- An annealing-electrochemical dealloying approach has been proposed for the creation of bimodal porous Cu materials and the approach has proved to be efficient and flexible in producing hierarchical porous Cu consisting of micro- and nano-sized (50-200 nm) porous structures from an as-cast $Al_{75}Cu_{25}$ (at.%) precursor alloy. The critical roles of annealing the as-cast $Al_{75}Cu_{25}$ precursor alloy in the proposed approach include (i) it decouples the lamellar eutectic structure and substantially increases the α-Al(Cu) phase size; both developments are essential for the production of the desired large porous structure; (ii) it reduces the solubility of Cu in the α-Al(Cu) phase and makes the subsequent dealloying of the α-Al(Cu) phase easier; and (iii) it decreases the critical potential (E_{crit}) value of the as-annealed $Al_{75}Cu_{25}$ precursor alloy and allows flexible selection of the applied potential for electrochemical dealloying, which is important for the creation of a homogenous hierarchical porous structure with fine ligaments (e.g. 52 nm).
- The most homogeneous bimodal porous Cu with the average ligament width of 52 nm was produced by electrochemical dealloying of the annealed $Al_{75}Cu_{25}$ alloy at the applied potential of -0.5 V, which is above the E_{crit} of the α-Al (Cu) but below that of the Al_2Cu phase. The complete dealloying of the Al_2Cu phase in the $Al_{75}Cu_{25}$ alloy is attributed to the beneficial effect of the dissolution of the Al atoms from the α-Al(Cu) phase, which offers penetration pathways for the electrolyte to interact with the Al atoms in the neighbouring Al_2Cu phase and therefore promotes dealloying of the Al_2Cu phase even at a low applied potential.
- The electrochemical dealloying of the ternary $Al_{67}Cu_{18}Sn_{15}$ alloy, which consisted of three phases of α-Al(Cu), Al_2Cu and Sn, was investigated. The presence of the Sn phase suppressed the dealloying of Al-based phases at the potential of -0.5 V, which is above the E_{crit} of the α-Al(Cu) but below that of the Al_2Cu phase. This was different from the complete dealloying of Al_2Cu observed in the dealloying of the binary $Al_{75}Cu_{25}$ at -0.5 V for the production of nanoporous Cu. At -0.2 V, two types of nanoporous structure resulted from the dealloying of Al_2Cu and α-Al, respectively, in the ternary $Al_{67}Cu_{18}Sn_{15}$. In addition, there was formation of scallop-type Cu_6Sn_5 on the as-dealloyed products at -0.2 V, indicative of the occurrence of realloying during the electrochemical dealloying of the ternary $Al_{67}Cu_{18}Sn_{15}$ alloy.

- Synchrotron radiation experiments were designed and Rietveld refinement analysis was used to understand the dealloying process of the as-cast $Al_{65}Cu_{35}$ alloy consisting of Al_2Cu and AlCu. Dealloying of Al_2Cu and AlCu occurred in a clear sequence due to crystallographic reason and this resulted in a hierarchical nanoporous Cu. Aside from this, it was identified that during the phase transformation from the Al_2Cu intermetallic phase to nanoporous Cu, α-Cu(Al) solid solution forms as an intermediate phase as a result of the high solubility of Al in the Cu lattice. With the progress of dealloying, the resolved Al atoms were removed gradually from α-Cu(Al). These results suggest that unless fully dealloying is realized, it is necessary to evaluate the possible impact of the residual Al on it e.g. the performance of nanoporous Cu used as the current collector materials for LIBs.
- The critical roles of crystal structure evolution during the dealloying of Al-Cu precursor alloys were discussed based on the results obtained from both ex-situ and in-situ dealloying experiments under synchrotron radiation. It was proposed that crystal structure evolution could alter the expected sequential dealloying behaviours of different intermetallic compounds. For instance, Al_2Cu and AlCu were expected to be dealloyed simultaneously due to their very similar corrosion potentials. However, they were dealloyed in clear sequence (Al_2Cu was dealloyed first). The reason can be attributed to different crystal structure evolution processes (i.e. easier from tetragonal Al_2Cu to cubic Cu than from monoclinic AlCu to cubic Cu). Apart from alloy composition, the crystal structure evolution may have played a significant role in dictating which phase is dealloyable. Al_4Cu_9 contains more Cu than the reported parting limit for Al-Cu alloys (Al50Cu50 (at.%)). However, it was dealloyed into Cu. The underlying reason could be that cubic Al_4Cu_9 can easily evolve into cubic Cu.
- The temperature sensitivity of intermetallic formation in the Cu-Sn system was confirmed by synchrotron studies of the $Al_{67}Cu_{18}Sn_{15}$ alloy subjected to dealloying at different temperatures (55 °C, 70 °C and 90 °C). The lowest temperature at which Cu_3Sn forms in the Cu-Sn system is now lowered to 55 °C. In addition, it has been confirmed that Cu_3Sn forms by the consumption of Cu_6Sn_5 and Cu.

The new experimental findings are expected to enrich the knowledge base in dealloying and provide an improved fundamental basis for the design and creation of advanced metallic materials *via* dealloying for wider industrial applications.

7.2 Future work

7.2.1 From the application perspective of as-dealloyed nanoporous metallic materials

Sn-based and Cu-based porous materials have been created in this research which meets the requirements for applications in LIBs. Only a preliminary assessment of porous Sn in LIBs has been performed. Nanoporous Cu is expected to be far more outperforming than microporous Sn. However, its performance has not been assessed as yet, where the lack of sufficient mechanical integrity has been a critical issue to the as-dealloyed nanoporous Cu materials.

The low mechanical integrity of the nanoporous Cu materials developed arises from: (i) the mechanical defects (microcracks, voids, shrinkages) which exist in the precursor alloy foils prior to dealloying; (ii) the existence of undesired intermetallic phases (which are brittle in nature) in the precursor alloy, and (iii) the inappropriate selection of dealloying electrolytes or processes which lead to uncontrollable dissolution and diffusion in the precursor alloys and therefore resulted in inhomogeneous nanoporous structures. These challenges might be addressed through utilizing a novel metal foils production technology (as discussed below) and through incorporating innovative fundamental developments to the dealloying practice made so far.

The metal foils production technology suitable for this purpose must meet the following requirements:

- It is a rapid solidification process and can be used to produce Cu-based alloy foils with an ultrafine homogeneous microstructure. The finer the microstructure of the precursor alloy, the more homogeneous the resultant nanoporous structure will be. Accordingly, a precursor alloy with an ultrafine or even a nanometric microstructure is always preferred.
- It can be used to produce Cu-based precursor alloy foils with different thicknesses and widths by varying the nozzle design and controlling melt flow and solidification rates. These characteristics can avoid the subsequent machining process such as cutting or polishing, which often introduces extra stress or contamination to the foil products.
- It is easy to change the superheat of the alloy melt and the solidification rate to achieve the optimization of the microstructure of the precursor alloys.

- It can realize large volume production for the production of the large scale of functional nanoporous Cu required in applications, e.g. up to several hundred meters per minute.

Following the improvement of mechanical integrity of the precursor alloy and the as-dealloyed products, systematic LIB studies of nanoporous Cu-Sn composites by tailoring experimental conditions is necessary. The exploration of the application of nanoporous Cu in heat and electrical transferring should be considered as well.

7.2.2 From the perspective of further understanding the dealloying process

In **Chapter 6** of this thesis, a number of new experimental findings have been derived from the ex-situ and in-situ synchrotron studies of a variety of Al-Cu and Al-Cu-Sn alloys. Based on the preliminary analysis of those experimental findings, we made certain understandings, such as the critical role of crystal structure evolution in creating hierarchical porous structures, and in revisiting the parting limit of Al-Cu alloy system, and the identification of formation of Cu_3Sn by the consumption of Cu_6Sn_5 and Cu. Our future studies will deal with:

1) Further systematic analyses (e.g. Rietveld Refinement analysis of each dataset) will be made of the ex-situ/in-situ synchrotron powder diffraction data.
2) Corresponding characterizations by other means, like SEM, TEM etc., of certain samples will be done to provide supplementary evidence for comprehensive understanding. In addition, the surface area measurements (such as BET and BJH) will be carried out as well, for robust results including surface area, porosity and pore distribution of the as-dealloyed porous materials.

It can lead to a more systematic understanding of not only dealloying of the Al-Cu and Al-Cu-Sn alloy systems, but also of other binary and/or ternary alloys. It can provide the improved fundamental basis for the design and creation of advanced metallic materials *via* dealloying for wider industrial applications.

Acknowledgments

I would like to acknowledge my principle supervisor, Prof Ma Qian. The value of his advice, unique and creative ideas and generous financial support is beyond quantification. I particularly want to appreciate Ma for training me to think critically and logically.

My co-supervisor Assoc Prof Ming Yan, deserves considerable credit for the initial offer, the constructive discussions and considerate encouragement all the time. I still don't know where his humility comes from and I do own him a lot of gratitude.

To my co-supervisor Prof Andrej Atrens, appreciate his generous support on the access of electrochemistry workstation and knowledge of electrochemistry.

Great thanks go to the financial support from China Scholarship Council (CSC) Scholarship, the University of Queensland International (UQI) Scholarship, Graduate School International Travel Award (GSITA) of UQ, RMIT Tuition Fee Wavier and Higher Degree by Research Travel Grant (HDRTG) of RMIT University.

Appreciate both of Centre for Microscope and Microanalysis (CMM) in UQ and RMIT Microscope and Microanalysis Facility (RMMF) for the facilities and scientific and technical assistance. Synchrotron XRD experiments were performed at the Australian Synchrotron Powder Diffraction Beamline (PD/8856, PD/7953, PD/7552).

I would like to thank the following people:

Dr Justin Kimpton of Australian Synchrotron for his generous advice on synchrotron beamline proposal submission, in-situ synchrotron experimental setting up, data analysis;

Dr Nathan Webster of CSIRO Mineral Resources Flagship, for his support on synchrotron experimental setting up, guidance on the refinement analysis by TOPAS;

Dr Mark styles of CSIRO Manufacturing Flagship, for his assistance on the synchrotron experimental setting up and overnight stay for the synchrotron experiments;

Prof Qijie Zhai and Prof Yulai Gao from the Center of Advanced Solidification Technology, Shanghai University, China for the access of the devices of melt-spinning and suction casting.

Dr Zhiming Shi of The University of Queensland for great help he offered related to the access of electrochemistry work station and analysis of electrochemical results;

Prof Yungui Chen of Sichuan University, China, for offering me an opportunity to stay in his group for two months, during which I started to know more about materials used in a battery and the entire battery field as well.

Colleagues in the University of Queensland and RMIT University. I'm so lucky that I could do the PhD in two places and I'm so grateful for your listening, sharing and companying.

Prof Frank Uwe Renner from Hasselt University, Belgium and A/Prof Takeshi Fujita from Tohoku University, Japan, the two examiners of this thesis, for their time, and positive and in-depth comments and suggestions.

I would like to thank my father back in China for his unconditional love and understanding. Finally to my mother: I have been firmly believing that you would be the happiest, the proudest one in the world if you knew your girl entered the university, did a master and now is finishing a PhD.